UNIVERSITÀ DI PISA

Corso di Laurea Magistrale in Fisica

Tesi di Laurea

Ageing and performance studies of drift chamber prototypes for the MEG experiment upgrade

Candidato:
Marco Venturini

Relatore:
dott. Giovanni Signorelli

Anno Accademico 2012-2013

A mia madre

Contents

Introduction **i**

I The $\mu \to e\gamma$ decay **1**

1 Theoretical background of $\mu \to e\gamma$ **3**
1.1 Experimental Foundations of Lepton Flavour Conservation 3
1.2 Lepton Flavour Conservation in the Standard Model 4
1.3 Neutrino Oscillations 6
1.3.1 Neutrino oscillations in the Standard Model 9
1.4 Charged Lepton Flavour Violation scenarios 10
1.4.1 Neutrino Oscillation induced cLFV 11
1.4.2 Seesaw Mechanisms 12
1.4.3 Grand Unification Theories and Supersymmetry 12
1.5 Searches for charged Lepton Flavour Violation 16

2 Searching for the $\mu \to e\gamma$ decay: the MEG experiment **19**
2.1 Characterisation of the $\mu \to e\gamma$ decay process 19
2.1.1 Prompt Background 20
2.1.2 Accidental Background 22
2.1.3 Single event sensitivity 23
2.2 The MEG experiment at PSI 24
2.2.1 Beam Line and Target 25
2.2.2 The Calorimeter 26
2.2.3 The positron spectrometer 28
2.2.4 Trigger and DAQ 32
2.2.5 Calibrations 33
2.3 MEG status and the MEG upgrade 34
2.3.1 Beam Line and Target 37
2.3.2 The Calorimeter 38

2.4 The positron spectrometer of MEG$^{\mathrm{UP}}$ 39
  2.4.1 The Drift Chamber 39
  2.4.2 The Timing Counter 42

II Preliminary tests of the prototypes of the new tracker 45

3 Physics of drift chambers 47
3.1 Drift chambers as detectors 47
3.2 Ionisation 47
3.3 Transport 49
3.4 Multiplication 50
  3.4.1 Dependence of the gain on density 52
  3.4.2 Space charge effects 53
  3.4.3 Statistical fluctuations of the gain 54

4 R&D on a single-cell prototype 55
4.1 The experimental setup 55
4.2 Prototype realization 57
4.3 Determination of prototype working point 60
4.4 Charge drift in Prototype I 64
4.5 Charge multiplication in Prototype I 68
  4.5.1 Voltage-current curve 68
  4.5.2 Linearity and space-charge effects 69
  4.5.3 Gain evaluation 70

5 Tracking with a drift chamber: three-cell arrangement 75
5.1 Particle tracking 75
5.2 Three–cell arrangement: the idea 77
5.3 Three-cell prototype realisation 78
5.4 Experimental setup 80
5.5 Drift chamber operation 83
5.6 Drift time–to–distance relations 85
5.7 Simple tracking in different configurations 87
5.8 Track reconstruction 91

III Ageing tests 93

6 Testing the lifetime of a drift chamber 95
6.1 Ageing of drift chambers 95

6.2 How a drift chamber gets old . . . 96
  6.2.1 The free radicals . . . 96
  6.2.2 Anodic coatings . . . 98
  6.2.3 Cathodic coatings . . . 99
  6.2.4 Pollutant and good materials . . . 100
6.3 Laboratory tests . . . 101
  6.3.1 Some sensitive physical parameters . . . 102
6.4 Ageing test procedures . . . 103

7 Preparation of the ageing tests 107
7.1 Charge accumulation in the new tracker . . . 107
7.2 The experimental setup . . . 108
7.3 X-ray production . . . 109
7.4 X-ray absorption . . . 111
7.5 Characterisation of the Moxtek X-ray source . . . 112
  7.5.1 Linearity test . . . 113
  7.5.2 Energy spectra . . . 113
  7.5.3 Angular distribution . . . 116
7.6 Characterisation of the Oxford X-ray source . . . 116
  7.6.1 Linearity test . . . 117
  7.6.2 Energy spectra: calibration . . . 117
  7.6.3 Energy spectra . . . 119
  7.6.4 Angular distribution . . . 121

8 Ageing tests 125
8.1 Ageing test on Prototype I . . . 125
  8.1.1 Temperature corrections . . . 126
  8.1.2 Part I . . . 126
  8.1.3 Part II . . . 129
  8.1.4 Summary . . . 130
8.2 Ageing test on Prototype II . . . 133
  8.2.1 Results . . . 136
8.3 Microanalysis of wires from Prototype I . . . 138
  8.3.1 Cathode I . . . 139
  8.3.2 Cathode II . . . 141
  8.3.3 Anode . . . 142

Conclusions and Outlook 151

Bibliography 155

Introduction

The MEG experiment aims at searching the $\mu \to e\gamma$ decay, prohibited in the framework of the Standard Model but foreseen in many of its extensions. MEG is currently taking data at the Paul Scherrer Institut (Zurich, Switzerland) and has recently published the analysis of data taken from 2009 to 2011, estabilishing a new upper limit on the branching ratio $\mathcal{BR}(\mu \to e\gamma) < 5.7 \times 10^{-13}$ at 90% CL, 20 times lower than the limit set by the previous experiment.

The experimental search of the decay is based on the measurement of the four-momentum of photons and positrons coming from the decays of muons at rest. Photon four-momentum is measured by a liquid xenon calorimeter, while the momentum of the positron is measured by a set of drift chambers immersed in a magnetic field, coupled to scintillating bars for accurate determination of the positron time. The analysis of data collected in 2012 is in progress, while a last run of data taking is expected to end at late August 2013, with the saturation of the sensitivity reach of the current experimental apparatus.

The MEG collaboration has recently proposed an upgrade of the experimental apparatus ($\mathrm{MEG}^{\mathrm{UP}}$): a new drift chamber and a xenon calorimeter with larger acceptance and granularity will be coupled to the current beam line and magnet. Such an upgrade can improve the sensitivity in the search for the decay of an additional factor 10 (down to a few 10^{-14}), where most of the extensions of the Standard Model foresee the existence of the decay.

The drift chamber of the MEG upgrade ($\mathrm{MEG}^{\mathrm{UP}}$) is a key element of the new apparatus. It is designed to improve the acceptance to the signal, keeping the material on the positron trajectory at minimum, since at the energies of the muon decay multiple scattering is the limiting factor in the measurement of the positron momentum. The drift chamber is composed of more than a thousand wires with stereo configuration, and is filled with a very low mass gas mixture of helium and isobutane. It must withstand a particle flux more intense than that in the current experiment (up to three times larger): at such rates gas molecules fragment and form deposits on the wire surfaces, thus reducing the performances of the chamber or in extreme cases making the detector not working. While designing a new detector, it is fundamental to test in details its performances by means of prototypes, and how the performances change because of the ageing of the detector itself, since the total charge collected on the hottest wires will be of the order of a few tenths of Coulombs per centimetre.

The topic of this thesis is the experimental study of the first prototypes realised, from their design and simulation. The prototypes were realised in the Pisa INFN laboratories and were characterised concerning their working points and their response to several kinds of radiation (α-particles, electrons, X-rays). From the analysis of the acquired data and through a simple tracking reconstruction procedure, an estimate of the resolutions achievable in the final detector was obtained in different working conditions, in order to direct the design of the new tracker.

For the ageing tests a new laboratory was set up from scratch; accelerated charge collection was induced on two prototypes by means of two X-ray sources, chosen and characterised conveniently. It will be shown how the realised prototypes can actually measure tracks of ionising particles, and withstand high radiation fluxes, highlighting the modifications induced by ageing.

The measurements performed in this work of thesis provided useful results for the design of the new drift chamber for MEG^{UP} , testing its performances as preliminary results.

In Chapter 1, the theoretical context of $\mu \to e\gamma$ searches is briefly explored, from the origin of Lepton Flavour Conservation in the Standard Model to the current scenarios for new physics. The experimental bases of the evolution of the theories are particularly stressed in a historical approach. Chapter 2 shows the experimental issues for $\mu \to e\gamma$ searches and how the MEG experiment has faced the challenge: the features and the obtained results are briefly discussed, focussing on the changes that are envisaged for MEG^{UP} and on its sensitivity reach.

Chapter 3 summarises some basic knowledge on drift chamber physics that will be useful in Chapter 4, where the realisation and the first signals of a single-cell prototype of the new tracker are presented. In Chapter 5 we present the design, the realisation and the test of a three-cell prototype. We will show in details, with a real prototype, the steps that are necessary to obtain a track, starting from the electrical signals, and we will show a possible way of obtaining an estimate of the single-hit resolution of the drift cells.

The last chapters of this thesis are focussed on the measurement of the ageing rate of the new tracker for MEG^{UP} by means of single-cell prototypes. After a quick overview on ageing phenomena and on the procedures used in laboratory tests (Chapter 6), the design and the setup of the ageing tests for MEG^{UP} drift chamber are discussed in Chapter 7, focussing on the choice of the working points of the whole apparatus. Finally in Chapter 8, ageing tests on two single-cell prototypes are described. The obtained results are presented, and for one of the prototypes, SEM and EDX analyses of aged wires are also shown.

Part I

The $\mu \to e\gamma$ decay

Chapter 1

Theoretical background of $\mu \to e\gamma$

In this chapter an experiment-driven introduction of the Lepton Flavour quantum number is presented. After discussing the experimental bases of Lepton Flavour Conservation and their realisation in the Standard Model, the first (and up to now the only) manifestations of Lepton Flavour Violations are shown: neutrino oscillations. Finally some scenarios of Flavour Violation in charged Leptons (cLFV) are introduced, skipping the technical details and highlighting the ones that predict cLFV amplitudes close to the sensitivity level of current experiments.

1.1 Experimental Foundations of Lepton Flavour Conservation

Since its discovery in 1936, the nature of the muon was a puzzle in early particle physics. In their article Anderson and Neddermeyer stated [1]:

> "There exist particles of unit charge with a mass larger than that of a normal free electron and much smaller than that of a proton [. . .]. The experimental fact that penetrating particles occur both with positive and negative charge suggests that they might be created in pair by photons and that they might be represented as higher mass states of ordinary electrons"

How to prove whether the muon is actually an excited state of the electron? If that were the case, the muon should be able to undergo the decay $\mu \to e\gamma$. The first attempts to search for the $\mu \to e\gamma$ were performed by Hincks and Pontecorvo [2], Sard and Althaus [3] and Piccioni [4]: after many efforts in improving the detection of gamma rays, they were able to rule out that $\mu \to e\gamma$ is one of the probable decay channels of the muon.

In the following years pions and strange particles were discovered, and the use of particle accelerators allowed the discovery of other mesons and baryons. It was a flourishing period for theorists too and the bases of the Standard Model (SM) were pinned down by Fermi, Feynman, Gell-Mann, Cabibbo and many others. Nevertheless there was still a basic experimental challenge: the direct detection of neutrinos. This was first achieved by Reines and Cowan with neutrinos from a nuclear reactor [5]. Soon thereafter neutrino interactions started to be probed with the use of accelerators, thus deeper studies were performed in neutrino physics and in particular in the search for an intermediate boson for the weak interactions. In 1962 Lederman, Schwartz and Steinberger following a hypothesis by Pontecorvo found that neutrinos obtained from pion decays convert to muons but not to electrons [6]. Since $\mathrm{BR}(\pi \to \mu\nu)/\mathrm{BR}(\pi \to e\nu) \sim 10^{-4}$, it seemed that neutrinos "remember" which particle they have been produced with. As they stated in their article, the existence of two kinds of neutrinos was an experimental fact closely entangled with the absence of the $\mu \to e\gamma$ decay:

> "A major difficulty of the Fermi theory at high energies is the necessity that it break down before the cross section reaches $\pi(\lambda/2\pi)^2$, violating unitarity. This breakdown must occur below 300 BeV in the center of mass. This difficulty may be avoided if an intermediate boson mediates the weak interactions. Feinberg pointed out, however, that such a boson implies a branching ratio $(\mu \to e\gamma)/(\mu \to e\nu\bar{\nu})$ of order 10^{-4}, unless the neutrino associated with muons are different from those associated with electrons. Lee and Yang have subsequently noted any general mechanism which could preserve unitarity should lead to a $\mu \to e\gamma$ branching ratio not too different from the above. Inasmuch as the branching ratio is measured to be 10^{-8}, the hypothesis that the two neutrinos may be different has found some favor. It is expected that if there is only one type of neutrino, then neutrino interactions should produce electrons and muons in equal abundance. In the event that there are two neutrinos, there is no reason to expect any electrons at all."

Therefore two new quantum numbers were assigned to leptons: the electron number L_e, being $+1(-1)$ for $e^-(e^+)$ and $\nu_e(\bar{\nu}_e)$ and 0 for other leptons, and muon number L_μ, similarly defined. Experiments seemed to dictate the conservation of flavour numbers, consequently forbidding flavour changing processes like $\mu \to e\gamma$. The SM was required to conserve lepton flavour.

Since then many other attempts were made in the search for Lepton Flavour Violation (LFV): from $\tau \to e\gamma$ to $K \to \pi e\mu$ to neutrinoless double beta decay $(Z, A) \to (Z + 2, A)\, e^-e^-$. No violation had been found until the discovery of neutrino oscillations (see Section 1.3).

1.2 Lepton Flavour Conservation in the Standard Model

The Standard Model of Fundamental Interactions (SM) is a gauge field theory which aims at describing the electromagnetic, weak and strong interactions of elementary particles[1]. The gauge group which it is based on is

$$SU(3)_\mathrm{C} \otimes SU(2)_\mathrm{L} \otimes U(1)_\mathrm{Y}$$

where $SU(3)_\mathrm{C}$ (colour symmetry) gives as gauge fields the mediators of strong interactions, $SU(2)_\mathrm{L}$ (weak isospin symmetry) and $U(1)_\mathrm{Y}$ (weak hypercharge symmetry) are related to the electroweak interactions.

---

[1] A short and uncomplete overview on Flavour physics in the Standard Model is presented. For a more detailed description of SM see [7, 8, 9]; for a brief but enlightening introduction see [10].

Focussing on the electroweak sector, the minimal coupling method allows us to introduce the interactions of matter particles with gauge bosons by replacing the ordinary derivative ∂_μ in the kinetic term of the Lagrangian with a covariant derivative $\mathcal{D}_\mu$ defined as

$$\mathcal{D}_\mu = \partial_\mu + i \sum_j g_j T_j^a A_\mu^{ja}$$

where g_j, T_j^a and A_μ^{ja} are the coupling constant, the a-th generator and the a-th gauge boson of the sub-group j ($SU(2)_\mathrm{L}$, $U(1)_\mathrm{Y}$), respectively. Minimal coupling makes the kinetic term covariant, but gauge invariance does not hold if ordinary mass terms are assumed for the particles of the theory; to solve this problem new fields are introduced (Higgs $SU(2)_\mathrm{L}$ doublet). Assuming a non-null vacuum expectation value $v \sim 174$ GeV for one of them, its interaction with fermions results in their mass terms, leading to a sponateous symmetry breaking of $SU(2)_\mathrm{L} \otimes U(1)_\mathrm{Y}$ into $U(1)_\mathrm{em}$.

In order to understand how flavour appears in the SM, it is necessary to have a look at matter particles. Quarks can be classified as representations of $SU(2)_\mathrm{L}$ in:

- three left-handed doublets $Q_\alpha = (u_{L\alpha},\, d_{L\alpha})$
- three right-handed up singlets $U_\alpha = u_{R\alpha}$
- three right-handed down singlets $D_\alpha = d_{R\alpha}$

where α is a flavour index ($u_\alpha = u, c, t,\ d_\alpha = d, s, b$). After the spontaneous symmetry breaking induced by the Higgs doublet (H), the electroweak SM Lagrangian for quarks is

$$\begin{aligned}\mathcal{L}_\mathrm{Q} = \sum_{\alpha,\beta=1}^{3} & i \left(\bar{Q}_\alpha \not{\mathcal{D}} Q_\beta + \bar{U}_\alpha \not{\mathcal{D}} U_\beta + \bar{D}_\alpha \not{\mathcal{D}} D_\beta \right) \delta_{\alpha\beta} \\ & + \lambda^U_{\alpha\beta} \left(Q^\dagger_\beta H U_\alpha + U^\dagger_\alpha H^\dagger Q_\beta \right) + \lambda^D_{\alpha\beta} \left(Q^\dagger_\beta H D_\alpha + D^\dagger_\alpha H^\dagger Q_\beta \right)\end{aligned}$$

where $\bar{f} = f^\dagger \gamma^0$ is the Dirac-conjugate bispinor of f. The kinetic+gauge terms are "diagonal" in flavour while the Yukawa terms (the other two) in general mix quarks with different flavours. Because of the limited number of free parameters, in the quark sector it is not possible to diagonalize simultaneously all the terms; this means that flavour (and mass) eigenstates d_α are different from interaction eigenstates $d'_\alpha = V_{\alpha\beta} d_\beta$, where $V_{\alpha\beta}$ is the Cabibbo-Kobayashi-Maskawa (CKM) matrix. This is how flavour violation is embedded in the quark sector of the theory.

In the Lepton Sector the situation is different: there is no experimental evidence of right-handed neutrinos (nor a neutrino mass measure). As representations of $SU(2)_\mathrm{L}$, leptons form three doublets $L_i = (\nu_{Li},\, l_{Li})$ and three singlets $E_i = l_{Ri}$, where $i = e, \mu, \tau$ is a flavour index.

After spontaneous symmetry breaking, the SM Lagrangian for the Lepton Sector is

$$\mathcal{L}_{\mathrm{LS}} = \sum_{\alpha=1}^{3} i\left(\bar{L}_\alpha \not{D} L_\beta + \bar{E}_\alpha \not{D} E_\beta\right)\delta_{\alpha\beta} + \lambda^E_{\alpha\beta}\left(L^\dagger_\alpha H E_\beta + E^\dagger_\beta H^\dagger L_\alpha\right) \tag{1.1}$$

In this case there is only one (presumably) non-diagonal matrix, which can be diagonalized by redefining the matter fields in a way that leave diagonal the kinetic+gauge terms. Therefore equation (1.1) becomes

$$\mathcal{L}_{\mathrm{LS}} = \sum_{\alpha=1}^{3} i\left(\bar{L}_\alpha \not{D} L_\alpha + \bar{E}_\alpha \not{D} E_\alpha\right) + \lambda^E_{\alpha}\left(L^\dagger_\alpha H E_\alpha + E^\dagger_\alpha H^\dagger L_\alpha\right) \tag{1.2}$$

Such a Lagrangian estabilishes Lepton Flavour Conservation in the SM: all the terms are diagonal in flavour.

1.3 Neutrino Oscillations

The measurement of neutrino masses has been (and still is) an experimental challenge taken on by many physicists (see *e.g.* [11]). Nonzero masses for neutrinos can be introduced in the SM with an additional Yukawa term in (1.2). In this way lepton flavour becomes analogous to quark flavour, *i.e.* violated[1]. Flavour eigenstates $\mid \nu_l \rangle$ are linear combinations of three neutrinos $\mid \nu_i \rangle$ with a well defined mass m_i [10, 12]. Neutrinos interact as flavour eigenstates, but propagate as eigenstates of the free-particle Hamiltonian (states with a well-defined mass).

In order to understand from an experimental point of view how this can be observed suppose[2] mixing between two families (say e, μ). If a $\mid \nu_e \rangle$ is produced at $\vec{x} = 0$ of some reference frame

$$\mid \nu\left(\vec{x} = 0\right)\rangle = \mid \nu_e \rangle = \cos\vartheta \mid \nu_1 \rangle + \sin\vartheta \mid \nu_2 \rangle$$

during its travel in free space the two components evolve indipendently, and at a generic $\vec{x}$

$$\mid \nu\left(\vec{x}\right)\rangle = e^{ip_1 x}\cos\vartheta \mid \nu_1 \rangle + e^{ip_2 x}\sin\vartheta \mid \nu_2 \rangle$$

Therefore there is a non-null probability that at a distance L from the production point the

---

[1] Note that a big difference lies in the fact that it is possible to produce (and detect) mass eigenstates of quarks *via* strong interactions (which are flavour-blind), while since neutrinos interact only weakly it is not possible to detect neutrino mass eigenstates.

[2] Neutrino oscillations are a subtle quantum-mechanical effect. The derivation presented is quite simplified: for a more accurate derivation see [10].

electron neutrino is detected as a muon neutrino:

$$\begin{aligned} P_{\nu_e \to \nu_\mu}(L) &= |\langle \nu_\mu \mid \nu(L) \rangle|^2 = \sin^2 2\vartheta \ \sin^2 \left(1.27 \, \frac{\Delta m^2 \, [\mathrm{eV}^2] \, L \, [\mathrm{m}]}{E \, [\mathrm{MeV}]} \right) \\ P_{\nu_e \to \nu_e}(L) &= 1 - P_{\nu_e \to \nu_\mu}(L) \end{aligned} \tag{1.3}$$

where E is the neutrino energy and $\Delta m^2 = m_1^2 - m_2^2$. Equation (1.3) is obtained in the ultrarelativistic limit, with $p_{1,2} = \sqrt{E^2 - m_{1,2}^2} \simeq E - m_{1,2}^2/2E$.

This very simplified version of the derivation of neutrino oscillation points out the main features of such a charming and complicated phenomenon:

- the use of the term "oscillations" instead of (for example) transitions. Neutrinos oscillate from one flavour to the other: after one period the probability to be back to the original flavour is one.
- the two parameters that characterise the oscillations (the mixing angle ϑ and the mass-square difference $\Delta m^2 = m_1^2 - m_2^2$) must both be nonvanishing to enable oscillations.

Considering three families, mixing appears as a lepton CKM matrix (known as PMNS mixing matrix[1]), which can be expressed in terms of three mixing angles (ϑ_{12}, ϑ_{13}, ϑ_{23}) and a phase δ:

$$U = \begin{pmatrix} 1 & 0 & 0 \\ 0 & \cos\vartheta_{23} & \sin\vartheta_{23} \\ 0 & -\sin\vartheta_{23} & \cos\vartheta_{23} \end{pmatrix} \begin{pmatrix} \cos\vartheta_{13} & 0 & \sin\vartheta_{13} e^{i\delta} \\ 0 & 1 & 0 \\ -\sin\vartheta_{13} e^{-i\delta} & 0 & \cos\vartheta_{13} \end{pmatrix} \begin{pmatrix} \cos\vartheta_{12} & \sin\vartheta_{12} & 0 \\ -\sin\vartheta_{12} & \cos\vartheta_{12} & 0 \\ 0 & 0 & 1 \end{pmatrix} \tag{1.4}$$

A full treatment of three-neutrino oscillations is more complex because of the entanglement of the different mixing angles and mass differences: oscillation probabilities have expressions that are more complicated than (1.3). Therefore (as usual) it is even more subtle to think up an experiment able to measure one of the parameters of the PMNS matrix. According to (1.3) the quantity E/L expresses the mass differences that can be explored by an experiment: the argument of the sinus function should be large in order to have a measurable effect. Oscillation effects can be observed in two ways, by appearance or disappearance. We give here a quick overview of some of the most important results, complemented by the 2012 result of $\vartheta_{13} \neq 0$ ([13] and references therein):

- **Solar neutrinos**. Nuclear fusion reactions taking place in the Sun release a great amount of energy as electron neutrinos. Neutrinos are therefore an important tool to study what happens in the innermost part of the Sun. The so-called solar neutrino problem came out in the late 1960s when Davis and Bahcall measured a flux of neutrinos from the Sun that was almost one third of the expected. Later on other experiments like Kamland and SNO

---

[1] after Pontecorvo, Maki, Nakagawa and Sakata.

found deficits of solar neutrinos too. In particular SNO showed both the disappearance of electron neutrinos and the appearance of neutrinos of different flavour. These experiments measured a mixing angle $\vartheta_\odot$ and a mass-square difference $\Delta m^2_\odot$ later identified with ϑ_{12} and Δm^2_{12}.

- **Atmospheric neutrinos**. Cosmic rays impinging on the Earth atmosphere create particle showers in which a lot of secondaries, mainly pions, are produced. In the decay chain $\pi \to \mu \to e$ three neutrinos are produced: one $\bar{\nu}_e$ (or one ν_e, according to the charge of the parent pion), one ν_μ and one $\bar{\nu}_\mu$. Therefore the ratio of muon neutrinos and antineutrinos to electron neutrinos and antineutrinos should be close to 2. In 1998 SuperKamiokande presented the first compelling evidence for neutrino oscillations, as a disappearance of muon neutrinos from atmospheric neutrinos and a corresponding lack of appearance of electron neutrinos (interpreted as tau neutrino appearance). Atmospheric neutrino measurements allow to determine ϑ_{23} and a square-mass difference $\Delta m^2_A = |\Delta m^2_{31}| \simeq |\Delta m^2_{32}|$.
- **Accelerator neutrinos**. Homemade neutrinos have the great advantage of a narrow and well-known spectrum and the possibility of choosing both oscillation length and energy (almost) *ad libitum.* In addition accelerators are the only significant source of tau neutrinos (and of high energy neutrinos that can oscillate into tau neutrinos and be detected by tau production), allowing both tau neutrino appearance and disappearance experiments.
- **Reactor neutrinos**. Nuclear reactors are a copious source of electron antineutrinos, clean of muon neutrino contaminations. This makes reactor neutrinos suitable for determining ϑ_{13}. Recently several experiments (such as RENO, Double-Chooz and Daya Bay) succeeded in measuring ϑ_{13}: before such results there was only an upper limit on ϑ_{13}, set by the CHOOZ and Palo Verde experiments. This represents a non-null mixing between the first neutrino family and the others. Moreover its value is very important because it opens up the possibilities for searching for CP-violation effects on neutrino oscillations (thus measuring δ) and for determining the type of neutrino mass spectrum (see below).

The existing neutrino oscillation data return the following values for the parameters [13]:

$$\begin{aligned}
\Delta m^2_{21} &\simeq 7.65 \times 10^{-5}\mathrm{eV}^2 && \text{from solar neutrinos} \\
\sin^2\vartheta_{12} &\simeq 0.304 && \\
\left|\Delta m^2_{31}\right| &\simeq 2.40 \times 10^{-3}\mathrm{eV}^2 && \text{from atmospheric neutrinos} \\
\sin^2 2\vartheta_{23} &\simeq 1 && \\
\sin^2 2\vartheta_{13} &\simeq 0.10 && \text{from reactor neutrinos}
\end{aligned} \tag{1.5}$$

Depending on the sign of Δm^2_{31} two of the possible scenarios for ν mass hierarchy are shown in Figure 1.1.

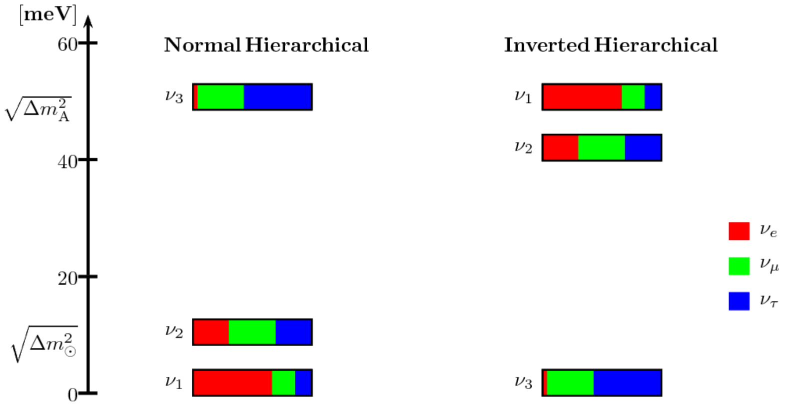

Figure 1.1 Two different scenarios for neutrino mixing (mass values are approximate). The colours represent the projections of mass eigenstates on flavour eigenstates, calculated insering values (1.5) in (1.4); δ contribution is not significant.

1.3.1 Neutrino oscillations in the Standard Model

Currently it is quite estabilished that neutrino oscillations are induced by neutrino mass mixing. Anyway the LFV mechanism mentioned in Section 1.3 is not the only possible one: there are two general ways to make neutrinos massive in the SM.

(i) **Dirac Massive Neutrino** This is the method mentioned at the beginning of this section and can be obtained introducing a right-handed neutrino ν_R neutral to all SM interactions[1]. It appears in the Lepton Sector Lagrangian (1.2) in a Yukawa term and returns a mass term $m_\nu \nu_R^\dagger \nu_L$ (Dirac mass):

$$\mathcal{L} = \mathcal{L}_{\mathrm{LS}} + \sum_{\alpha,\beta=1}^{3} \left(\bar{\nu}_{R\alpha} \not{\partial} \nu_{R\alpha} + \lambda^N_{\alpha\beta} L^\dagger_\alpha H \nu_{R\beta} + \mathrm{H.c.} \right)$$

(ii) **Majorana Massive Neutrino** It is possible to introduce a non renormalizable term in the SM Lagrangian as a low-energy manifestation of heavy new physics:

$$\mathcal{L} = \mathcal{L}_{\mathrm{LS}} + \sum_{\alpha,\beta=1}^{3} \frac{\lambda_{\alpha\beta}}{\Lambda_L} \left(L^\dagger_\alpha H \right) \left(L^\dagger_\beta H \right) + \mathrm{H.c.} \tag{1.6}$$

where Λ_L is has the dimensions of a mass and indicates the energy scale of LFV new physics. This in turn gives the Majorana mass term $m_{\alpha\beta} \nu_{L\alpha} \nu_{L\beta}$. Such $m_{\alpha\beta}$ is similar to PMNS matrix in (1.4) but contains two more phases as parameters. From a dynamical point of view, it not only breaks lepton flavour conservation but the conservation of the

---

[1] its neutrality is fundamental because of the absence of an experimental evidence.

lepton number itself[1], giving a nonzero amplitude for the neutrinoless double beta decay.

These are two possible manifestations of LFV, but what are the physical mechanisms underlying such statements is unknown. In addition, given that neutrinos are massive, it is not clear if there is a way to reproduce such small neutrino masses without taking it as a matter of fact. This point, together with the hierarchy problem of neutrino masses (*i.e.* which is the true situation between the two shown in Figure 1.1), has been dealt with in many contexts: some of the theories clarifiying these aspects predict nonzero amplitudes for charge Lepton Flavour Violation (cLFV) and will be briefly described in the next section.

1.4 Charged Lepton Flavour Violation scenarios

The muon is a lucky particle from an experimental point of view: it is easy to produce, it has an almost-macroscopic mean life, it has a very limited number of decay channels that are free from the complications of strong interactions and hadron structures. These facts make the muon a useful tool to probe the SM and to search for new physics: many experiments looked (and are looking) for deviations from SM predictions in its decay amplitudes, its gyromagnetic factor (the famous $g-2$) and in the distribution of its decay products. Current experimental values for its mass and lifetime are [13]

$$\begin{aligned} m_\mu &= (105.6583715 \pm 0.0000035)\,\mathrm{MeV} \\ \tau &= (2.1969811 \pm 0.0000022) \times 10^{-6}\,\mathrm{s} \end{aligned}$$

Muons decays almost exclusively in the channel[2] $\mu^- \to e^- \nu_\mu \bar{\nu}_e$. Figure 1.2 shows the Feynman diagram of the process. Neglecting corrections of order $(m_e/m_\mu)^2 \sim 10^{-5}$, the SM prediction for its decay width is

$$\mathit{\Gamma}_\mu = \frac{G_\mathrm{F}^2 m_\mu^5}{192\pi^3} \sim (2.2\,\mu\mathrm{s})^{-1}$$

where $G_F \simeq 1.166 \times 10^{-5}$ GeV^{-2} is the Fermi coupling constant.

---

[1] In all the SM terms bispinors representing fermions wavefunctions are contracted with a Hermitean conjugate spinor ($u_L^\dagger u_L$, $e_L^\dagger \nu_L \ldots$). This fact gives two $U(1)$ global symmetries (Baryon number, Lepton number) to the SM Lagrangian since the tranformations

$$f \to e^{i\alpha} f\,, \quad f^\dagger \to e^{-i\alpha} f^\dagger \qquad \text{(separately for quarks and leptons)}$$

leave the Lagrangian unchanged. A f^2 term like Majorana mass breaks this symmetry in the Lepton Sector.

[2] Radiative and non-radiative decays cannot be clearly separated. For gamma energies above 10 MeV the Branching Ratio is $(1.4 \pm 0.4)\%$. The probability of the decay with an electron pair in place of the gamma is $(3.4 \pm 0.4) \times 10^{-5}$. So far no other decay channels have been observed.

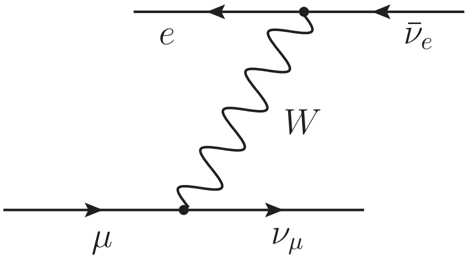

Figure 1.2 Feynman diagram for the muon decay in the SM.

1.4.1 Neutrino Oscillation induced cLFV

From the introduction of neutrino mixing in the SM, it naturally follows a nonvanishing amplitude for $\mu \to e\gamma$: in Figure 1.3 the Feynman diagram of the process is shown.

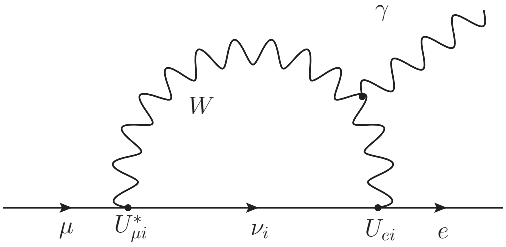

Figure 1.3 Feynman diagram due to neutrino oscillations for $\mu \to e\gamma$.

The amplitude of the process can be estimated comparing Figure 1.2 with Figure 1.3. Pictorially the latter differs from the former in “closing” the two neutrino lines (*i.e.* enabling oscillations) and adding a photon emission. Therefore the decay width of the process can be estimated to be

$$\Gamma \sim \frac{G_\mathrm{F}^2 m_\mu^5}{192\pi^3} \times \alpha \times \left| \sum_{i=1}^{3} U^*_{\mu i} U_{ei} \frac{m_i^2}{M_W^2} \right|^2 \tag{1.7}$$

where α is due to the electromagnetic vertex and the oscillation factor is a kind of three-family version of equation (1.3), with the oscillation taking place during a W's lifetime[1]. Neutrino masses can be approximated using the mass-square differences. Even taking the coefficients of the PMNS matrix of the order of unity and considering three times the biggest of the mass-squared differences, the predicted Branching Ratio is [14]

---

[1] The insertion of neutrino masses is necessary in order to have a nonvanishing amplitude because $\sum_i U^*_{\mu i} U_{ei} = 0$ (U is unitary).

$$\mathrm{BR}\,(\mu \to e\gamma) \equiv \frac{\Gamma}{\Gamma_\mu} \lesssim \frac{1}{137}\left(3 \times 1 \times \frac{2.4 \times 10^{-3}\,\mathrm{eV}^2}{(8.1 \times 10^{10}\,\mathrm{eV})^2}\right)^2 \simeq 10^{-52}$$

that is an unmeasurably small number. The absence of a measurable amplitude for $\mu \to e\gamma$ in the SM implies that any observation of the process would be a clear signal of new physics.

1.4.2 Seesaw Mechanisms

Seesaw models describe how to obtain nonrenormalizable terms like $(L^\dagger H)^2$ in (1.6) as a low energy limit of a new theory[1] [12, 10, 15]. There are three types of seesaw models according to the new particles introduced: for example we consider a minimal formulation of type-I seesaw, with three extra fermion singlets ν_R with mass $M \gg 1$eV. In this case the Lagrangian becomes

$$\mathcal{L} = \mathcal{L}_{\mathrm{SM}} + \frac{1}{2} M^N_{\alpha\beta} \nu_{R\alpha} \nu_{R\beta} + \lambda^N_{\alpha\beta}\, L^\dagger_\alpha H_\beta\, \nu_R \,+\, \mathrm{H.c.}$$

giving the mass terms

$$\begin{pmatrix} \nu_{L\alpha} & \nu_{R\alpha} \end{pmatrix} \begin{pmatrix} 0 & \lambda^N_{\beta\alpha} v \\ \lambda^N_{\alpha\beta} v & M^N_{\alpha\beta} \end{pmatrix} \begin{pmatrix} \nu_{L\beta} \\ \nu_{R\beta} \end{pmatrix}$$

There are two extreme cases:

- If $M^N_{\alpha\beta} \gg \lambda^N_{\alpha\beta} v$ the eigenstates of the mass matrix are three Majorana ν_R with mass matrix $M^N_{\alpha\beta}$ and three Majorana ν_L with mass matrix $m^\nu_{\alpha\beta} = -(\lambda^N_{\alpha\gamma} v)^T\,(M^{N^{-1}})_{\gamma\delta}\,(\lambda^N_{\delta\beta} v)$. Here is the seesaw: the heavier ν_R, the lighter ν_L.
- If $M^N_{\alpha\beta} \ll \lambda^N_{\alpha\beta} v$ we get three Dirac mass terms with mass $m^\nu_{\alpha\beta} = \lambda^N_{\alpha\beta} v$.

In this context cLFV can follow for example from weak interaction couplings of right-handed neutrinos and charged leptons, which are determined by requiring to reproduce neutrino oscillation data. Seesaw predicted rates depend on a few parameters and, for some values of them, are close to current experiments sensitivities. See the tight correlation between PMNS parameters and the predicted Branching Ratio of $\mu \to e\gamma$ in Figure 1.4.

1.4.3 Grand Unification Theories and Supersymmetry

Almost all the SM predictions are found to be in an incredible agreement with experimental data. Except a few (yet significant) experimental issues, such as muon $g-2$, neutrino masses and Dark Matter, the Standard Model presents some unsatisfactory theoretical aspects:

(i) Is it possible to unify all the interaction mediators as gauge bosons of a unique group broken at some energy scale? Is it possible to join all matter fields as a few (or unique) representations of such a big gauge group?

---

[1] Just like Fermi theory is a low energy approximation of SM weak interactions.

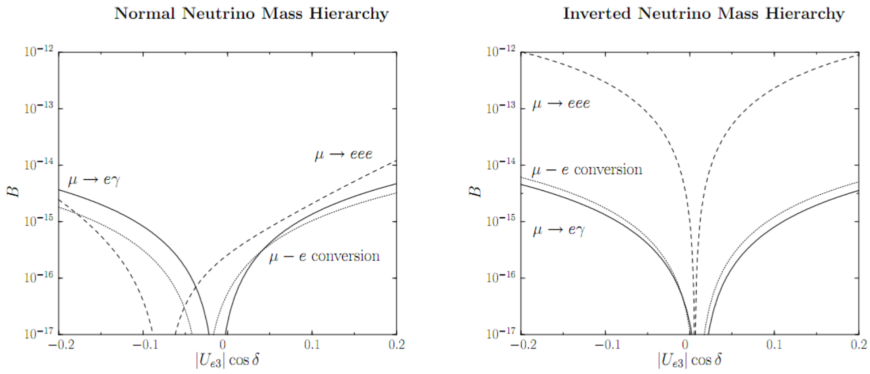

Figure 1.4 The Branching Ratios (BRs) for $\mu \to e\gamma$ (solid line) and $\mu \to eee$ (dashed line), and the normalized Capture Rate (CR) for $\mu - e$ conversion in Ti (dotted line) as a function of $|U_{e3}|\cos\delta$ in a scenario with a triplet Higgs (figure from [16]).

(ii) Why are lepton masses so much smaller than the electroweak symmetry breaking scale v? ("Flavour Problem")

(iii) Why the SM energy scale is so smaller than the Planck mass $M_{\text{Pl}} \simeq 10^{19}$ GeV/c^2? ("Hierarchy Problem")

Theories aiming at answering such questions are called Grand Unification Theories (GUTs). Such theories are based on larger gauge symmetries that are assumed to be broken at some energy scale into the usual SM gauge symmetry. A representative example of such theories is the naive $SU(5)$ GUT. Matter fields are grouped only in two multiplets (for each generation). Six new gauge bosons are predicted, having GUT-scale masses and couplings violating both lepton and baryon number (yet preserving an accidental symmetry $B - L$). Thus nonvanishing amplitudes are predicted for both $\mu \to e\gamma$ and for proton decay. The theory provides also a tunable connection between lepton and quark masses. However SuperKamiokande limit on proton lifetime excluded such naive $SU(5)$ GUT.

Currently the most promising GUTs providing a measurable amplitude for $\mu \to e\gamma$ lie in a Supersymmetry context. Supersymmetric (SUSY) models are the favourite candidates for physics Beyond the Standard Model[1]. They postulate a mirror symmetry, broken at some energy scale[2], which associates to each SM fermion (boson) a boson (fermion) companion. Each gauge boson has also, as a supersymmetric partner, a fermionic gaugino (photino, zino…), each fermion has a sfermion (smuon, sneutrino, squark…). In Minimal Supersymmetric Standard Model, electroweak symmetry breaking needs two Higgs doublets. SUSY in general allows lepton-slepton transitions, therefore any mixing in sleptons can provide cLFV. Figure 1.5 shows a Feynman

---

[1] For an introduction to supersymmetries see the first chapters of [17].

[2] Supersymmetry breaking is necessary because otherwise supersymmetric particles (sparticles) should have the same mass of their SM companions, so they would have been already observed.

diagram for $\mu \to e\gamma$ with slepton mixing [18].

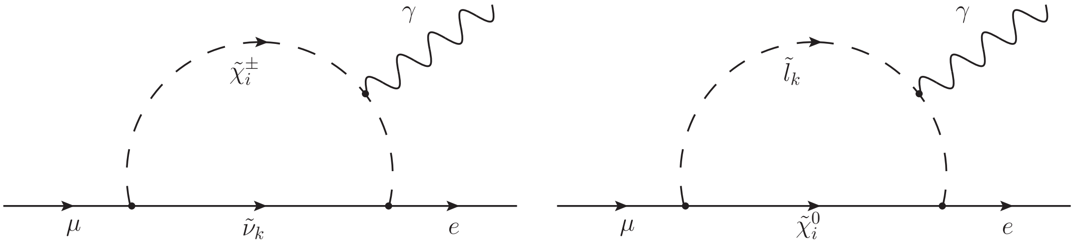

Figure 1.5 Slepton-chargino (left) and slepton-neutralino (right) contributions to $\mu \to e\gamma$ in Minimal Supersymmetric Standard Model.

Large nondiagonal terms in slepton mass matrix can be induced by top-quark quantum corrections. TeV-scale supersymmetry may solve all of the SM problems above mentioned, and in a wide area of parameters space give a predicted Branching Ratio $\mathcal{BR}(\mu \to e\gamma)$ of about 10^{-13} (see Figure 1.6).

In addition SUSY theories predict quite strong correlations between $\mathcal{BR}(\mu \to e\gamma)$ and other relevant physical quantities. In particular there is a tight link between $\mathcal{BR}(\mu \to e\gamma)$ and muon $g-2$: in a mixing context, the former depends on the (μ, e) amplitude of mixing, while the latter on the (μ, μ) amplitude[1]. Therefore a low $\mathcal{BR}(\mu \to e\gamma)$ upper limit can significantly constrain other predicted values and viceversa. For instance see in Figure 1.7 and 1.8 the correlation with ϑ_{13} and muon $g-2$ anomaly $\Delta a_\mu = a_\mu^{\text{exp}} - a_\mu^{\text{SM}}$ in two different SUSY theories.

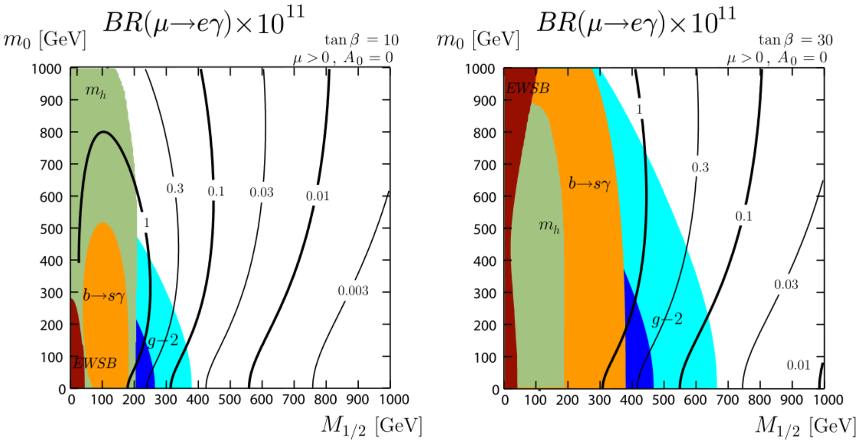

Figure 1.6 $\mathcal{BR}(\mu \to e\gamma)$ as a function of the universal SUSY boson mass m_0 and the universal SUSY fermion mass $M_{1/2}$ in a SUSY $SU(5)$ GUT with Right-handed Neutrinos. Coloured areas are excluded by other measurements (figure from [19]).

---

[1] the link between the two amplitudes will be clearer in the next section.

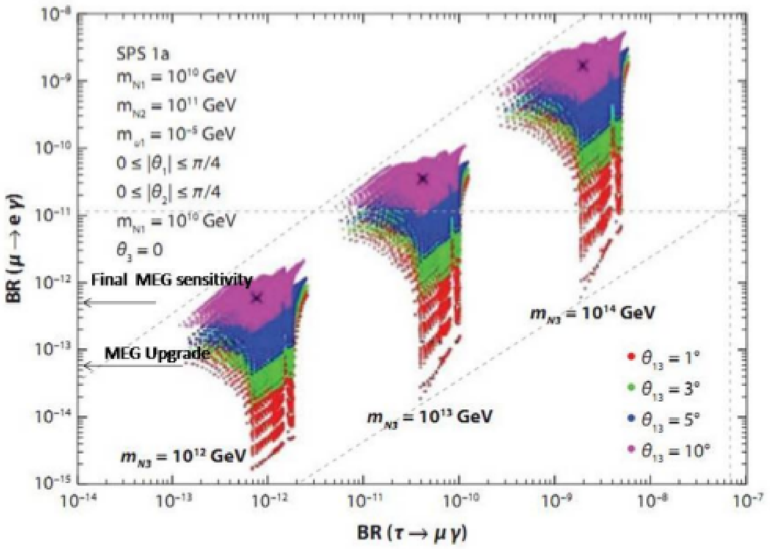

Figure 1.7 SUSY seesaw model predictions for $\mu \to e\gamma$ versus for $\tau \to e\gamma$ as a function of the largest of the masses of the right-handed neutrinos introduced and of ϑ_{13} (figure from [20]).

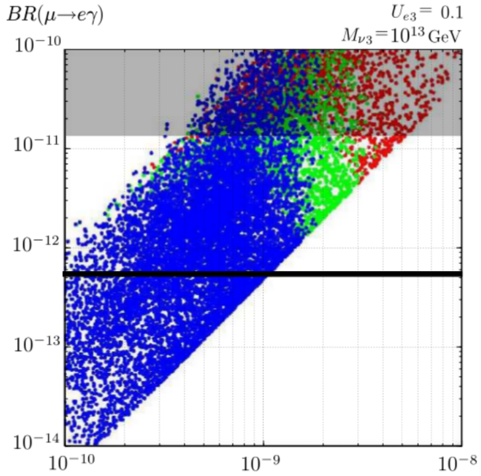

Figure 1.8 Muon $g-2$ anomaly versus $\mathcal{BR}(\mu \to e\gamma)$ in a SUSY $SU(5)$ GUT with Right-handed Neutrinos. Green (blue) points satisfy the constraints from $\mathcal{BR}(B \to X_s\gamma)$ at the 99% C.L. (90% C.L.) limit. The grey region is excluded by an old experimental upper bound on $\mathcal{BR}(\mu \to e\gamma)$. The thick black line is the current MEG upper limit (figure from [19]).

1.5 Searches for charged Lepton Flavour Violation

The $\mu \to e\gamma$ process is strictly related to two other cLFV processes: $\mu \to eee$ and $\mu - e$ conversion of muons captured by nuclei, which are both suppressed in the SM[1]. In order to compare the various cLFV amplitudes, a model-independent effective Lagrangian can be used [21] where only tree-level diagrams contribute to $\mu \to e\gamma$

$$\mathcal{L} = \frac{m_\mu}{(\kappa+1)\Lambda^2}\bar{\mu}_R\sigma_{\alpha\beta}e_L F^{\alpha\beta} + \frac{\kappa}{(\kappa+1)\Lambda^2}\bar{\mu}_R\gamma_\alpha e_L \bar{f}\gamma^\alpha f \tag{1.8}$$

where κ is an adimensional parameter and Λ represents the energy scale of cLFV physics; f represents a general fermion that is an electron in $\mu \to eee$ or a quark in $\mu - e$ conversion. Notice that for $\mu \to e\gamma$ only the first term contributes. Muon $g-2$ anomaly can be taken into account by adding an additional term, analogous to the first in (1.8) with $(\bar{\mu}_R, e_L)$ replaced with $(\bar{\mu}_R, \mu_L)$. Figure 1.9 shows the parameters space that can be explored for a given sensitivity in the three cLFV channels.

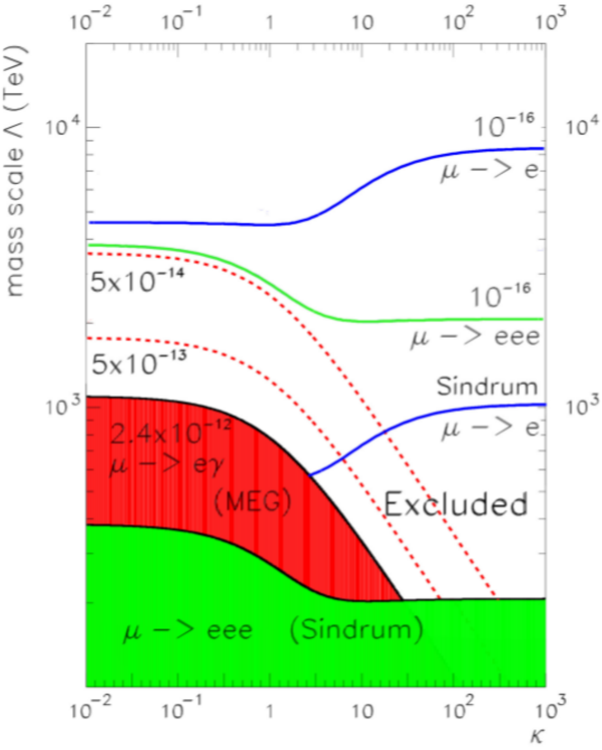

Figure 1.9 Sensitivities in $\mu \to e\gamma$, $\mu \to eee$ and $\mu - e$ conversion plotted in the (Λ, κ) plane (figure from [21]).

---

[1] As a rough estimate, their amplitudes can be considered α times smaller than that of $\mu \to e\gamma$ (there is one more electromagnetic vertex).

The current upper limits on such processes are

$$\begin{aligned} \mathcal{BR}(\mu \to e\gamma) &< 5.7 \times 10^{-13}\,(90\%\,\text{C.L.}) && \text{from MEG} \\ \mathcal{BR}(\mu \to eee) &< 1.0 \times 10^{-12}\,(90\%\,\text{C.L.}) && \text{from SINDRUM} \\ \mathcal{CR}(\mu\text{Au} \to e\text{Au}) &< 6.1 \times 10^{-13}\,(90\%\,\text{C.L.}) && \text{from SINDRUM II} \end{aligned}$$

Figure 1.10 shows the experimental upper limit estabilished as a function of the year in the most sensitive cLFV channels.

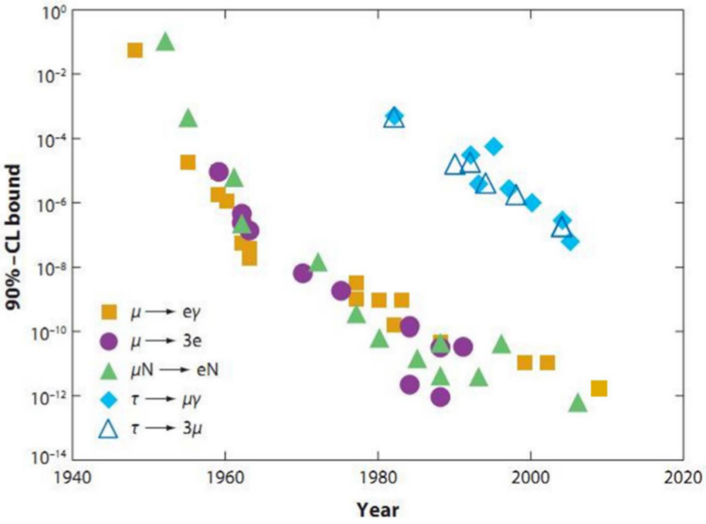

Figure 1.10 Experimental upper limit on the most sensitive cLFV processes as a function of the year (figure from [21]).

It is clear that the search of all three cLFV processes is important in order to understand the mechanisms beyond lepton flavour violation. The MEG experiment, described in the following Chapter, searches for $\mu \to e\gamma$ while other experiment in the USA, Europe and Japan are planned to search for $\mu \to eee$ (Mu3e at PSI) and $\mu \to e$ conversion (Mu2e at Fermilab, Comet at J-Park).

Summary

Charged lepton flavour violating decays are prohibited in the framework of the Standard Model, but many of its extensions predict measurable values for such decays. Several experiments are running or being designed to set a limit or to measure such processes.

Chapter 2

Searching for the $\mu \to e\gamma$ decay: the MEG experiment

After showing the characteristics of the $\mu \to e\gamma$ decay, we will describe the MEG apparatus ad its performances. Years of operation showed that in order to increase the detector sensitivity a re-design of the key elements of the apparatus is necessary. The proposed upgrade is therefore described, paying special attention to the new tracker.

2.1 Characterisation of the $\mu \to e\gamma$ decay process

The $\mu \to e\gamma$ decay has a very simple kinematic signature: it is a two-body decay, so in the reference frame where the muon is at rest the electron and the photon have the same energy, equal to half of the muon mass[1] $E = m_\mu/2 = 52.83$ MeV (see Figure 2.1).

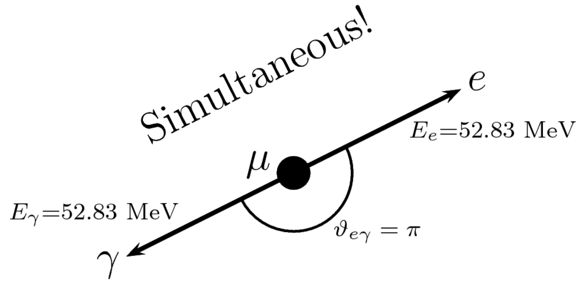

Figure 2.1 Kinematics of the $\mu \to e\gamma$ decay in the reference frame where the muon is at rest. The four fundamental parameters are shown.

To identify experimentally the process one should look for a photon and a positron:

---

[1] neglecting corrections due to the nonzero electron mass of order $(m_e/m_\mu)^2 \sim 10^{-5}$.

Experiment (Year)	Rate [Hz]	Duty f.	σ_{Ee}	$\sigma_{E\gamma}$	$\sigma_{te\gamma}$	$\sigma_{\vartheta e\gamma}$	(90% CL) Upper Limit
TRIUMF (1977) [22]	2×10^5	100%	10.3%	9.9%	6.7 ns	80 mrad	3.6×10^{-9}
SIN (1980) [23]	5×10^5	100%	8.7%	9.3%	1.4 ns	–	1×10^{-9}
E328 (1982) [24]	2.4×10^6	6.4%	8.8%	7%	1.9 ns	37 mrad	1.7×10^{-10}
Crystal Box (1988)[25]	4×10^5	6.6%	8%	8%	1.7 ns	37 mrad	4.9×10^{-11}
MEGA (1999) [26]	2.5×10^8	6.5%	1.2%	4.5%	1.6 ns	15 mrad	1.2×10^{-11}
MEG (2013) [27]	3×10^7	100%	0.6%	1.7%	0.12 ns	13 mrad	5.7×10^{-13}*
MEG$^{\mathrm{UP}}$ (2016?)[21]	7×10^7	100%	0.25%	1%	0.08 ns	6.5 mrad	6×10^{-14}

Table 2.1 Historical progress of $\mu \to e\gamma$ searches. Values for the MEG experiment refers to the last results, while those for the MEG upgrade are indicative. *not final.

(i) coming from the decay of positive muons at rest, positive muons being preferred in order to avoid nuclear capture;

(ii) moving collinearly back-to-back, *i.e.* $\vartheta_{e\gamma} = \pi$;

(iii) detected in coincidence, *i.e.* $\Delta t_{e\gamma} = 0$;

(iv) having exactly an energy $E = m_\mu/2$ both.

It is clear that in order to precisely identify the process, good angular, timing and energy resolutions are required (see in Table 2.1 the resolutions of various experiments and the $\mathcal{BR}$ limit they could set). There are two major backgrounds that can mimic a $\mu^+ \to e^+\gamma$ event signature: a prompt background from radiative muon decays $\mu^+ \to e^+\nu_e\bar{\nu}_\mu\gamma$ with neutrinos that carry away little energy, and an accidental background from a coincidence of uncorrelated events that produce a positron and a photon with the required kinematic parameters.

2.1.1 Prompt Background

Radiative muon decays can sometimes mimic a $\mu^+ \to e^+\gamma$ signal: because of the smallness of neutrino masses, the possibility of rejecting this background depends on how good the resolutions are. The measured energies should approach their maximum values, in normalized units $x = 2E_e/m_\mu \simeq 1$ and $y = 2E_\gamma/m_\mu \simeq 1$. In the kinematic region of interest ($x \simeq 1$, $y \simeq 1$ and $z \equiv \pi - \vartheta_{e\gamma} \simeq 0$), the differential branching ratio of radiative decay is given by [28]

$$\mathrm{d}\,\mathcal{BR}(\mu^+ \to e^+\nu_e\bar{\nu}_\mu\gamma) \simeq \frac{\alpha}{4\pi}\times \left[(1-x)^2\,(1-P_\mu\cos\vartheta_e) + \left(4(1-x)(1-y) - \frac{1}{2}z^2\right)(1+P_\mu\cos\vartheta_e)\right]\mathrm{d}x\,\mathrm{d}y\,\mathrm{d}z\,\mathrm{d}\cos\vartheta_e \tag{2.1}$$

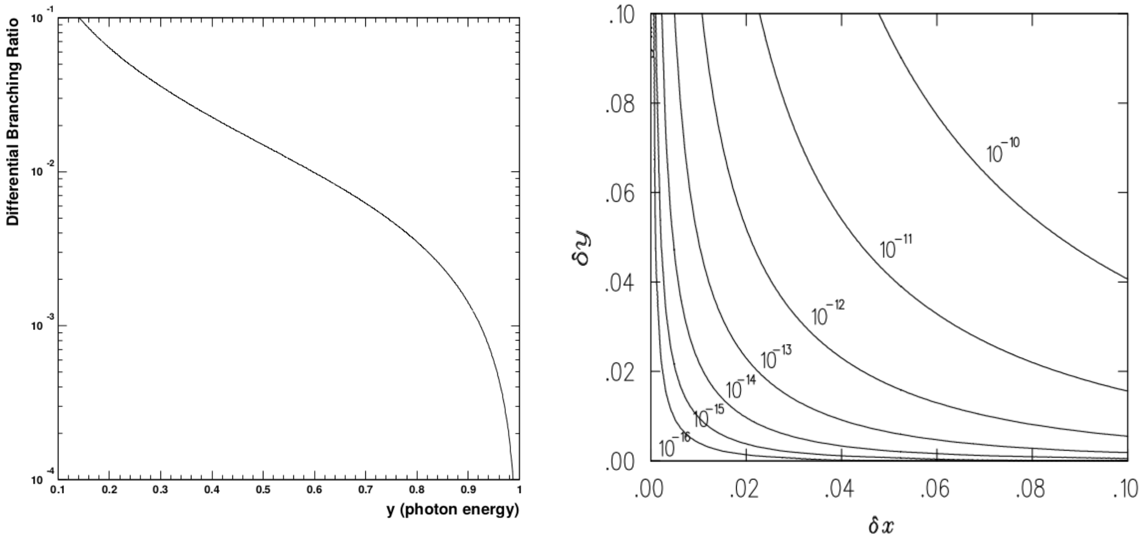

(a) (b)

Figure 2.2 The differential Branching Ratio of radiative muon decays as a function of the normalized energy of the photon y (on the left). Effective Branching Ratio of radiative muon decays as a function of the normalized positron energy resolution δx and the normalized photon energy resolution δy. Figure from [28].

where α is the fine-structure constant, P_μ is the magnitude of the muon spin polarization and ϑ_e is the angle between the muon spin and the positron momentum direction. Notice that at $x = 1$ and $y = 1$ the differential branching ratio vanishes, so the radiative muon decay background is due to finite resolution effect only. Figure 2.2(a) shows the differential Branching Ratio as a function of y only, obtained integrating equation (2.1) in x, z and $\cos\vartheta_e$.

The number of background events can be estimated by integrating equation (2.1) over the experimental resolutions

$$
\begin{aligned}
\frac{\mathrm{d}\,\mathcal{BR}(\mu^+ \to e^+\nu_e\bar{\nu}_\mu\gamma)}{\mathrm{d}\cos\vartheta_e} &= \int_{1-\delta x}^{1} \mathrm{d}x \int_{1-\delta y}^{1} \mathrm{d}y \int_{0}^{\mathit{\Delta}_z} \mathrm{d}z \, \frac{\mathrm{d}\,\mathcal{BR}(\mu^+ \to e^+\nu_e\bar{\nu}_\mu\gamma)}{\mathrm{d}x\,\mathrm{d}y\,\mathrm{d}z} \\
&\simeq \frac{\alpha}{16\pi}\left[J_1\left(1 - P_\mu \cos\vartheta_e\right) + J_2\left(1 + P_\mu\cos\vartheta_e\right)\right]
\end{aligned}
\tag{2.2}
$$

where δx, δy and δz are the half width of the $\mu^+ \to e^+\gamma$ signal region (*i.e.* the resolutions) in x, y and z, respectively; $\mathit{\Delta}_z \equiv \min\left(\delta z,\ \sqrt{(1-x)(1-y)}\right)$. For $\delta z > 2\sqrt{\delta x \delta y}$, J_1 and J_2 are given by

$$
\begin{aligned}
J_1 &= (\delta x)^4 (\delta y)^2 \\
J_2 &= \frac{8}{3} (\delta x)^3 (\delta y)^3.
\end{aligned}
$$

Therefore the rate of background events scales with the sixth power of the resolutions: to achieve an event sensitivity below 10^{-10}, resolutions of a few percent are needed (see Figure 2.2(b)).

2.1.2 Accidental Background

Experiments looking for $\mu \to e\gamma$ need large statistics of muon decays to probe such very small Branching Ratios: an important feature of the last experiments is the intensity of the muon beam. However very high rates lead to a sensible increase of accidental background events. An estimate of the probability that a measured coincidence is due to accidental background is given by [28]

$$
\begin{aligned}
B_{\text{acc}} &= R_\mu \times f_e^0 \times f_\gamma^0 \times \Delta t_{e\gamma} \times \frac{\Delta\omega_{e\gamma}}{4\pi} \\
&\simeq R_\mu \times 2\delta x \times \left[\frac{\alpha}{2\pi} (\delta y)^2 \left(\log \delta y + 7.33 \right) \right] \times 2\delta t \times \frac{(\delta\vartheta)^2}{4}
\end{aligned}
\tag{2.3}
$$

where

- R_μ is the muon rate.
- f_e^0 is the integrated fraction of positron spectrum in the normal muon decay (the main source of 52.83 MeV positrons) within the signal region; since the positron spectrum is almost flat around $x \sim 1$, integration of the Michel spectrum from $1 - \delta x$ to 1 yields $f_e^0 \simeq 2\delta x$.
- f_γ^0 is the integrated fraction of photons summed over all the processes that can produce 52.83 MeV photons within the energy resolution of the experiment. For radiative muon decays, integration of the differential Branching Ratio over all the kinematic variables in the complete range but y only in the signal region, yields

  $$f_\gamma^0 \simeq \frac{\alpha}{2\pi} (\delta y)^2 \left[\log \delta y + 7.33 \right]$$

  Notice the quadratic dependence on the photon energy resolution, due to the falling nature of the γ-*bremsstrahlung* spectrum.
- $\Delta t_{e\gamma}$ is the full width of the timing coincidence, $\Delta t_{e\gamma} \simeq 2\delta t$.
- $\Delta\omega_{e\gamma}$ is the full width of the signal region for angular constraint of the back-to-back kinematics. It is related to the angular resolution by $\Delta\omega_{e\gamma}/4\pi \simeq (\delta\vartheta_{e\gamma})^2/4$.

The number of accidental background events in a time window T is given by

$$N_{\mathrm{acc}} = R_{\mu} \times T \times B_{\mathrm{acc}} \propto R_{\mu}^{2} \times T \times \delta x \times \delta t \times (\delta y)^{2} \times (\delta\vartheta)^{2} \tag{2.4}$$

For example if $R_{\mu} = 3 \times 10^{7}$ Hz, $\delta x = 1\%$, $\delta y = 5\%$, $\delta\vartheta = 10$ mrad and $\delta t = 1$ ns the expected number of accidental background events in a six-month run is $\simeq 40$! Notice that if the contribution from the radiative muon decay background scales linearly with the muon rate (being its amplitude rate-independent), accidental background contribution scales quadratically with the rate. Therefore, in order to have less than one accidental background event, the maximum muon rate is dictated by the experimental resolutions.

Radiative muon decay is not the only source of high enegy photons: other contributions to accidental background come from *bremsstrahlung* or from annihilation in flight of Michel positrons. The importance of such processes depends on the materials along the positron path. Figure 2.3 shows that annihilation-in-flight contribution (with a muon stopping target of 50 mg in thickness) dominates for energy resolutions better than 0.8 MeV (1.5%).

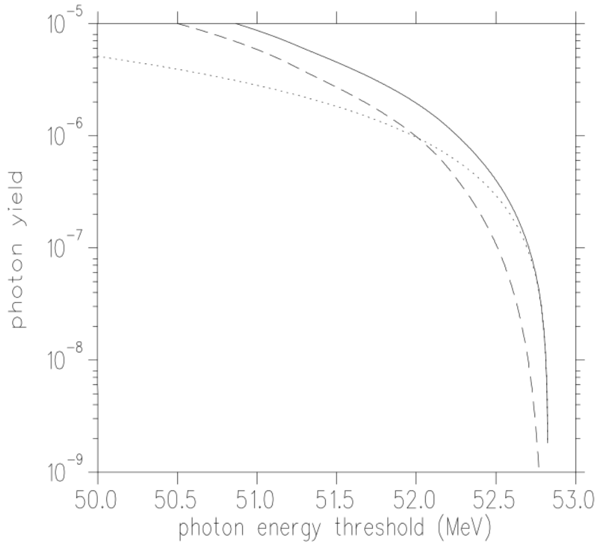

Figure 2.3 Integrated rates of two sources of accidental background as functions of the photon energy: the dotted line is the contribution from positron annihilation in flight (assuming a mass-thickness of 50 mg for the muon stopping target), the dashed line represents photons from radiative muon decays. The solid line is the sum of the two. Figure from [28].

2.1.3 Single event sensitivity

The number of expected signal events depends on the solid angle Ω subtended by the detectors (the acceptance of the apparatus), on the efficiencies of the detectors $(\varepsilon_e, \varepsilon_\gamma)$ and of the selection criteria (ε_s). In a measurement time T, for a given branching ratio $\mathcal{BR}$ it yields

$$N_\mathrm{sig} = R_\mu \times T \times \mathcal{BR} \times \varOmega \times \varepsilon_e \times \varepsilon_\gamma \times \varepsilon_\mathrm{s} \tag{2.5}$$

Dividing equation (2.5) to equation (2.4), one finds that the signal to noise ratio is inversely proportional to the muon rate.

$$\frac{N_\mathrm{sig}}{N_\mathrm{acc}} \propto \frac{\mathcal{BR} \times \varOmega \times \varepsilon_e \times \varepsilon_\gamma \times \varepsilon_\mathrm{s}}{R_\mu \times \delta x \times \delta t \times (\delta y)^2 \times (\delta\vartheta)^2} \tag{2.6}$$

Therefore if high rates are needed from a statistical point of view, on the other hand with too high rates the background becomes unbearable. From equation (2.5) it is possible to compute for which $\mathcal{BR}$ the experiment would see one events (in absence of background): this called the Single Event Sensitivity (SES). SES therefore summarises the performances of the detector: to have a high SES, acceptance and efficiencies should be maximized. In addition to be able to reject the background (see equation 2.6) good resolutions on the kinematic parameters are required, with special attention on photon energy and emission angle, whose contribution is squared.

2.2 The MEG experiment at PSI

The MEG experiment is looking for the $\mu \to e\gamma$ at the Paul Scherrer Institut (PSI) in Switzerland, which provides one of the most intense continuous muon beams in the world. Low-energy μ^+ are stopped in a very thin target, where they decay: the choice of μ^+ instead of μ^- is necessary to avoid nuclear capture. The apparatus consists of two detectors (see Figure 2.4), very sensitive to the

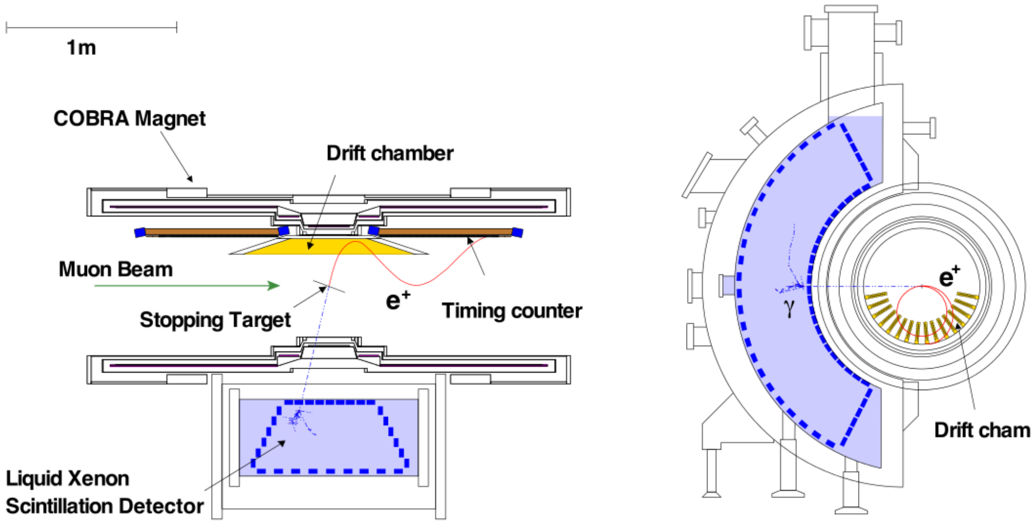

Figure 2.4 Schematic view of the MEG experiment with a signal event displayed. Figure from [29].

kinematic key-parameters: a liquid-xenon detector (for energy, position and time measurements of the photon) and a spectrometer composed of a drift chamber system (which measures momentum and position of the positron) and two timing counters (for measuring the positron time), immersed in a non-homogeneous magnetic field. In the following we give a description of the experiment, focussing on the differences with respect to its proposed upgrade MEG$^{\text{UP}}$.

2.2.1 Beam Line and Target

Muons are produced from a primary beam of protons with an energy of 590 MeV impinging on a 4 cm thick rotating graphite wheel. During the collision secondary particles are produced, mainly pions. Some of the π^+s are stopped in the target and decay at rest. Muons from such pion decays have a fixed momentum 29.7 MeV/c, due to two–body decay kinematics. However the range of daughter muons is of the order of the millimetre, so only muons produced in the outer layer of the target (called "surface muons") can escape.

The $\pi E5$ channel, placed at 175° from the proton stream, collects[1] positive particles (μ^+, e^+,π^+). For the MEG experiment it is tuned to a momentum of 28 MeV/c, and only μ^+ and e^+ are present in the beam. A schematic of the beam line is reported in Figure 2.5. The large positron contamination in the beam is efficiently removed by an electrostatic separator coupled to a lead collimator which damps the positron component of the beam. The separator is placed between two triplets of magnetic quadrupoles focussing the beam before and after entering the separator. The coupling between the beamline and the detector is realised through the Beam Transport Solenoid (BTS); here the beam passes through a Mylar foil with a thickness of 300 µm, in order to tune μ^+ energy so that the fraction of muons stopped in the detector target is maximized.

Muons cross the detector volume, which is filled with helium for the mechanical stability

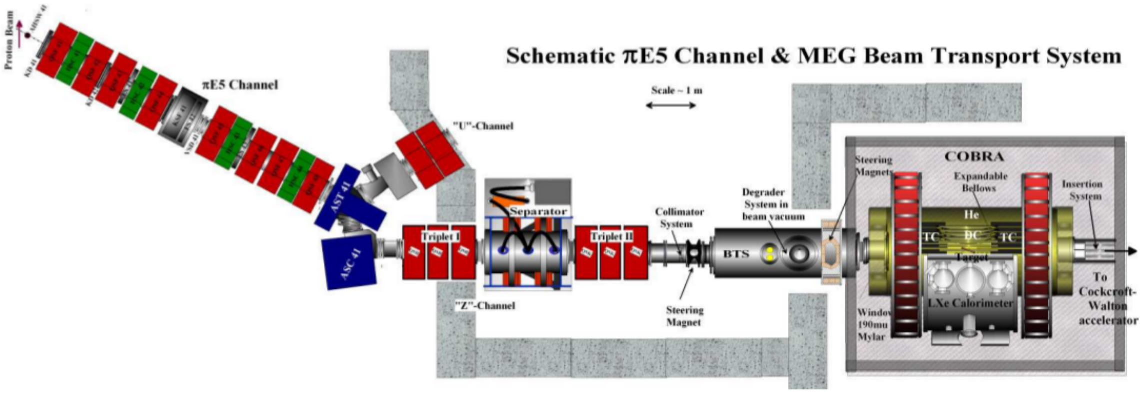

Figure 2.5 The $\pi E5$ channel delivering muons to the MEG detector. Figure from [29].

---

[1] actually the channel can also be tuned for selecting negative pions, used in the calibration of the calorimeter.

of the apparatus, and stop on the target. The beam spot size on the target has a $\sigma_{x,y} \simeq 1$ cm. The target is an elliptycal sheet of polyethylene ($(\mathrm{CH}_2)_n$) with a thickness of 205 µm and major (minor) axis of 10 (4) cm (see Figure 2.6).

Muons do not impinge perpendicularly on the target: the angle between the muon beam and the normal to the target is $\sim 70°$, in order to minimize energy loss for positrons emitted in the tracker acceptance.

The following convention on the reference system is used:

- z is the axis parallel to the muon beam and passing through the centre of the target
- φ is the azimutal angle referred to the z axis, $\varphi = 0$ points opposite to the calorimeter.
- ϑ is the polar angle

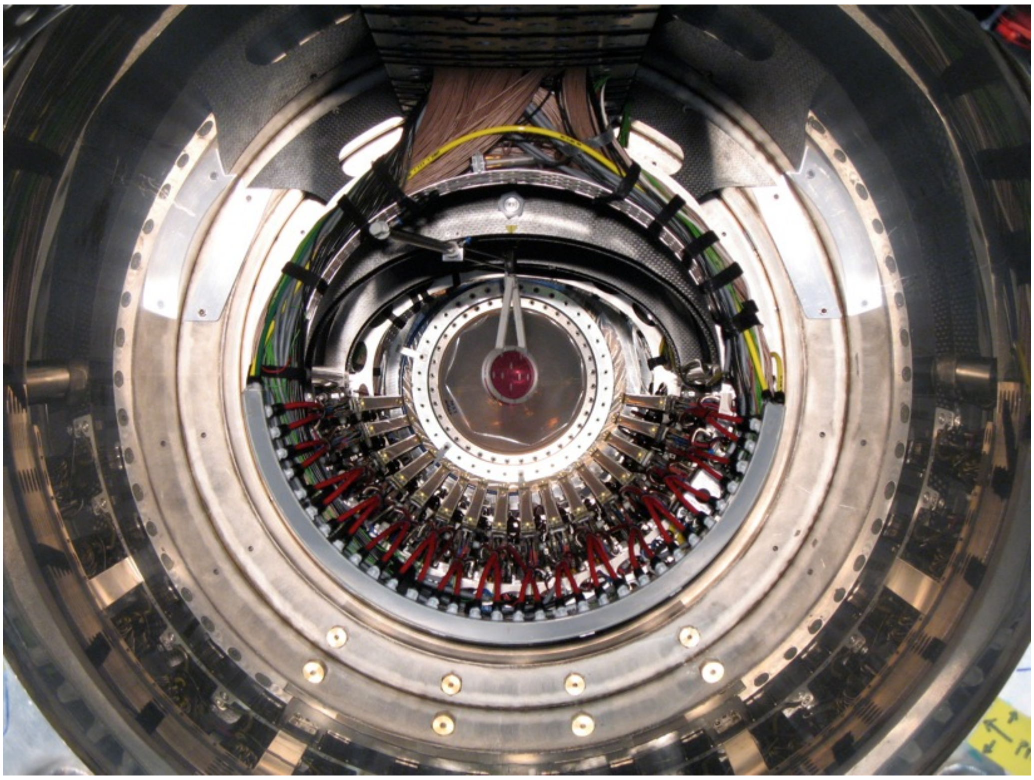

Figure 2.6 Picture of the target and the array of drift chambers in the MEG detector.

2.2.2 The Calorimeter

To reject the continuous background, it is fundamental to measure to good accuracy energy, direction and time of photons. These requirements are met by a liquid xenon calorimeter. Liquid xenon was chosen for the following reasons:

- small radiation length (X_0 = 2.7 cm) and high light–yield (the energy deposit needed for the emission of a scintillation photon is about 20 eV). These characteristics confer to xenon high detection efficiency, small leakage for electromagnetic showers and good energy resolution.

- three main mechanisms are involved in scintillation, with all the time constants being lower than 50 ns. Such a fast response results in reduced pile–up probability and in a superior timing resolution (of less than 100 ps).

The calorimeter is shown in Figure 2.4 and Figure 2.7: it is placed at 65 cm from the target and extends for a radial depth of 45 cm. It has an acceptance of 11 % for photons emerging from the target, corresponding to 120° in φ and to the interval $|\cos\vartheta| < 0.35$.

The liquid xenon volume is seen by 2” Vacuum-Ultra-Violet sensitive photomultipliers (846 units) covering the six internal faces of the vessel, and is placed in a cryostat that keeps xenon temperature stable at about 165 K.

Energy and timing resolution of the calorimeter are extracted from the calibrations, discussed in the following. Energy resolution depends on the position of γ-ray conversion: the measured values are σ_E/E =2.7% for conversions within 8 mm from the inner face, 2.0% for conversions between 8 mm and 3 cm from the inner face and 1.7% for deeper conversions. Timing resolution is measured to be 67 ps. Both energy and timing resolutions turned out to be slightly worse than the design value ($\sim$ 1.2% and 45 ps respectively).

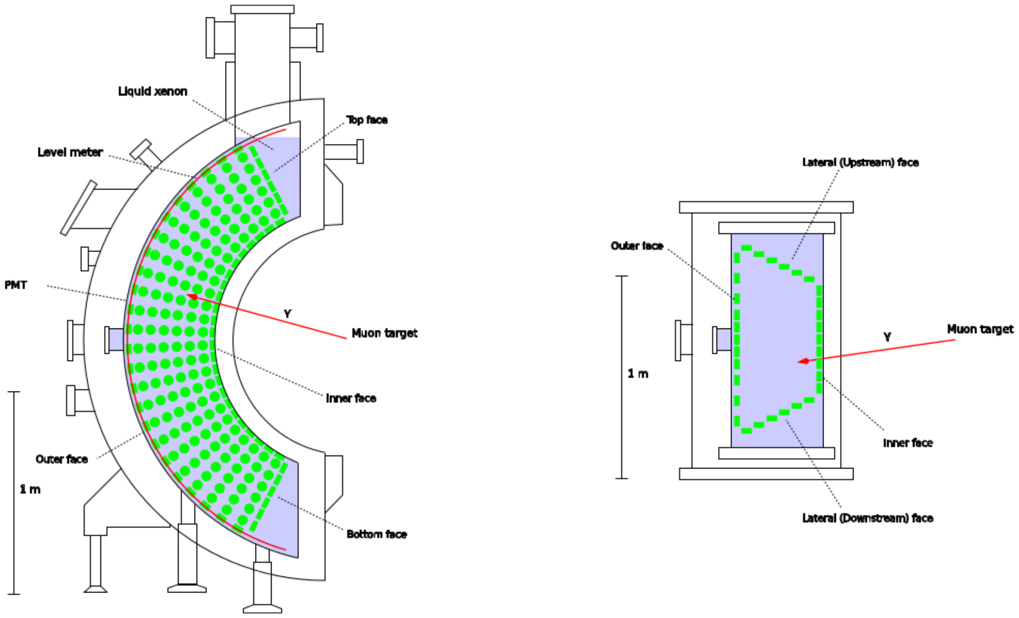

Figure 2.7 Lateral and top views of the liquid xenon calorimeter. Figure from [29].

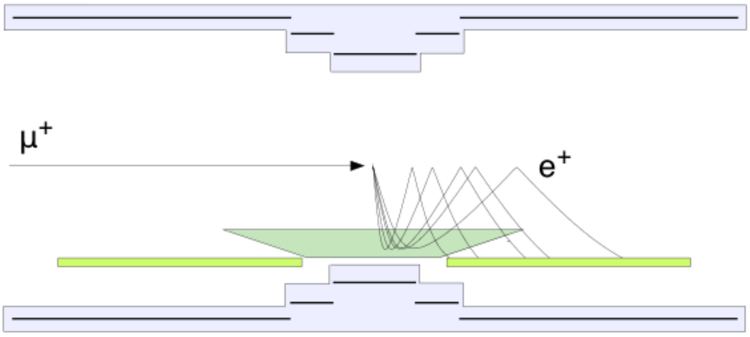

Figure 2.8 Schematic highlighting the independence of the bending radius on the emission angle. Figure from [29].

2.2.3 The positron spectrometer

The positron spectrometer consists in a set of sixteen modules of drift chambers placed in the intense magnetic field generated by the COBRA (COnstant Bending RAdius) superconducting magnet and in arrays of scintillators used as timing counters.

The COBRA magnet generates a gradient magnetic field, ranging from 1.27 T at the centre of the spectrometer volume to 0.49 T in the proximity of the endcaps. Two compensation coils reduce the magnetic field down to the value of 50 G in the region of the xenon detector to avoid the loss of performance of the PhotoMultiplier Tubes (PMTs). The peculiarity of this magnetic field configuration is that positrons emerging from the target follow a trajectory with almost constant bending radius, *i.e.* with slight dependence on the emission angle, as shown in Figure

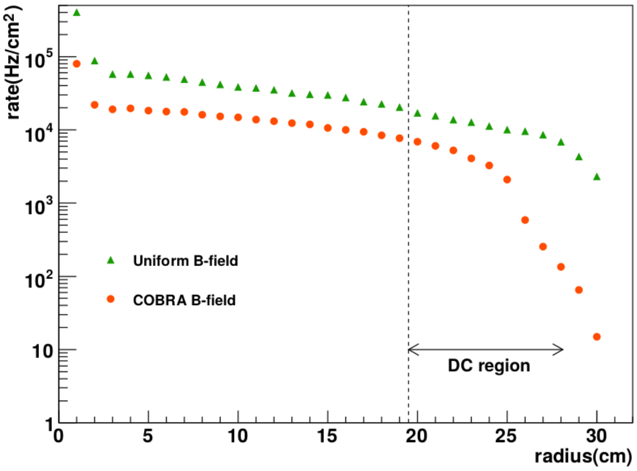

Figure 2.9 Positron rate as a function of the distance from the target in the case of solenoidal field and with COBRA. Figure from [29].

2.8, as opposed to a conventional solenoid magnet in which the radius depends on the transverse momentum.

Figure 2.9 shows how this is efficient in avoiding excessive occupancy of the drift chamber volume by the tracks: COBRA magnetic fields reduces by about an order of magnitude the Michel positron rate on the chamber region, with no reduction on the signal.

Drift chamber system

The tracking apparatus consists of 16 drift chamber modules with trapezoidal shape; the single module is shown in Figure 2.10. They are mounted with the minor base of the trapezoid being positioned on the inner coil of the magnet, as shown in Figure 2.8. The modules are placed on a half circle, with 10.6° intervals, and the sensitive volume of the modules spreads from $r = 19.3$ cm to $r = 27.9$ cm (see Figure 2.6). The gas mixture filling the drift region is helium–ethane (50:50), while the outer part is filled with helium.

The single module contains two independent detector planes, made of an array of alternating field and sense wires (with a pitch of 4.5 mm) enclosed by two cathode foils each (see Figure 2.11). The wire length varies from 82.8 cm (the innermost wire) to 37.6 cm (the outer wires). The two wire arrays are staggered by 4.5 mm in order to solve left–right ambiguity. The distance between the cathode foils is 7 mm, while between the two planes of the module there is a gap of 3 mm. In order to minimize the amount of material, cathode foils are made of a layer of 12.5 µm thick polyamide with a 250 nm aluminum deposition having a zigzag etching with period 5 cm, used for the z measurement.

The determination of the z-coordinate is realised in two steps. First with the charge division

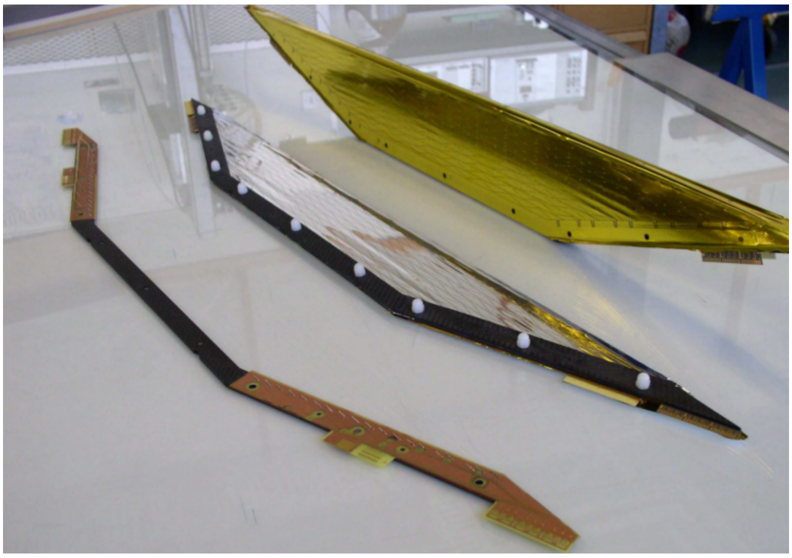

Figure 2.10 Drift chamber module. Figure from [29].

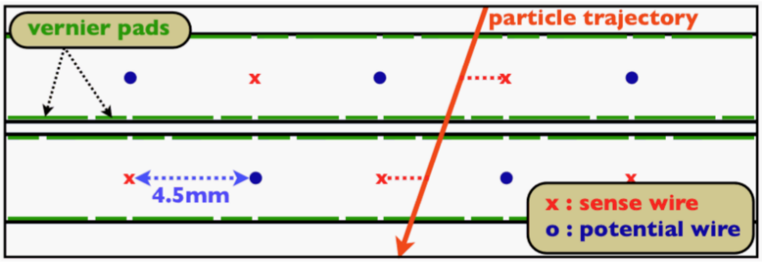

Figure 2.11 Schematic of the two detector planes in a drift chamber module. Figure from [29].

method, that is measuring the different charges collected at the two ends of the wire: anodes are Ni–Cr resistive wires, so the longer is the portion of the wire on which signals propagate, the larger is the resistance seen by the signals. This allows a determination of the z-coordinate with a resolution of about 1 cm. At this point a more accurate determination is provided by cathodes: the deposited aluminum has a periodic double-wedge structure (Vernier pads, in Figure 2.12), and the two half-foils have independent readout, so that the measurement of the asymmetry in charge collection on the two pads conveys the information on the z-coordinate. In the two cathode foils enclosing a plane of the detector, the patterns are displaced by a quarter-period. The single-hit resolution, *i.e.* the accuracy in the determination of the impact parameter on a wire, is 210 µm in the core and 780 µm in the tail. The resolution on z, obtained through Vernier pads, is about 550 µm. The resolution on the positron angle is determined from data of events where the positron makes two turns in the drift chamber system. The obtained values are $\sigma_{\vartheta_e} \sim 9.4$ mrad and $\sigma_{\varphi_e} \sim 8.7$ mrad, to be compared with the resolution goal of $\sigma_{\varphi_e,\vartheta_e} \sim 5$ mrad. Finally the energy resolution of the drift chamber at 52.83 MeV is measured through the determination of the Michel spectrum endpoint (see Figure 2.13). The measured Michel spectrum is fitted by a function which includes the theoretical Michel spectrum, scaled by the acceptance of the detector and convolved with a Gaussian resolution. The obtained value is $\sigma_{E_e} = 330$ keV. The obtained resolutions are

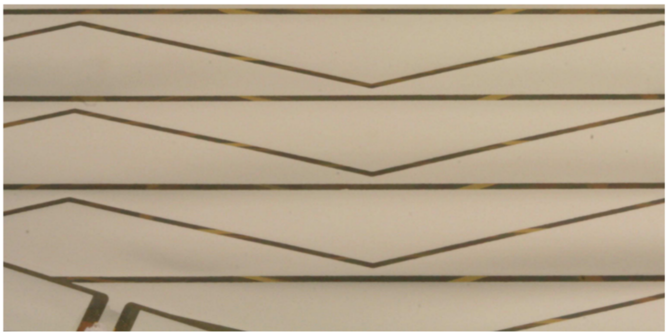

Figure 2.12 Zig-zag structure of Vernier pads: cathode foils are divided in two subcathodes by etching the aluminum deposition.

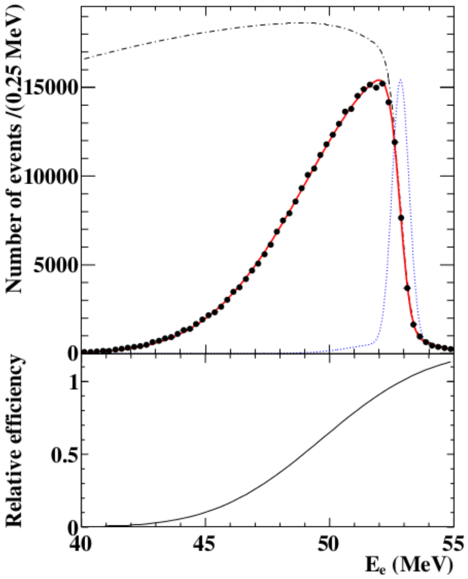

Figure 2.13 Michel positron energy spectrum used in the measurement of the drift chamber energy resolution. Figure from [29].

worse than the design values ($\sigma_r \approx 200$ µm, $\sigma_z \approx 300$ µm, $\sigma_{\vartheta,\varphi} \approx 5$ mrad, $\sigma_E \approx 200$ keV), mainly for two causes: an increased noise level in the signals and unexpected chamber instability, which prevented the use of some chambers for most of the run period, reducing the number of hits and therefore worsening the spectrometer performance.

Timing Counters

The plastic timing counters are used in the determination of the positron time (see Figure 2.14). Two identical hodoscopes are placed at the two sides of the drift chambers along the z axis (the green bars in Figure 2.8). They cover an azimutal angle of 145° at a radius of 29.5 cm and extend from $z = \pm 25$ cm to $z = \pm 95$ cm.

Each hodoscope consists of a layer of 256 scintillating fibres, read by avalanche photodiodes, placed on the top of an array of 15 scintillating bars, which are coupled to fine-mesh fast photomultipliers. Bars and fibres are oriented perpendicularly, with the bars being parallel to the z axis. The layers are read at both ends and the difference of the arrival times of the signal at the two ends of the bars is used for z measurement, in addition to the position of the fired fibre.

The timing resolution of the detector is determined through tracks hitting on multiple bars. The measured time resolutions of the bars is 60 ps, in accordance with expectations.

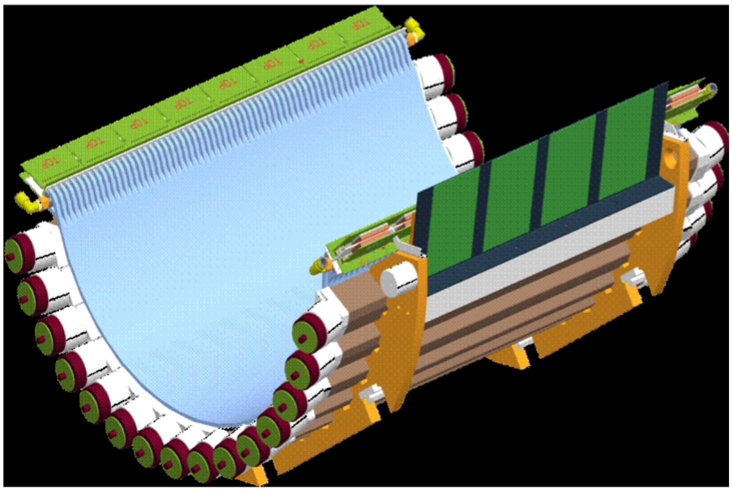

Figure 2.14 Scintillating bars and fibres of the timing counter. Figure from [29].

2.2.4 Trigger and DAQ

At very high rates, it is important to have a fast and efficient trigger system. In MEG the trigger is implemented in a cascaded custom mode VME boards, whose synchronous operation is guaranteed by a set of ancillary boards distributing a common 100 MHz clock signal. The trigger system has a tree–structure, with three different levels: at the first level analog signals are digitized by means of 100 MHz flash-ADC, which allows the determination of the signal amplitude (at the permille level) and timing (within a few nanonseconds). A basic event reconstruction is performed for the single detectors. In the upper levels the information from the different detectors is collected and estimates of the kinematic variables are obtained, thus providing (or not) the trigger signal. The signals used for trigger selection come from the scintillating bars of the timing counter and the calorimeter: requirements are set on observables that can be computed in a very short time and give a rough estimate of one of the kinematic key parameters. They are

- the sum of the light collected by the PMTs in the internal and lateral faces of the calorimeter (photon energy);
- the waveform and the position of the PMT with the largest signal (photon timing and direction);
- the fired fibres and bars of the timing counter (positron timing and momentum[1]).

Signals from the detectors are digitized by a waveform digitizer chip, the Domino Ring Sampler 4 (DRS4). Calorimeter and timing counters signals are sampled at a frequency of

---

[1] the threshold in momentum is given by the requirement of a signal in the timing counter, which is hit only by positrons with $p \gtrsim 45$ MeV.

1.6 GHz, while signals from the drift chamber are acquired at 0.8 GHz; such frequencies make the knowledge of the waveforms at the 50 ps level possible. This is necessary to exploit the detectors timing resolutions and for reducing the pile-up of events.

2.2.5 Calibrations

The stability of the working points of the detectors is periodically checked through calibrations, aiming at monitoring the resolution changes on the various kinematic variables, the absolute energy scales and the position of the zero for time and direction. For this purpose a rich set of calibration procedures has been developed.

The calibrations of the absolute energy scale of the calorimeter are presented in Table 8.1. The xenon detector is tested over a wide energy range:

- α-sources deposited on thin wires are placed inside the detector, and are used probe the response at low energy (5.5 MeV). In addition they permit daily monitoring of the PMT quantum efficiencies and the liquid xenon optical properties.
- intermediate energies are probed through nuclear reactions induced by 400÷700 keV protons from a Cockcroft-Walton accelerator on a $Li_2B_4O_7$ target. Figure 2.15 shows a recorded spectrum. In addition to the measurement of the energy scale and resolution, the reaction $\mathrm{B}(p,\gamma)\mathrm{C}$ allows the timing intercalibration between the calorimeter and the timing counters, through the detection of time coincident 4.4 and 11.6 MeV photons.
- The high energy range is probed through π^0 decays from π^- charge exchange of protons in a liquid H_2 target.

Drift chambers operation is monitored through coherent Mott scattering of positrons on the carbon atoms of the polyethylene target. A positron beam is easily obtained from the positron component of the MEG beam by changing the working point of the electrostatic separator.

	Process	Energy	Frequency
Charge exchange	$\pi^- p \to \pi^0 n$ $\pi^0 \to \gamma\gamma$	$55, 83, 129$ MeV	year / month
Radiative $\mu-$decay	$\mu^+ \to e^+\nu_e\bar{\nu}_\mu\gamma$	52.8 MeV endpoint	week
Proton accelerator	$^7\mathrm{Li}(p,\gamma_{17.6})^8\mathrm{Be}$	14.8, 17.6 MeV	week
	$^{11}\mathrm{B}(p,\gamma_{16.1})^{12}\mathrm{C}$	4.4, 11.6, 16.1 MeV	week
Nuclear reaction	$^{58}\mathrm{Ni}(n,\gamma_9)^{59}\mathrm{Ni}$	9 MeV	daily
Radioactive source	AmBe	4.4 MeV	daily

Table 2.2 Calibrations of the liquid xenon calorimeter energy scale, with the energies probed and the frequency of operation.

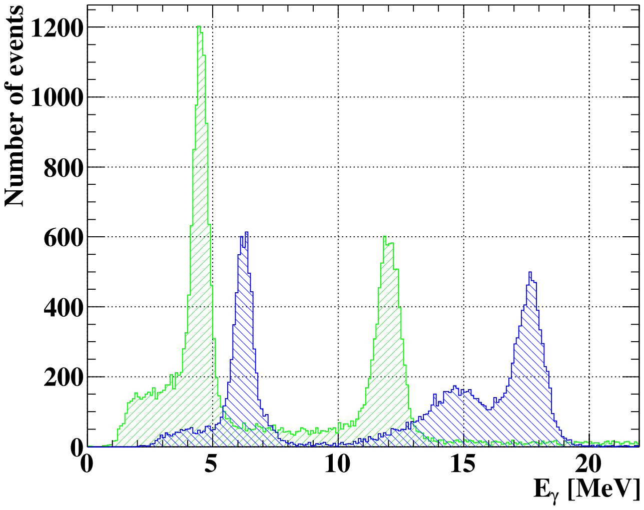

Figure 2.15 Spectrum of photons recorded by the liquid xenon calorimeter coming from nuclear reactions induced by the protons: $^{11}\mathrm{B}(p,\gamma)\,^{12}\mathrm{C}$ (green line) and $^{7}\mathrm{Li}(p,\gamma)\,^{8}\mathrm{Be}$ (blue line).

This method provides an additional measurement of the angular and momentum resolution, a measurement of the spectrometer acceptance and an independent check of the spectrometer alignment.

Mott scattered positrons have an average momentum close to the incident momentum of 53 MeV/c, with a measured sigma of 450 keV/c that includes also the spread of incident positron energy.

2.3 MEG status and the MEG upgrade

The MEG collaboration has recently (May 2013) published a new constraint on the $\mathcal{BR}$ for the $\mu \to e\gamma$ decay [27]. The analysis of data taken in the years 2009–11 improved the past constraint of 2.4×10^{-12} @ 90% CL to the upper limit

$$\mathcal{BR} < 5.7 \times 10^{-13} \text{ @ } 90\%\,\mathrm{CL}$$

after collecting about 3.6×10^{14} muon stops on the target.

In Figure 2.16 the event distribution for data is displayed in the signal region; the variables of interest are the positron energy E_e, the photon energy E_γ, the time delay $t_{e\gamma}$ and the cosine of the angle between the reconstructed trajectories of the particles $\cos\vartheta_{e\gamma}$.
Accidental background events are seen close to the signal region, displayed as confidence intervals at 68, 90 and 95 % probability (the curves on the plots). Such events lower the experiment

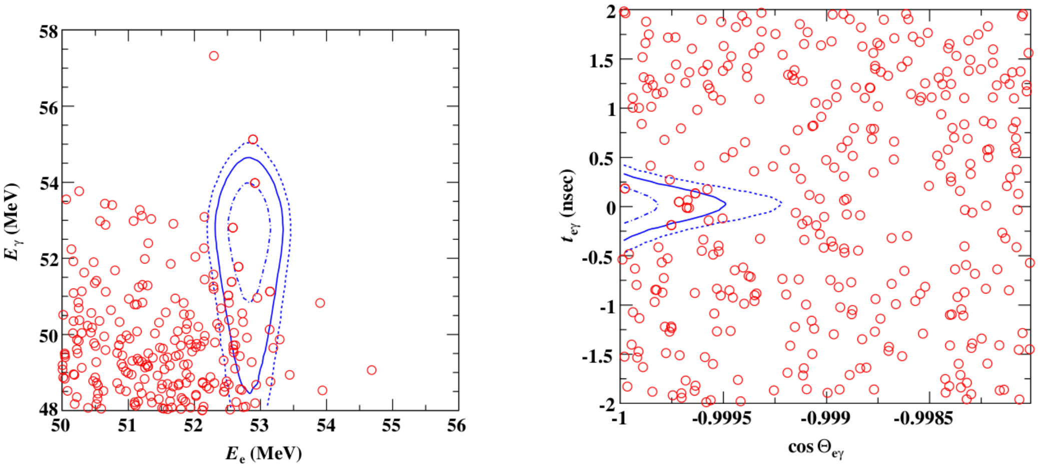

Figure 2.16 Event distribution in the E_γ vs E_e and $t_{e\gamma}$ vs $\cos\vartheta_{e\gamma}$ planes for data acquired by the MEG experiment. See the text for an explanation. Figure from [27].

sensitivity, which does not increase linearly with the acquired data anymore.

Further analyses of data taken in 2012 and 2013, with a larger sample of stopped muons (about a factor 2), will approach to the ultimate limit of sensitivity dictated by accidental background.

Foreseen and measured resolutions and efficiencies of the MEG detector are shown in Table 2.3: if the calorimeter almost fulfills the predicted performance, for the positron spectrometer the obtained resolutions are worse than expected, in particular for the drift chamber.

Variable	Foreseen MEG	Obtained MEG	Foreseen MEG$^{\mathrm{UP}}$
ΔE_γ(%)	1.2	1.7	1.0
Δt_γ (ps)	43	67	–
γ position (mm)	$4(u, v)$, $6(w)$	$5(u, v)$, $6(w)$	$2.6(u)$, $2.2(v)$, $5(w)$
ΔP_e (keV)	200	306	130
e^+ angle (mrad)	$5(\varphi_e)$, $5(\vartheta_e)$	$8.7(\varphi_e)$, $9.4(\vartheta_e)$	$5.3(\varphi_e)$, $3.7(\vartheta_e)$
Δt_e (ps)	50	107	–
$\Delta t_{e\gamma}$ (ps)	65	122	84
e^+ efficiency (%)	90	40	88
γ efficiency (%)	> 40	63	69
trigger efficient(%)	∼99	∼99	∼99

Table 2.3 Foreseen and obtained resolutions on the kinematic parameters in MEG and expected perfor-maces of the MEG upgrade. $(\hat{u}, \hat{v}, \hat{w})$ is the reference system in which the calorimeter is a parallelepiped with $\hat{u} \parallel \hat{z}$, $\hat{v} \parallel \hat{\varphi}$ and $\hat{w} \parallel -\hat{r}$. Values are taken from [21].

It has been recently proposed an upgrade of the MEG experiment, MEG$^{\mathrm{UP}}$ [21]. Current resolutions do not allow the possibility to go below a few $\times 10^{-13}$ on the branching ratio for $\mu \to e\gamma$, since sensitivity saturates because of accidental background. However with limited modifications of the experimental apparatus, resolutions and acceptances can be improved so that a final sensitivity of 6×10^{-14} can be reached in three years of running. Expected resolutions and efficiencies are reported in Table 2.3.

Figure 2.17 shows schematically the modifications of the experimental apparatus that will be performed, namely:

1) A higher muon stopping rate.

2) A thinner target with lower contribution of multiple scattering on the positron and photon trajectories.

3) A new positron tracker, with a reduced radiation length and a higher resolution.

4) A new tracking procedure for the positron, which exploits the measurement of the impact point on the timing counter.

5) A new timing counter, with higher granularity and resolutions.

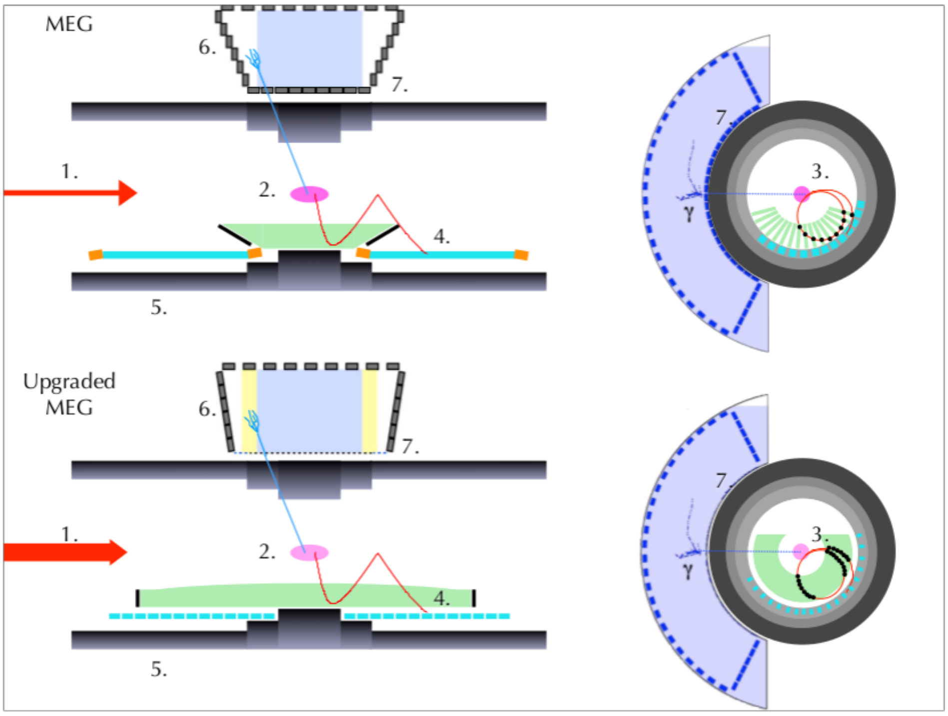

Figure 2.17 Improvements of the MEG detector. The numbers correspond to the list in the text. Figure from [21].

6) Extension of the calorimeter acceptance.
7) Improvement of the calorimeter performaces for photons converting close to the entrance face.

According to such modifications, the trigger system and DAQ will be improved as well, in order to match their performances with those of the new detectors. These modifications could take place in a limited time span: the aim of the upgrade is to perform little improvements of the apparatus in order to gain a large sensitivity improvement.

Here follows a quick overview of the proposed upgraded detectors, whose calibrations will be same of the current experiment.

2.3.1 Beam Line and Target

For the current MEG experiment the muon stopping rate optimising the signal sensitivity is 3×10^7 Hz. An increase in the muon rate must be necessarily accompanied with the improvement of the experimental resolutions, in order to keep accidental background low. On the other hand, the improved performaces of the upgraded detectors can allow a muon rate up to three times higher. Target thickness estabilishes the intrinsic resolution on the determination of the relative angle between photon and positron because of multiple scattering. The reduction of multiple scattering can be achieved by reducing the target thickness, but target thickness is related to the muon momentum: the more energetic the muon, the thicker the target in which the muon is completely stopped. The momentum of the muon beam is currently selected by the magnetic optics of the πE5 channel, which for MEG trasmits only surface muons. In principle it is possible

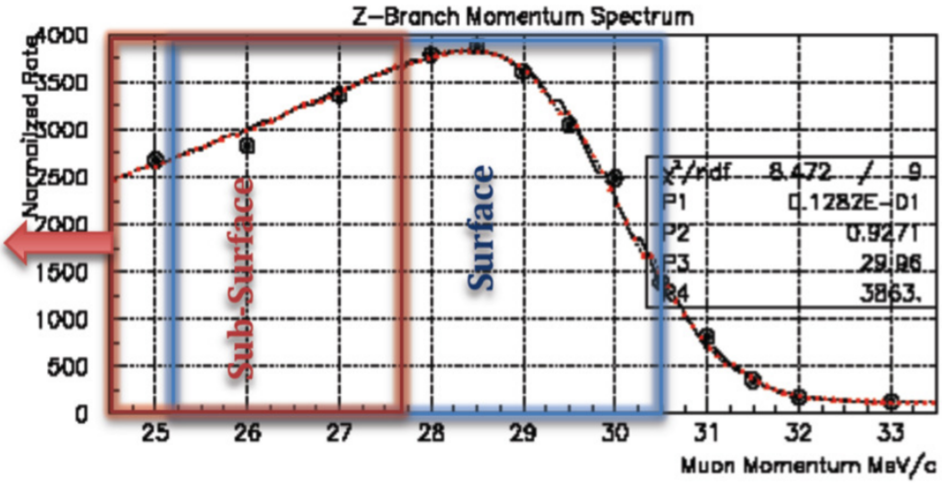

Figure 2.18 Momentum distribution of the muons provided by the $\pi E5$ channel, fitted by a $p^{3.5}$-distribution folded with a Gaussian resolution function. The momentum spread of surface and subsurface muons are highlighted. Figure from [21].

to select muons in a momentum window centered at about 26 MeV/c ("subsurface muons"), so that the required thickness of the target can be lower. Figure 2.18 shows the measured momentum spectrum of muons emerging from the graphite target. In the case of subsurface muons a target with a thickness of 140 µm placed at 15° succeeds in stopping muons. This and other scenarios are under study.

2.3.2 The Calorimeter

The xenon calorimeter has a resolution dependent on the depth of the γ-conversion. Figure 2.19 shows the different resolutions for shallow and deep photons (*cfr.* resolutions listed above).

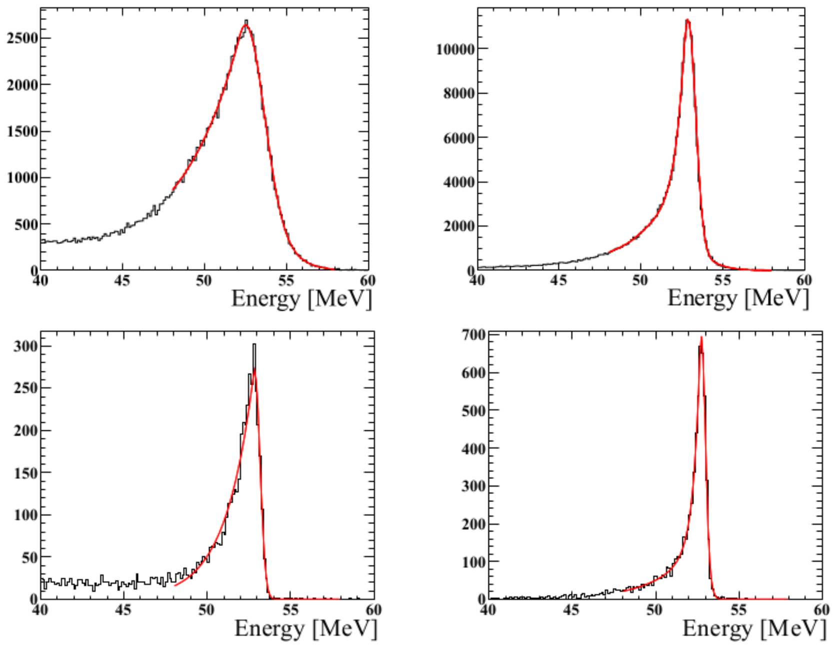

Figure 2.19 Monte Carlo simulation of the energy response of the xenon calorimeter in MEG (the upper plots) and MEG$^{\mathrm{UP}}$ (the lower plots), for shallow (conversion point within 2 cm from the entrance face) and deep (conversion at more than 2 cm from the entrance face) event. Figure from [21].

This is due to the non-uniform PMT coverage of the front face, therefore in MEG$^{\mathrm{UP}}$ the 246 2" PMTs in the entrance face will be replaced by smaller photosensors, the first option being $1 \times 1\,\mathrm{cm}^2$ Silicon PhotoMultipliers (SiPMs) (see Figure 2.20). The imaging power is thus greatly increased.

The layout of the lateral faces will be modified too in order to avoid shadow areas, which result in a reduced acceptance. The proposed structure is visible in Figure 2.21, where the wider acceptance region is highlighted.

Monte Carlo simulations show that in the new configuration the resolutions are improved for both shallow and deep events, mainly because of the more uniform photon-collection efficiency

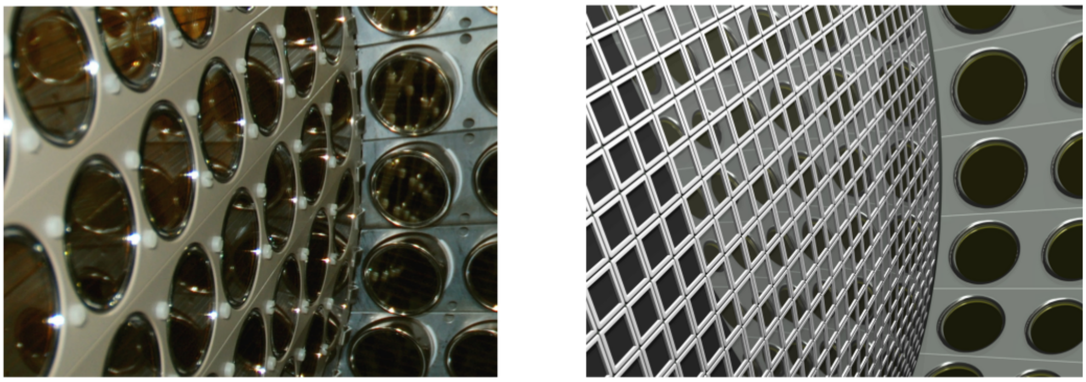

Figure 2.20 Current and upgraded front face of the calorimeter. Figure from [21].

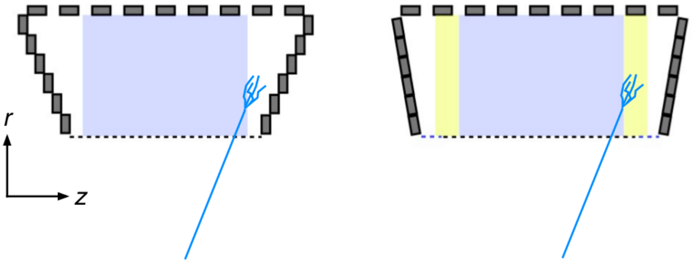

Figure 2.21 Acceptance increase of the upgraded calorimeter due to the changes in the lateral faces. The upgraded fiducial volume is highlighted. Figure from [21].

(see Figure 2.19). The returned values of the resolutions are 1.1 % for shallow events and 1.0% for deep events. The smaller size of the photosensors on the entrace face can bring also an improvement on the timing resolution of the calorimeter, which is evaluated in simulations as about 84 ps, with the possibility of further improvements.

2.4 The positron spectrometer of MEG$^{\text{UP}}$

The new positron spectrometer consists of a hyperbolic drift chamber, *i.e.* a cylindrical drift chamber with stereo wires, and a pixelated timing counter. In the new configuration positrons traverse less material along their path, and the capabilities of matching the information from the two detectors are powered. Figure 2.22 shows a schematic view of the new spectrometer.

2.4.1 The Drift Chamber

The new tracker is a single volume cylindrical drift chamber with the axis parallel to the muon beam. The geometrical parameters of the detector are under development, we now describe the state–of–the–art of wire disposition. It extends in the radial coordinate from 17 cm to 25 cm at

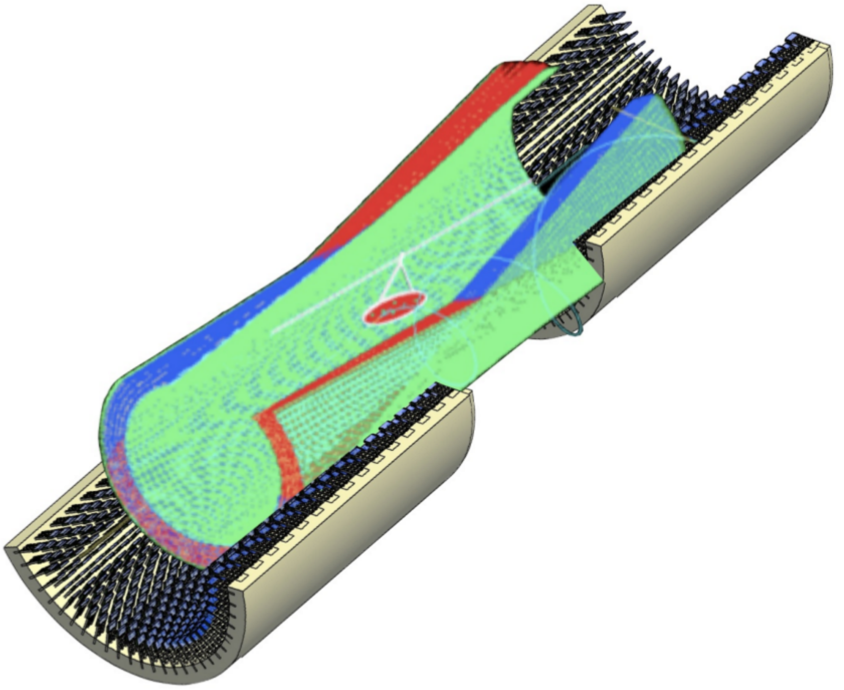

Figure 2.22 The new spectrometer of the MEG upgrade: the single volume cylindrical wire chamber and the pixelated timing couter. Figure from [21].

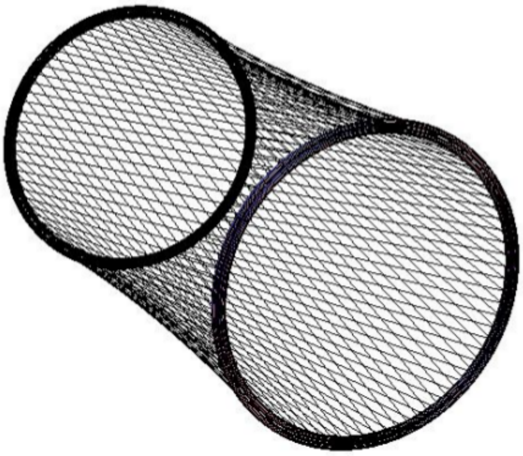

Figure 2.23 Schematic of a field wire layer of the new drift chamber. Wires are placed at both positive and negative stereo angles in order to close the cells of the upper and the lower sense wire layer. Figure from [21].

$z = 0$, and from 20 cm to 28 cm in proximity of the endcaps, at $z = \pm 90$ cm. The hyperbolic profile along z of the chamber comes from the stereo configuration of wires, which are not parallel to the z axis but form a stereo angle (with respect to the z axis) varying from 8° in the outermost layers to 7° in the innermost ones. The 10 sense wire planes, each embedded between two field wire planes, have alternating stereo angles ($\pm 7^\circ \div 8^\circ$). Such configuration conveys information for reconstructing the z coordinate. Figure 2.23 shows the ground mesh realised by field wires.

Drift cells thus extend along the detector length forming a stereo angle with the z axis. The single drift cell (shown schematically in Figure 2.24) has an approximately squared shape with a width of ~7 mm, and has a sense wire placed at the centre surrounded by eight field wires. The external layer of field wires is surrounded by a layer of guard wires for shaping the electric field on the outer cells. The azimutal angle covered by the tracker is dictated by the calorimeter acceptance. The φ span of the drift chamber is therefore about 270°. Figure 2.25 shows three tracks on the $z = 0$ plane with momentum 52.8 MeV/c. The total number of sense wires is about 1200, while the field wires are about 6400.

As counting gas a low–mass mixture of helium and isobutane will be used in the fractions 85:15 or 90:10. This allows the minimization of the total number of radiation lengths for the new tracker: 1.24×10^{-3} and 1.10×10^{-3} radiation lengths for the 85:15 and 90:10 mixtures respectively, to be compared with 1.7×10^{-3} radiation lengths of the present tracker. To reduce the total radiation length the field wires, which should initially be 40 µm gold–plated tungsten wires, were changed to 40 µm silver–plated aluminum wires. Anodes will be gold–plated tungsten wires with a diameter of 20 µm.

Stereo wires allow the possibility of reconstructing the z-coordinate of the hit, but, because

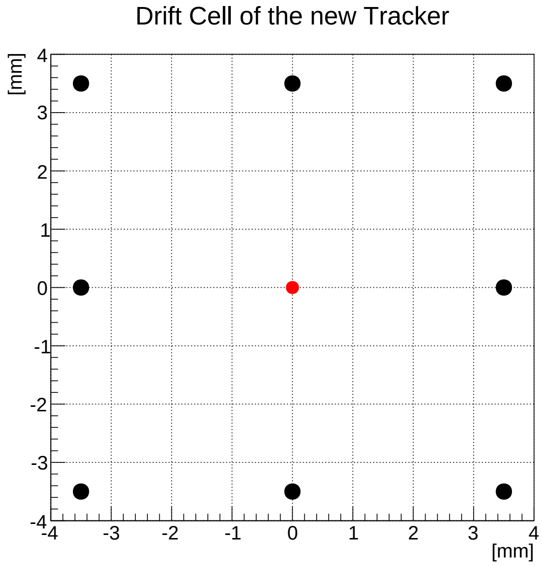

Figure 2.24 Schematic of the drift cell of the new tracker. Wire diameters are not on scale.

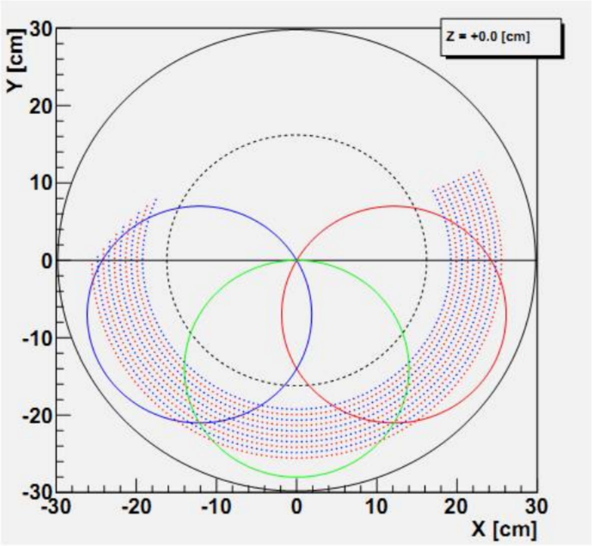

Figure 2.25 Example of three tracks at $z = 0$ in the acceptance of the calorimeter. Figure from [21].

of pile-up, current pattern recognition algorithms should be supported by an additional "coarse-grained" method of determining z. In MEG this is performed through charge division, but the wires of the new tracker have a too low resistivity, so the method is not feasible. Currently a possibility of determining the z-coordinate with an uncertainty of the order of 10 cm is represented by the measurement of the difference of the arrival times of the signal at the two ends of the wire.

The performances of the new drift chamber are under study. A measurement of the single-hit resolution in the the two possible gas mixtures has been performed in INFN Lecce, with an array of three drift tubes. The obtained resolutions are ~160 µm in helium-isobitane 90:10 and ~ 140 µm in 85:15 mixture, but include the effect of Coulombian multiple scattering in the 200 µm thick copper walls of the tubes. A similar estimate of single hit resolution will be described in Chapter 5, using a three-cell prototype, which is free from such multiple scattering contribution. The momentum and angular resolution have been obtained with Monte Carlo simulations assuming an average single-hit resolution of 120 µm. For a 140 µm thick target at 15°, the estimated momentum resolution is 125 keV/c, and the angular resolutions are $\Delta\varphi_e = 6.2\,\mathrm{mrad}$ and $\Delta\vartheta_e = 4.9\,\mathrm{mrad}$.

2.4.2 The Timing Counter

The present timing counters cannot stand a positron rate increased of a factor 2÷3. It is necessary to segment the detector: the proposed detector is a pixelated timing counter consisting of many scintillator tiles coupled to Silicon PhotoMultipliers (SiPMs). The layout of the new detector is shown in Figure 2.26.

The single pixel module has an area of $30{\times}90\,\mathrm{mm}^2$ and a thickness of 5 mm. At each side,

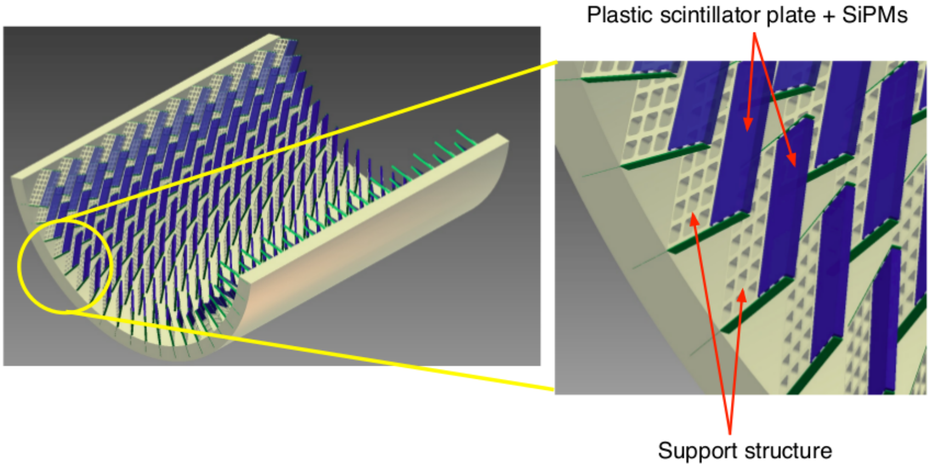

Figure 2.26 The new pixelated timing counter. Figure from [21].

light is collected by two SiPMs connected in series whose signal is directly send to a WaveDream board, the evolution for MEG$^{\text{UP}}$ of the DRS4, 2 GHz waveform digitizer.

The segmentation of the timing counter brings an intrinsic potential in improving the timing resolution, coming from the possibility of averaging the positron hit time over over the multiple hit pixels. This can be realised using the track reconstructed by the drift chamber, in order to take into account travelling time between the hit pixels (see Figure 2.27).

Preliminary performances show a resolution of about 56 ps using the hit on a single pixel, with the possibility to go down 30÷40 ps with multiple hits measurements.

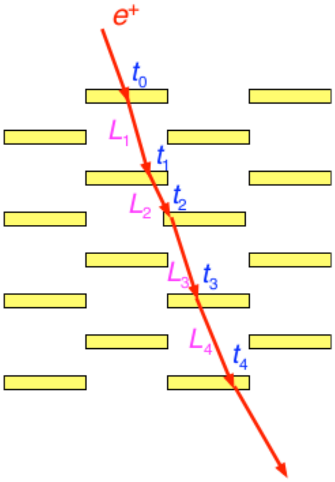

Figure 2.27 Example of the determination of positron timing by using multiple hits in the timing counter pixels. The track as reconstructed by the drift chamber is necessary for the estimation of the time of flight of the positron through the pixels. Figure from [21].

Summary

The MEG experiment has recently set a new upper limit of the $\mu \to e\gamma$ branching ratio. The process has a simple kinematics but very good resolutions are needed in order to discard the huge background. In order to improve its sensitivity, an upgrade of the experiment has been proposed; the new drift chamber will be a key detector in the upgrade, with performances and acceptance higher than that of the current experiment.

Part II

Preliminary tests of the prototypes of the new tracker

Chapter 3

Physics of drift chambers

In this chapter a quick overview of the basic physical phenomena happening in a drift chamber is presented, with the purpose of providing a framework on which the construction, the set up and the tests of the prototypes realised in this work of thesis will be clearer.

3.1 Drift chambers as detectors

Particle detection with drift chambers takes place in four phases: a particle looses energy in the detector volume (ionisation), electron-ion pairs drift towards the electrodes (transport), in the nearby of the anode electrons make avalanches (multiplication) and finally the signals from different wires are matched in order to determine particle trajectory (reconstruction). In this chapter the first three steps are discussed, in a way that does not mean to be comprehensive but aims only at introducing/reviewing some fundamental concepts of drift chamber that will be useful in the following chapters. Two basic references are suggested for a more complete treatment of the subject: the lectures by Sauli [30], a milestone in drift chamber physics, and the more recent book by Blum, Riegler and Rolandi [31]. In the following pages the physical parameters are described in the context of the prototypes tested during the work of this thesis, which mimic the configuration of the tracker for the MEG upgrade: we have in mind a $7 \times 7\,\mathrm{mm}^2$ drift cell filled with a gas mixture of helium and isobutane (in the relative concentrations of 90:10 and 85:15 in pressure) with an electric potential difference between anode and cathode of about 1.5 kV.

3.2 Ionisation

Charged particles are generally detected in their passage through matter by means of their energy loss. Among the various mechanisms that can account for it, only ionisation is relevant in drift chambers, mainly because of the low density of the detector (gas). The average amount of energy loss by a charged particle through incoherent Coulomb collision with the electrons of the medium

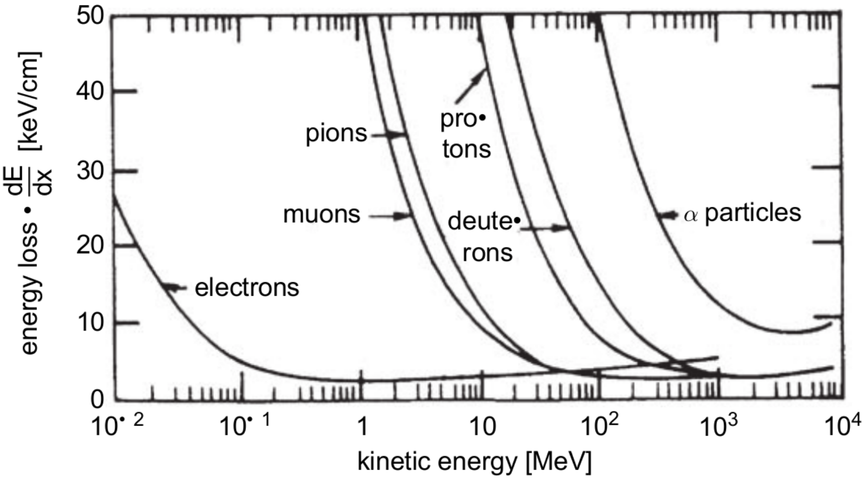

Figure 3.1 Mean energy loss distribution for several particles. Figure from [32].

is well-described by the Bethe-Bloch formula, plotted in Figure 3.1. Qualitatively, energy loss is large for slow particles, reaches a minimum and then increases again, but more slowly. The projectile dependence of the energy loss lies in a z^2/β^2 behaviour for energies smaller than the minimum ionising energy, where z is the projectile charge and β is its reduced velocity. Such behaviour explains two important features visible in Figure 3.1: the different values of the energy loss at the minimum of ionisation for electrons, muons, protons ($|z| = 1$) with respect to alpha particles ($|z| = 2$); the increase of minimum ionising energy with the increasing mass of the projectile, since β of minimum ionising particles (MIP) is fixed.

From a microscopic point of view, ionisation energy loss results from single processes of electron extractions [33]. In dense media one can neglect the discrete nature of energy deposits, but in gases single ionisation events, called clusters, can be observed. The cluster distribution is uniform in space, the mean distance between two clusters being given by the mean free path for ionisation encounters $\lambda = 1/n\sigma$, where n is the number density of the gas and σ is the ionisation cross section. Therefore the mean number of clusters (primary ionisation) n_P along a distance L is given by the ratio L/λ; since ionisation events are independent, n_P is a Poisson variable, and thus the travelled space between encounters has an exponential distribution. During ionisation encounters, extracted electrons have a broad energy distribution and in case of "close" collisions (*i.e* with high momentum transfer), secondary ionisation may occur: high-energy electrons (δ-rays) can produce in turn new electron-ion pairs. Secondary ionisation is in general the result of the thermalisation of primary electrons, which are slowed down by inelastic collisions. The total number of pairs produced is given by

$$n_T = \frac{\varDelta E}{W_i} \tag{3.1}$$

where ΔE is the energy loss in the gas volume considered and W_i is an effective (*i.e.* measured) average energy to produce one pair in the medium i. Experimentally it is found that W does not depend on the initial energy above a few keV for electrons and a few MeV for α particles [31]. For helium $W_{\mathrm{He}} = 41$ eV while for isobutane $W_{i\mathrm{C_4H_{10}}} = 23$ eV. As a measure of the contribution of secondary ionisation, one can consider the ratio n_T/n_P, which expresses the mean “pairs yield” for each cluster, which is 1.3 for helium and 4.2 for isobutane.

3.3 Transport

Once electrons and ions thermalize, they have very small energies (of the order $kT \approx 25$ meV) and start to drift under the effect of the electric field. However on their way they suffer from inelastic collisions with gas molecules that randomize their direction of motion. A macroscopic average velocity can be defined: the drift velocity. Such quantity depends on the thermodynamic conditions of the gas, the excitations cross sections and the electric field. It is found that the drift velocity (w) depends almost linearly on the electric field; it is therefore useful to define the mobility of the gas for ions and electrons as a reduced gas velocitiy

$$\mu^{\pm}(E) = w^{\pm}/E$$

Actually for ions μ^+ is a costant to good approximation, while for electrons this is true only at moderately low electric fields, for two reasons: electrons are much lighter than ions so the energy acquired between two collisions can be much greater than thermal energy; at such energies the collision cross sections varies rapidly, passing through maxima and minima, as a quantum effect between the drifting electrons and the gas electrons [30]. Figure 3.2 shows the electron drift velocities for the two gas mixtures of helium and isobutane at Standard Temperature and Pressure (STP): 20 °C and 1 atm, calculated in the framework of the Garfield++ [34] program.

Estimating an average electric field in the cell of the order 2 kV/cm ($\sim$ 1.5kV/0.7cm), the drift velocity is found to be $\approx$ 3 cm/µs, therefore the characteristic time for an electron to cross the cell is $\sim$ 200 ns.

While drifting, ions and electrons experience the randomization of their trajectory due to diffusion, as a consequence of the same collisions that keep their drift velocity constant. The result is a Gaussian smearing of their position with variance $2Dt$, where t is the drift time and D is the diffusion coefficient. Actually diffusion acts differently in the longitudinal or transverse direction, as much as the mean longitudinal and tranverse velocities are different. While tranverse diffusion is somehow harmless, longitudinal diffusion sets an irreducible limit on the accuracy to which one can measure drift times and distances.

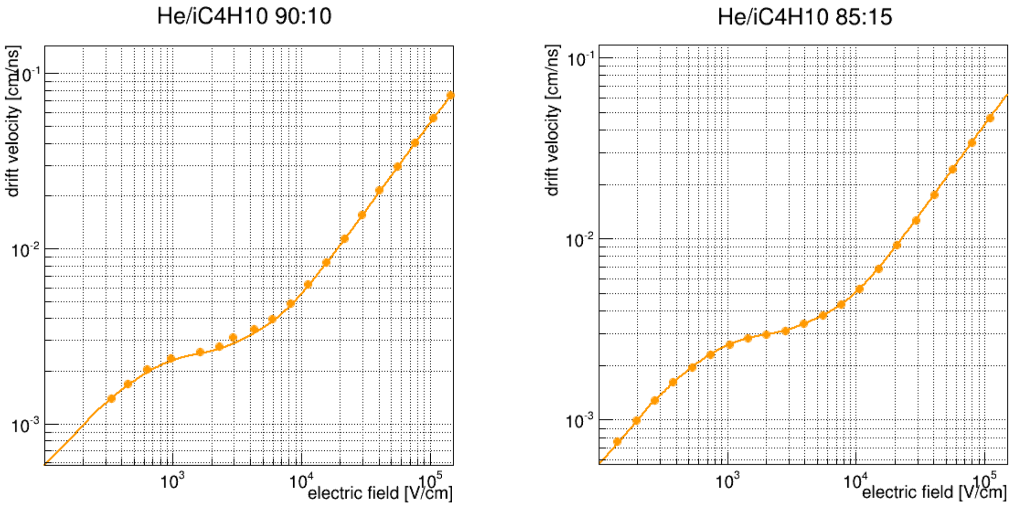

Figure 3.2 Drift velocities in two mixtures of helium and isobutane at STP.

3.4 Multiplication

When electrons approach the sense wire, its strong electric field (up to 10^5 kV/cm) increases their velocity by an order of magnitude or more (see Figure 3.2). If their energy increases over the ionisation potentials of the gas molecules, electron-ion pairs can be produced. The mean free path for ionisation is a function of the electric field and therefore of space; it is nonzero only over an electric-field threshold, that is the electric field at which drifting electrons gain an energy

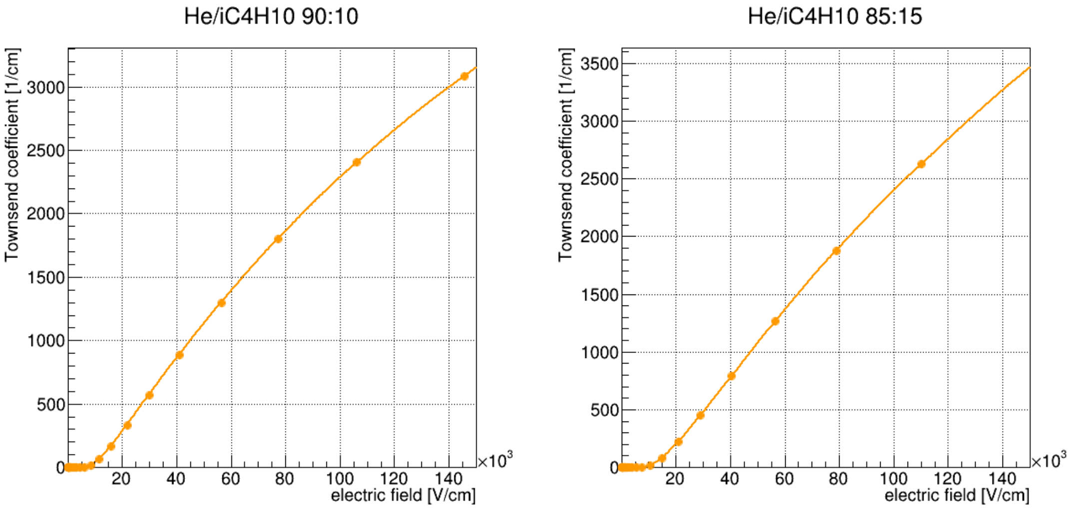

Figure 3.3 First Townsend coefficient in two mixtures of helium and isobutane at STP.

equal to the lowest ionisation energy of the gas molecules. The inverse of the mean free path is called the first Townsend coefficient α and represents the mean number of pairs produced per unit length. In Figure 3.3 Garfield++ calculations of the first Townsend coefficient for the two gas mixtures of helium and isobutane are reported at STP.

If multiplication occurs, signals coming from an ionising track are amplified by a factor G, the gain or multiplication factor of the cell, that is given by

$$G = \frac{N}{N_0} = \exp\left[\int_{r_0}^{a} \alpha(r)\mathrm{d}r\right] \tag{3.2}$$

where N_0 is the number of electrons that reach the point r_0 at which the field E_0 is just sufficient to start an avalanche, and N is the number of electrons at the wire radius a. According to Figure 3.3, one can assume that for $E > E_0$ the first Townsend coefficient is proportional to E.

Since in the proximity of the wire $E(r) = \kappa V/r$ where V is the anode high voltage and κ is a constant depending on the cell geometry, the first Townsend coefficient can be written as

$$\alpha(r)\mathrm{d}r = \alpha(E)\left(\frac{\mathrm{d}E}{\mathrm{d}r}\right)^{-1}\mathrm{d}E = \alpha(E)\frac{\kappa V}{E^2}\mathrm{d}E \tag{3.3}$$

So one may express the gain as a function of the high voltage applied to the anode[31]. Assuming $\alpha = \beta E$, equation (3.2) can be written as

$$\log G = \int_{E_0}^{E_a} \beta E \frac{\kappa V}{E^2}\mathrm{d}E = \kappa\beta V \log\frac{E_a}{E_0} = \kappa\beta V \log\frac{V}{V_0} \tag{3.4}$$

where $V_0 = aE_0/\kappa$ is the high voltage at which the electric field on the anode surface is E_0. The dependence of the gain on the applied voltage is therefore exponential, and is given by the Diethorn formula [31]

$$G = \left(\frac{V}{V_0}\right)^{\kappa\beta V} \tag{3.5}$$

Figure 3.4 shows the collected charge as a function of anode voltage. Four regions (operation modes) can be recognised:

I) Inefficient collection. The initial ionisation (primary and secondary) is not detected since the drift velocity is so small that the drift path is bigger than the mean free path for recombination.

II) Ionisation counter. The deposited charge is efficiently collected, but not amplified.

III) Proportional counter. Over a certain threshold voltage V_0 (V_T in the figure) multiplication occurs, and the charge collected is proportional to the initial ionisation events. Proportionality is gradually lost at increasing voltages when space charge effects lead to saturation. The width of this region is determined by many factors, *in primis* the dielectric strength of

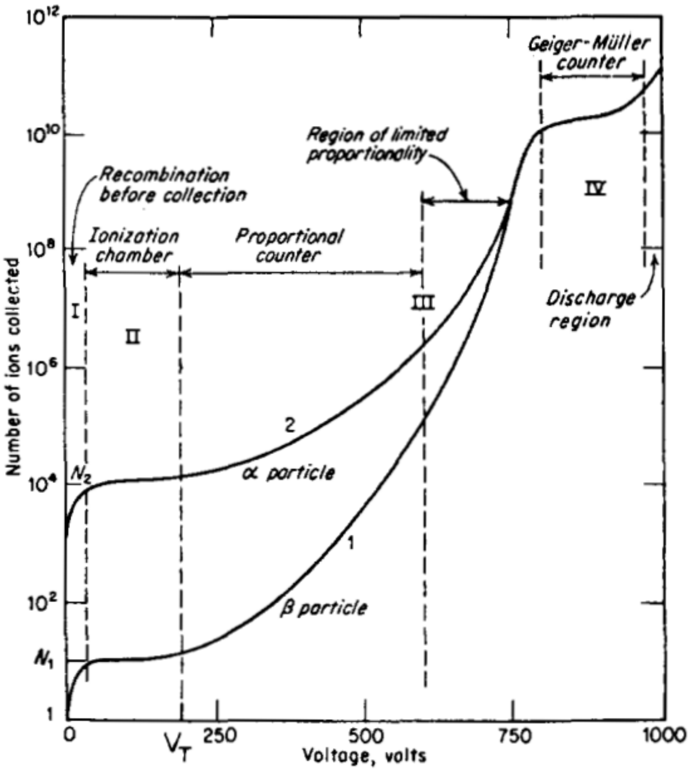

Figure 3.4 Operational modes of a wire chamber. Figure from [30].

the gas mixture, that is the minimum electric field which produces breakdown in absence of external radiation.

IV) Geiger-Müller regime. Any dependence on the original ionisation is lost and every event initiates a global discharge.

The range of the voltages at which all the original ionisation is collected, with no spurious counts due to discharges, is usually referred to as the “efficiency plateau”, and includes the regions II) and III).

3.4.1 Dependence of the gain on density

The dependence of the gain on the gas lies in both its composition and thermodynamics; the effects of impurities or additives are not easily to quantify, since in principle one has to include the various cross sections for excitation and ionisation. Gain variations with temperature and pressure can be deduced by the gain dependence on density, through the law of ideal gases. Since the collision mean free path is inversely proportional to the gas density[1], the minimal field E_0,

---

[1] actually if one writes the mean free collision length as $\lambda = 1/n\sigma$, there is also a dependence on n in σ, since the cross section is a function of the collision energy distribution which in turn depends on E/ρ. However for

being in turn inversely proportional to the mean free path, is proportional to the density

$$E_0 \propto \frac{1}{\lambda} \propto \rho \qquad \Rightarrow \qquad E_0(\rho') = E_0(\rho)\frac{\rho'}{\rho}$$

So equation (3.4) becomes

$$\frac{\mathrm{d}G}{G} = \mathrm{d}\log G = -\kappa\beta V \mathrm{d}\log E_0 = -\kappa\beta V \mathrm{d}\log\rho = -\kappa\beta V \frac{\mathrm{d}\rho}{\rho} \tag{3.6}$$

for small relative variations $\mathrm{d}\rho/\rho$. The gain is therefore a power law of the density with index $-\gamma = -\kappa\beta V$. Using ideal gas law $P \propto \rho T$ one obtains

$$\frac{G'}{G} = \left(\frac{\rho'}{\rho}\right)^{-\gamma} = \left(\frac{P'}{P}\right)_T^{-\gamma} = \left(\frac{T'}{T}\right)_P^{\gamma} \tag{3.7}$$

where the pressure (temperature) dependence holds if temperature (pressure) are kept constant. The quantity γ can be measured directly through equation (3.7). Notice that the dependence on T and P are opposite; we shall make use of this relation during ageing measurements.

3.4.2 Space charge effects

After an avalanche has reached the anode, positive ions slowly drift towards the cathode. If an drifting electron is up to multiplicate in the vicinity of the anode, it experiences a lower electric field and this results in a reduced multiplication. Space charge effects are clearly visible both in presence of high fluxes of radiation and at very high gain. In order to quantify such effects, one can consider an approximate change of the "anodic" potential[1] to be proportional to the particle rate R and to the gain

$$\frac{\Delta V}{V} = KGR$$

For small variations of the gain one can assume [30] the gain saturation having an exponential dependence on the voltage drop

$$G' = G\, e^{-KGR} \tag{3.8}$$

The gain dependence on the rate of incoming radiation can explain why in Figure 3.4, α-particle and β-particle signals have different proportionality slopes.

---

small density variations one can assume σ to be constant.

[1] in principle it is the difference between the nominal anodic potential and the effective potential that attracts electrons: space charge makes the electric potential smoother in the proximity of the wire thus lowering the electric field.

3.4.3 Statistical fluctuations of the gain

The gain of a multiplication process represents the size of the avalanche initiated by a single electron. Its probability distribution comes from the random nature of multiplication, which is characterised by a mean free path depending on the electric field and on the gas molecules ionisation energies. Several models aim at describing such fluctuations[31], borrowing probability distributions from other phenomena, like population growth, epidemic diffusion and electromagnetic showers. However in a drift chamber the gain is usually not referred to as the size of single-electron initiated avalanches, but as the ratio between the total charge collected and the number of electrons that started the avalanche. For k initiating electrons, the total number of ions collected N is given by

$$N = n_1 + n_2 + \cdots + n_k$$

where n_i is the yield of the avalanche initiated by the i-th electron. If k is sufficiently large[1], assuming the variables n_i to have a mean $\bar{n}$ and a variance σ_n and to be independent (thus k not too high in order to avoid space charge effects) the central-limit theorem states that the N distribution can be approximated to a Gaussian, with mean $\bar{N} = k\bar{n}$ and variance $S^2 = k\sigma_n^2$. Therefore the collected charge distribution of an ionising track is the convolution between the Gaussian distribution of the gain and the distribution of the energy loss by the incoming particle, as we will see in the next chapter.

Summary

In this Chapter we reviewed the physics behind particle detection by means of a drift chamber, with particular emphasis on aspects that will have some role in the following measurements.

---

[1] in 7 mm of He-iC_4H_{10} 90:10 a MIP creates 20 electron-ion pairs.

Chapter 4

R&D on a single-cell prototype

In this chapter the realisation and the functioning tests on the first single-cell prototype realised are presented. Following a chronological point of view, the preparation of the experimental apparatus needed for the tests is summarised at first. A description of the prototype is then presented, from its design to its realisation to the determination of its working point through Garfield++ simulations. Finally the tests on the prototype are introduced: the first signals acquired allowed studies on the evaluation of primary ionisation, drift and multiplication properties.

4.1 The experimental setup

The tests on the first prototypes of the new tracker were performed in a laboratory that has been set up from scratch. The experimental setup needed for such tests consists of three items, indipendently developed and then assembled:

- A gas line, which can supply the counting gas to the testing prototype at tunable fluxes and pressure.
- A sealed box as gas volume, which can contain the prototype under test avoiding gas contamination. As in the final detector the drift chamber has a single volume, so the various prototypes consist in a solid structure holding the stretched wires, which has to be inserted in the box.
- An X-ray source, needed for the ageing tests of prototypes, which will be described in Chapter 7.

For safety reasons the X-ray source and the gas chamber were placed into a safe-box with dimensions $1 \times 1 \times 1\,\mathrm{m}^3$ made of two lead foils enclosed by two aluminum slabs, each with a thickness of 1 mm. Before focussing on the detector itself, a description of the gas system feeding the chamber is provided.

The gas mixtures used in the prototype tests are made of helium and isobutane in two different concentrations, 90:10 and 85:15 in pressure. In order to guarantee the stability and the performance of the detector, high-purity mixtures were chosen: helium 5.5 (which means purity greater than 99.9995%) and isobutane 3.5 (purity greater than 99.95%). Although high gas flow was needed for the tests, the gas cylinders (containing already mixed gas) could not be kept at high pressure (200 bar). Since the vapor pressure of isobutane at 15°C is 2.56 bar[35], the gas pressure in the cylinder should be lower than 25.6 bar for 90:10 mixture and 17.1 bar for the 85:15 mixture, in order to avoid the partial pressure of isobutane to be larger than 2.56 bar. Excessive pressures lead to the liquefaction of the isobutane, thus altering the gas composition. Therefore the gas was supplied by four 50–litre cylinders at 16 bar for the 90:10 mixture and 10.7 bar for the 85:15, resulting in a total gas storage of respectively 3.2 $\times 10^6$ cm^3 and 2.1 $\times 10^6$ cm^3 at 1 bar.

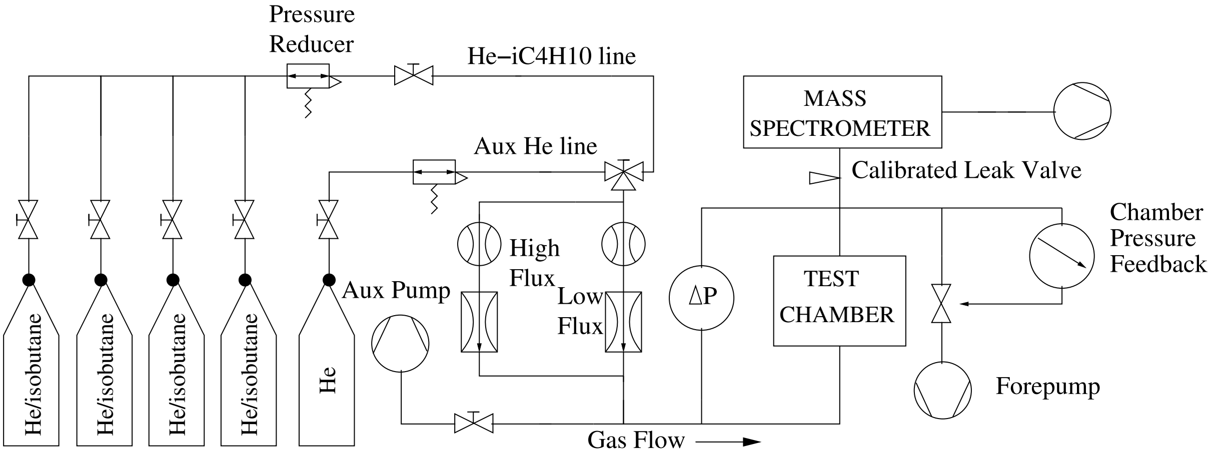

Figure 4.1 Schematics of the gas circuit.

Figure 4.1 shows the line assembled for the gas flow in the test chamber. It can be divided into three parts

- **Gas supply**. Two lines were realised, the main helium-isobutane line and an auxiliary line that can be fed with pure helium or another gas mixture. The gas flow is measured and controlled by two flow meters MKS 1179B, one (high flux) with a full scale of 200 sccm[1] and the other (low flux) with a full scale of 15 sccm. The flow rate is set by a four-channel flow controller MKS 647C, which acts on the flow meters.
- **Gas control in the chamber**. The chamber volume must be in stable conditions. For this reason two alternatives were implemented: an absolute pressure measurement and differential pressure measurement between inlet and outlet. Since drift chamber performances are very sensitive to absolute pressure variations, in the tests presented in this thesis only the absolute pressure was controlled and kept constant by a MKS 250E pressure

---

[1] Standard Cubic Centimers per Minute.

controller that reads pressure measurement from the pressure meter MKS Baratron 722B and regulates the opening of an outlet flow control valve MKS 248B accordingly. The outlet valve is connected to a forepump, so that its opening and closing determines the amount of gas exiting the chamber.

- **Auxiliary branches**. Two more connections to the chamber volume were made. One is needed for connecting a vacuum pump to the chamber thus avoiding contamination of the gas mixture coming from air residuals. The other one lets the gas flow through a calibrated leak valve RIAL VFCR to a Residual Gas Analyser (RGA) Extorr XT100, which allows to take mass spectra to measure qualitatively gas composition. The latter works at very low pressures (of the order of 10^{-6} mbar), so its detection volume is connected to a turbomolecular pump Pfeiffer and the measuring pressure is determined by the leak valve opening.

In Figure 4.2 a picture of part of the gas system, placed upon the safety box, is shown. In the background the four cylinders are visible, while in the foreground from right to left there are the gas inlet of the chamber (entering the box), the parallel with the differential pressure meter, the absolute pressure meter, the flow control valve and at the end the forepump.

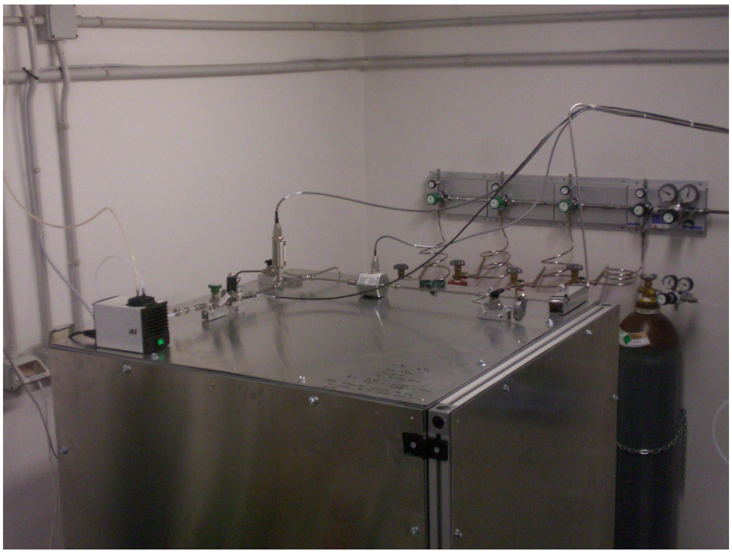

Figure 4.2 Picture of the gas system of the chamber.

4.2 Prototype realization

In order to faithfully reproduce the behaviour of the new tracker, a drift cell as close as possible to that envisaged for MEG$^{\mathrm{UP}}$ was implemented. The cell structure is reproduced on two FR4 Printed Circuit Boards (PCBs), supported by four rods, with wires stretched between the PCB holes. The first prototype realised (Prototype I) has a single cell surrounded by guard wires, needed for shaping the electric field inside the cell. The elementary cell consists of an anode wire placed at the centre of a square having cathode wires on its vertices and on the midpoints of its sides.

The PCB used in realising the single–cell prototypes is shown in Figure 4.3; it can be alternatively used to realise a 3 × 3 cell configuration.

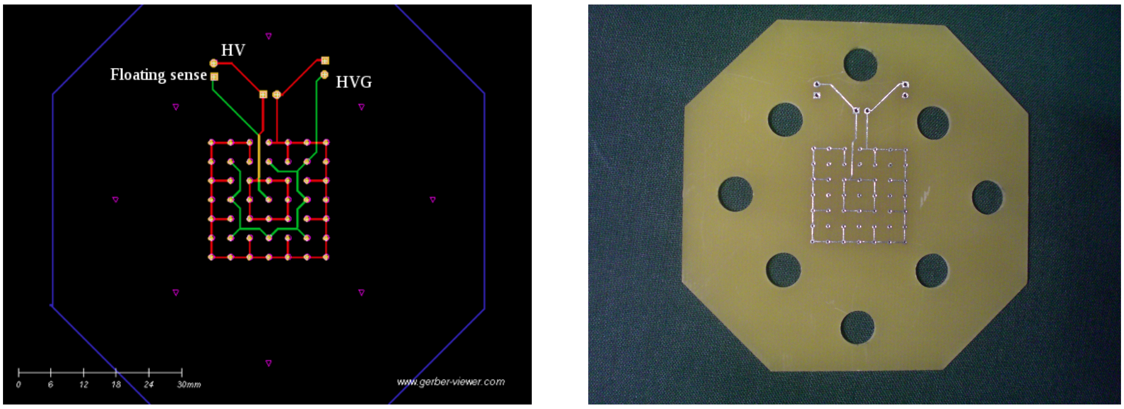

Figure 4.3 PCB schematics and picture for single–cell prototypes.

On the PCB there is a matrix with 7 × 7 holes for wire soldering and six pads (on the top of Figure 4.3) for power supply and wire readout. The central hole, which hosts the anode, is isolated from the other holes of the matrix, whereas the eight holes surrounding it (where the cathode wires will be placed), are at a common potential. Eight outer cells can be wired, but for these tests only their anodes are soldered, used as guard wires to shape the field of the inner cell according to a Garfield++ simulation presented later in this chapter. The remaining holes of the matrix are left empty. The eight big holes placed around the holes for the wires were used for the prototype assembly: on the four corner holes, 20-cm long PEEK rods were placed. The wires used in Prototype I were gold-plated tungsten wires, with a diameter of 25 µm for the anode wire and of 80 µm for cathode and guard wires. In order to close the drift lines (in a way that will be clear in the next section) inside the volume embraced by the two PCBs, the rods were surrounded by cable sockets and connected to each other, thus providing an external common ground.

Usually in drift chambers, anodes have positive high-voltage, whereas cathodes are grounded. Since for ageing tests anode current measurements are needed, we adopted a shifted potential configuration, in order to measure directly the anode current with a picoamperometer. Therefore in our case, high voltage is applied to field wires and guard wires (at different values) through a 4.7 MΩ resistor and the anode is floating with respect to the box, it is only connected to the data acquisition apparatus (see Figure 4.4).

The wiring procedures were performed in the clean room of INFN, Pisa. Figure 4.5 shows the

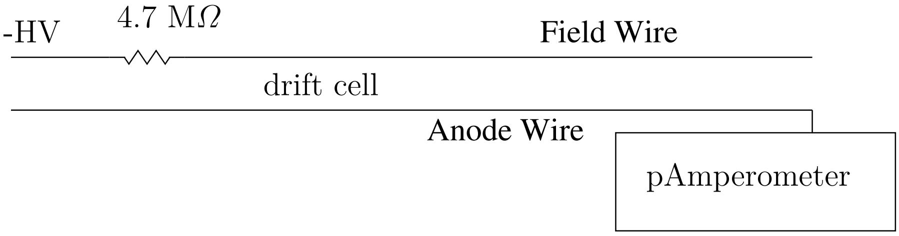

Figure 4.4 Circuit of power supply and readout of Prototype I.

wiring apparatus in its latest version. The wires are inserted one by one, from the top PCB to the bottom PCB with the prototype placed vertically. The wire spool turns around a fixed pivot, and the outcoming wire slithers on a clean-room wipe soaked with isopropyl alcohol. The wire is then inserted in its top and bottom holes, with the wire left protruding a few centimetres under the lower PCB. After soldering the wire on the upper PCB, a 30 gramme weight is attached to the lower end of the wire in order to apply the same tension to all the wires[1]. The wire is then soldered in the lower PCB and the wire stubs are cut away.

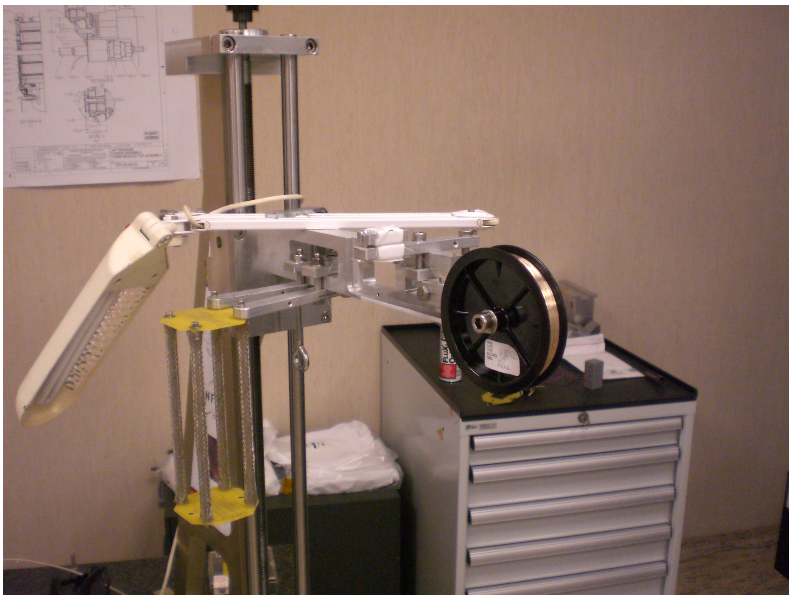

Figure 4.5 Wiring apparatus. The wire slides from the spool (on the right–hand side of the picture) into the prototype (on the left–hand side).

Wiring is a very delicate procedure, as regards cleanliness and fragility: even taking the wire with pliers produces mechanical deformation that prevent the wire from stretching in the right way.

The finished prototype is shown in Figure 4.6, where one can see the central cell and the

---

[1] gain non-uniformity and chamber instability can arise owing to mechanical imperfections.

outer wires. In order to check real time functioning of the chamber a radioactive source of ^{241}Am was glued on a screw and fastened to a supporting rod by means of a teflon cable tie (blue in the figure). As a sealed clean box a standard conflat CF100 ultra-high-vacuum cross was adopted; such choice brings two valuable benefits: its cleanliness (being made of stainless steel) and its shielding to high frequency noise on wires (working as a Faraday cage). Two opposite flanges of the cross are tapped with two 150-µm Mylar windows, in order to let radiation go in and out the chamber with moderate absorption or scattering. The other flange hosts the gas inlet and three feedthroughs, two for the high-voltage supply and one for the signal; on the last flange, only the gas outlet was placed. For the integration of the prototype in the chamber, a C-shaped support fastens the prototype (namely the rods) to the flange with the electrical feed-throughs (visible in Figure 4.6). In this way the wires are centred with respect to the axis connecting the centres of the flanges with the Mylar windows. In addition the bracket provides electrical contact between the rods and the cross, which is therefore the common ground.

Figure 4.6 Prototype I in INFN Pisa clean room.

4.3 Determination of prototype working point

Once the setup was assembled, the choice of the high voltages of the wires were made through Garfield++ simulations. In this first test the gas mixture was helium–isobutane 90:10. Calculations assume infinite wires: since we are interested in the behaviour in the central part of our wires ($\sim$ 3 cm on a total length of 20 cm), and the cell width is much smaller than the wire

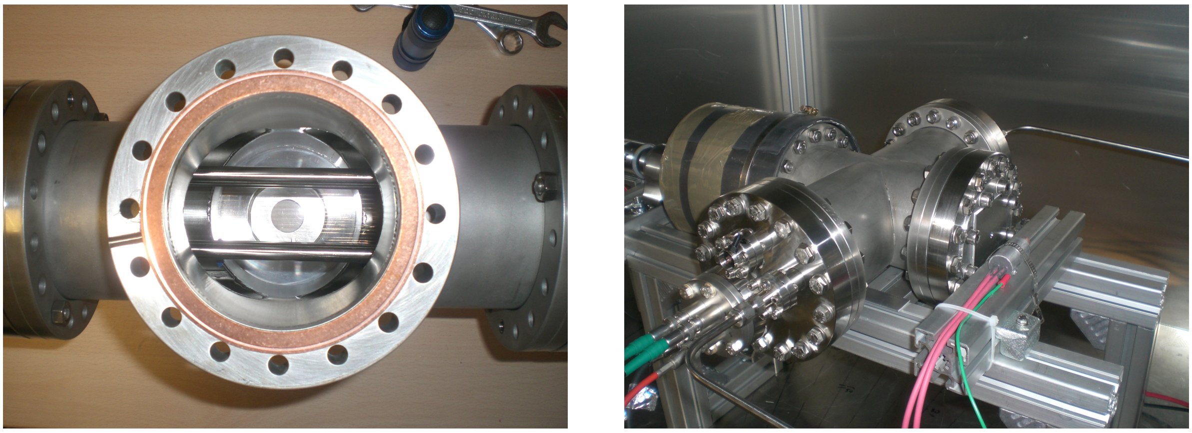

Figure 4.7 CF–100 cross after the integration of the prototype (left) and with the gas and electrical connections plugged (right). On the right-hand figure the X-ray source (on the left) and a sodium iodide detector (on the right) are visible (any discussion is deferred to Chapter 7).

length (0.7 cm versus 20 cm), boundary effects are negligible. Guard-wire voltages were chosen in order to keep a moderately low electric field on cathode surfaces: in order to avoid multiplication on cathodes, an upper limit of 20 kV/cm was placed on cathode electric field (see Figure 3.3). As a first test, a conservative working point was chosen: −1250 V for cathode wires and −1000 V for guard wires (see Figure 4.8), so that multiplication is controlled on the anode and absent on the other wires.

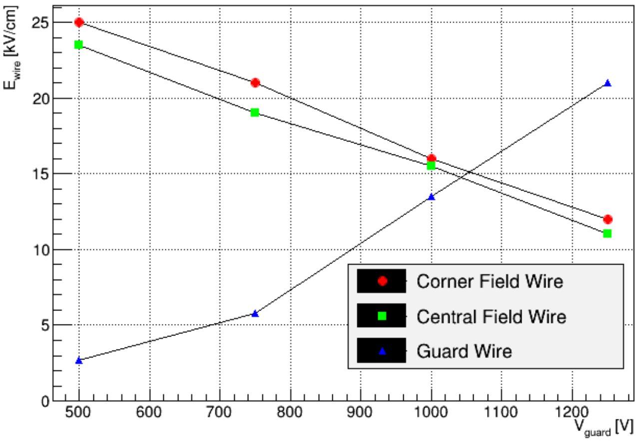

Figure 4.8 Electric field on wire surfaces at different values of guard wire voltages.

Figure 4.9 shows the electric field in the cell and in the proximity of the sense wire. The mean electric field in the drift region is about 1kV/cm, while on the anode surface it reaches 140 kV/cm, thus enabling multiplication (see Figure 3.3).

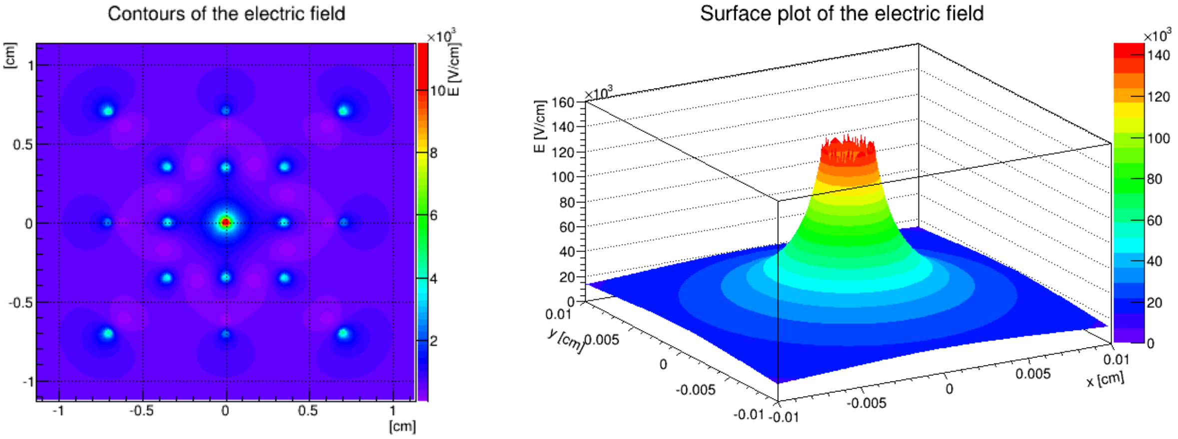

Figure 4.9 Map of the electric field in the drift cell (left) and close to the anode wire (right).

The multiplication factor of the cell was simulated with Garfield++. The program allows the creation of an electron-ion pair at a generic point in the cell; after drifting it creates an avalanche and the gain is calculated as the size of such avalanche. As explained in Section 3.4, the probability distribution of the size of the avalanches initiated by a single electron is not important for gain determination; what really matters is its mean value and its standard deviation. The gain distribution returned by Garfield++ is shown in Figure 4.10 and has a mean value of ∼ 9000 and a standard deviation of ∼ 7000.

Guard wires are also needed for shaping the electric field in order to have definite drift region: drift lines are shown in Figure 4.11 and show that ion pairs created outside the cell do not drift towards the anode, thus limiting charge collections to be the same of a cell in the final chamber.

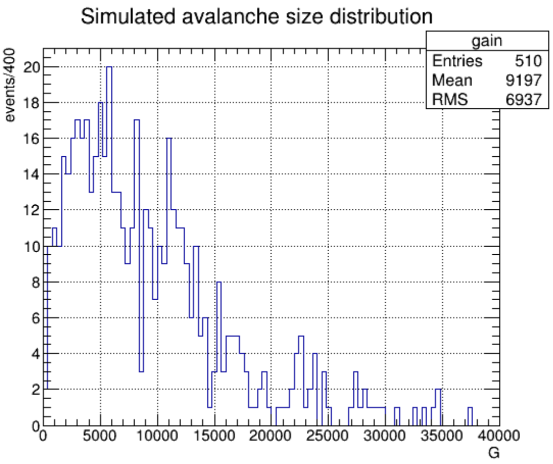

Figure 4.10 Avalanche size distribution simulated with Garfield++.

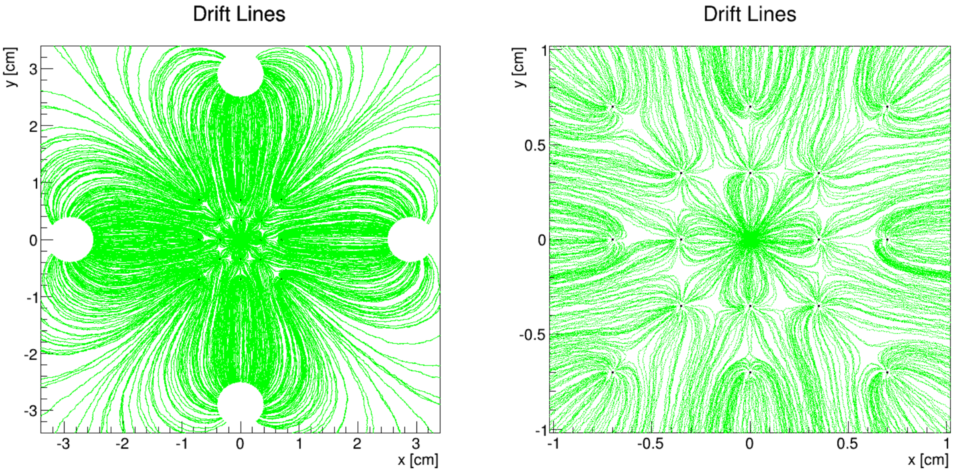

Figure 4.11 Drift lines in the prototype. It is appreciable that pairs created inside the cell converge to the anode with no leakage, while outer pairs drift to the rods.

Outside the cell, drift lines converge to the four rods. It is important to notice that in this configuration the anode wire collects the same charge as if the cell were in an infinite matrix. The charge collected by the cathodes, on the other hand, is a factor two (four) lower for edge (corner) cathodes respectively, since multiplication occurs only inside the cell.

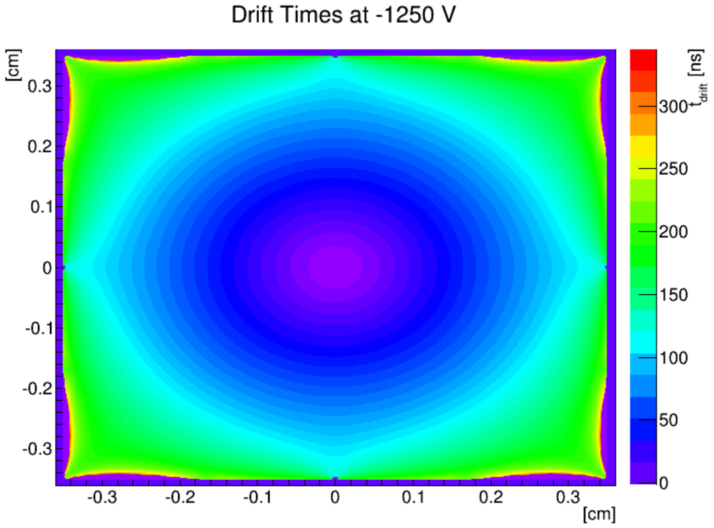

Figure 4.12 Drift times.

For short integration times, signal development is given by the drift times of electrons: Figure 4.12 shows the simulated drift times of electrons. It is noteworthy that up to drift distances of 3 mm (or drift times of 100 ns) cylindrical approximation holds: for larger distances isochrones deviate from circular shape. Anyway except in low field areas electrons leave the whole cell clear in about 250 ns.

4.4 Charge drift in Prototype I

Wire high-voltages were provided by a CAEN N470 module installed in a NIM crate. In series between the power supply and the prototype a 4.7 MΩ was placed, in order to damp high voltage fluctuations and protect the wires in case of discharges, to limit the total current. The check of the chamber functioning was performed with americium α-particle signals. Americium decays to neptunium with an emission of a $\sim$ 5.5 MeV α particle

$$^{241}\mathrm{Am} \rightarrow {}^{237}\mathrm{Np}^{*}\ \alpha$$

Neptunium is left in an excited state most of the times, and de-excitation X-rays are emitted[1] in the $\mathrm{Np}^{*} \rightarrow \mathrm{Np}$ transition at characteristic X-ray energies of 26.34 and 59.54 keV. In the most probable decay channels alpha particle energy can be 5.486 MeV (85%) or 5.443 MeV (13%).

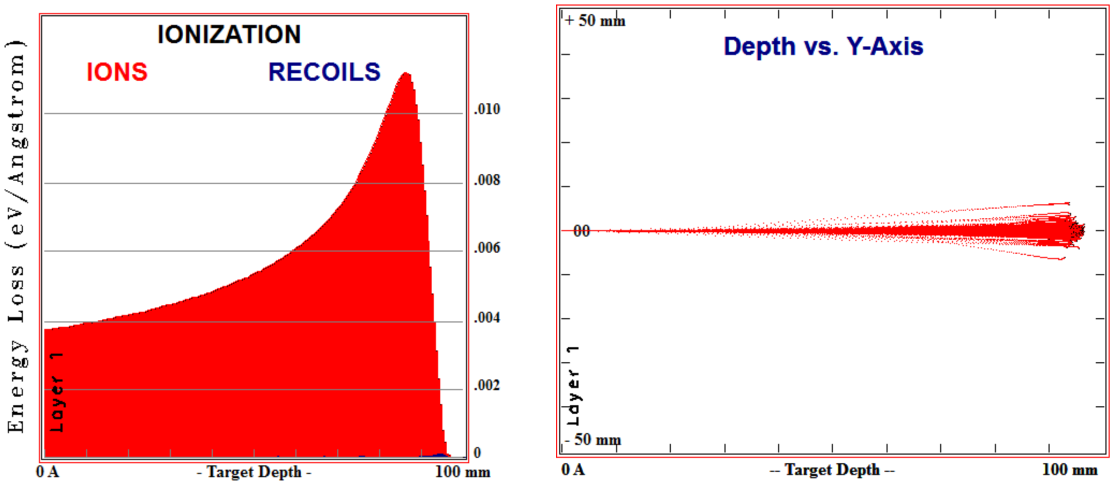

Figure 4.13 Energy loss (left) and range (right) of 5.486–MeV alpha particles in helium-isobutane 90:10 calculated with the SRIM program.

Figure 4.13 shows the range and the energy loss of 5.486–MeV alpha particles in the used gas mixture, calculated with the “Stopping and Range of Ions in Matter” (SRIM) program[36].

The distance travelled by the alpha particles before entering the cell, spreads from 2.15 cm to 7.8 cm depending on the impinging angle of the alpha particle (see Figure 4.14).

The length of the track inside the cell varies from 0.7 cm to 2.55 cm accordingly[2]. Therefore the energy deposits on the cell range from 315 keV up to about 2 MeV in the proximity of

---

[1] X-ray spectra of the americium source are presented in chapter 7.

[2] in the case the α-particle passes through all the cell width.

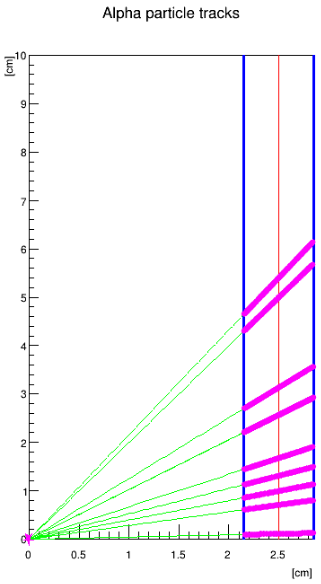

Figure 4.14 Simulated tracks of alpha particles entering the cell at different angles.

the Bragg peak. Since the energy loss is about four orders of magnitude larger than the mean energy for creating a cluster, the number of clusters per unit length is so large that tracks can be considered continuous with a good approximation. We want to study the expected signal caused by an α-particle. Suppose an alpha particle is crossing the cell with impact parameter b, being its line of flight parallel to the cell borders, as in Figure 4.15. Ionisation clusters are uniformly distributed along the track, *i.e.* $P(x)\mathrm{d}x = 1/\lambda\,\mathrm{d}x$. For simplicity we assume the drift velocity w

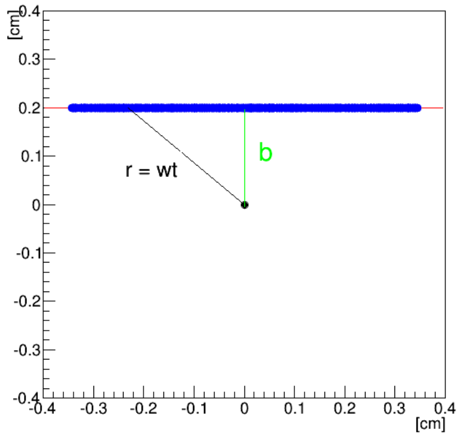

Figure 4.15 Example of an α-particle track.

to be constant in space. The distribution of the drift times of ionisation clusters is given by

$$\frac{\mathrm{d}N}{\mathrm{d}t} = \frac{\mathrm{d}N}{\mathrm{d}x}\frac{\mathrm{d}x}{\mathrm{d}r}\frac{\mathrm{d}r}{\mathrm{d}t}$$

Since $r^2 = x^2 + b^2$

$$\frac{\mathrm{d}N}{\mathrm{d}t} = \frac{1}{\lambda}\frac{r}{x}w = \frac{w}{\lambda}\frac{r}{\sqrt{r^2 - b^2}} = \frac{w}{\lambda}\frac{wt}{\sqrt{w^2t^2 - b^2}} = \frac{w}{\lambda}\frac{t}{\sqrt{t^2 - (b/w)^2}}$$

The divergence at $t = b/w$ is usually referred to as jacobian peak. Since drift lines and times are symmetric under rotations around the anode wire up to a distance of about 3.5 mm, we can restrict to the case of a circular drift cell. From an experimental point of view this can be realised by setting a temporal cut on signals, say 150 ns.

Figure 4.16 shows the time distribution of clusters from a track with impact parameter $b = 2$ mm at a drift velocity $w = 3$ cm/µs crossing the cell at $t = 0$.

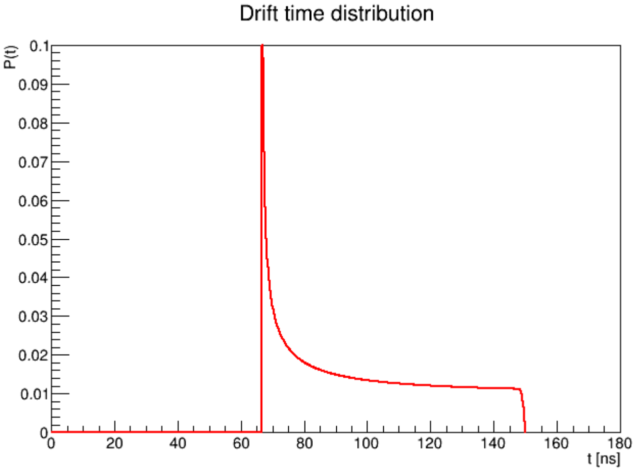

Figure 4.16 Theoretical signal of a continuous track with impact parameter $b = 2$ mm, drift velocity $w = 3$ cm/µs, truncated at 150 ns.

For a more realistic view, the arrival-time distribution of clusters from a straight track was obtained with a Monte Carlo simulation. Once a track is generated (as in Figure 4.15), cluster positions are extracted randomly from a uniform distribution. The cluster density chosen is 500 cluster/cm (less than the $\mathcal{O}(10^4)$ estimated above, but enough for approximating the continuous limit). Instead of assuming a constant drift velocity, to each cluster was associated the corresponding drift time calculated by Garfield++, as in Figure 4.12. The drift time distribution is then folded with an assumed single–cluster signal, giving a simulated waveform for the considered track. A Gaussian white noise was added to each track. Figure 4.17 shows three simulated waveforms for different tracks and three α-particle signals acquired with a DRS4 evaluation

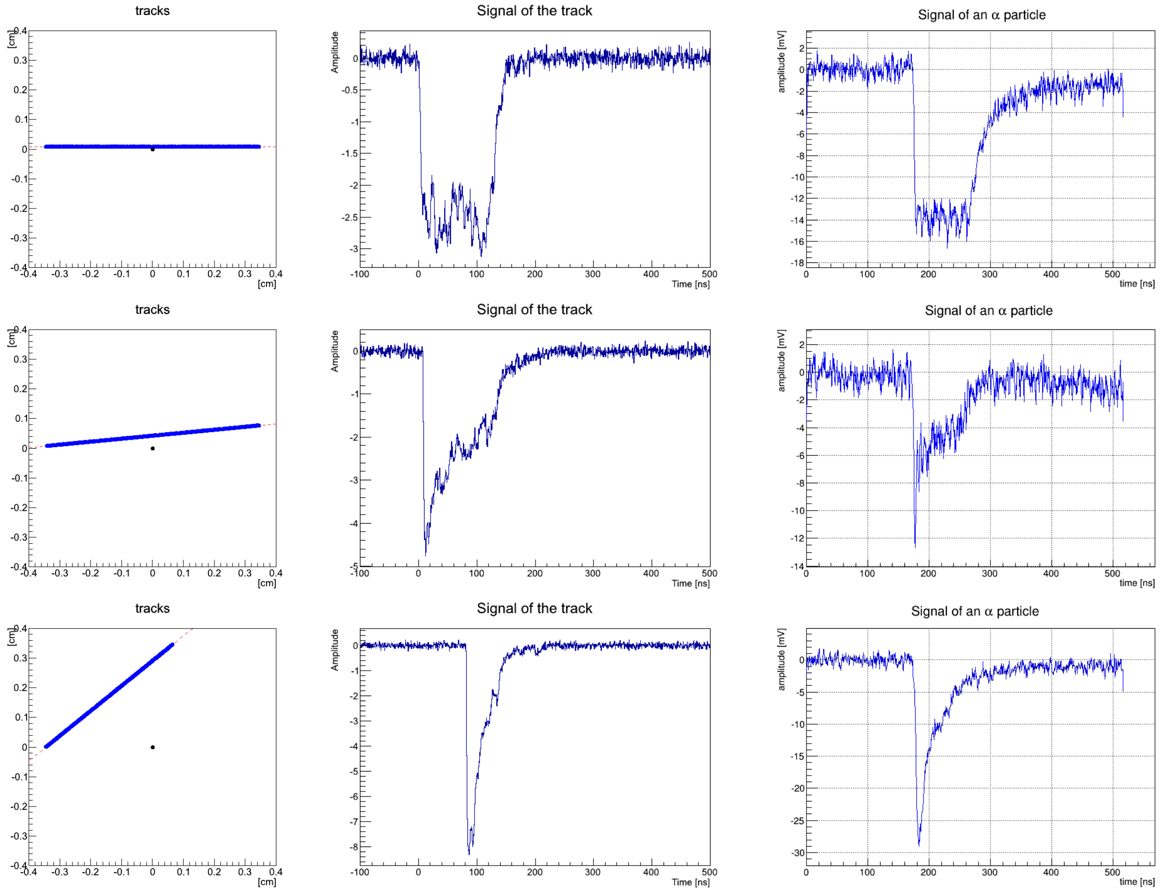

Figure 4.17 Simulated track, simulated signals and detected signals at three different impact parameters, in cases a), b) and c).

board[1]. It is clear the analogy with Figure 4.16 in both simulated and acquired waveforms: we can associate different signal shapes detected by the waveform digitizer to corresponding configuration in the simulation.

The duration of the signal depends only[2] on the impact parameter. In particular it is mainly the impact parameter that dictates the shape of the waveform: the three cases shown in Figure 4.17 are

a) $b \to 0$ (physically $b \ll \lambda$). The jacobian peak is not present since equation (4.4) in such limit shows no singularity. The distribution of the arrival times is therefore flat.

b) $\lambda < b < d_{\text{cell}}$. The jacobian peak is superimposed to a uniform distribution with the maximum drift time as endpoint.

---

[1] which is the same used in the MEG experiment.

[2] except for external region where drift is slow due to weak electic fields.

c) $b \sim d_{\mathrm{cell}}$. The jacobian peak spreads on all the waveform.

In case a) the width of the signal estimates the time needed for an electron to drift half cell, and thus the mean drift velocity in the cell. From the waveform reported in Figure 4.17 we obtain

$$w \simeq \frac{0.35\,\mathrm{cm}}{110\,\mathrm{ns}} = 3.18\,\mathrm{cm}/\mu\mathrm{s}$$

in agreement with previous estimates.

The variation on the track length for data accounts only for the amplitude of the signal, since it results as a larger number of clusters per unit length once the track is projected on the drift plane (orthogonal to the wires). Figure 4.14 shows tracks simulated at several angles.

4.5 Charge multiplication in Prototype I

4.5.1 Voltage-current curve

The second step for the characterisation of the prototype was the measurement of the current–voltage curve at constant irradiation, in order to find the different operational points of the chamber (as in Figure 3.4). Primary ionisation was provided by an X-ray tube (see Chapter 7). Anode current was measured with a Keithley Sourcemeter 2635A, whose resolution is of the order of the picoAmpere. The measured current as a function of the high voltage is shown in Figure 4.18 and is well described by a function of the form $\mathrm{p}_2(V/\mathrm{p}_0)^{\mathrm{p}_1 V}$ (see equation 3.5), with a threshold potential value of $V_0 = \mathrm{p}_0 = 746 \pm 20$ V.

During the test semi–proportional and Geiger regimes were avoided in order to prevent

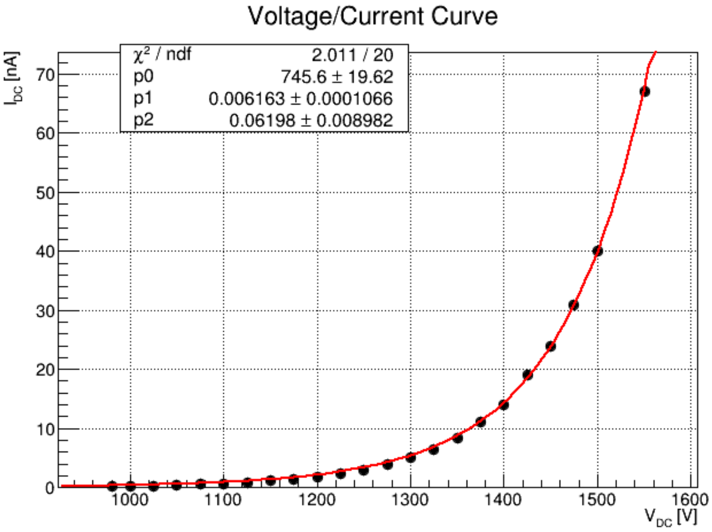

Figure 4.18 Current–voltage curve for Prototype I.

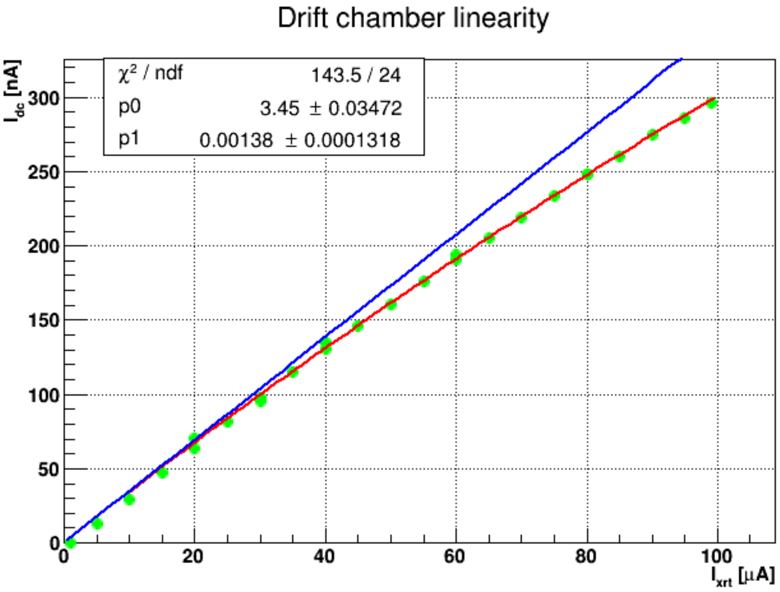

Figure 4.19 Anode current as a function of the X-ray tube emission current. Saturation due to space-charge is visible.

the damage of the chamber. Further tests however excluded the presence of discharges up to $V = 2$ kV.

4.5.2 Linearity and space-charge effects

The wire current at which space charge limits the proportionality of the chamber can be also estimated by irradiating the chamber at increasing doses. The X-ray tube was used as tunable source: the linearity of the X-ray beam with respect to the current flowing through it was checked with a 1” sodium iodide detector. The characteristics of the experimental setup and the results will be discussed in Chapter 7. Now we focus on the drift chamber behaviour. Gain loss due to space charge effects can be parameterised as in equation (3.8). The anode current is given by

$$I_{\rm dc} = RG' = RGe^{-KRG} \tag{4.1}$$

where R is the rate of primary ionisation and G is the non–saturated gain. In our case we do not know R but $I_{\rm xrt} = \varepsilon R$, where ε is an unknown constant representing the “efficiency” of X-ray conversion in the cell. Figure 4.19 shows the anode current $I_{\rm dc}$ plotted against the X-ray tube current $I_{\rm xrt}$. The curve is well described by a function of the form

$$I_{\rm dc} = {\rm p}_0 I_{\rm xrt} e^{-{\rm p}_1 I_{\rm xrt}} \tag{4.2}$$

The red line in Figure 4.19 is the fitted function, while the blue line indicates the proportionality in absence of saturation, obtained setting $p_1 = 0$.

From a comparison between equations (4.1) and (4.2), one obtains

$$p_0\varepsilon = G \qquad\qquad p_1\varepsilon = KG$$

so that $K = p_1/p_0$, while the multiplication factor cannot be deduced since ε is unknown. The subtraction of space-charge effects will have a basic role in ageing measurements.

4.5.3 Gain evaluation

Measuring the gain of a drift chamber is a difficult procedure, since many unknown factors, such as variations of the track length (thus the amount of the deposited energy) or space-charge effects, can affect its determination. For measuring the multiplication factor, the strategy is to compute the total charge of the track pulses and to extract the charge corresponding to one deposited electron. The pulse charge is given by

$$\frac{V[\mathrm{mV}] \times \mathit{\Delta} t[\mathrm{ns}]}{R[\mathit{\Omega}]} = I[\mathrm{mA}] \times \mathit{\Delta} t[\mathrm{ns}] = Q[\mathrm{pC}]$$

where R is the shunt resistance. However the integration of the waveforms is non-trivial, because of the low signal-to-noise ratio and the instability of the baseline (see the second waveform in Figure 4.17). For gain measurements three sources were available: α-particles, X-rays and MIPs such as cosmic rays and electrons from a ^{90}Sr source. Figure 4.20 shows signals of the different particles, a few features are visible. α-particle signals are continuous over the whole drift time interval, X-ray signals consist in a narrow pulse within a few tens of nanoseconds, while in MIP signals different clusters are visible and extend on a wider time interval. The amplitudes of the signals are quite similar because of different amplification and different high voltage of the chamber. Alpha signals are not affected by a low signal-to-noise ratio, but cannot provide a measurement of the gain, because of the spread in the tracks length resulting in different numbers of primary electrons (see Figure 4.14).

X-ray signals

The most likely processes for X-ray interactions in the used gas mixture for $E_\gamma \lesssim 10$ keV are photoelectric effect and Compton effect (see Figure 4.21 for helium). Compton scattering results is an accelerated electron and a lower energy X-ray, with higher photoelectric effect cross section. In both cases the interaction results in one or more keV electrons: in order to understand the basics mechanism, we focus on photoelectric effect. Since in helium and isobutane electron binding energies are far lower than E_γ, the result of the interaction is an electron with almost the same energy of the X-ray. Such keV electrons start ionising the gas for a distance that in principle may be calculated by integration of the Bethe–Bloch formula, but in practice its

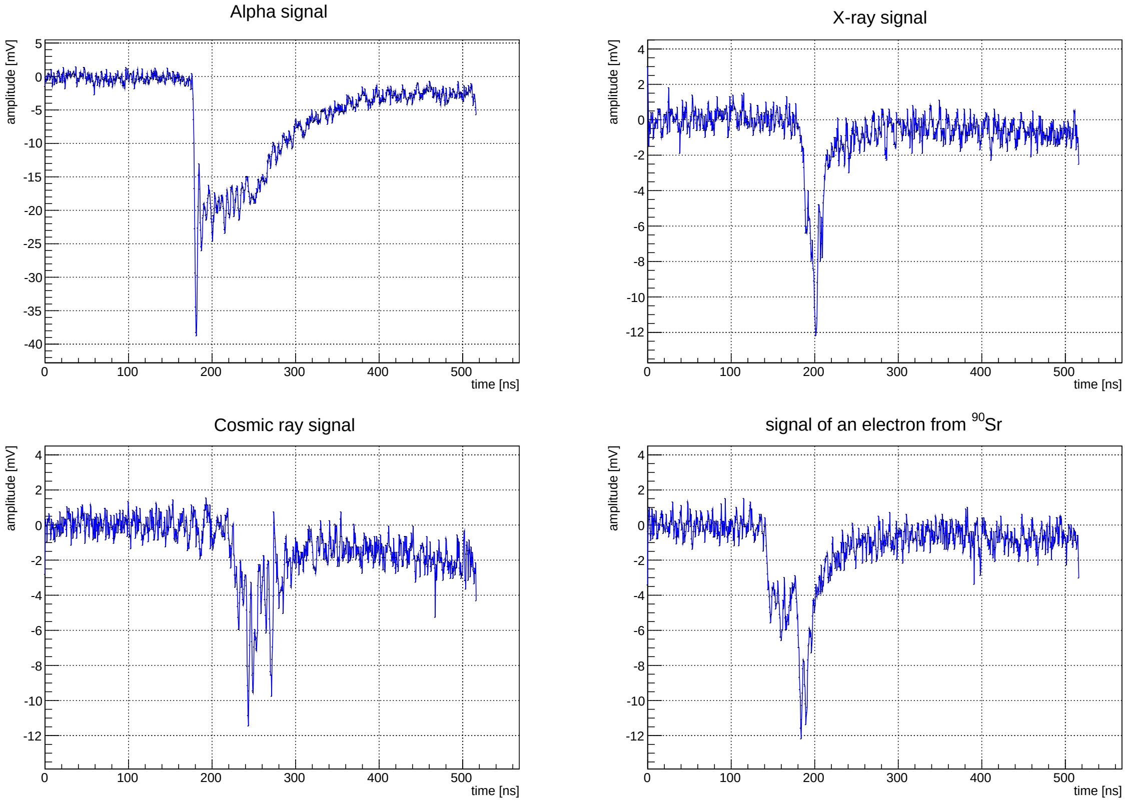

Figure 4.20 Signals of different particles. See the text for a desciption.

trajectory is randomized by multiple scattering effects. An experimental-based practical range is defined, which can be parameterised by different formulae (from [30] and [31] respectively)

$$R(E) = \frac{1\text{g/cm}^3}{\rho}\, 0.71 \left(\frac{E}{1\,\text{MeV}}\right)^{1.72} \text{cm} \qquad E \lesssim 100\,\text{keV} \tag{4.3}$$

$$R(E) = \frac{1\text{g/cm}^3}{\rho}\, A\, E \left(1 - \frac{B}{1 + C\,E}\right) \text{cm} \qquad 300\,\text{eV} < E < 20\,\text{MeV} \tag{4.4}$$

with $A = 5.37 \times 10^4\,\text{keV}^{-1}$, $B = 0.9875$ and $C = 3.123 \times 10^{-3}$ keV. Figure 4.22 shows the effective range in the two parameterisations ([30] dotted line, [31] solid line) in 85:15 and 90:10 helium-isobutane gas mixtures.

In our measurements, X-rays are produced by two X-ray tubes. In case of W-target X-ray tube, the radiation line is W–$L_\alpha \simeq 8.4$ keV [38]. If one approximates the specific energy loss in helium and isobutane being the same, the average number of electron-ion pairs produced by such photoelectrons is given by

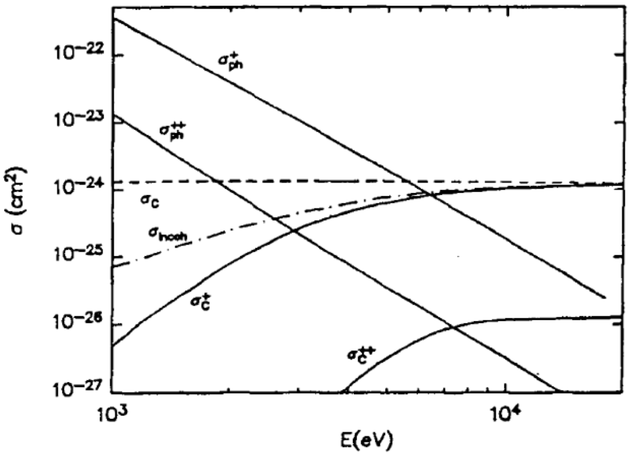

Figure 4.21 Cross sections for photabsorption σ_{ph}^{+} and Compton scattering σ_{C}^{+} of X-rays in helium. Figure from [37].

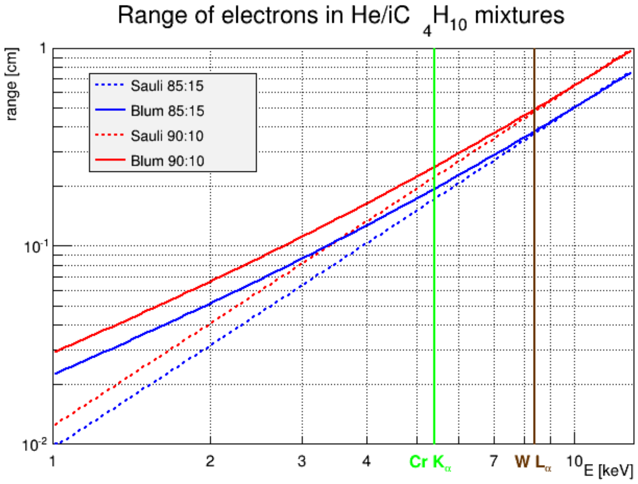

Figure 4.22 Effective electron range in the two gas mixtures according to two different models.

$$N_e = E_\gamma \left(\frac{90\%}{W_{\text{He}}} + \frac{10\%}{W_{\text{iC}_4\text{H}_{10}}} \right) \simeq 220$$

However the range of a 8.4 keV electron is about 5 mm, that is a significant fraction of the cell size. Charge leakage is therefore large and the amount of primary ionisation is variable. In case of a Cr-target X-ray tube, the involved X-ray line is the Cr–$K_\alpha \simeq 5.4$ keV [38]. At this energy the number of primary electrons is about 140 and the range of the photoelectron is about 2 mm, with reduced charge leakage.

MIP signals

Cosmic ray muons have the two appreciable advantages: small fluctuations in the energy loss coming from the energy distribution, and straight tracks almost unaffected by multiple scattering. However the very small cell dimensions lead to a very low rate. As an alternative source of MIPs, a ^{90}Sr source was used. Strontium undergoes β decay in the reaction

$$^{90}\mathrm{Sr} \rightarrow ^{90}\mathrm{Y}\, e\, \bar{\nu}_e \qquad T_{1/2} = 28.79\,\mathrm{y},\; Q = 0.546\,\mathrm{MeV}$$

Yttrium in turn decays to zirconium

$$^{90}\mathrm{Y} \rightarrow ^{90}\mathrm{Zr}\, e\, \bar{\nu}_e \qquad T_{1/2} = 64\,\mathrm{h},\; Q = 2.28\,\mathrm{MeV}$$

The mean number of electron–ion pairs produced per unit length by a 2.28 MeV electron in the case of 90:10 gas mixture is computed as follows.

$$\frac{\mathrm{d}N_T}{\mathrm{d}x} = \frac{\mathrm{d}E}{\mathrm{d}x'}\,\rho\,\frac{1}{W}\bigg|_{\mathrm{He}} \times f_{\mathrm{He}} + \frac{\mathrm{d}E}{\mathrm{d}x'}\,\rho\,\frac{1}{W}\bigg|_{\mathrm{iC_4H_{10}}} \times (1 - f_{\mathrm{He}}) \simeq 29.6\,\mathrm{pairs/cm}$$

whereas in the case of 85:15 mixture it yields 40.8 pairs/cm. Energy loss data have been taken from [13] and are reported in Table 4.1.

Gas	ρ	$\frac{\mathrm{d}E}{\mathrm{d}x}(MIP)$	W
He	1.69×10^{-4} g/cm^3	1.826 MeV cm^2/g	41 eV
iC$_4$H$_{10}$	2.51×10^{-3} g/cm^3	2.123MeV cm^2/g	23 eV

Table 4.1 Helium and isobutane gas properties.

Being the cell large 7 mm the average ionisation is respectively 20.7 and 28.6 pairs. This results in very small signals: supposing a signal width of about 10 ns (short pulse, thus higher amplitude), the amplitude can be estimated as

$$V = \frac{Q}{\Delta t}\,R = \frac{n_T\,G}{\Delta t}\,R \simeq \frac{20.7 \times 1.6 \times 10^{-19}\mathrm{C} \times 10^4}{10\,\mathrm{ns}}\,50\,\Omega \simeq 0.2\,\mathrm{mV}$$

Signals are too close to the noise level even if an amplification $\times\,10$ is provided, so that it is not possible to obtain an evaluation of the gain. We need a preamplifier placed inside the drift chamber, so that only the signal is amplified. In the next Chapter we will use a custom preamplifier, which provides a better signal-to-noise ratio.

Summary

In this Chapter we showed the operation of a single-cell prototype as regards the measurement of its working point, response to radiation and gain. In the next Chapter we will use a more refined prototype, to test all the chain involved in particle tracking with a drift chamber.

Chapter 5

Tracking with a drift chamber: three-cell arrangement

In this Chapter we illustrate the ideas behind particle tracking in drift chambers by using a small three-cell drift chamber prototype. We will start from its design, construction and electrical simulation. We will determine its operating parameters, from time offset calibration to drift time-distance relation. We will show how it is possible to estimate the single-hit resolution and perform basic track reconstruction.

5.1 Particle tracking

In cylindrical drift chambers particle trajectories are generally reconstructed measuring the impact parameters of the track on sense wires. The measurement of the spatial resolution has a key importance, in particular in relation to different choices of chamber characteristics such as the gas mixture, the multiplication factor and the geometry of the wires (*e.g.* the elementary cell width). A basic parameter for the performance of track reconstruction is the single–hit resolution, *i.e.* the uncertainty on the impact parameter determination on a single cell. Generally the impact parameter is reconstructed from the drift distance of the first ionisation cluster arriving on the anode. Because of the discreteness of ionisation sites, the nearest cluster from the sense wire has a drift distance that is always larger than the impact parameter (which is after all the shortest distance by definition). Figure 5.1 clearly shows this issue.

The estimate of the impact parameter from the drift distance has therefore a bias that depends on the mean free path for ionisation: the larger the cluster density, the smaller the bias. This effect is particularly limiting for low mass drift chambers, since in light gas mixtures, cluster density is very small. Figure 5.2 shows the single-hit resolutionas a function of the impact parameter measured by the KLOE experiment in 90:10 helium-isobutane mixture. The estimated individual contributions are also shown. In our range (below 3.5 mm), primary ionisation

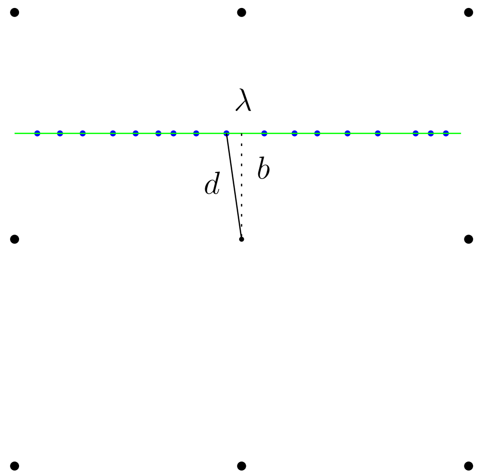

Figure 5.1 Bias in the estimation of the impact parameter from drift distance.

dominates, even if in our gas mixture (85:15) its contribution is reduced by about 25% [1]. In this Chapter we perform a very simple tracking of electrons from a ^{106}Ru source and obtain an estimate of the spatial resolution achieved using drift distances, through a three-cell prototype reproducing the conditions of the MEG$^{\mathrm{UP}}$ drift chamber. The obtained resolution will be the starting point for optimisation studies towards the realisation of of the MEG$^{\mathrm{UP}}$ drift chamber.

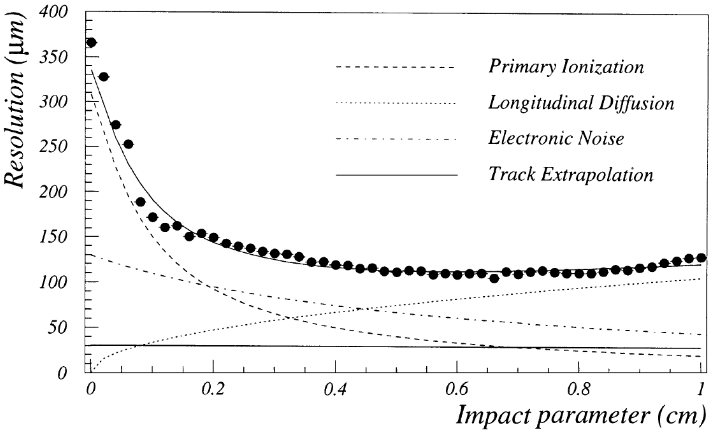

Figure 5.2 Single-hit resolution in 90:10 helium-isobutane mixture measured by the KLOE experiment. Figure from [39].

5.2 Three–cell arrangement: the idea

In order to measure the spatial resolution and solve left-right ambiguity we exploited the staggering of sense wires. Figure 5.3 shows an array of three drift cells, the central one having the sense wire staggered by a quantity Δ with respect to the other two sense wires. When an ionising particle passes through the three cells, clusters arrive on the anode a_i after a drift time t_i, related to a drift distance d_i. Depending on the impinging angle ϑ of the particle, the impact parameters b_i on the three cells are given by

$$\begin{aligned} b_1 &= A \sin\vartheta \\ b_2 &= (A+l)\sin\vartheta \pm \Delta\cos\vartheta \\ b_3 &= (A+2l)\sin\vartheta \end{aligned} \tag{5.1}$$

where the ± is given by the sign of ϑ. For small track angles, *i.e.* for almost vertical tracks

$$\frac{b_1+b_3}{2} - b_2 = \pm\Delta\cos\vartheta \simeq \Delta \tag{5.2}$$

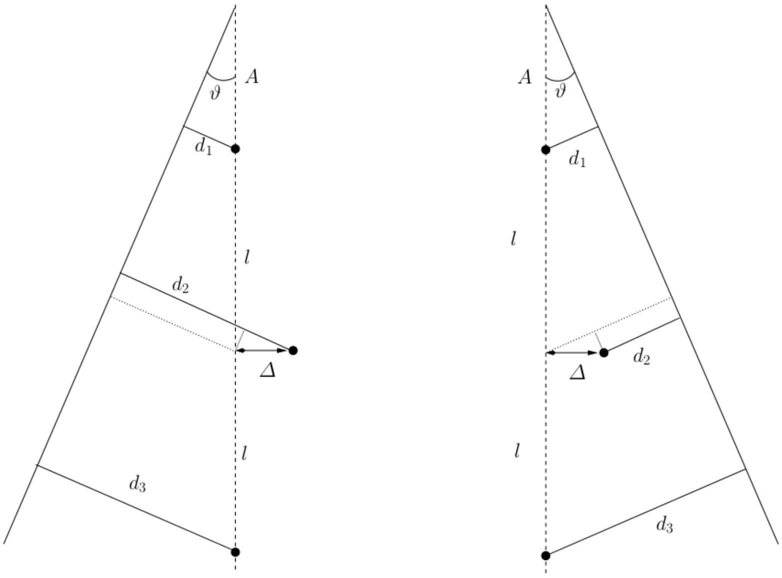

(a) (b)

Figure 5.3 Drift distances in three-cell configuration and solution of the left-right ambiguity.

---

[1] as seen in Section 4.5, the number of clusters per centimetre from a MIP particle is about 40 for 85:15 mixture and 30 for 90:10 mixture.

Therefore from the measured drift distances d_i, since the expectation value $\langle d_i \rangle \simeq b_i$, we can build an estimator

$$\mathcal{S} = \frac{d_1 + d_3}{2} - d_2 \tag{5.3}$$

whose expectation value is $\pm\mathit{\Delta}$ and whose variance is given by

$$\sigma_{\mathcal{S}}^2 \simeq \sum_{i=1}^{3} \left| \frac{\partial \mathcal{S}}{\partial d_i} \right|^2 \sigma_{d_i}^2$$

yielding

$$\sigma_{\mathcal{S}} \simeq \sqrt{\frac{3}{2}} \sigma_d \tag{5.4}$$

The three–cell arrangement allows therefore to gain an indirect measurement of the spatial resolution: after measuring the drift distances for several tracks, one can compute $\mathcal{S}$ for each event and find its distribution. Two peaks should be visible (corresponding to the cases (a) and (b) in Figure 5.3), and from the resolution on $\mathit{\Delta}$ one finds the resolution on b. However two requirements have to be met:

$$\mathit{\Delta} \ll l \quad \text{and} \quad \sigma \ll \mathit{\Delta} \tag{5.5}$$

The stagger must be smaller than the cell width, since for tracks passing in between the anode wires equation (5.2) does not hold. If the resolution is comparable with the stagger, the left-right ambiguity cannot be solved.

5.3 Three-cell prototype realisation

The wire configuration needed for the implementation of a three-cell prototype was studied through Garfield++ simulations. We wanted to mimic a small section of the full-size drift

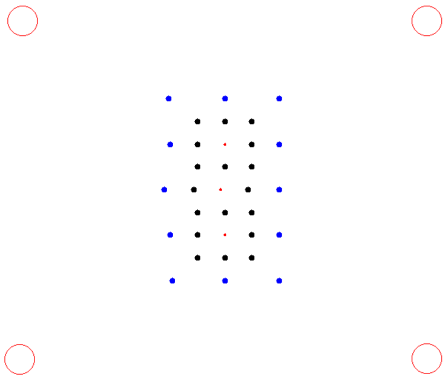

Figure 5.4 Implementation of the three–cell configuration.

chamber, therefore we simulated three consecutive squared cells with common field wires, each cell having a width of 7 mm. The anode wire of the central cell was staggered by 500 µm, to meet the requirements expressed in (5.5). In order to avoid electric field distortions in the central cell, the two cathode wires that are not shared with the other cells were displaced as well by 500 µm. In this case there is no need of operating in the shifted potential configuration since we are not interested in measuring the anode current (as for Prototype I). In order to prevent the anodes from collecting ions originating outside of the cell, guard wires were included, surrounding the three cells. Our simulations showed that when kept at a low positive high voltage, 12 guard wires succeed in bounding drift lines inside the cells, without increasing the electric field on cathodes considerably. The design of the prototype is shown in Figure 5.4.

In the simulations the wire voltages were set in order to have a gain of about 1×10^5 and this is achieved with 1500 V on the anode wires and 300 V on the guard wires. Figure 5.5(a) shows the contour plot of the magnitude of the electric field, while the drift lines of electrons are shown in Figure 5.5(b). The electric field in the proximity of an anode and a cathode is shown in Figure 5.6: notice that the electric field on the cathode is below the multiplication threshold.

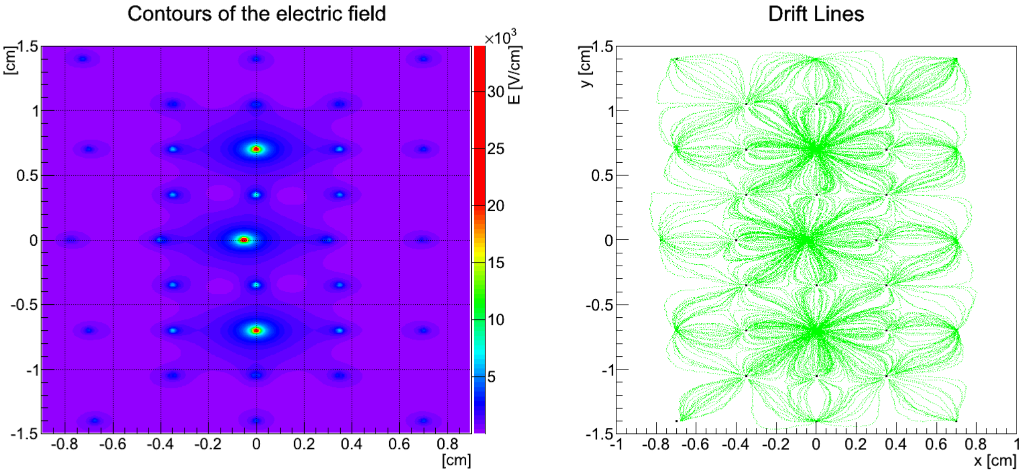

(a) Contour plot of the magnitude of electric field in the prototype, calculated with Garfield++.

(b) Drift lines of electrons through the cells, calculated with Garfield++.

Figure 5.5 Electric and drift properties of the three–cell prototype.

Because of the need of comparing signals from different cells it was important to know the drift and multiplication properties of each cell. The simulated gain distributions for the three cells are shown in Figure 5.7: the mean gain is for all the three cells of about 1.3×10^5, with a slightly lower value for the central cell.

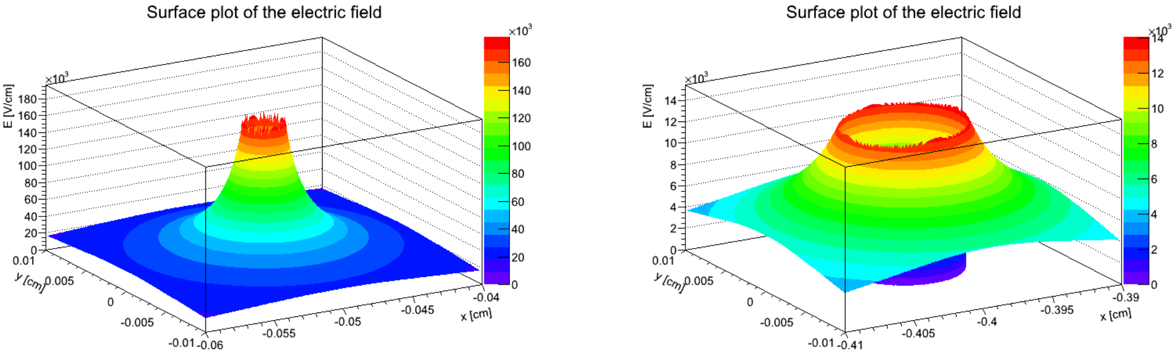

Figure 5.6 Surface plot of the electric field near the central-cell sense wire (on the left), and near a field wire shared by the upper and the central cell (on the right).

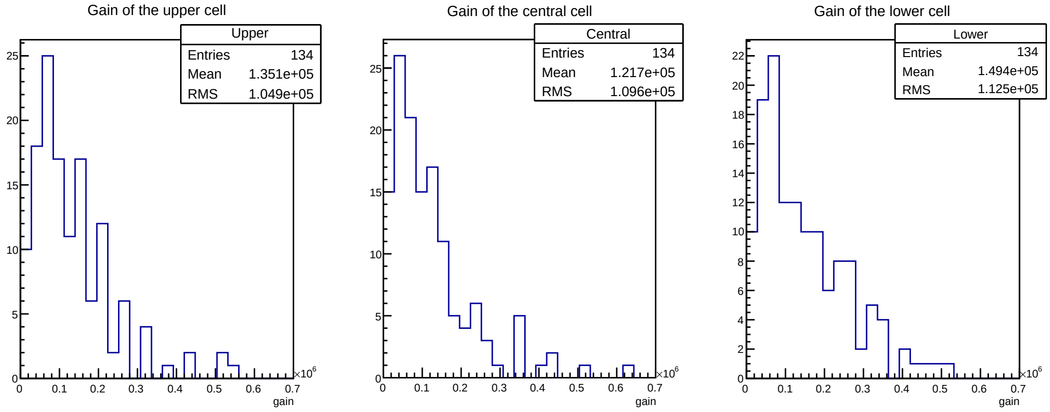

Figure 5.7 Gain distributions for the three cells.

5.4 Experimental setup

As for Prototype I, the configuration of wires was implemented on two PCBs. A scheme and a picture of the PCBs used to wire the prototype are shown in Figure 5.8. The part used for realising the three–cell arrangement is only that enclosed in the white dotted rectangle in Figure 5.8; the other cells in the figure were designed for different tests with just one PCB production. The wires chosen for the prototype are W (Au) 20-µm wires as anodes and Al (Ag) 80-µm wires for cathodes and guard wires. The prototype length is 20 cm, with four stainless-steel rods stretching the wires.

Concerning the electrical connections, special attention was paid to the stability of the high voltage and to the impedance matching of the read-out of the sense wires. They are necessary for reducing noise and signal reflections. Having the sense wire at high voltage implies that the noise from the power supply appears directly on signals. This effect is absent in shifted potential configuration, as in Prototype I, where the anode is not connected to the high voltage.

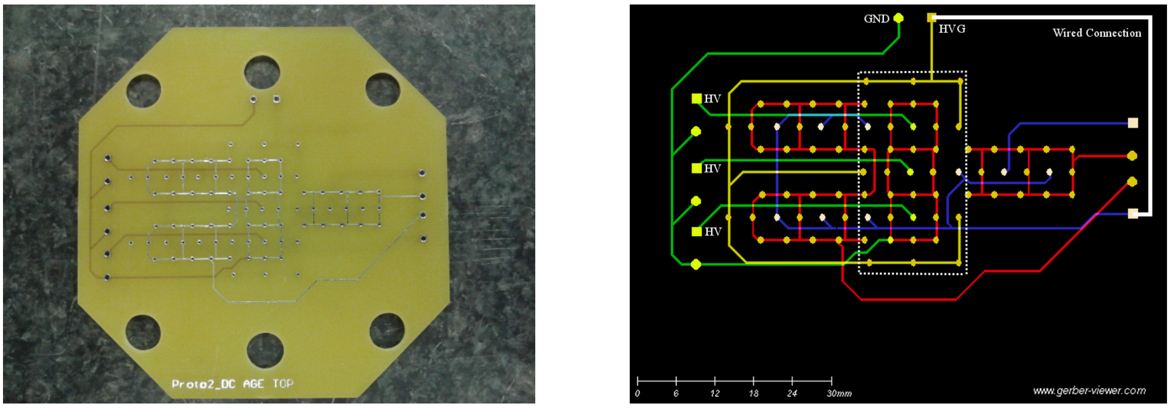

Figure 5.8 Printed circuit board for the three-cell configuration. The rods were placed on the four external big holes on the PCB (image on the left). The holes used for the three–cell arrangement are enclosed in the white dotted rectangle (image on the right). The applied voltages are HV for the sense wires, HVG for the guard wires and GND for the field wires (connected to the rods too).

Figure 5.9 shows supply and readout circuits of the three sense wires.

Power supply The capacitor C_{HV} is needed to keep the high voltage stable: any resistive loss of voltage due to charge drift in the chamber is compensated by the charge stored in $C_{\mathrm{HV}} = 4$ nF. Since each sense wire has its capacitor, they are decoupled. In addition the series $R_{\mathrm{HV}}C_{\mathrm{HV}}$ works as a passive low-pass filter, attenuating high-frequency noise from the high-voltage power supply. In order to have a low cutoff frequency, a big resistance has been chosen for $R_{\mathrm{HV}} = 1.8\,\mathrm{M}\Omega$.

Readout Output signals are read at one extremity of the sense wires. A capacitor C decouples the high-voltage, and the AC signal is thus preamplified of a factor 7 by a custom preamplifier designed at INFN Lecce as a prototype for the front-end of final drift chamber. The preamplifier has a bandwidth of $\approx 700\,\mathrm{MHz}$ for a gain of ~ 7 and needs a low voltage power supply (GND, ± 3 V). A 330 Ω resistor is needed on both ends to match the impedance of the cell, avoiding reflections of signals through the wire.

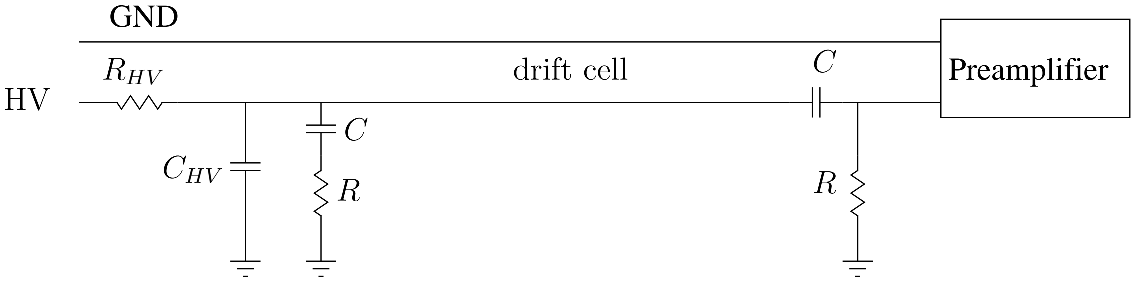

Figure 5.9 Circuit of the power supply and the readout of a sense wire.

Guard wires are power-supplied through a resistor with $R_{\mathrm{HV}} = 1.8\,\mathrm{M}\Omega$. The preamplified signals were acquired through a waveform digitizer with four channels, the Domino Ring Sampler (DRS).

We designed and built a plexiglass gas tight box to host the three-cell prototypes.The box dimensions are $100 \times 100 \times 500$ mm^3; each face has a thickness of 1 cm, except for two thin windows with dimensions $30 \times 120 \times 1$ mm^3 placed on two opposite faces (top and bottom) to have a preferential input for radiation. The small lateral faces are equipped with high voltage (for the wires) and low voltage (for the preamplifier supply) feedthroughs as well as feedthroughs for gas inlet and outlet. The box has a top cover which is tightened by twenty screws with the use of an O-ring. (see Figure 5.10). The internal faces of the boxes were covered with a thin aluminum foil, in order to have a surrounding common ground to screen the wire from outside high frequency noise.

Figure 5.10 Plexiglass box realised for resolution measurements with a three–cell prototype.

Figure 5.11 shows the prototype before being inserted in the gas box. On the right the circuitry for power supplying is shown, while the three–channel preamplifier is connected on the left.

For selecting cosmic ray tracks, two plastic scintillators can be placed above and below the box: because of their very fast response[1], they provide the trigger. For selecting events from radioactive source tracks, just one scintillator can be placed below the box, to provide trigger (being the source placed on the top of the thin window), since the low energy of the β-ray is not enough to cross two scintillators.

---

[1] actually the fundamental property exploited is the fact that in our regime the arrival time of the signal from the scintillator does not depend on the trajectory of the ionising particle.

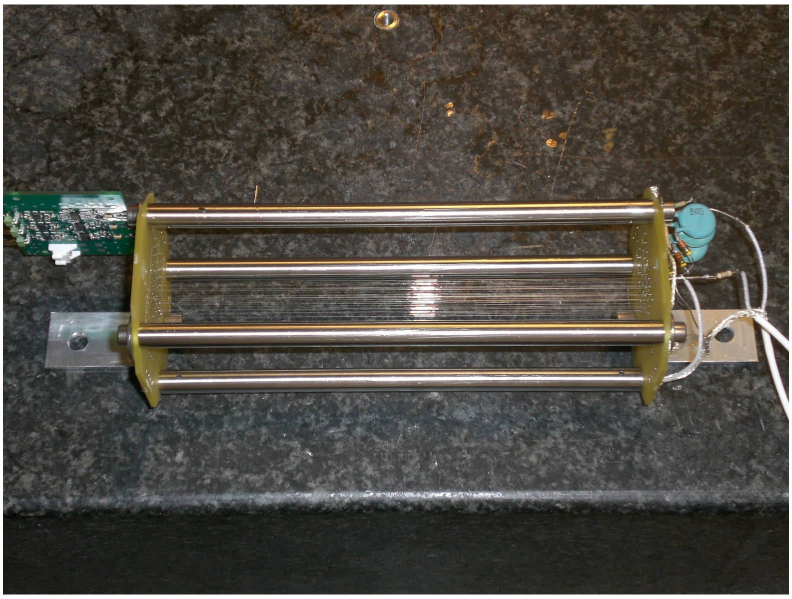

Figure 5.11 Three–cell prototype: the power supply and readout connections are visible. The two L–shaped supports attached to the PCBs are used for anchoring the prototype on the plexiglass box.

After installing the prototype, the plexiglass box was sealed and connected to the gas line described in Chapter 2. As counting gas, the mixture helium–isobutane (85:15) was used. The flux was set to 5 sccm, corresponding to a gas volume exchange every about 15 hours.

5.5 Drift chamber operation

In order to improve the signal-to-noise ratio, we operated the chamber at a slightly larger high voltage (1700 V), corresponding to a gain of about 10^6. The guard–wire voltage was correspondingly set to 375 V. The maximum limit on the temporal width of an ionisation signal is set by the maximum drift time in the cell: Figure 5.12 shows the drift times computed on the three cells. The distribution is quite similar in the three cells and the drift times are lower than 100 ns, except for the area close to the cathode wires.

Though the box and the system were designed to operate with cosmic rays, we made preliminary measurements with a Ruthenium source, whose activity was enough to reduce the data acquisition of $\sim$ 1000 events to a few minutes, opposed to a few days needed by using cosmic rays. Ruthenium $\beta-$decays through the reaction

$$^{106}\mathrm{Ru} \rightarrow^{106} \mathrm{Rh}\, e\, \bar{\nu}_e \qquad\qquad T_{1/2} = 373.6\,\mathrm{d},\ Q = 0.0394\,\mathrm{MeV}$$

Rhodium in turn decays into Palladium

$$^{106}\mathrm{Rh} \rightarrow ^{106}\mathrm{Pd}\, e\, \bar{\nu}_e \qquad T_{1/2} = 29.8\,\mathrm{s},\ (75\%)\ Q = 3.54\,\mathrm{MeV}$$

The high–energy component of the electron energy spectrum is selected by putting 500 µm of copper in front of the trigger scintillator. Figure 5.13 shows the waveforms of a track: the different ionisation clusters are visible, and the temporal width of the signals is about 100 ns. From the three waveforms it is possible to see the fact that the central wire is staggered. If this were not the case, the three leading edges of the waveforms should lie in a straight line.

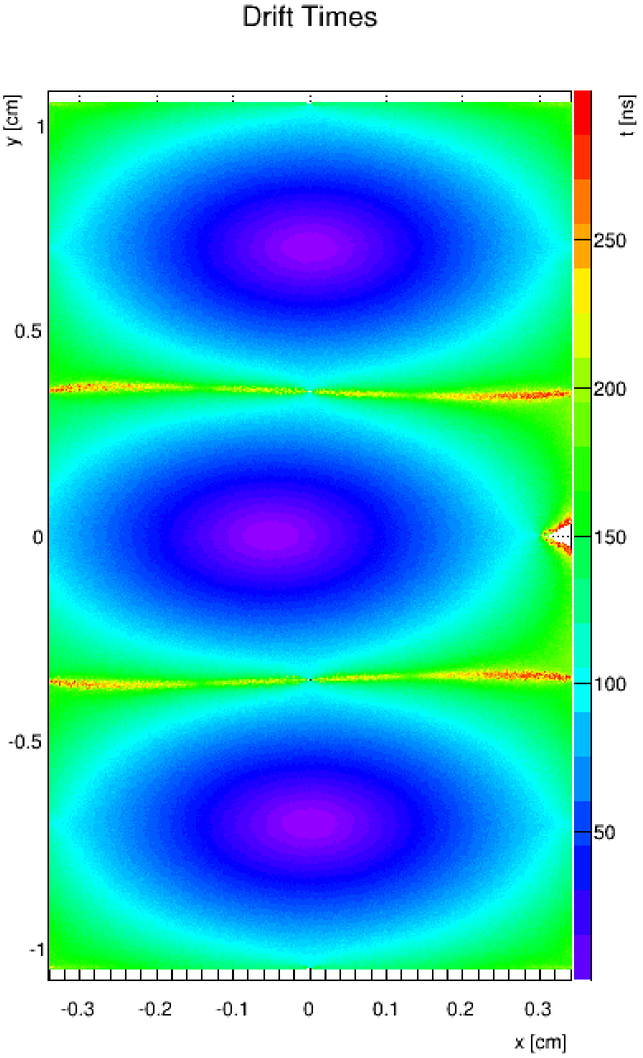

Figure 5.12 Drift time distribution on the three cells computed with Garfield++.

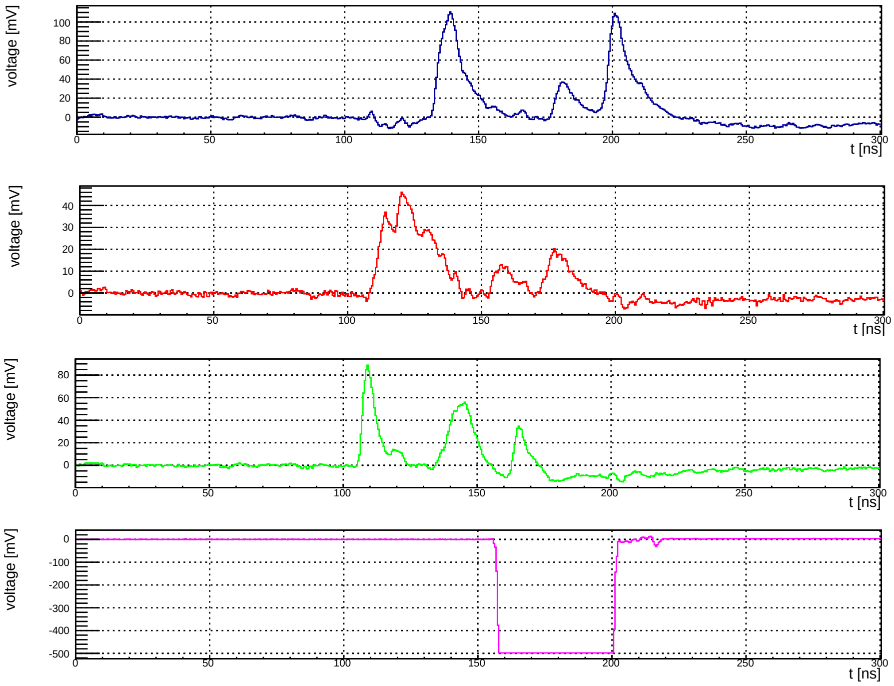

Figure 5.13 Track of an electron from the Ruthenium source: from top to bottom the waveforms in the upper cell, central cell, lower cell and trigger scintillator.

5.6 Drift time–to–distance relations

The three-cell configuration has an enormous advantage: it is possible to measure the drift time-space relations and compare them to the Garfield++ simulations. For particle tracking, the drift time-space relations have a key importance: in a drift cell one can only measure the difference between the arrival time of the signal on the anode wire and the time of the trigger. Then one has to obtain the drift distance from the drift time measurement: any uncertainty (or misknowledge) of the drift space-time relations is reflected on the results.

The drift time-to-distance relation was simulated with Garfield++, as shown in Figure 5.14. The curve is well described by a function of the form

$$r(t) = a\sqrt{t} + bt \tag{5.6}$$

Before measuring the time-to-distance relation one must perform the so-called "t_0 calibration", *i.e.* determine the time offset between the different cells and the trigger. For each track the four waveforms (as in Figure 5.13) are acquired. In each waveform the arrival time of the signal is extracted at fixed threshold: it is the time at which the amplitude of the signal reaches 5 mV. The distribution of arrival times (with respect to the trigger time) is then plotted for each cell as in Figure 5.15, and can be described by the product of two error functions. If one assumes

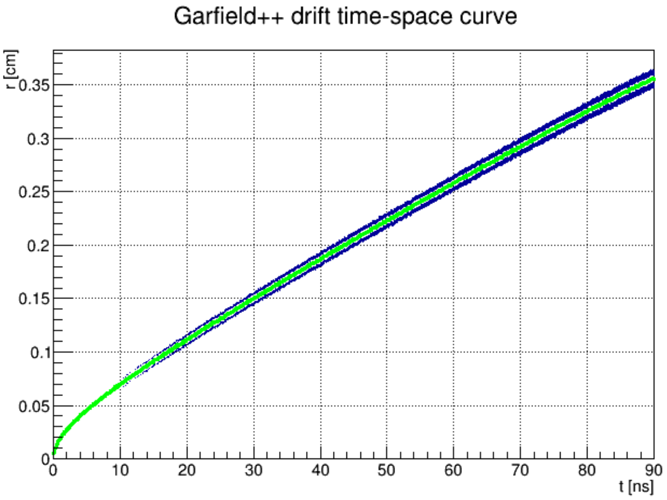

Figure 5.14 Drift time-to-distance relation computed with Garfield++.

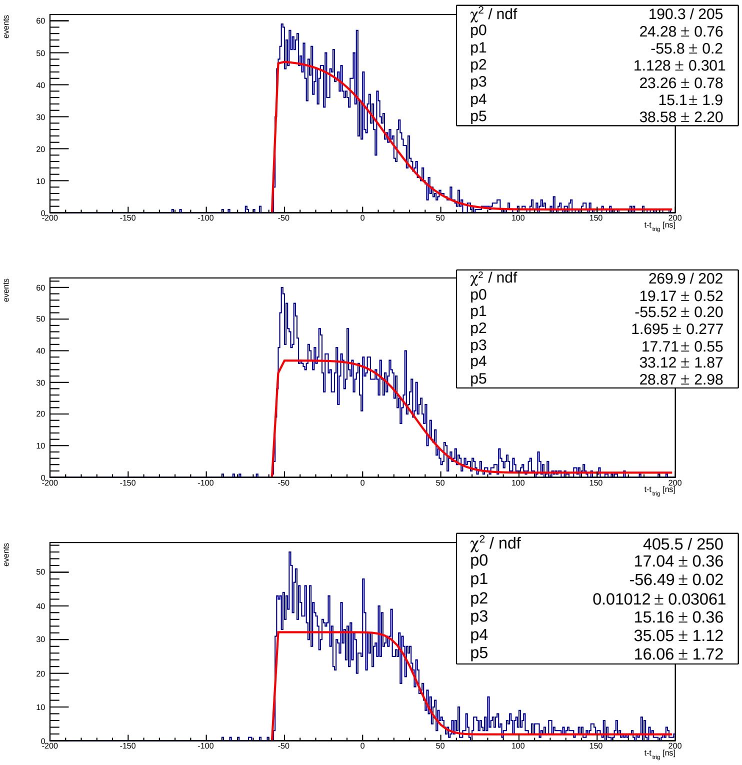

Figure 5.15 Distribution of the time of the signal of (from top to bottom) the upper, central and lower cell, subtracted by the trigger time.

that the impact parameter of the track is uniformly distributed from zero to 3.5 mm (half–cell width) [1], a constant drift velocity would project uniformity of space into uniformity in time distribution. The product of two error functions mimics a uniform distribution with smooth borders which are due to the fact that time resolution is finite. The time offset of each wire is thus set to zero adding to the time difference between wire and trigger signals the value of the mean of the "rising" error function returned by the fit.

The determination of the drift space–time relation is then performed through an iterative method. At the beginning a seed function is chosen: we start from a straight line (*i.e.* $a = 0$)[2]. At each step of the procedure:

1) Drift distances for the upper and the lower cell are computed from the measured times using the reference function.

2) The corresponding drift distance in the central cell is obtained through equation (5.2), and the sign of the stagger term is determined from whether the mean of the drift times of the upper and lower cell is larger or smaller than the time measured in the central cell. In formulae

$$\begin{aligned} d_2 &= (d_1 + d_3)/2 + \mathit{\Delta} \qquad && \text{if} \quad t_2 > (t_1 + t_3)/2 \\ d_2 &= (d_1 + d_3)/2 - \mathit{\Delta} \qquad && \text{if} \quad t_2 < (t_1 + t_3)/2 \end{aligned} \tag{5.7}$$

   Such calculated drift distance is associated to the measured drift time for the central cell and is plotted on a $r - t$ graph.

3) The graph containing events from all the tracks is then fitted to a function of the form in equation (5.6). The fit function is then used as reference function in the next iteration for the upper and lower cell.

The procedure ends when the returned values differ from the values of the previous step by less that one part in 10^4. Figure 5.16 shows the function evolution during iterations. The converged function (the last in Figure 5.16) is in agreement with that returned by the Garfield++ simulations.

5.7 Simple tracking in different configurations

We used the above procedure to perform simple tracking from a ruthenium source in two different configurations, to mimic different conditions of the positron tracks in the MEG$^{\mathrm{UP}}$ detector. In configuration (a) in Figure 5.17 we studied the chamber response to vertical tracks, in configuration (b) we studied its response to tracks with a pitch angle of $\sim 45°$, more similar to the positron trajectories in the MEG$^{\mathrm{UP}}$ experiment. Once the drift time-to-distance relation

---

[1] in our case this is not true since tracks from the radioactive source are not exactly vertical.

[2] the dependence of the resulting parameters from the initial values is found to be negligible.

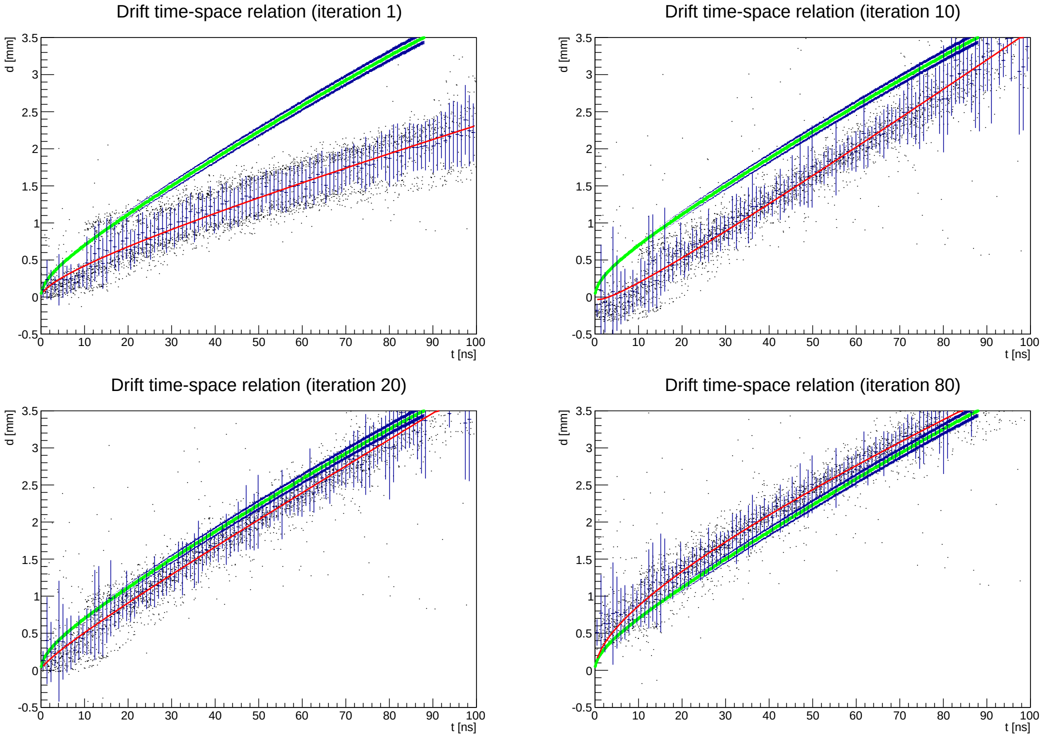

Figure 5.16 Evolution of the measurement of the drift time-distance relations.

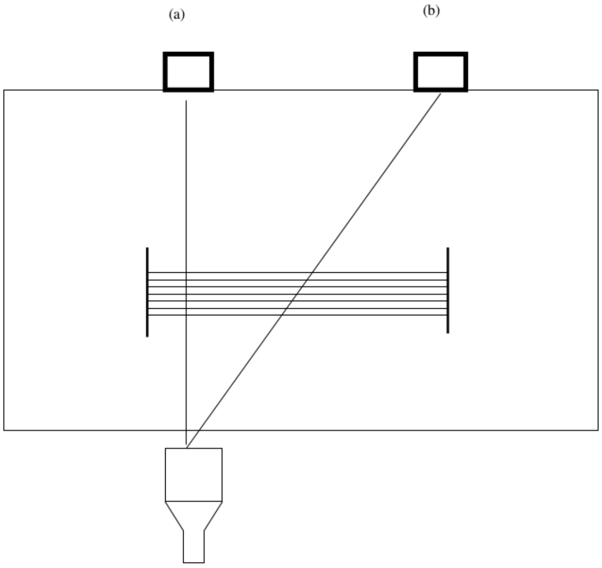

Figure 5.17 Configurations for vertical (a) and slanted (b) tracks.

is obtained, the quantity $\mathcal{S}$ was computed from the measured drift times; its distribution is depicted in Figure 5.18 (a),(b). The distribution is bimodal as expected from equation (5.2). It is well described by the sum of three Gaussian functions, two with mean $\mu^{\pm} = \pm\Delta$ and one with mean zero due to the wrong reconstruction of tracks or to tracks for which equation (5.2) does not hold, *e.g.* for tracks that pass in between the wires ($d_{1,2,3} < 500$ µm).

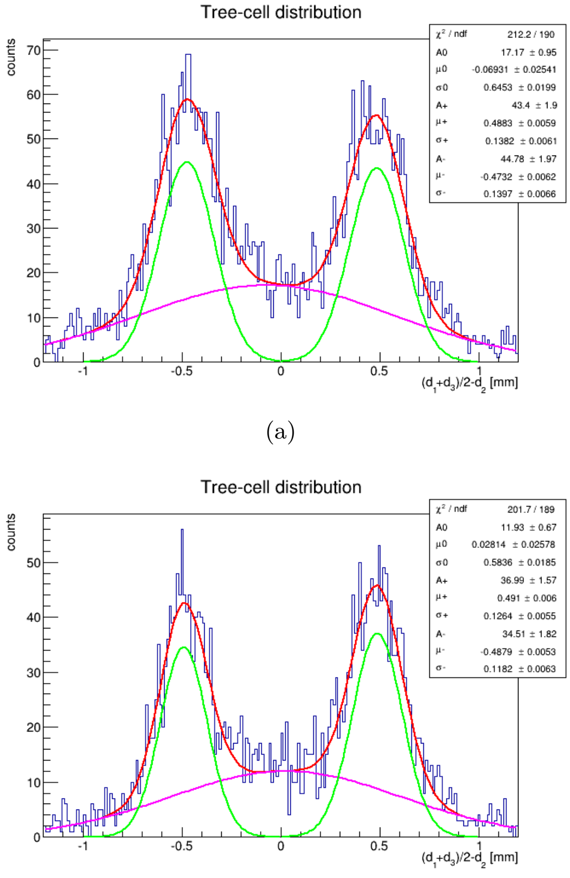

(a)

(b)

Figure 5.18 Distribution of $\mathcal{S}$ measured with vertical (a) and slanted (b) tracks from ^{106}Ru.

This contribute is visible in Figure 5.19, where the estimate of the impact parameter on the central cell obtained from the upper and lower cells is plotted against its measured value. Data lie on two lines parallel to the bisector of the axes representing tracks passing through the two different sides of the cell (see Figure 5.3). The other events are clustered in the proximity of $d_2 \sim 0.5$ mm and are given by the tracks passing in between the anodes.

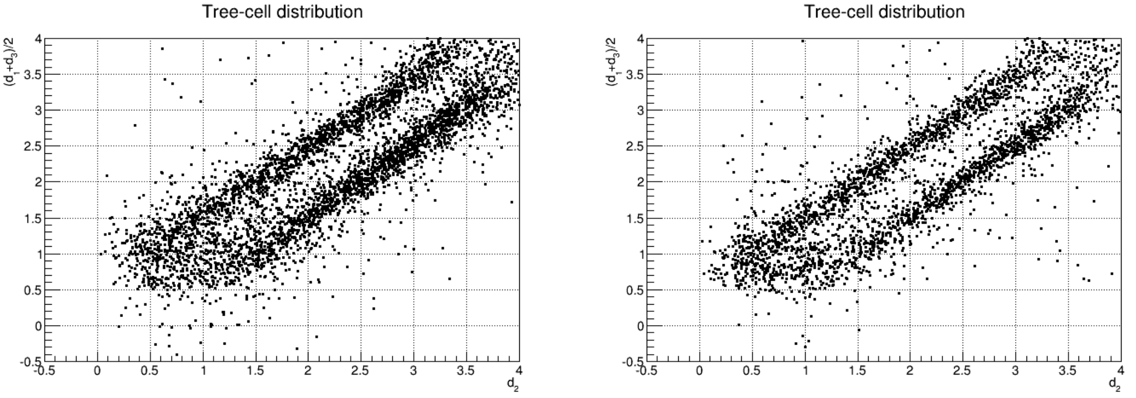

(a) (b)

Figure 5.19 Estimate of the impact parameter on the central cell obtained from the upper and lower cells plotted against its measured value for vertical (a) and slanted (b) tracks from ^{106}Ru.

The value returned by the fit in Figure 5.18 for the parameters are

$$\mu^+ = (0.488 \pm 0.006)\,\mathrm{mm} \qquad \sigma^+ = (0.138 \pm 0.006)\,\mathrm{mm}$$
$$\mu^- = (0.473 \pm 0.006)\,\mathrm{mm} \qquad \sigma^- = (0.140 \pm 0.007)\,\mathrm{mm}$$

for configuration (a) and

$$\mu^+ = (0.491 \pm 0.006)\,\mathrm{mm} \qquad \sigma^+ = (0.126 \pm 0.006)\,\mathrm{mm}$$
$$\mu^- = (0.488 \pm 0.005)\,\mathrm{mm} \qquad \sigma^- = (0.118 \pm 0.006)\,\mathrm{mm}$$

for configuration (b).

The returned parameters for the two peaks of each distribution are compatible. The value obtained for the stagger Δ is slightly lower than 500 µm, but it is within the uncertainty on the positioning of the anode wires in the holes of the PCBs (having 500 µm of diameter). The estimate for the single-hit resolution of the prototype is therefore

$$\sigma_d \simeq \sqrt{\frac{2}{3}}\sigma_\Delta = \sqrt{\frac{2}{3}}\,\frac{\sigma^+ + \sigma^-}{2} \simeq (113 \pm 3)\,\mu\mathrm{m}$$

in case of configuration (a) and

$$\sigma_d \simeq \sqrt{\frac{2}{3}}\sigma_\Delta = \sqrt{\frac{2}{3}}\,\frac{\sigma^+ + \sigma^-}{2} \simeq (99 \pm 3)\,\mu\mathrm{m}$$

in case of configuration (b).

For electrons with an energy ≈ 2.5 MeV the multiple scattering induced by the gas mixture is non negligible and can be estimated to be $\sigma_{\mathrm{MS}} \approx 50$ µm. If we assume that

$$\sigma^2_{a,b} = \sigma^2_{\lambda(a,b)} + \sigma^2_{\mathrm{MS}}$$

we can compute by difference

$$\sigma^2_{\lambda(a)} = (101.3)^2$$
$$\sigma^2_{\lambda(b)} = (85.4)^2$$

whose ratio (~ 1.4) is within errors compatible with the different track lengths ($\sim \sqrt{2}$).

5.8 Track reconstruction

Once the drift time-to-distance relation was determined, we performed a very simple tracking procedure. In the approximation of vertical lines, hits were reconstructed as having the same y of the hit wire and with x equal to the measured drift distance. The obtained tracks are shown in Figure 5.20 and are compatible with the detector acceptance, except for some tracks that result from multiple scattering of electrons in the plexiglass walls.

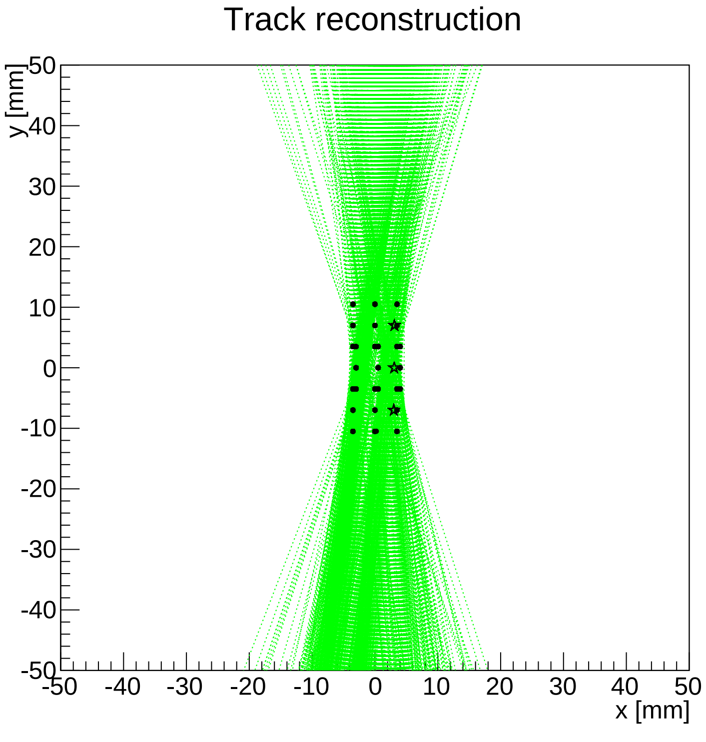

Figure 5.20 Reconstructed tracks of electrons from ^{106}Ru.

Summary

In this Chapter we showed the operation of a simple three-cell prototype. We used the prototype to illustrate the basis of tracking in gaseous drift-chambers. Preliminary measurements of single-hit resolutions are very promising and show values of $\sigma \approx 100$ µm in a configuration very close to that expected for the MEG$^{\mathrm{UP}}$ experiment. Future campaigns of measurements with cosmic rays are envisaged, to confirm this value and to study its dependence on the various operating parameters.

In the following chapters we will concentrate on the main focus of this thesis: drift chamber ageing.

Part III

Ageing tests

Chapter 6

Testing the lifetime of a drift chamber

This Chapter provides an overview on ageing phenomena in drift chambers, concerning its causes and manifestations. The presentation is focussed on the ageing causes and effects from which the tracker of MEG$^{\text{UP}}$ *can suffer. A list of the working parameters affecting ageing is provided, with two aims: finding clean assembly procedures and materials, and learning how to realise a faithful ageing test for the new tracker.*

6.1 Ageing of drift chambers

Wire chambers are often one of the key detectors in a high-energy physics experiment; they are also one of the most delicate, therefore it is very important to check if they can keep their performance for the whole duration of the experiment. Two aspects can endanger the normal functioning of the detector: mechanical deformation (breaking or loss of tension of wires) and radiation-induced degradation. The former is a matter of stress calculations, the latter is a mix of chemistry, electromagnetism and material sciences. The radiation-induced problems limiting the useful lifetime of wire chambers are generically referred to as ageing effects, and the most common (and feared) are gain loss, worsening of energy resolution, self-sustained current discharge and sparking.

In the last forty years or so, the widespread use of wire chambers triggered laboratory tests aimed at understanding the factors accelerating or slowing down the ageing of such detectors. Such tests showed that even contamination of the gas at the part-per-million level, wrong materials or “dirty” techniques used in the assembly of the detectors can lead to a short life expectation. *A posteriori* observations of aged wire chambers showed substantial wire surface degradation of both anodes and cathodes, in the form of solid or liquid (grease-like) deposits which modify the shape and the electrical properties of the wires. They can result from the chemical attacks of a wire surface by active species produced in avalanches, coupled to volatile pollutants. However the chemistry of wire chamber ageing has not yet been investigated in depth and it is not possible to systematically separate good materials and operations from the bad ones. Some knowledge for understanding the chemical reactions involved in wire ageing may be borrowed from plasma chemistry. Actually the working conditions of plasma chemistry (low pressure, high gas flow, radiofrequency discharges) are very different from those of wire chambers (atmospheric pressure, moderate gas flow, dc discharges). However estimates of key parameters, such as electron mean energies and of E/P ratios[1], suggest that the two systems share similar chemistry. Such analogy has been verified in some experiments. Anyway, since the formation of deposits results from the competition of several processes (of both polymerization and ablation) with rates that are generally not known at high pressures, there is not yet a comprehensive understanding of drift-chamber chemistry. As a general reference we adopted the review on wire chamber ageing by Kadyk [40] and to the "*Proceedings of the International Workshop on Aging Phenomena in Gaseous Detectors*" hold in 2001 at Desy, Hamburg, Germany [41].

6.2 How a drift chamber gets old

The symptoms of a wire chamber that begins to age can be divided into two categories:

(i) loss of gain value and uniformity, resulting also in the reduction of the efficiency plateau and in the loss of energy resolution;

(ii) electrical breakdown, in the form of self-sustained current discharge, sparking and dark currents.

These phenomena can appear independently and are due to the formation of deposits on the anode and cathode wires, respectively. A great practical difference between the two classes is that the former just limits the performances of the detector (which may usually be restored by increasing the high voltage of the wires), while the latter makes the detector inservible[2]. Before dealing in details with the differences of the two coatings, a general introduction to the chemistry of wire chambers is presented.

6.2.1 The free radicals

One of the first studies of plasma chemistry was done on the breakup of methane (CH_4) in discharges at low pressure. The expected result was the formation of ethylene (C_2H_4) and hydrogen through the reaction

$$2\,CH_4 \rightarrow C_2H_4 + 2H_2$$

and therefore a 50% pressure increase, due to the increased number of molecules. Actually only a slight pressure rise was observed [42]. Further studies showed that some reactions taking place

---

[1] with E being the magnitude of the electric field and P the gas pressure.

[2] at least as long as some practice of rejuvenation (additives, wire heating) are made on the chamber.

in the discharge lead to the formation of non-volatile species condensating upon the electrodes. These were the first evidences of discharge-induced deposit formation.

In our case the gas is a mixture of helium and isobutane; fast electrons or photons generated in avalanches interact with the gas molecules by excitation, ionisation or (for the isobutane) fragmentation.

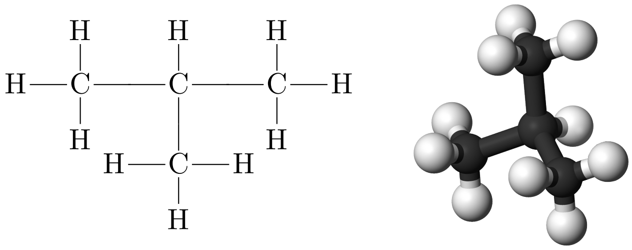

Figure 6.1 Isobutane chemical structure.

Organic compounds fragmentation leads to the production of a lot of daughter molecules: in isobutane (see Figure 6.1) deprotonation or breakup of the bonds between the carbon atoms can occur. Figure 6.2 shows the mass spectrum of isobutane: it represents the mass-to-charge ratio of the ions produced bombarding a small amount of gas with 70 keV electrons. It is visible that isobutane fragments in ions such as CH_3^+ ($m/z = 15$) and $C_3H_7^+$ ($m/z = 43$); neutral molecules like methane (CH_4) are produced too. After the discharge, ions are drifting towards the cathode and may either recombine or be collected, while neutral molecules wander in the chamber. New species are therefore introduced in the gas and may be involved in the next avalanches, fragmenting and producing in turn other molecules. Among them, some species, called free radicals, are neutral (thus electrically inert) but have unpaired valence electrons,

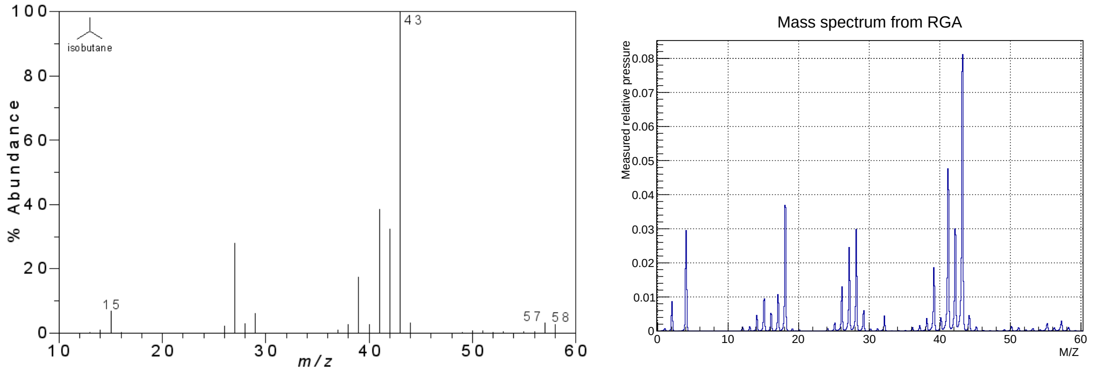

Figure 6.2 Isobutane mass spectrum [43] (left image). On the right a mass spectrum of 90:10 helium isobutane mixture acquired with the RGA is shown: the fragmentation pattern of isobutane is clearly visible. In addition we can see the helium peak (A=4) and the typical pattern of Oxygen, Nitrogen and water vapour (~ 32, 28 and 18 respectively).

thus are chemically very active. For example, $CH_3\cdot$ and $C_3H_7\cdot$ have an unpaired electron, while $CH_2:$ (which results from methane fragmentation) has two unpaired electrons, as indicated by "·" and ":". They are produced in higher concentration than ions, since the energy required for fragmentation is lower than ionisation energy. The important (namely devastating) role played by free radicals in wire chamber ageing is related to their ability to polymerize: a simple example of this behaviour is represented by chain reactions of $CH_2:$ with $C_3H_7\cdot$

$$C_3H_7\cdot + CH_2 : \rightarrow C_4H_9\cdot$$

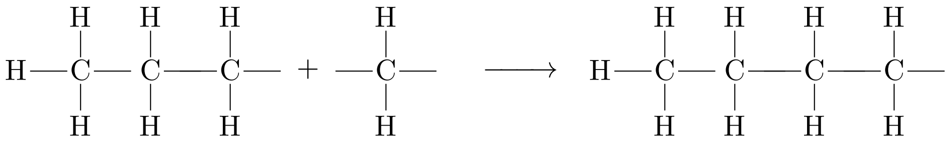

$$\mathrm{H-\overset{H}{\underset{H}{C}}-\overset{H}{\underset{H}{C}}-\overset{H}{\underset{H}{C}}-} + \mathrm{-\overset{H}{\underset{H}{C}}-} \longrightarrow \mathrm{H-\overset{H}{\underset{H}{C}}-\overset{H}{\underset{H}{C}}-\overset{H}{\underset{H}{C}}-\overset{H}{\underset{H}{C}}-}$$

$$C_4H_9\cdot + CH_2 : \rightarrow C_5H_{11}\cdot$$

In this way long chains of $(CH_2)_n$ (polyethylene-like) are produced. Polymer growth can start either in the gas or on electrode surfaces, but in both cases their increasing weight and electric dipole interactions make them fall on wires (see Figure 6.3).

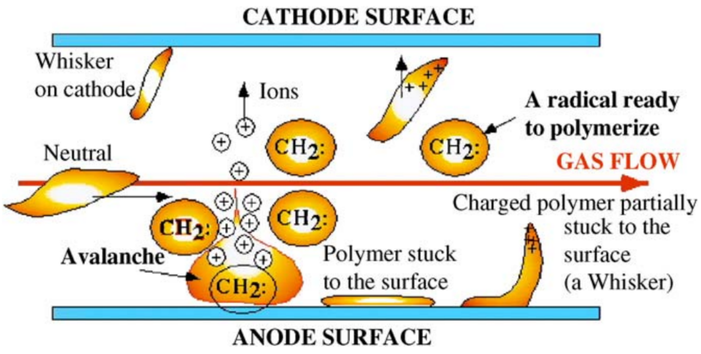

Figure 6.3 Schematics of polymers growth and deposition. Figure from [44]

6.2.2 Anodic coatings

Depending on the used gas mixture and the impurities wandering in the detector, deposits lying on the anode wire surface can be very different, solid or liquid, uniform or spotted, conductive or insulating (see *e.g.* Figure 6.4). The largest effect of conductive coatings is the gain drop due to the increase of wire radius: a 0.5 µm coating on a 25 µm wire leads to a 4 % decrease of the electric field in the proximity of the wire, which results in a 20 ÷ 40% gain drop, depending on the cell geometry.

For insulating coatings, the electric field modifications come from both the increased thickness of the wire and dielectric effects. In addition, the charge collection results from the balance between the avalanche progress and the charge leakage through the insulating layer, so that the gain becomes rate-dependent[1]. The "time structure" of signals is modified too, making cluster identification difficult: this can lead to a single-cluster waveform which is different in different points of the same wire.

However coatings are generally deposited non-uniformly, thus allowing outlets for charge collection. On the other hand, local gain variations worsen the energy-loss resolution of the chamber (if the primary ionisation is determined by pulse-height or collected charge distribution), and nonuniform efficiency shortens the high-voltage plateau length.

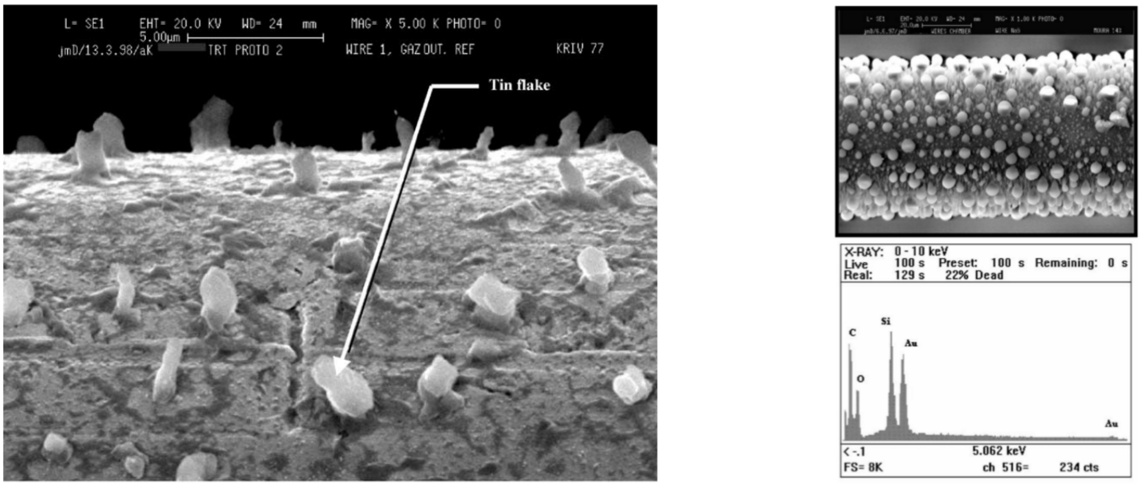

Figure 6.4 SEM and EDX analyses (see Chapter 8) of anode wires from ageing tests for the CMS experiment. Figures from [45].

6.2.3 Cathodic coatings

If insulating coatings covering anode wires have undesirable effects, on cathodes the results are even worse. Insulating layers prevent ions from reaching the cathode (and being neutralised), therefore charge accumulates on the coating surface, as much as results from the balance between ion flux and the resistivity of the layer. A very large electric dipole field is thus produced, and when it exceeds the threshold for field emission, electrons are pulled off the cathode (see Figure 6.5). Such electrons in part recombine with the ions stopped on the layer surface, in part enter the gas, drift and multiplicate, producing positive ions. In turn ions will then deposit on the coating, increase the dipole field and the field emission on cathodes. A positive feedback is therefore estabilished and excessive dark currents will flow through the chamber.

---

[1] Or, more correctly, it acquires an additional factor of rate dependence (as in the case of space charge).

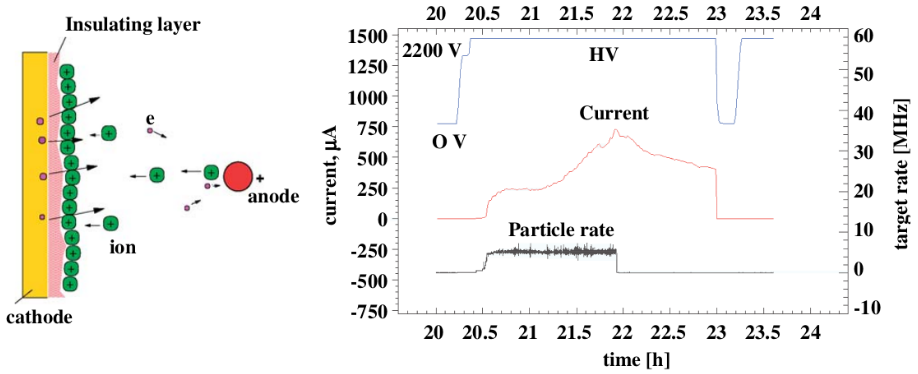

Figure 6.5 Malter effect schematic: positive ions amass on an insulating layer (left). On the right a typical self-sustained current caused by Malter effect; these dark currents have a decay time of the order of several hours. Figure from [44]

As shown in Figure 6.5, even the removal of the ionisation source does not stop such currents, that will continue with a slow decay time unless the high-voltage of the chamber is switched off. This behaviour is called Malter effect, and accounts for permanent damage in many experiments in high energy physics. Such insulating coating can be made of hydrocarbon polymers from the quenching gas, various pollutants or metal oxide coatings on the cathode; especially in the case of aluminum wires Malter effect can be fatal, being aluminum oxide a very good insulator[1]. In this case the onset of electrical breakdown is almost immediate, since the metal oxide is already present, whereas polymerization takes a while to form a layer on the cathode.

6.2.4 Pollutant and good materials

The first studies on gas chamber lifetime were performed on Geiger-Müller counters and showed that even small concentrations of gas pollutants or wrong adhesive tapes used in the detector assembly can have dramatic effects on the chamber ageing. Particular attention should be paid in avoiding outgassing materials, which alter the chemical composition of the gas with unpredictable effects. Analysis of wire deposits on aged chambers help in correctly classifying good and bad materials used in chamber and plumbing. Usually aged wires are inspected with Energy Dispersive X-ray spectroscopy (as in Figure 6.4 on the right), which provides the chemical composition of the deposits.

Silicon has been detected in many cases, even it is often not clear where it comes from. Its common sources are silicon vacuum greases, silicone oil bubblers, O-ring grease, and FR4 boards. It also may be present as silane (SiH_4) contamination in the gas cylinder. Silicon has the same valence of carbon, so they have similar chemical behaviour. However silicon compounds are heavier than the corresponding carbon ones: CO_2 is volatile, while SiO_2 is not and may deposit on wire surfaces. During the intense chamical activity following a discharge, in presence of silicon

---

[1] in fact aluminum wires are generally silver-plated, as in our prototypes.

new compounds can form, such as silicones and silicates, respectively

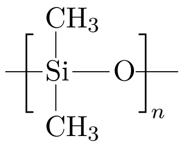

$$-\!\left[\overset{\displaystyle CH_3}{\underset{\displaystyle CH_3}{\mathrm{Si}}}-\mathrm{O}\right]_n\!-$$

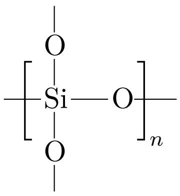

$$-\!\left[\overset{\displaystyle |\atop \mathrm{O}}{\underset{\displaystyle \mathrm{O}\atop |}{\mathrm{Si}}}-\mathrm{O}\right]_n\!-$$

made of monomers that can build chains of alternating silicon and oxygen atoms, with hydrocarbons groups (as CH_3) or oxygen atoms appended on the silicon atom.

Oxygen is also commonly found on wire coatings. It can come from air residual on the chamber, air infiltrations in the gas system or from the outgassing of detector constituents. It is often put in the gas mixture as additive for its capabilities in etching deposits on wires and in neutralising free radicals before they polymerize. Table 6.1 reports good and bad materials commonly used (or avoided) in gas chambers.

Gas plumbing		*Chamber Materials*	
Stainless steel	very good	Fiber glass/epoxy (G10, FR4)	probably OK
Nylon	very good	Plexiglas	OK
PVC	very bad	Mylar	OK
Silicon grease	bad	Kapton	good
Teflon	good	Aluminum (assembly)	OK
Chlorinated cleaning solvents	very bad	Aluminum (wires)	bad
Isopropyl alcohol	very good		(if not plated)

Table 6.1 Commonly used materials in wire chambers [40].

6.3 Laboratory tests

In the absence of a complete theory of ageing in wire chambers, testing the goodness of the gas mixture and of the material needed in drift chamber assembly has a high priority. Since it is not possible to carry on several test experiments, which will need too much time, the ageing of the apparatus is studied through accelerated laboratory tests on small prototypes, under the assumption (likely but not yet proven) that ageing scales with the collected charge. Prototypes are irradiated by means of high-intensity radioactive sources (such as ^{55}Fe) or X-ray generators. Being the gain loss the most interesting effect to quantify, the parameterisation chosen for the ageing rate is

$$\mathcal{R} = -\frac{1}{G_0}\frac{\mathrm{d}G}{\mathrm{d}Q}\left(\frac{\%}{\mathrm{C/cm}}\right) \tag{6.1}$$

where G_0 is the initial gain, G is the measured gain and Q is the collected charge per unit length.

6.3.1 Some sensitive physical parameters

Experiments proved that ageing rates depend not only on the collected charge, but on many other operating conditions which should be scaled adequately to the radiation dose rate. In particular sensible parameters are found to be [40]:

(i) **Gain**. As the gain of the chamber (thus the current density and the avalanche development) is increased, the ageing rate has been found to decrease. This effect is not very large but significant: going from the avalanche mode ($G\sim 10^{4\div5}$) to the streamer mode ($G\gtrsim 10^{6}$) the value of $\mathcal{R}$ can decrease up to 50%. Therefore ageing test are usually performed keeping the gain as close as possible as the one of the final detector. A possible explanation to the dependence of $\mathcal{R}$ on the gain can be that the induced space charge weakens the electric field and increases the size of the avalanche; this results in a lower density of free radicals produced per unit charge. Another possible mechanisms can be the saturation of the pollutants present in the avalanche volume, but this effect is coupled to the gas flow dependence.

(ii) **Gas flow rate**. One may expect that high gas flows reduce the ageing rates since free radicals and pollutants are swept away from the chamber volume at higher rates. On the other hand higher flows supply more "bricks" (monomers or impurities) for polymer growth during the avalanche progress. These are two competitive mechanisms, as can be seen in Figure 6.6. However wire chamber experiments show an ageing rate decrease with increasing gas flow (as in the right side of the plot in Figure 6.6). A rule of thumb used of scale the gas flow rate from the final detector to the ageing test prototypes is to keep the gas volume exchange rate constant.

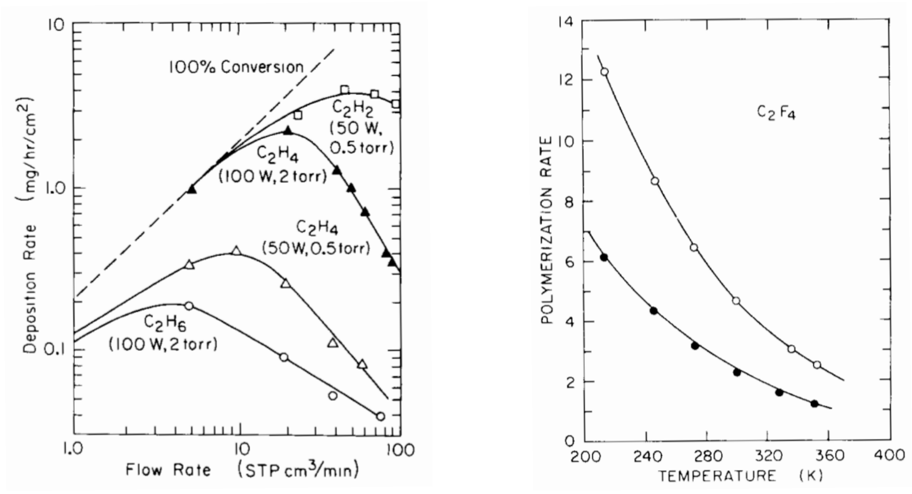

Figure 6.6 Plasma chemistry studies on the dependence of the polymer deposition rate on the gas flow rate (left) and on temperature (right).

(iii) **Gas density and purity**. Higher pressures for the operations of the chambers imply a shorter mean free path for electrons, thus a lower drift energy, but also a higher concentration of molecules which can produce free radicals. These two effects go in opposite directions, but in this case a clear density behaviour cannot be inferred from experiments results. Temperature variations can also alter the ageing rate of the detector, supporting or contrasting polymerization rates. Figure 6.6 shows a sharp drop of polymerization rates with increasing temperature. Therefore it is important for ageing tests to reproduce the operating conditions of the final detector. Gas purity is also a key parameter, so the mixture used in the ageing tests should be the same (*i.e.* from the same producer, with the same purity) that will fill the final wire chamber.

(iv) **Radiation intensity and size of the irradiation area**. The fundamental assumption in ageing rate is (almost) independent of the radiation intensity. Actually space charge and gas heating effects can modify polymers growth and impurity deposition. A high irradiation level can convey the effects of points (i) and (iii).

6.4 Ageing test procedures

Different procedures of ageing rate measurements can return different values of $\mathcal{R}$, as explained by Blinov [46]. There are two commonly used methods: monitoring the gain through the anode wire current or through pulse-height variations of a certain line.

The first one is the most used and consists in measuring the anode wire current at constant irradiation. Assuming proportionality between current and gas gain, the ageing rate is given by

$$\mathcal{R} = -\frac{1}{G_0}\frac{\mathrm{d}G}{\mathrm{d}Q} = -\frac{1}{I_0}\frac{\mathrm{d}I}{\mathrm{d}Q} \tag{6.2}$$

However if the irradiation intensity is too high, saturation effects occur: for high radiation rates the anode current is not proportional to the multiplication factor (see Section 4.5) so equation (6.2) does not hold.

Expressing the anode current in terms of the non–saturated current $I_{\mathrm{NS}} = RG$, we have

$$I = I_{\mathrm{NS}}\, e^{-K\, I_{\mathrm{NS}}}$$

Under the assumption of small deviations from linearity, *i.e.* $K\, I_{\mathrm{NS}} \ll 1$, we can approximate

$$I \simeq I_{\mathrm{NS}}\, e^{-KI}$$

so that we can simplify the saturation gain loss by computing

$$\mathcal{R} = -\frac{1}{G_0}\frac{\mathrm{d}G}{\mathrm{d}Q} = -\frac{1}{I^0_{\mathrm{NS}}}\frac{\mathrm{d}\, I_{\mathrm{NS}}}{\mathrm{d}Q} = -\frac{1}{I_0 e^{KI_0}}\frac{\mathrm{d}}{\mathrm{d}Q}\left[I\, e^{KI}\right] \tag{6.3}$$

In addition current measurements suffer from variations of environmental conditions, like pressure and temperature changes. It is crucial to compare measurements performed at the same working point, in order to prevent mistaking a current decrease due to pressure variation for gain loss.

The other estabilished procedure for measuring ageing rates consists in monitoring a peak in the pulse height spectrum of a radioactive isotope, such as ^{55}Fe, ^{90}Sr or ^{106}Ru. X-ray or β sources are preferable in order to restrain charge leakage in the cell: the choice depends on the used gas mixture, and for low-mass mixtures (in particular helium based) leakage can be a limiting factor. The monitored source should have a low activity, otherwise pile-up and space charge can modify the spectral distribution: it cannot be the one used for irradiation. If a twin source is placed in a non-irradiated area, a real time quantification of the ageing suffered by the detector can be performed, in a way that is independent of environmental conditions, which are simplified by reporting the ratio of the "aged" to the "control" peak positions. In this case the ageing rate is parameterised by

$$\mathcal{R} = -\frac{1}{G_0}\frac{\mathrm{d}G}{\mathrm{d}Q} = -\frac{1}{A_0}\frac{\mathrm{d}A}{\mathrm{d}Q} \tag{6.4}$$

being A the the ratio between the aged peak position and the control one. This procedure allows also to investigate gain nonuniformity, studying the evolution of the peak width. Figure 6.7 shows ^{55}Fe spectra degradation at four different irradiation levels, from ageing tests performed for the CDF experiment.

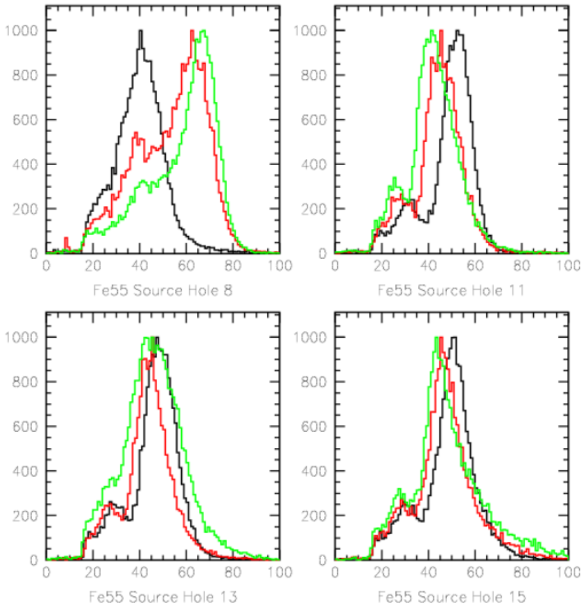

Figure 6.7 ^{55}Fe spectra at different irradiation levels: before (black histogram), in the middle (red histogram) and at the end (green histogram) of the ageing test. Figure from [47]

Among the different sources exploited, MIP sources are preferable: X-rays (or even worse slow hadrons) produce a very dense ionising track and therefore gas amplification saturates at lower multiplication factors. This results in an underestimation of the ageing rate, in a way similar to that expressed in equation (6.3).

Summary

In this Chapter we reviewed the causes of ageing and the parameters that can enhance or limit ageing effects. We also showed ageing tests procedures found in literature, highlighting their reliability and their limits.

Chapter 7

Preparation of the ageing tests

The design and the preparation of the experimental setup for the ageing tests are discussed in this Chapter. After the determination of the ageing issues of the new $\mathrm{MEG^{UP}}$ *tracker, the experimental setup is presented and particular care is placed on the description and the characterisation of the two X-ray tubes used as irradiating sources. The response of the chamber to X-rays has also been studied, in order to be able to recognise which variations of the chamber operation can be due to ageing.*

7.1 Charge accumulation in the new tracker

In order to evaluate the charge collected by the wires of the tracker, the key parameter is the positron rate. Figure 7.1 shows the flux of positrons Φ_e in the detector volume at a muon rate of $R_\mu = 10^8\,\mu^+/\mathrm{s}$. The yellow curved lines represent the hyperbolic layers of the tracker, while the trapezoid is a module of the old drift chamber.
For an expected muon rate of $7 \times 10^7\,\mu^+/\mathrm{s}$, the fluxes in figure must be scaled by a factor 0.7, thus giving a maximum flux of 31.5 kHz/cm^2 on the innermost layer. The charge per unit length of wire is given by the particle rate (flux × area), multiplied by the ionisation yield of positrons in the transverse dimension of the cell (7 mm), multiplied by the gain of the cell. Only positrons with momentum larger than $\sim$ 45 MeV/c cross the sensitive volume; therefore all the positrons are MIPs. In 85:15 gas mixture of helium and isobutane, for a gain of 10^5 it gives a maximum current on a centimetre of wire

$$I = (31.5\,\mathrm{kHz/cm^2} \times 0.7\,\mathrm{cm} \times 1\,\mathrm{cm}) \times (40.6\,e/\mathrm{cm} \times 0.7\mathrm{cm}) \times 10^5 = 10\,\mathrm{nA} \qquad (7.1)$$

For 90:10 mixture the maximum current is 7.3 nA/cm.

Therefore the total charge collected in three data acquisition years (630 days, $\sim$ 50 Ms) is $\sim$ 500 mC/cm for the 85:15 mixture and $\sim$ 400 mC/cm for the 90:10.

During ageing tests, in order to collect the same charge within a month of operation, the

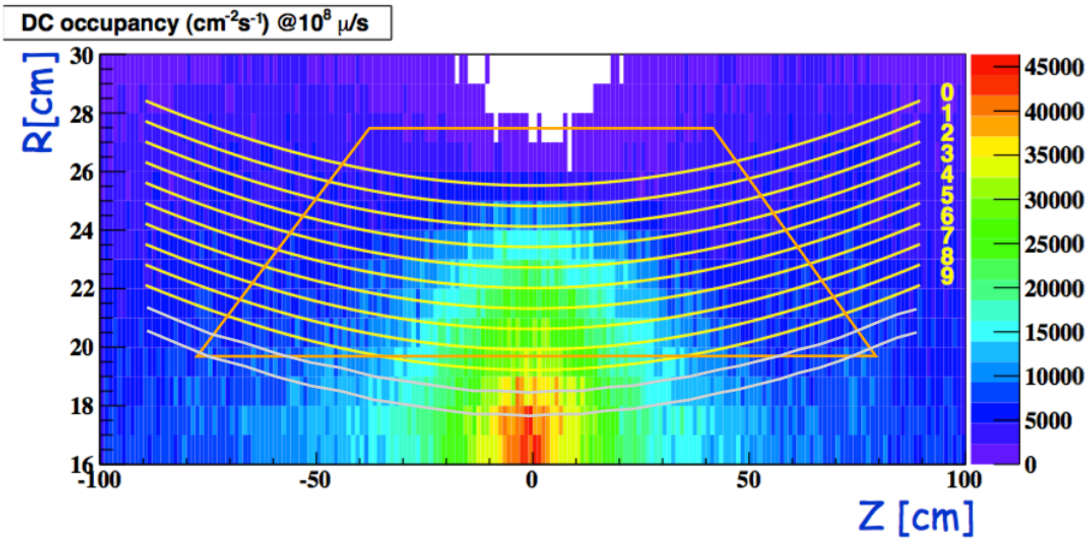

Figure 7.1 Positron flux within the drift chamber volume at a muon rate of 10^8 μ/s.

current per centimetre must be about twenty times larger. As regards ionisation yields, MIPs are not very efficient, when compared to α-particles or X-rays, whose specific ionisation is much larger.

In the following tests, two X-ray tubes are used as irradiating sources. They are preferred to common radioactive X-ray sources (such as ^{55}Fe) because of the high rate of X-rays they can produce (equivalent to that of a radioactive source with activity of the order of the Curie) and their tunability. In addition they are safer than radioactive sources, since they can be switched off without exposition to radiation; furthermore an X-ray tube can provide different lines through X-ray fluorescence.

In the next section a brief description of the experimental apparatus is provided, in order to select the X-ray tubes working points.

7.2 The experimental setup

The experimental setup for ageing measurements is sketched in Figure 7.2: the CF-100 cross containing the single-cell prototype is placed between the X-ray source and a scintillator used to independently monitor the X-ray rate. The irradiation area is set by a collimator that can be placed directly on the flange of the cross or on the X-ray source itself. The radiation exiting the cross is damped by a lead cylinder with a thickness of 2 mm, with a 0.6 mm collimator to prevent the scintillator from being overirradiated.

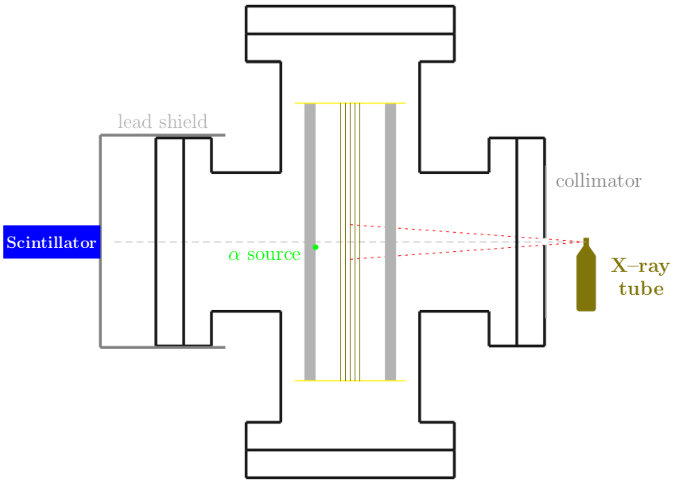

Figure 7.2 Sketch of the experimental setup for ageing measurements.

7.3 X-ray production

Two X-ray sources were used in ageing prototypes: a Moxtek Magnum for the first part of the ageing test on Prototype I and an Oxford Apogee for the following tests. In this section, a generic description of X-ray tube functioning is presented; in the following sections the characterisations of the sources will be described, together with the determination of the working points of the sources.

As an example of the structure of an X-ray tube, a scheme of the Oxford Apogee X-ray tube is reported in Figure 7.3. X-rays are produced by *bremsstrahlung* from energetic electrons impinging on a metallic target, *e.g.* chromium, tungsten, molybdenum, *etc.* Electrons are emitted by a tungsten filament in which an intense current flows (~ 1 A), and accelerated to the target by a high voltage of the order of tens of kiloVolts. The tube housing is lead-lined, for a complete absorption of off-focused radiation. The filament is made of tungsten so that it can withstand great amounts of heat, and is surrounded by a focusing cup that prevents the electron beam from spreading all over the tube. Focusing cups produce narrow electron beams. The target material is required to be a good heat conductor to dissipate energy and to have high atomic number to improve X-ray production efficiency. Electrons do not impinge perpendicularly on the target, otherwise almost all the radiation would be absorbed in the target itself. The target has a slope of about 10° with respect to the plane perpendicular to the electron beam. This yields a valuable benefit: a large impact area (useful to heat dissipation) is projected on a small focal spot size for X-rays, of about 250×100 µm^2. However the anode angle represents the maximum angle of the X-ray beam on the “downstream” side: X-rays emitted at larger angles are damped in the anode. This can result in an asymmetry of the X-ray angular distribution (heel effect). A thin beryllium window keeps the tube sealed and vacuum-resistant with the minimum amount of

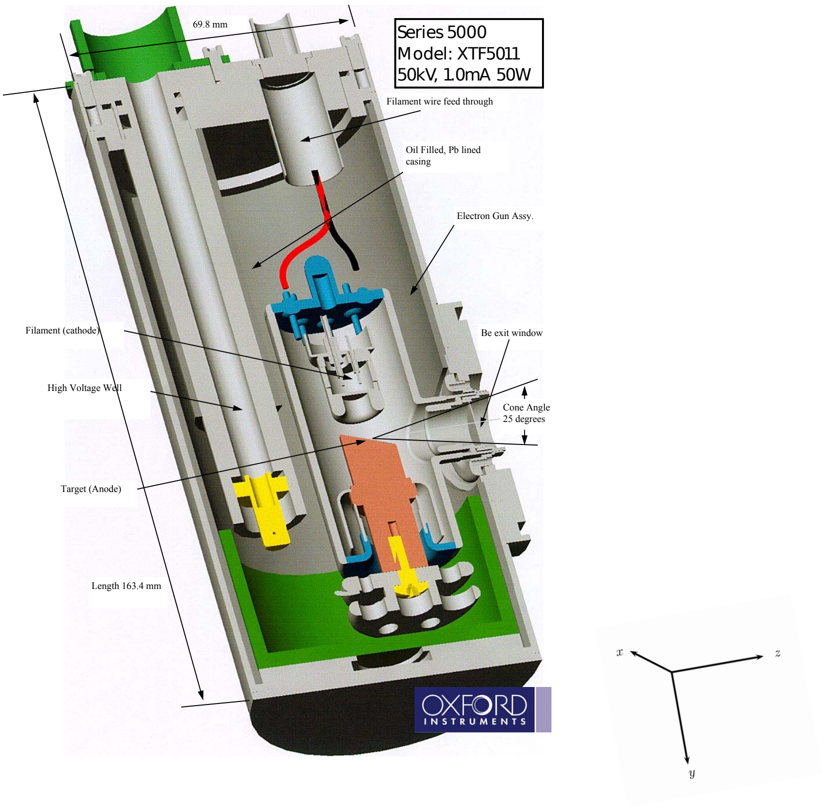

Figure 7.3 Scheme of the X-ray tube Oxford Instruments Apogee XTF5011.

material and limits the angular spread of X-ray beam to about 25°.

The energy spectrum of X-rays emitted by a tube is quite complicated to predict: the $1/E$ decrease with energy has a physical endpoint related to the applied high voltage, while at low energy absorption by air, beryllium window and the anode itself become important. In addition the proportions of characteristic radiation and continuous *bremsstrahlung* spectrum are not easily deducible. A quite good expression for the continuous component of the spectral distribution of X-rays is known as Kramers law[48]

$$I(E)\mathrm{d}E = c \times i \times Z \times \frac{(E_0 - E)}{E}\mathrm{d}E \tag{7.2}$$

where i is the tube current, Z is the atomic number of the anode, E_0 is the endpoint energy. The constant c includes the X-ray production efficiency, which has an approximate dependence on the tube high voltage squared[49].

7.4 X-ray absorption

In Chapter 4, the interactions of X-rays in the detector have been described; in ageing tests we are interested in the efficiency of the absorption of X-rays, since large quantities of charge are needed inside the cell. The attenuation of the intensity I_0 of an X-ray beam traversing matter is exponential, with a mean free path

$$\lambda = \frac{1}{n\sigma} \equiv \frac{1}{\mu\rho} \tag{7.3}$$

where n is the number density of atoms in the medium, σ is the absorption cross section, ρ is the mass density and μ is the mass attenuation coefficient. In our context it is important to know the absorption of X-rays in the detector materials and in the cell. Figure 7.4 shows the mean free path of X-rays in the materials traversed by X-rays from the source to the cell of the prototype: air from the source to the CF-100 cross, the Mylar window on the entrance flange and 12 cm of the gas mixture inside the cross. The mean free path is a little smaller for the 85:15 mixture, because of its higher density.

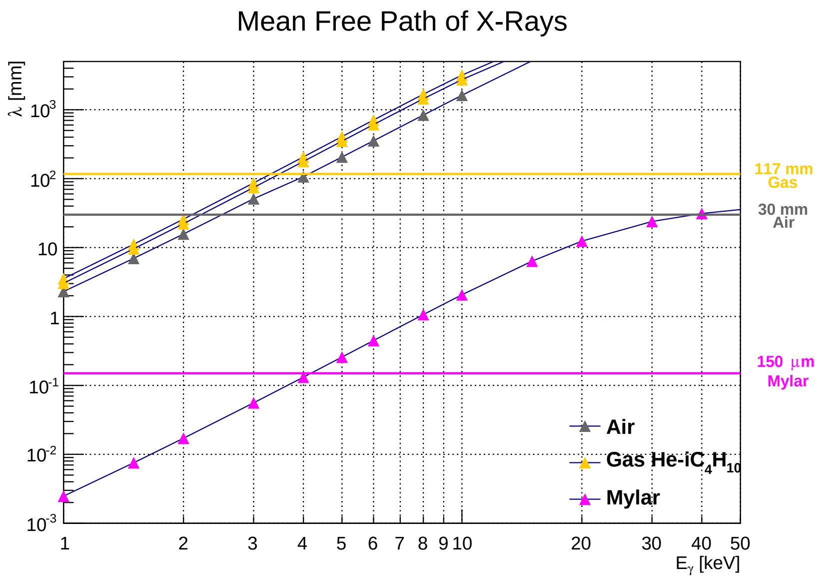

Figure 7.4 Mean free path of X-rays as a function of their energy in the materials traversed by the particles before entering the sensitive cell. The mean free path for both mixtures have been plotted. Data have been taken from [50].

As long as the distance from the X-ray source to the CF-100 cross is lower than 10 cm, the low-energy component of the X-ray spectrum is cut below 4 keV by the absorption in the Mylar window. Since at 4 keV the mean free path in the gas mixture is about 20 cm, the mean absorption of X-rays in the 7 mm wide cell is

$$1 - e^{-7/200} \simeq 3\%$$

At higher energies the mean free path increases, thus the conversion efficiency becomes even lower. In addition for energies lower than ∼ 5 keV, photoelectrons tracks become comparable with the cell dimensions (see Figure 4.22), resulting in charge leakage. A larger contribution of Compton effect is also obtained and the X-ray beam thus spreads modifying the size of the irradiated area.

Ideally the X-ray source should therefore produce radiation with moderately low energy but high enough to survive the absorption in the material before the cell. In order to avoid high power dissipation at low yield of X-rays converted in the cell, the X-ray tube working point should be determined experimentally.

7.5 Characterisation of the Moxtek X-ray source

As mentioned above in the first part of the ageing test on Prototype I the irradiating source was a Moxtek Magnum 40 kV X-ray gun (Figure 7.5). The characterisation of the source had a pivotal importance in understanding the experimental setup needed and in defining correct procedures. Under this perspective, the characterisation of the Oxford Apogee will be more detailed than that of the Moxtek Magnum.

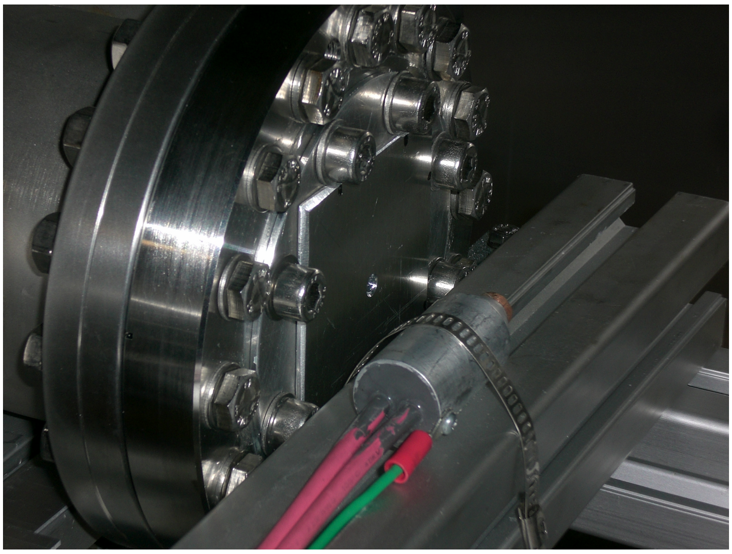

Figure 7.5 Moxtek Magnum X-ray gun placed in front of the CF-100 cross.

In the Moxtek Magnum the tungsten anode is grounded, and the high voltage can be set from −4 kV to −40 kV, with a maximum electron current of 0.1 mA. Its nominal focal spot size is 300 µm, and the nominal angular spread of the produced X-radiation is 50°.

The apparatus used for the characterisation of the source is shown in Figure 7.6. The X-radiation is detected with a Saint Gobain NaI X-ray detector 1XMP 040B with a PA-12 preamplifier and shaper. The NaI (Tl) crystal has a diameter of 1” for a thickness of 1 mm, covered by a thin beryllium window. The preamplifier is power supplied at 12 V, while the high voltage of the photomultiplier was set to 900 V. For rate measurements, the signal from the crystal preamplifier is shortened with a Ortec 570 Amplifier (10×, 0.5 µs), then discriminated by a LeCroy 623B Discriminator connected to a CAEN N93B Gate Generator (2 µs gate). In the end the signal is connected to a Multiscaler. For spectrum measurements the signal is sent to a DRS4 evaluation board, which digitalizes the waveforms. The pulse height distribution is then computed from the waveform amplitudes.

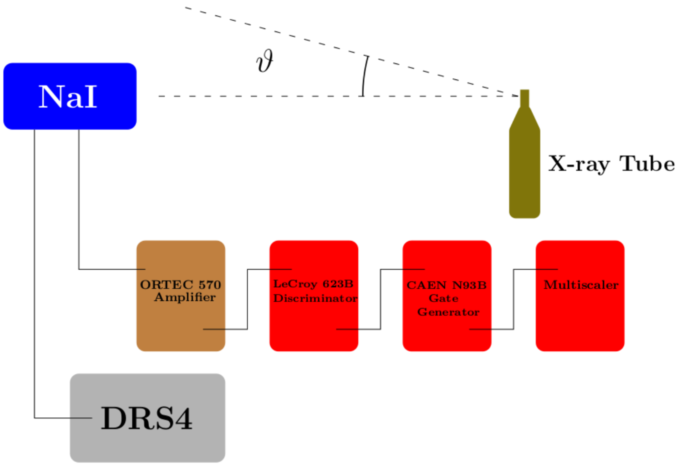

Figure 7.6 Experimental apparatus for the characterisation of the Moxtek Magnum 40 kV X-ray gun.

7.5.1 Linearity test

As a first test the linearity between the current flowing in the X-ray tube and the X-ray output was checked. The X-ray flux at several X-ray tube current values was measured by counting the rate of the sodium iodide detector.

Data are shown in Figure 7.7: the curve presents saturation at high current, due to the dead time $\varDelta t$ of the counting apparatus (the 2 µs of the gate). Once a dead time correction is applied to the measured rate R_m [32]

$$R = \frac{R_m}{1 - \varDelta t R_m}$$

the actual rate is proportional to the X-ray tube current. The importance of checking such linearity will be clear in the next chapter.

7.5.2 Energy spectra

For the calibation of X-ray spectra, an ^{241}Am source was used (see Chapter 4). In Table 7.1 the X-ray lines emitted in the detection window (5 keV - 70 keV) are reported. The X-rays originate

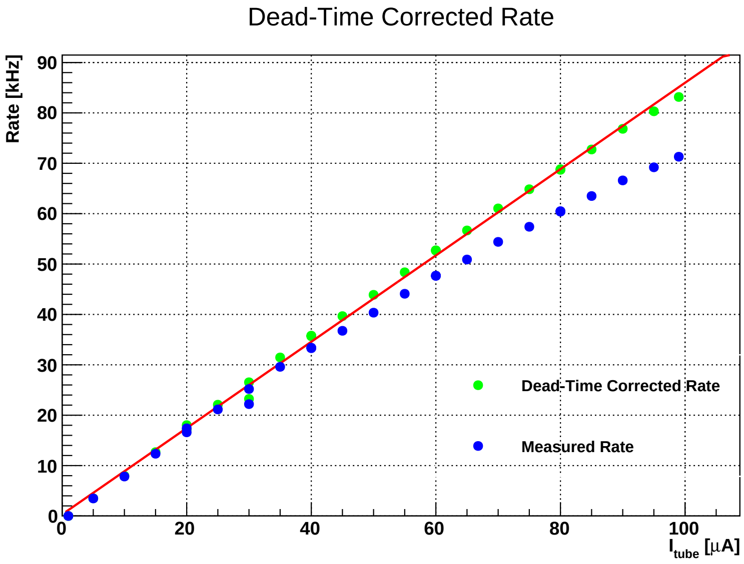

Figure 7.7 Linearity between the X-ray tube current and the X-ray rate.

from two different processes: the de-excitation of the neptunium nucleus (26.34 keV, 59.54 keV) and the rearrangement of electron shells after the nuclear decay (the remaining lines).

Emission Line	Energy [keV]	Relative Intensity
L α_1	13.94	90
L α_2	13.76	10
L β_1	17.75	100
L β_2	16.84	~ 20
L β_3	17.99	~ 20
L β_4	17.06	20
L γ_1	20.79	~ 25
L γ_3	21.34	~ 5
L l	11.89	~ 5
Np*	26.34	67
Np*	59.54	100

Table 7.1 X-ray emission lines from ^{241}Am. Np* stands for the nuclear transition lines of the de-excitation of the Neptunium nucleus of the decay $^{241}\text{Am}\rightarrow {}^{237}\text{Np}^{*}\ \alpha$, while the others are the characteristic radiation of electron transitions in Neptunium. The relative intensities are expressed separately for the two group. Values from [38].

Figure 7.8 shows the pulse height distribution of the X-rays emitted by the tube, superimposed to the energy spectrum of X-rays from the ^{241}Am. Only three peaks are visible: a broad peak containing the unresolved $L_{\alpha,\beta,\gamma}$ lines, the nuclear peak at 59.54 keV and an additional peak

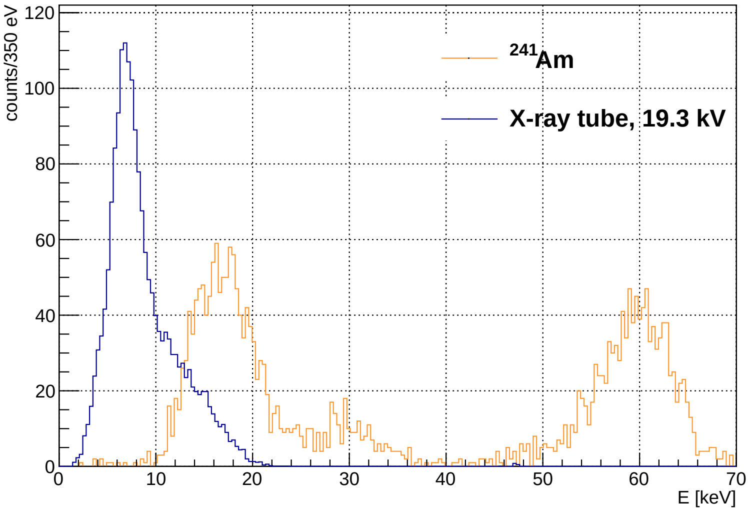

Figure 7.8 Pulse height distribution of the ^{241}Am and of the Moxtek Magnum X-ray gun at 19.3 kV.

at about 30 keV: the escape peak. When an X-ray of energy E interacts through photoelectric effect, an electron is kicked off from a iodine atom with energy $E - E_\mathrm{b}$, where E_b is the binding energy of the electron. The vacancy produced in the shell is then occupied by an outer electron with the emission of an X-ray. Such X-rays are generally absorbed in the detector (producing scintillation light, just like photoelectrons), allowing the detection of all the original energy E. But when the X-ray escapes from the detector, the total energy detected is $E - E_\mathrm{b}$.

From the spectrum of the X-ray tube in Figure 7.8 it is not clear if the peak represents the L_α line of tungsten, or if it is a threshold effect due to X-ray absorption or to signal acquisition. This ambiguity comes from the poor energy resolution of sodium iodide detectors at low energies, which is a statistical effect. The light-output L_ph of a sodium iodide scintillator is about 4×10^4 scintillation photons for 1 MeV of energy absorbed in the crystal. However only a fraction η_C of the scintillation light is collected by the photocathode, whose Quantum Efficiency (QE), *i.e.* the mean number of photoelectrons produced per incident photon, is smaller than 1. Therefore using reference values[32], the number of photoelectrons produced by a 8.4 keV X-ray is

$$N_\mathrm{pe} = L_\mathrm{ph} \times 8.4\,\mathrm{keV} \times \eta_\mathrm{C} \times QE \simeq 4 \times 10^4 \times \frac{8.4\,\mathrm{keV}}{1\,\mathrm{MeV}} \times 70\% \times 25\% \simeq 59$$

Anyway the number of photoelectrons follows a Poisson distribution, therefore the expected resolution is

$$\frac{\Delta E}{E} \sim \frac{\Delta N_\mathrm{pe}}{N_\mathrm{pe}} = \frac{\sqrt{N_\mathrm{pe}}}{N_\mathrm{pe}} \simeq 13\%$$

which means that a 8.4 keV monochromatic signal (neglecting leakage) is detected as a Gaussian distribution with mean 8.4 keV and standard deviation of about 1 keV.

Therefore the peak in Figure 7.8 is the sum of the low-energy component of the X-radiation with the broad peak of the tungsten line superimposed.

7.5.3 Angular distribution

The angular distribution of the X-rays emitted by the Moxtek tube was measured keeping the source fixed and rotating the sodium iodide detector on the safe box plane. The obtained angular distribution is shown in Figure 7.9. The distribution is fairly flat on an angular coverage of about 35°.

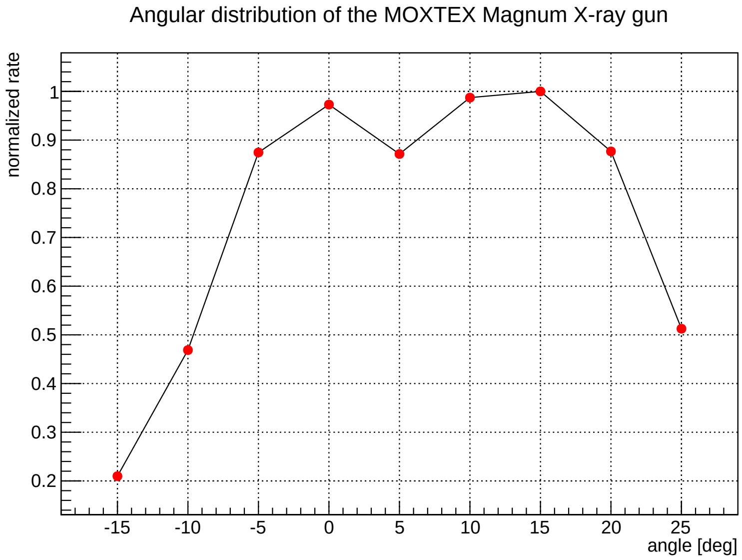

Figure 7.9 X-ray rate as a function of the angle to the Moxtek Magnum X-ray gun.

7.6 Characterisation of the Oxford X-ray source

From the tests on the Moxtek Magnum we learned that

- A sodium iodide crystal has poor resolution for the measurement of X-ray energy spectra.
- A Multi-Channel-Analyzer would make easier the measurements of pulse-height distributions.
- A solid apparatus for the measurement of the X-ray beam divergence is needed.

Several improvements were done on the apparatus for the characterisation of the Oxford Apogee XTF5011. A large sodium iodide crystal Saint-Gobain BICRON 3MW3/3 with diameter

3” and height 3” was used for both rate and spectrum measurements. NaI signals are shaped and amplified by the ORTEC 570 amplifier. A $3 \times 3\,\mathrm{cm}^2$ BC404 plastic scintillator coupled to a Hamamatsu H10580 fast photomultiplier was also available for rate measurements. Signals from the plastic scintillator are amplified by a Phillips 776 Amplifier and discriminated by a CAEN Discriminator mod. 84 which is then connected to the Multiscaler.

For high resolution measurements a silicon detector Amptek XR-100CR with PX2CR power supply and amplifier was exploited. Pulse height distributions are obtained through a Multi-Channel-Analyzer (MCA) ORTEC Maestro-32.

7.6.1 Linearity test

In order to avoid dead-time effects, for the linearity tests the plastic scintillator was used. The rate of X-rays is reported as a function of the X-ray tube current in Figure 7.10.

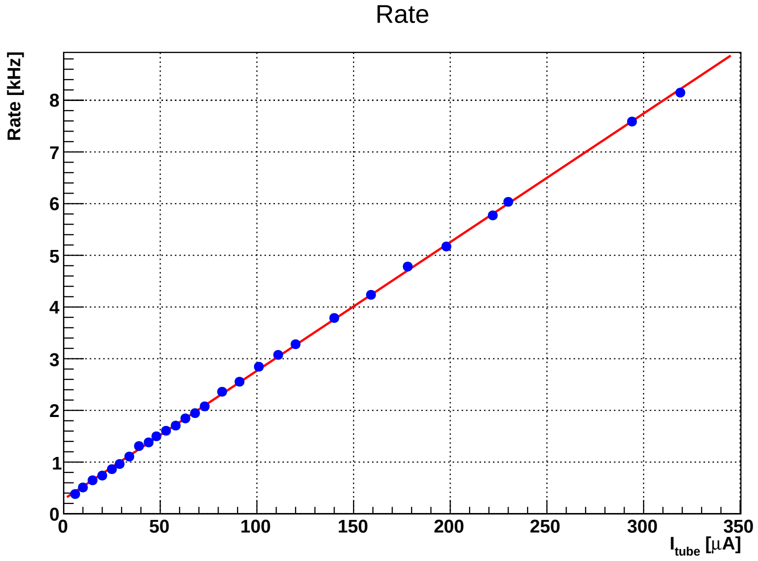

Figure 7.10 X-ray rate as a function of the current to the Oxford X-ray tube.

Linearity is fulfilled without any need for corrections, thanks to the much shorter signals.

7.6.2 Energy spectra: calibration

From Figure 7.8 it is clear that the sodium iodide detector is not the most suitable detector for measuring X-ray spectra at the energies involved. Both the large cylindrical NaI and the silicon detector were used for comparision. At low energies a very important feature of a detector is the material it is made of, that is the matter a particle has to trespass in order to be detected. The large sodium iodide has a 0.5 mm aluminum casing, which attenuates all the radiation with energy below say 12 keV, as shown in Figure 7.11. A thin beryllium coating should be preferred, since it is almost transparent to X-rays with energy above 2 keV.

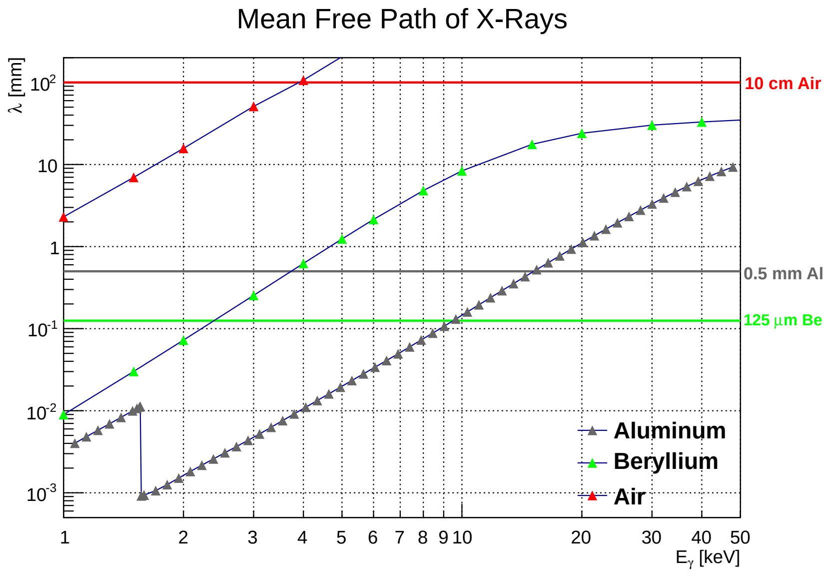

Figure 7.11 Mean free path of X-rays as a function of their energy in aluminum, beryllium and air. Data have been taken from [50].

Figure 7.12 shows clearly this issue, comparing the spectrum of the ^{241}Am source acquired with the large sodium iodide detector with the one acquired with a silicon detector XR-100CR. The spectra differ in both width and amplitude of peaks. The very high resolution of silicon

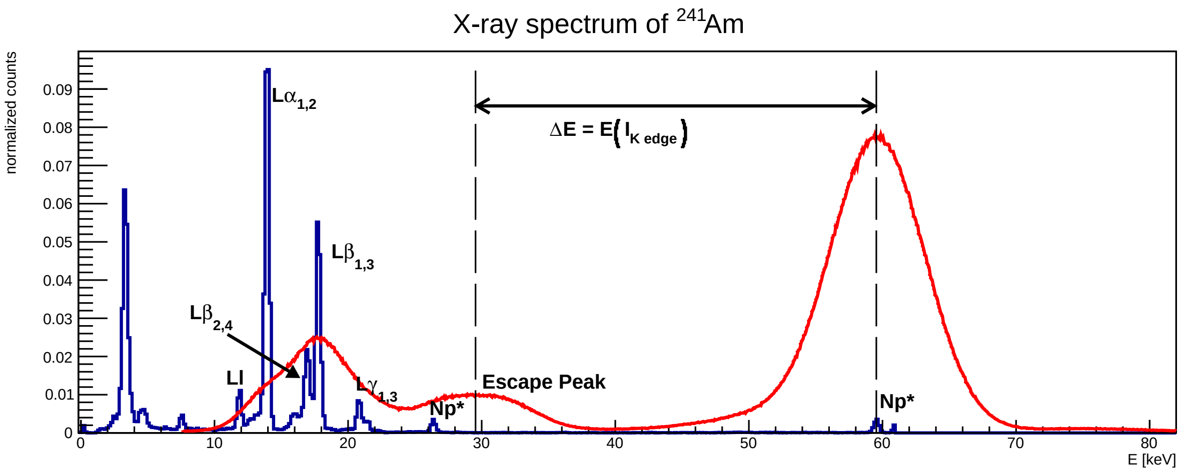

Figure 7.12 X-ray spectrum of ^{241}Am, acquired by the NaI scintillator (black line) and by a silicon detector XR-100CR (red line).

detector is due to several aspects, *in primis* to the very high “light-output”[1], which lowers the statistical fluctuation. The L-lines of Neptunium (see Table 7.1), due to the rearrangement of electron shells following the decay of the nucleus, are seen as a unique broad peak by the sodium iodide. On the other hand the different amplitudes of the peaks come from two concomitant aspects: the efficiency of silicon detector, due to the decreasing absorption of X-rays in silicon at increasing energies (just like in Figure 7.11 for other elements); secondly, the absorption of low energy X-rays in the aluminum window of the sodium iodide.

In this case the americium spectrum provided a precise calibration of the MCA.

7.6.3 Energy spectra

The energy spectrum of the Oxford Apogee was acquired with the Amptek XR-100CR. A silicon detector can be permanently damaged if exposed to a high X-ray flux. Therefore for the acquisition of the spectra, a 1-mm thick tungsten collimator with a 0.1×0.1 mm^2 window was placed in front of the detector. The tube was kept at minimum current, and spectra at different values of the tube high-voltage were taken. In order to avoid X-ray absorption in air, the source was placed as close as possible to the detector; anyway this was possible only for low values of high voltage, because of the squared dependence of the X-ray intensity on the tube high voltage. The measured spectrum is the emission spectrum scaled to the efficiency of the silicon detector (see Figure 7.13), which takes into account the attenuation in the beryllium window (25.4 µm) and the absorption of X-rays in silicon (500 µm).

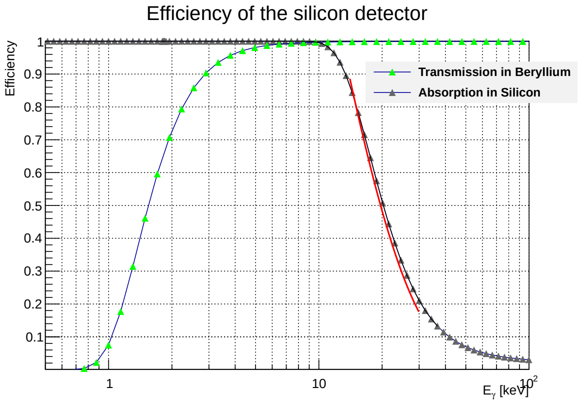

Figure 7.13 Efficiency of XR-100CR. The red line is the contribution of absorption from the spectrum in Figure 7.14 (see full text). Data have been taken from [50].

Figure 7.14 shows the spectrum obtained at 30 kV. The detector was placed at 60 cm from the source: the low energy component of the spectrum is therefore filtered by the beryllium window of the source and by 60 cm of air (and by the production anode itself). The spectrum is

---

[1] actually pairs-output, *i.e.* the number of electron-hole pairs created per unit of energy absorbed.

well described for energy above 12 keV by the Kramer law

$$N(E) = A\frac{(E_0 - E)}{E}e^{-E/\varepsilon} \tag{7.4}$$

folded with the efficiency of the detector, using a reparameterisation $1 - e^{-l/\lambda(E)} \simeq e^{-E/\varepsilon}$. The fitted values for the parameters are

$$E_0 = 29.33 \pm 0.21$$
$$\varepsilon = 9.81 \pm 0.24$$

The red line in Figure 7.13 is a fitted exponential with fixed slope $-1/\varepsilon$: it reproduces with good agreement the absorption in silicon.

For a suggestive glance, the function (7.4) was then extrapolated backward (the red line in the figure)[1]. In addition to the continuous component, the spectrum shows the imprint of the anode of the tube: the Kα and Kβ lines of Chromium at 5412 eV and 5947 eV.

Figure 7.15 shows the spectrum at 10 kV, realized with the detector close to the source. The spectrum is shown also after computing attenuations due to 150 µm in Mylar and 116.5 mm in helium-isobutane gas mixture 85:15.

The effect of absorption is the attenuation of the component at energy lower than the

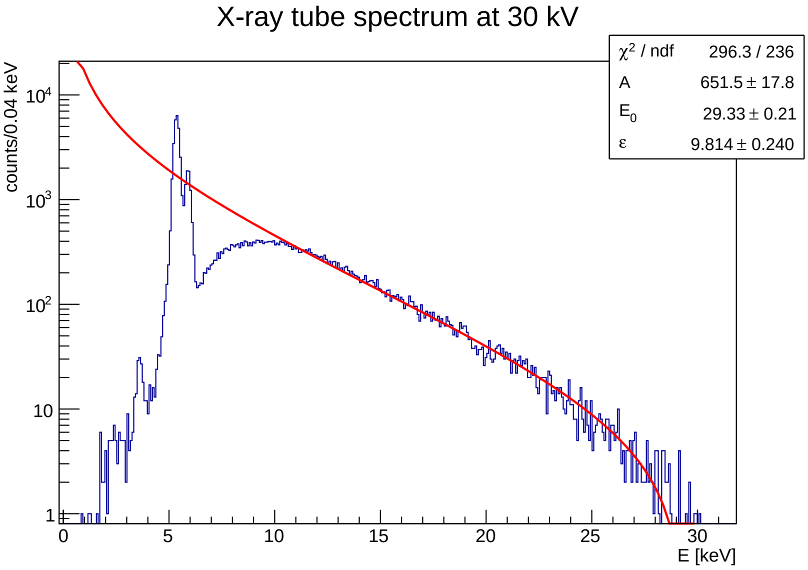

Figure 7.14 Energy spectrum of the X-ray tube at 30 kV. The red line represents the deduced unfiltered spectrum.

---

[1] The multiplicative factor $e^{-E/\varepsilon}$ is reasonable only for $E > 12$ keV, but for lower energies its contribution is of the order of the unity and does not affect the estimate.

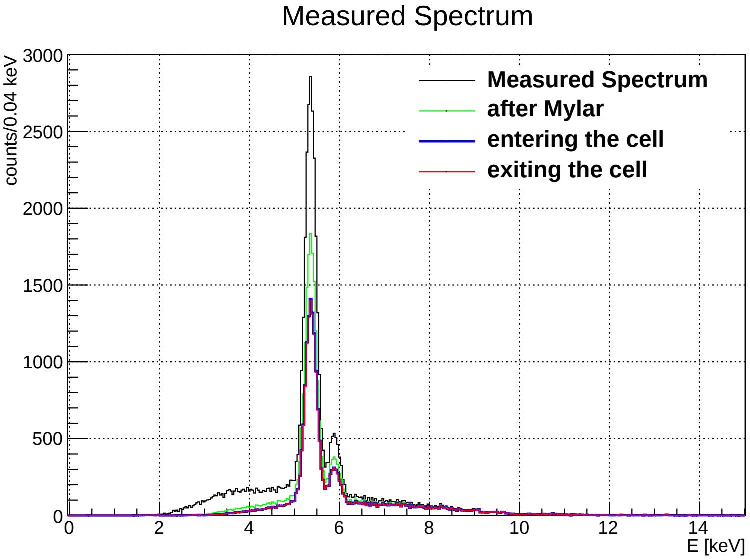

Figure 7.15 Measured spectrum of the Oxford Apogee at 10 kV. The absorption contributions of Mylar and gas mixture are reported.

chromium lines. For the values of the applied high voltage the two Chromium lines constitute the great part of the emitted radiation. They can be used as an additional calibration point, in order to verify the correctness of the energy scale.

As a working point for the ageing measurements, we chose the high voltage at which the spectrum of the X-rays absorbed in the cell is in large part made of the chromium lines. Figure 7.16 shows the spectrum of the radiation absorbed in the cell computed from the measured spectrum including absorption. The two chromium X-lines represent the 73 % of the absorbed radiation and this configuration was chosen for the ageing tests.

7.6.4 Angular distribution

While for the Moxtek Magnum the collimation of the X-rays entering the drift chamber can be performed only on the upstream flange, for the Oxford Apogee direct collimation in the proximity of the beryllium window is possible. Such solution is preferable since X-rays are not emitted outside the drift chamber, avoiding spurious counts on the monitor scintillator that arise from scattering inside the safety box.

The X-rays coming from the X-ray tube are essentially emitted by a point-like source within a cone of nominal half-aperture angle of 12.5° (because of the lead casing inside the tube) in absence of heel effect.

In order to efficiently collimate the X-rays, the divergence of the X-ray beam was measured. In addition, for *bremsstrahlung* radiation the angular distribution is not isotropic, so the X-ray rate was measured at several angles on the $x - z$ and $y - z$ planes (the reference system is shown

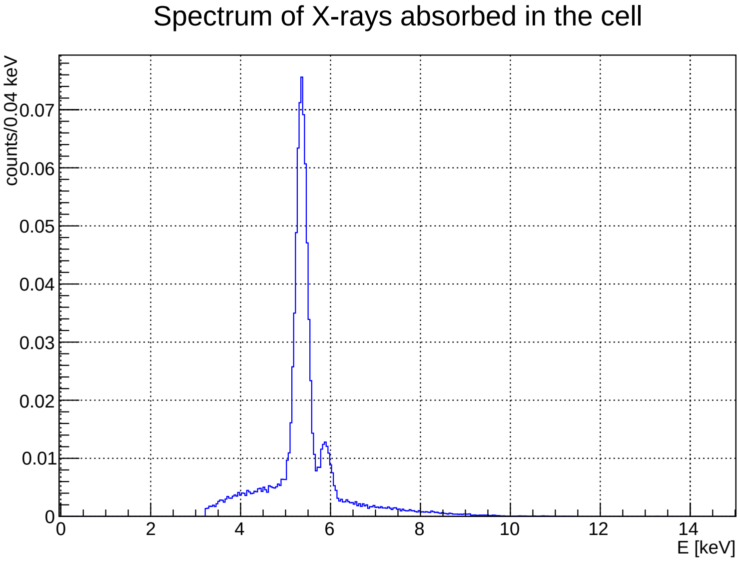

Figure 7.16 Spectrum of the radiation absorbed in the cell volume with the high voltage of the X-ray tube at 10 kV.

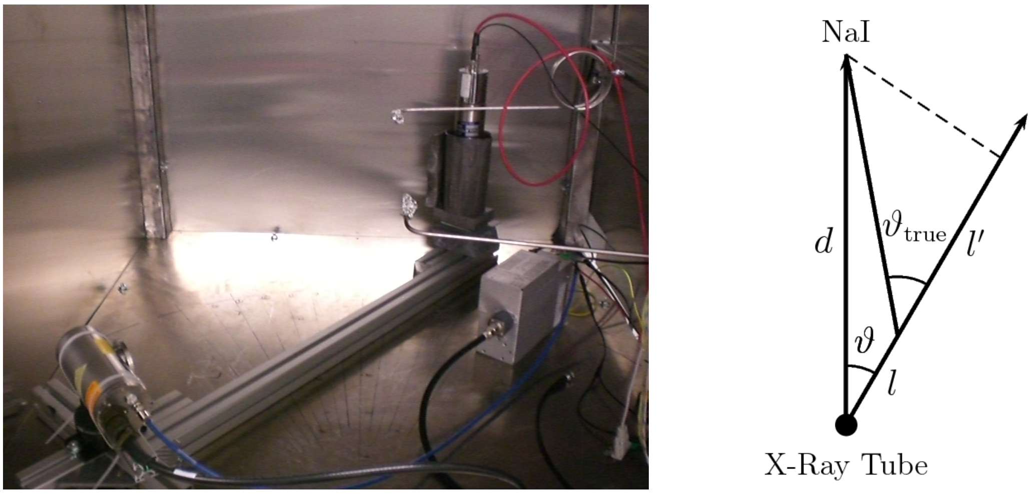

Figure 7.17 Experimental setup and measured quantities.

in Figure 7.3), to check the presence of some correlation between X-ray energy and emission angle. The experimental setup is shown in Figure 7.17. The X-ray tube was placed on a positioning goniometer and the centre of the cylindrical case of the tube was aligned with the centre of the goniometer. The large NaI detector was placed at a distance of about 80 cm. Actually the focal spot of X-rays does not lie on the centre of the tube case: it is off-centre by about 1 cm. Therefore the angle measured by the positioning goniometer is different from the actual angle (see Figure 7.17). Let l be the distance between the focal spot and the centre of the cylinder and

d the distance from the focal spot to the detector; the relation between the measured angle ϑ and the effective angle ϑ_{true} is

$$\begin{cases} d\cos\vartheta &= l + l' \\ d\sin\vartheta &= l'\tan\vartheta_{\text{true}} \end{cases} \quad\Rightarrow\quad \tan\vartheta_{\text{true}} = \frac{\sin\vartheta}{\cos\vartheta - l/d}$$

i.e. the correction is of order $l/d \sim 1\%$.

In order to have a well-defined measuring angle and a not-too-high rate, the sodium iodide was shielded by a 1 mm thick lead foil with a slit[1] of about 1 mm × 5 cm. Rates were measured integrating the spectra recorded by the MCA in 60 seconds. The measured distributions are shown in Figure 7.18.

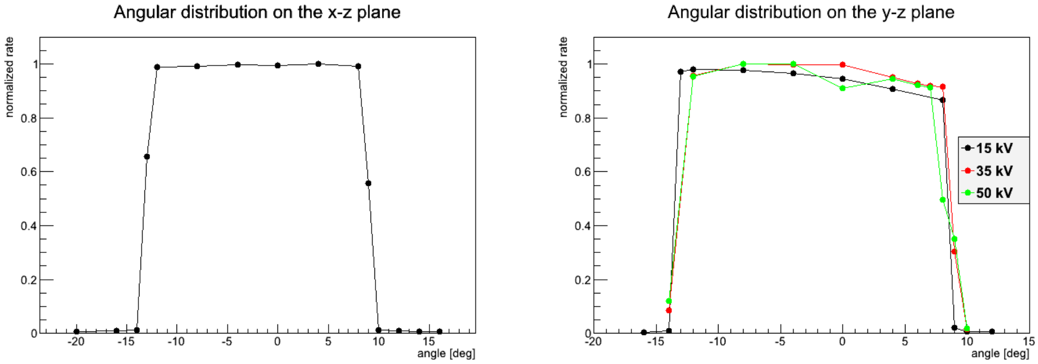

Figure 7.18 Angular distributions of X-rays on the $x - z$ (left) and $y - z$ (right) planes.

The measured angular spread of the X-ray beam is 22° on both $x - z$ and $y - z$ planes. The slight asymmetry of the rates along the $y - z$ plane could be due to the larger probability of forward radiation for decelerating electrons. Such asymmetry should increase at larger electron energy, but such trend cannot be inferred from Figure 7.18.

Summary

In this Chapter we discussed the issues in realising ageing tests for the MEG$^{\text{UP}}$ drift chamber and the experimental apparatus needed for the tests. The geometrical and spectral characteristics of the irradiating sources were studied and their working points were determined, so we are ready for start ageing prototypes in the next Chapter.

---

[1] A slit allows to average over one dimension while scanning the perpendicular one.

Chapter 8

Ageing tests

In this Chapter the realisation of the ageing tests is presented, including the implementation of the corrections that are necessary to determine gain losses. The ageing rate is finally measured and SEM and EDX analyses of aged wires are presented.

8.1 Ageing test on Prototype I

The first ageing test was performed on Prototype I. Wires are made of gold-plated tungsten with a diameter of 25 µm for the anode and 80 µm for cathodes and guard wires. The materials inside the drift chamber are

- FR4 PCBs and PEEK rods
- Mylar windows and Kapton tape
- Teflon cables for connecting the PCBs to the feedthroughs
- solders used for connecting the wires on the PCB holes
- the stainless steel CF-100 cross

which are all clean and good materials (see Chapter 6). Two different X-ray sources, two gas mixtures and several working conditions (high voltage, gas flow rate...) were tested. Field configurations, drift and multiplication properties for the initial working point were described in Chapter 4.

The ageing-test procedure chosen is to monitor the anode wire current through the Keithley sourcemeter. As explained in Chapter 6, two main problems arise in such procedure: environmental condition dependence and space charge effects. The former is cured by monitoring the gas temperature and subtracting from the measured current the temperature-induced variations through equation (3.7). Space charge effects are instead taken into account from the saturation arising in linearity curves.

8.1.1 Temperature corrections

As shown in Section 3.4, temperature and pressure have, to good approximation, equal albeit opposite effect on the multiplication factor. The dependence obtained is

$$\frac{G'}{G} = \left(\frac{\rho'}{\rho}\right)^{-\gamma} = \left(\frac{P'}{P}\right)_T^{-\gamma} = \left(\frac{T'}{T}\right)_P^{\gamma} \tag{8.1}$$

The coefficient γ for temperature corrections was determined by measuring the current variations observed while changing the pressure in the test chamber (see Figure 8.1). The scanned pressure interval is from 982 mbar to 1000 mbar. For simplicity the plotted quantities are $\log(P/P_0)$ and $\log(I/I_0)$, so that γ is the slope of the obtained line.

A linear fit returns a value

$$\gamma = 3.14 \pm 0.03\,.$$

However since γ depends on the physical parameters defining the multiplication factor (such as the electric field near the anode) it can change during the ageing test.

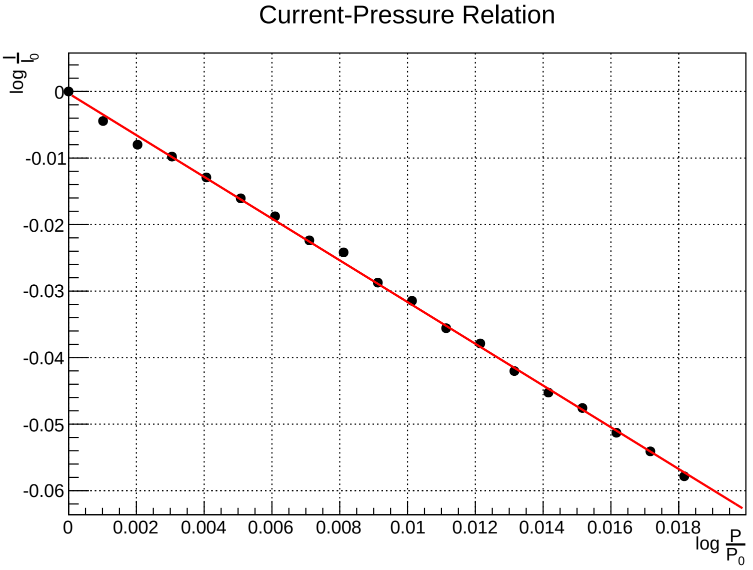

Figure 8.1 Prototype I anode current as a function of the gas pressure.

8.1.2 Part I

The ageing test on Prototype I started using the Moxtek Magnum as irradiating source: the source was placed at 3 cm from the Mylar windows of the CF-100 cross, while for the X-ray beam a 5-mm lead collimator with a thickness of 2 mm was used. The irradiated portion of the cell, at 12 cm from the Mylar window is 2.5 cm. The experimental apparatus is shown in Figure

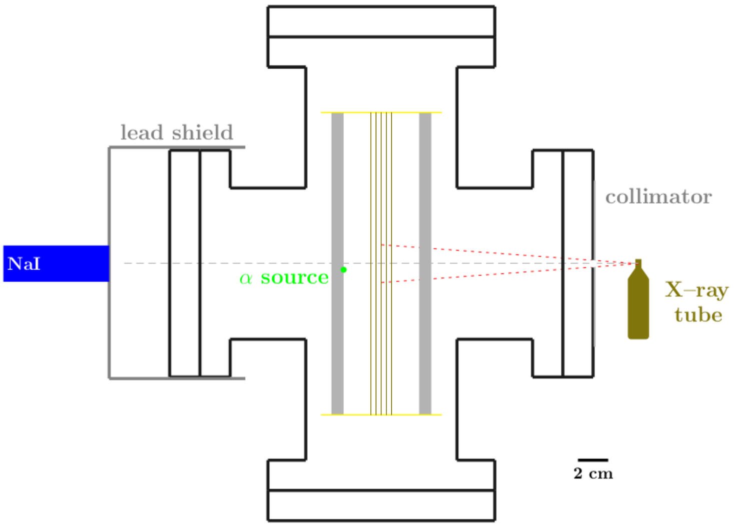

Figure 8.2 Experimental apparatus for the first part of the ageing test on Prototype I.

8.2. The used gas mixture is helium-isobutane 90:10. Assuming for the final detector two gas volume exchanges per day, at an acceleration factor of 20 the gas volume exchange in the CF-100 cross should be of the order of one every half hour. The gas flow rate was set to 40 sccm, which allows a gas volume (3.5 litres) exchange every about 1.5 hours. The X-ray tube high voltage was set to 35 kV, with an electron current of 80 µA. Figure 8.3 shows the wire chamber anode current at different X-ray tube high voltage and current values. Curves are fitted to the function $I_{\mathrm{dc}} = \mathrm{p}_0 I_{\mathrm{xrt}} e^{-\mathrm{p}_1 I_{\mathrm{xrt}}}$ to take space charge effects into account. The returned values are

$$
\begin{aligned}
p_0 &= 4.59 \pm 0.03 \\
p_1 &= (2.1 \pm 0.1) \times 10^{-3}
\end{aligned}
$$

At the set working point, the anode wire current is 124 nA/cm which corresponds to an acceleration factor of ~ 17. The 1” sodium iodide was used as X-ray rate monitor.

Temperature was monitored through a resistive temperature sensor Pt-100, placed on the external side of the CF-100 cross. Temperature data were collected and stored with an OMRON ZR-RX45 data logger.

Figure 8.4 shows the current as a function of the time normalized to that on the 17/11. The pink line is the measured current and fluctuations due to temperature (which is represented, normalised to 26°C, as the green line) are clearly visible. Data corrected from temperature variations according to formula 8.1 are reported in black points. The stability of the X-ray flux is also checked (blue points).

After having collected about 100 mC/cm, that is the equivalent of one data acquisition year, irradiation was stopped and the high voltage was increased in order to recover the original gain

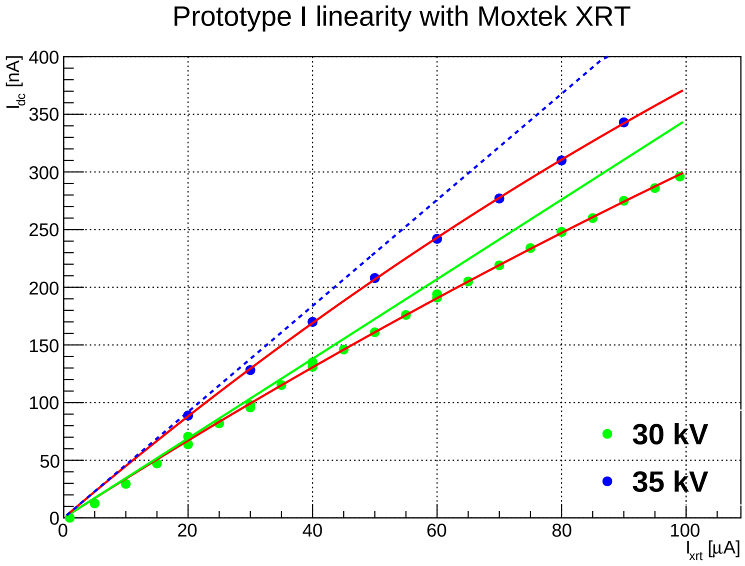

Figure 8.3 Prototype I anode current as a function of the Moxtek Magnum X-ray tube current at two different values of the high voltage.

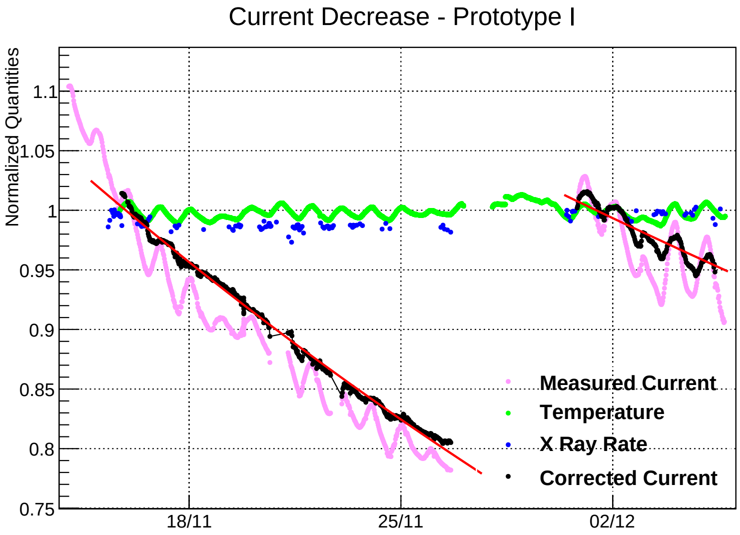

Figure 8.4 Normalised current, temperature and X-ray rate as functions of the irradiating time (part I). The current after the subtraction of the fluctuations due to temperature variations is also shown.

and the original current per unit length. The new high voltage was 1295 V for field wires and 1037 V for guard wires, *i.e.* a ~3% voltage increase was necessary to recover a ~20% gain drop.

8.1.3 Part II

In the second part of the ageing test on Prototype I, some parameters were changed:

- The chamber high voltage was increased to 1720 V
- A new X-ray source was used, the Oxford Apogee.
- As gas mixture, helium-isobutane 85:15 was used.
- The size of the irradiated area was reduced from 2.5 cm to 1.8 cm.
- The gas flow was reduced to 5 sccm.

The X-ray beam was collimated by a 4-mm steel collimator with 1.5 cm of thickness. The X-ray source was placed at 4.1 cm from the Mylar window of the CF-100 cross, thus defining the width of the X-ray spot on the cell volume. The X-ray rate was monitored with the BC404 scintillator, with the same circuitry of the previous measurements (see Section 7.6.1).
Saturation effects in the drift chamber current are visible in Figure 8.5. The fitted parameters are

$$p_0 = 4.6 \pm 0.1$$
$$p_1 = (2.3 \pm 0.1) \times 10^{-3}$$

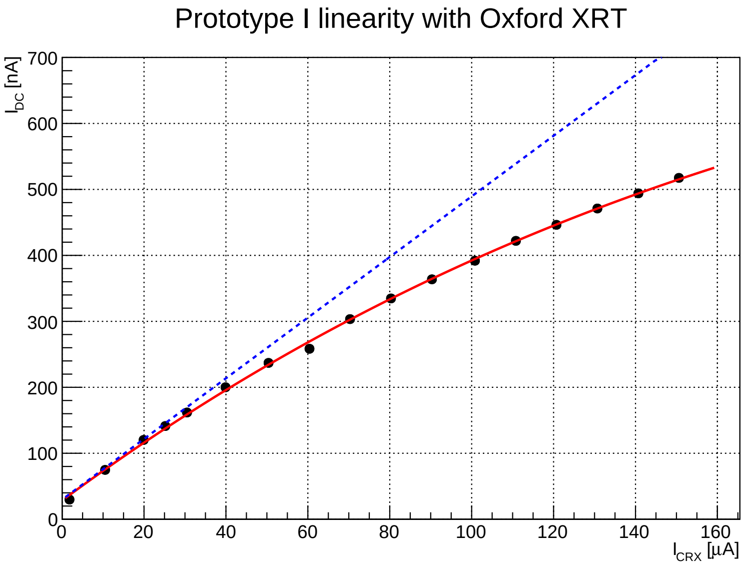

Figure 8.5 Prototype I anode current as a function of the Oxford Apogee X-ray tube current.

The X-ray tube high voltage was set to 10 kV and the electron current was 55 µA, for an initial drift chamber anode current of 175.6 nA/cm corresponding to an acceleration factor ∼18.

Figure 8.6 shows the observed current decrease. When additional 45 mC/cm were collected, the X-ray tube emission current was doubled, yielding a drift chamber anode current of 260 nA/cm (acceleration ∼ 26).

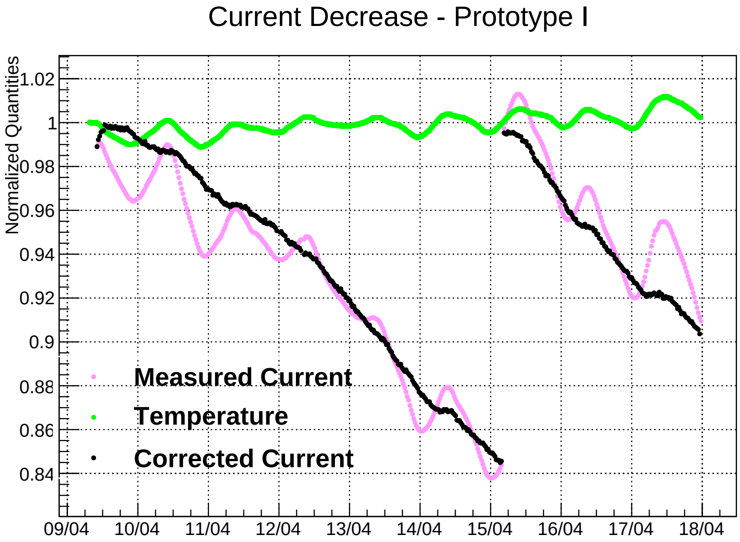

Figure 8.6 Normalised current and temperature as functions of the irradiating time (part II). The current after the subtraction of the fluctuations due to temperature variations is also shown.

8.1.4 Summary

As explained in Chapter 6, the correct parameterisation of the gain loss is in terms of the charge collected by the anode wire, in the form of the parameter (see equation 6.1)

$$\mathcal{R} = -\frac{1}{G_0}\frac{\mathrm{d}G}{\mathrm{d}Q}\left(\frac{\%}{\mathrm{C/cm}}\right)$$

Figure 8.7 shows the plot of the normalised current as a function of the collected charge. The configuration changes are also shown: there is no appreciable modification of the gain loss slope correlated with such changes. Anyway the curve has two different slopes (see Figure 8.8):

- from 0 C/cm to 0.03 C/cm gain loss is very sharp and the fitted current decrease is 1034%/ (C/cm).
- from 0.03 C/cm to 0.32 C/cm the fit returns a current decrease of 98%/ (C/cm).

where Q is the collected charge.

We would like to recall that these tests are done to reproduce the irradiation of the hottest part of the drift chamber, namely a few centimetres on the innermost wire. Already a few

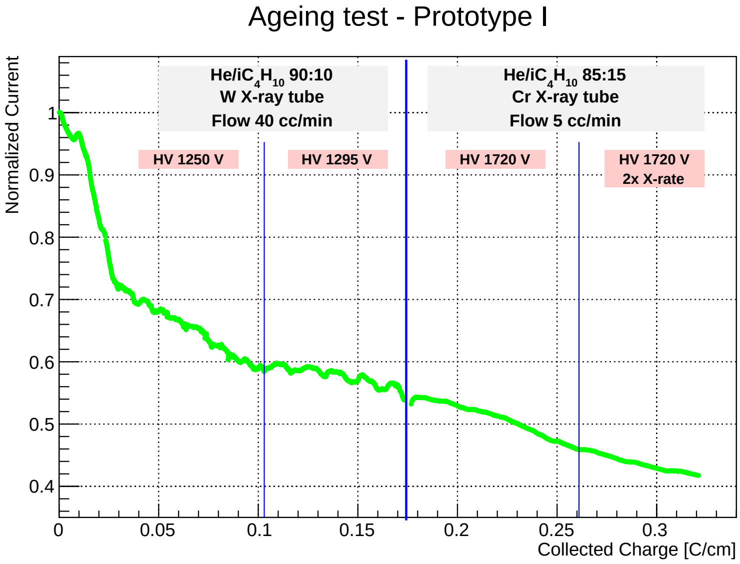

Figure 8.7 Normalised current as a function of the charge per unit length collected by the anode wire. The changes of working conditions are also shown.

centimetres away from this position, the expected total charge is lower by a factor of $3 \div 4$ (see Figure 7.1).

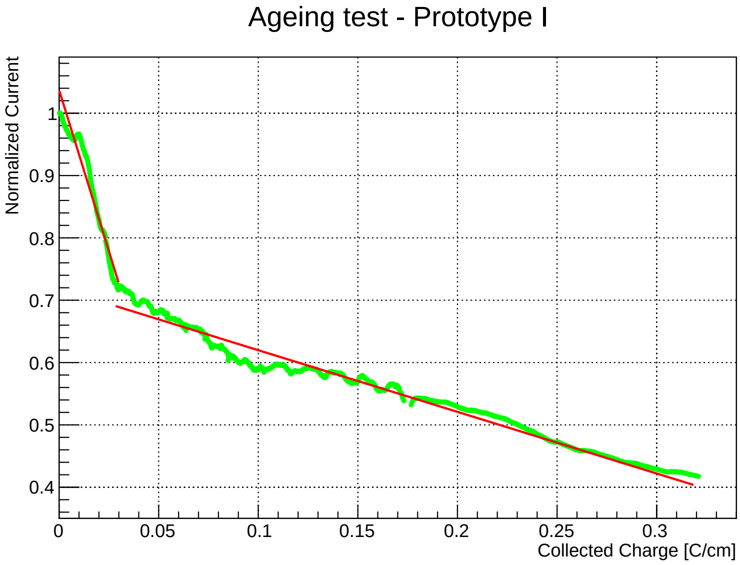

Figure 8.8 Fitting of the normalised *current* as a function of the charge per unit length collected by the anode wire.

For the determination of $\mathcal{R}$ the non-linearity between current and gain must be considered.

Using formula (6.3), one can measure the decrease of the non-saturated current, *i.e.* of gain. Taking into account temperature correlation, since it is the gain that depends on the temperature as T^γ, we first correct by the factor e^{KI}, thus obtaining a linear function of the multiplication factor, and then apply temperature corrections. The obtained gain-charge curve is shown in Figure 8.9: this is mandatory not to underestimate the ageing rate. Therefore the ageing rate measured with Prototype I is

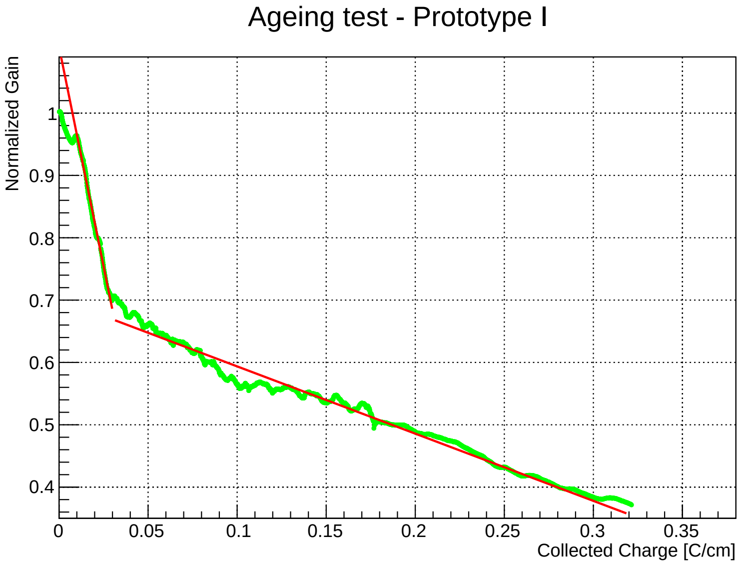

Figure 8.9 Fit of the normalised *gain* as a function of the charge per unit length collected by the anode wire.

$$\mathcal{R} = \begin{cases} 1408\,\%/\,(\mathrm{C/cm}) & \text{if } \quad Q < 0.03\,\mathrm{C/cm} \\ 108\,\%/\,(\mathrm{C/cm}) & \text{if } 0.03 < Q < 0.320\,\mathrm{C/cm} \end{cases}$$

It is important to notice that no appreciable change of the operating conditions was done in correspondence of the big slope change. Sudden changes of the gain loss rate have been already observed in literature [40]. A possible explanation can be that gain loss rate is large while deposits are gradually growing around the anode, since both the electric field and the conductivity of the anode surface are decreasing; when all the anode surface is covered, the accreting of the layer produces a relatively lower gain loss.

To complete the ageing measurements, additional 169 mC/cm were collected by the prototype at high current density (∼ 1 µA/cm). After that the presence of discharges or dark currents was checked, but the operation of the chamber was normal. The total charge collected by the anode was therefore about 500 mC/cm on a length of 18 mm (all the ageing test), and about 180 mC/cm on a length of 25 mm.

8.2 Ageing test on Prototype II

A second ageing test was performed in order to check the resistance to radiation hardness of 80 µm silver-plated aluminum wires (used as cathodes) and of 20 µm gold-plated tungsten wires, used as anodes. As explained in Chapter 6, aluminum cathodes are very sensitive to ageing, therefore any imperfection on the silver plating can result in Malter effect. If the ageing test on Prototype I showed moderate gain loss for 25 µm gold-plated anode wires, it is not straightforward to deduce the resistance to radiation of 20 µm wires: at fixed deposition rate, an anode surface smaller of 20 % should undergo a higher relative gain loss. Therefore a second single-cell prototype (Prototype II) was assembled (see Figure 8.10). The experimental setup of this ageing test was the same that was used for Prototype I.

Figure 8.10 Picture of Prototype II in INFN Pisa clean room.

The operating parameters and the materials used in the ageing tests of Prototype I and Prototype II are listed in Table 8.1.

The ageing test procedure was the same of Prototype I, *i.e.* measurement of the anode current decrease. However in order to gain an additional evaluation of gain loss, two collimated americium α-sources were placed inside the prototype (visible in Figure 8.10), one (which we will call Source 1) pointing to the irradiated area and one (Source 2) to a portion of the cell that

	Prototype I	Prototype II
Cell parameters:		
Anode	25 µm W (Au)	20 µm W (Au)
Cathodes	80 µm W (Au)	80 µm Al (Ag)
Gas mixture	90:10 - 85:15	85:15
Gas flow rate	40 sccm - 5 sccm	15 sccm
Cell gain	$\sim 1 \times 10^4$	$\sim 3 \times 10^4$
Irradiation spot	2.5 cm - 1.8 cm	3 cm
Accelerating factor	×17 - ×26	×10 - ×20
Materials:		
Rods	PEEK	aluminum
α source	–	Teflon and Kapton as collimators

Table 8.1 Comparison between the operating parameters in the ageing tests of Prototype I and Prototype II.

will not be aged. In order to identify from the beginning the two peaks in the charge spectra, α-particles from Source 1 impinge almost perpendicularly on the cell, while those from Source 2 have a large pitch angle: in this way the number of ionisation clusters inside the cell is different in the two cases (see Chapter 4) and the charge distributions of the two signals can be distinguished from the beginning. The sources were placed on the heads of two screws tightened to one of the aluminum rods by two cable ties; they were collimated by a 1 mm thick Teflon tube covered by Kapton tape so that a few millimetres of the cell are illuminated by Source 1 and a few centimetres by Source 2. The evaluation of gain loss through α-particles will thus be obtained as a decrease in the value of the ratio between the mean charge collected from α-particles from Source 1 (in the portion of the anode wire that experiences ageing) and the mean charge collected from α-particles from Source 2. In this way the contribution of temperature variations on the gain are canceled. However the very high cluster density in tracks from α-particles implies strong space charge effects, that in this case cannot be easily estimated. The ratio of the charges of the two peaks should therefore decrease more slowly than the gain at increasing collected charge. Nevertheless the ratio can be used to independently monitor gain loss, at least qualitatively if not quantitatively.

The determination of the working points of the chamber was performed as for Prototype I through Garfield++ simulations. The high voltage of the field (guard wires) was set to 1425 V (1220 V), yielding a gain of about 3×10^4. The avalanche size distribution obtained with Garfield++ is shown in Figure 8.11

On Prototype II gas temperature was monitored through a Pt-100 sensor, placed inside the gas volume instead of outside the CF-100 cross (as for Prototype I): in this way temperature measurements are not affected by any thermal conduction issues. As for Prototype I, before

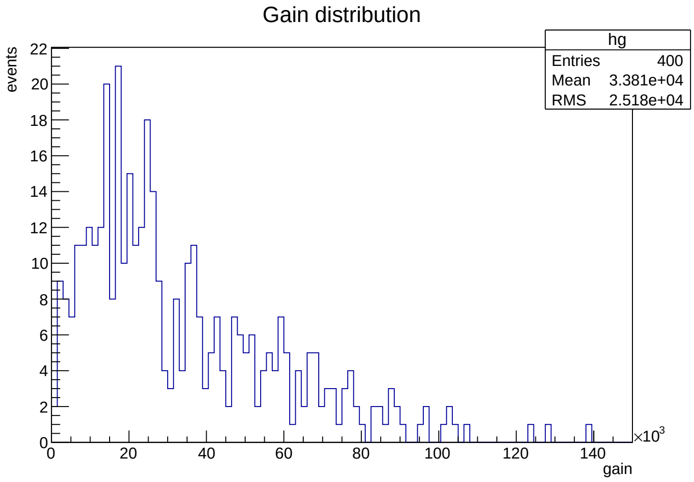

Figure 8.11 Avalanche size distribution of Prototype II simulated with Garfield++.

starting the ageing test the dependence of the current on pressure variations was studied: the curve is shown in Figure 8.12 (*cfr.* Figure 8.1). The measured value for the γ coefficient is slightly larger than that measured for Prototype I

$$\gamma = 3.27 \pm 0.02\,.$$

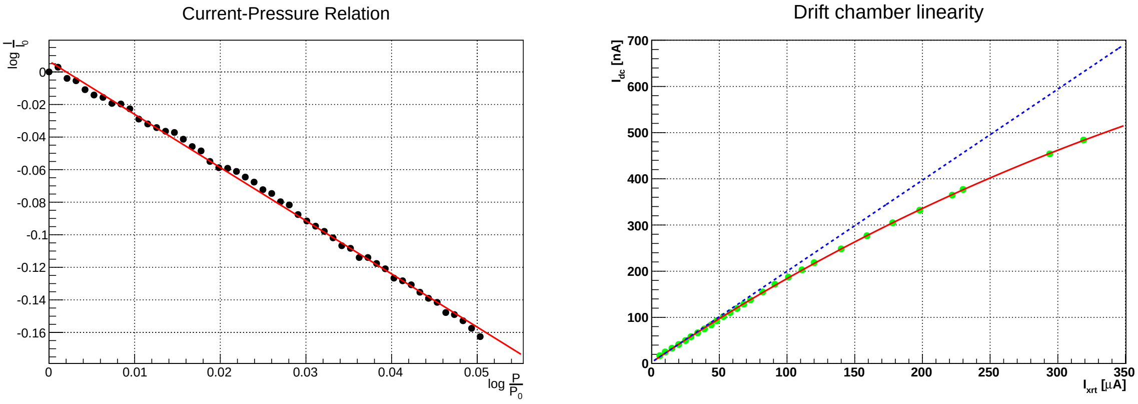

Figure 8.12 Prototype II anode current as a function of the gas pressure and as a function of the Oxford Apogee X-ray tube current.

Space-charge effects were evaluated as for Prototype I by a linearity curve, which is well described by the function $I_{\rm dc} = {\rm p}_0 I_{\rm xrt} e^{-{\rm p}_1 I_{\rm xrt}}$. The curve is shown in Figure 8.12(right). The values returned for the parameters are

$$\begin{aligned} p_0 &= 1.97 \pm 0.01 \\ p_1 &= (8.4 \pm 0.2) \times 10^{-4} \end{aligned} \tag{8.2}$$

The size of the area irradiated by X-rays is 3 cm, set by a 5.5 mm steel collimator. The X-ray tube high voltage was intially set to 10 kV at a current of 55 µA yielding an anodic current of about 300 nA, corresponding to a current per unit length of 100 nA/cm (accelerating factor ~ 10). The working point was then then raised to 12 kV at about 240 µA corresponding to an anodic current of about 600 nA (200 nA/cm), so an accelerating factor ~ 20.

The first check on the chamber operation was the measurement of charge spectrum of signals induced by α-particles. The spectrum was obtained by acquiring the waveforms of α-particle signals with the DRS4. Figure 8.13 shows an acquired spectrum: the two peaks are visible, with a continuous component of the spectrum among them due to slanted tracks from Source 2 that do not cross the whole length of the cell. The spectrum is well described by a sum of three Gaussian functions. The peak due to α-particles from Source 1 is smaller by a factor ~ 5. Care was taken in not to cut the lower peak with the threshold.

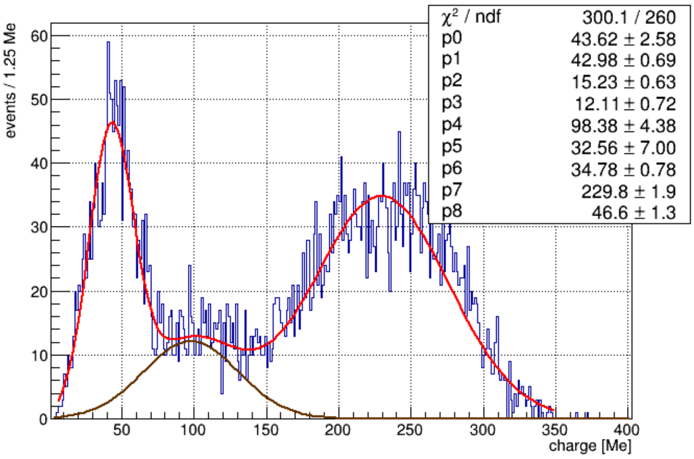

Figure 8.13 Charge spectrum of signals from α-particles.

8.2.1 Results

Figure 8.14 shows the current decrease as a function of the collected charge. The ratio of the α-particles peaks is also shown, and decreses as well, even though as expected its slope is smaller than that of the current decrease.

In order to determine the factor $\mathcal{R}$, space charge corrections were computed, as for Prototype I, from the values in formula (8.2). The result is shown in Figure 8.15: the slope is almost

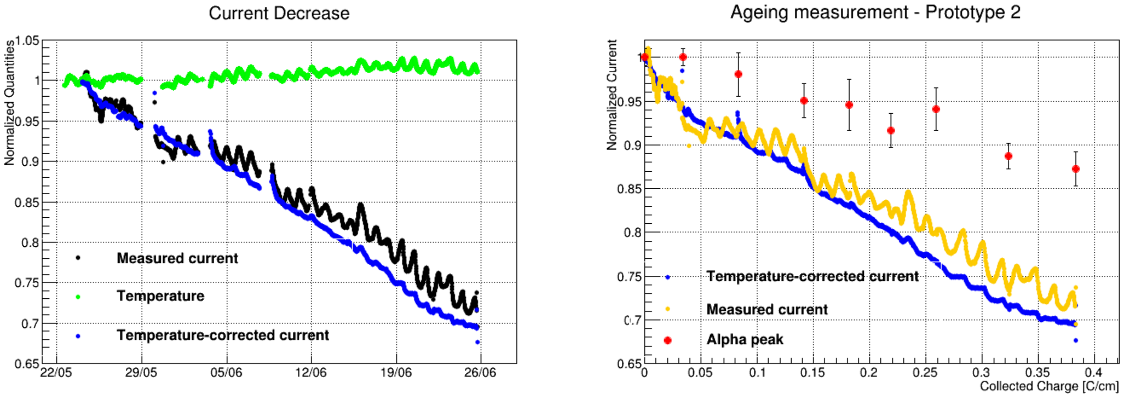

Figure 8.14 Normalized current as a function of time (left) and as a function of the charge per unit length collected by the anode wire (right). The variation of the ratio between the peaks of α-particles is also shown.

constant and the value returned by the fit is

$$\mathcal{R} = 90.9 \pm 0.3\%/(\mathrm{C/cm})$$

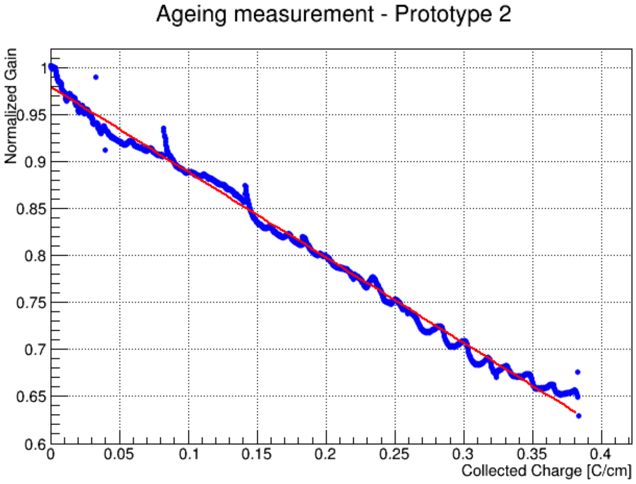

Figure 8.15 Fit of the normalized gain as a function of the collected charge.

This result is a little more promising than that obtained from the ageing test on Prototype I: the largest difference in gain loss is the abrupt descrease in the first part of the ageing test on Prototype I, absent with Prototype II. The value of $\mathcal{R}$ obtained with Prototype II is consistent with that obtained in the second part of the ageing test on Prototype I, within 20%. In both cases there are indications that gain loss should not be a limiting factor for the new tracker for MEG$^{\mathrm{UP}}$. Other tests are on plan to verify the compatibility of all the materials that should be included in the final drift-chamber.

8.3 Microanalysis of wires from Prototype I

We analyzed aged wires of Prototype I at the Scanning Electron Microscope (SEM) facility of the Università del Salento, Lecce. SEM analysis consists in scanning the samples with an electron beam and detecting secondary electrons in the material, thus allowing sample reconstruction. For SEM analysis, samples must be fixed on a disk with diameter 5 cm through small adhesive carbon pads (see Figure 8.16). Three wires were analyzed: two edge cathodes and the sense wire.

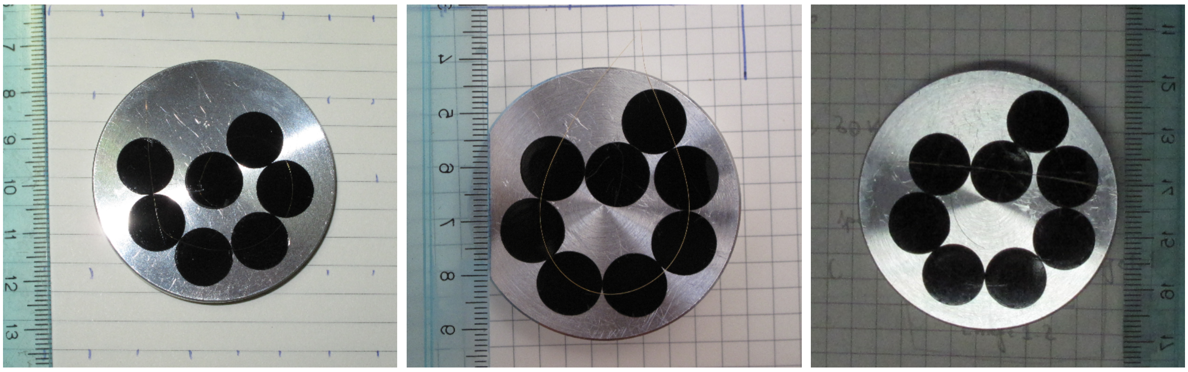

Figure 8.16 Samples for SEM analysis of three wires: from left to right the anode, Cathode I and Cathode II.

From one of the cathodes (the first in Figure 8.16, Cathode I) and from the anode wire, centered portions of about 12 cm were selected[1]. The sample from the other cathode (Cathode II) was about 4 cm long, and care was taken in putting the side looking at the sense wire on the top, in order to be sure that any non-uniformity detected on the wire was due to ageing instead of being due to a twist of the wire.

We also performed Energy Dispersive X-ray (EDX) microscopy on the wires: this consists in detecting the characteristic X-radiation coming out from the sample due to the excitation of atoms induced by the electron beam. Spectra are analogous to those of an X-ray tube, but have multiple lines of characteristic radiation from the components of the sample. The data acquisition software provides a semi-quantitative analysis of the concentrations of the chemical elements in the sample. On the resulting spectra, the continuous component of the X-radiation is subtracted. The electron beam energy determines the penetration depth, thus the portion of wire probed. In Table 8.2 the ranges of electrons at several energies in gold and polyethylene are reported. Polyethylene is reported as an example for organic-polymer compounds, like the deposits that may be found on wire surfaces.

---

[1] We recall that the total charge collected by the anode was about 500 mC/cm on a length of 18 mm and about 180 mC/cm on a length of 25 mm.

	$E_e = 5$ keV	$E_e = 10$ keV	$E_e = 20$ keV
Gold	0.2 µm	0.4 µm	1 µm
Polyethylene	1.3 µm	2.5 µm	8.4 µm

Table 8.2 Electron range in gold and polyethylene (taken as a term of comparison for organic-polymer compounds) as a function of energy. Data taken from [43].

8.3.1 Cathode I

SEM images on Cathode I present no visible deposits induced by ageing. Pictures in Figure 8.18, 8.19, 8.20 were taken at six different locations on the wire (shown in Figure 8.17). The images captured at magnification 7500× show the wrinkles of gold plating, while in those at magnification 750× the wire surface appears smooth with isolated dust (see Figure 8.20)

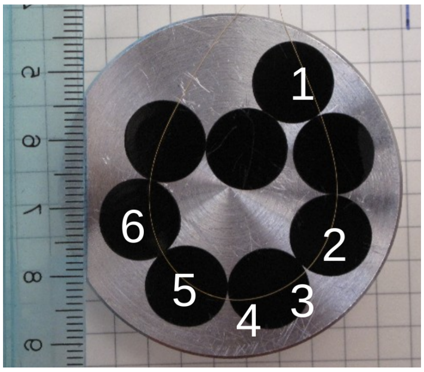

Figure 8.17 Cathode I sample: numbers represent the analyzed areas.

EDX microscopy on the six points showed the presence of carbon, gold and tungsten (see Figure 8.24). Carbon concentration is of the order of the percent (in weight), which gradually increases approaching to the centre of the wire. Since no other elements are observed (except gold and tungsten), carbon may come from human contamination, contamination from the graphite disks or actual presence of deposits. However the correlation between carbon concentration and position supports the last option.

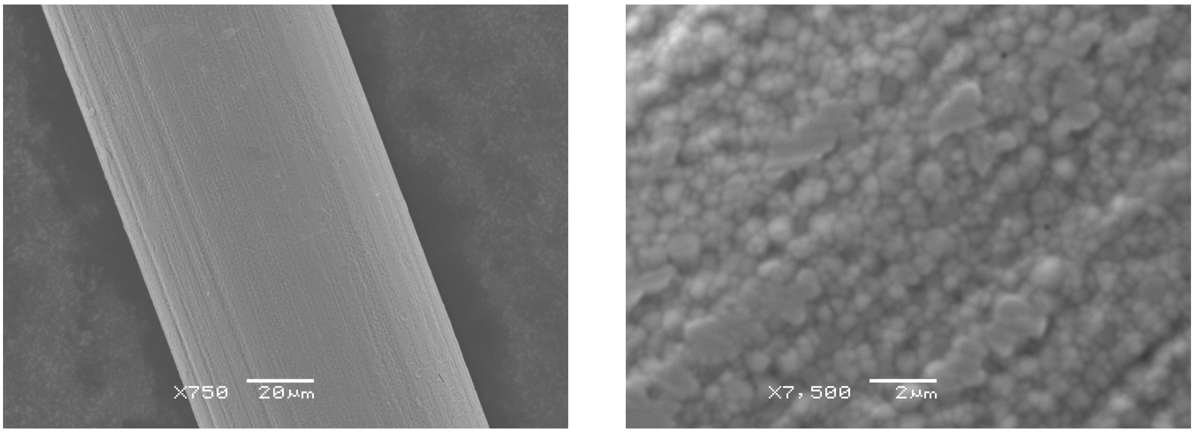

Figure 8.18 SEM images taken at point 1 of Cathode I (see Figure 8.17).

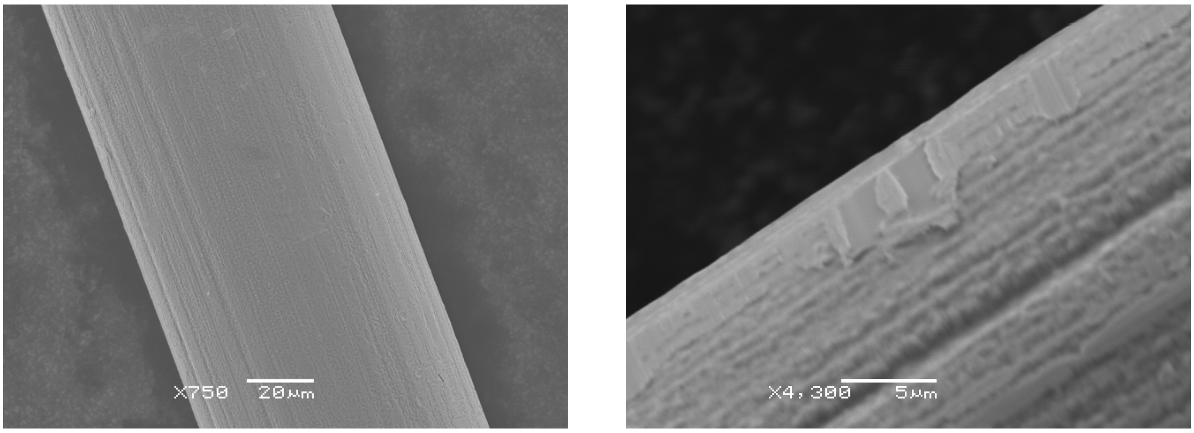

Figure 8.19 SEM images taken at point 3 of Cathode I (see Figure 8.17).

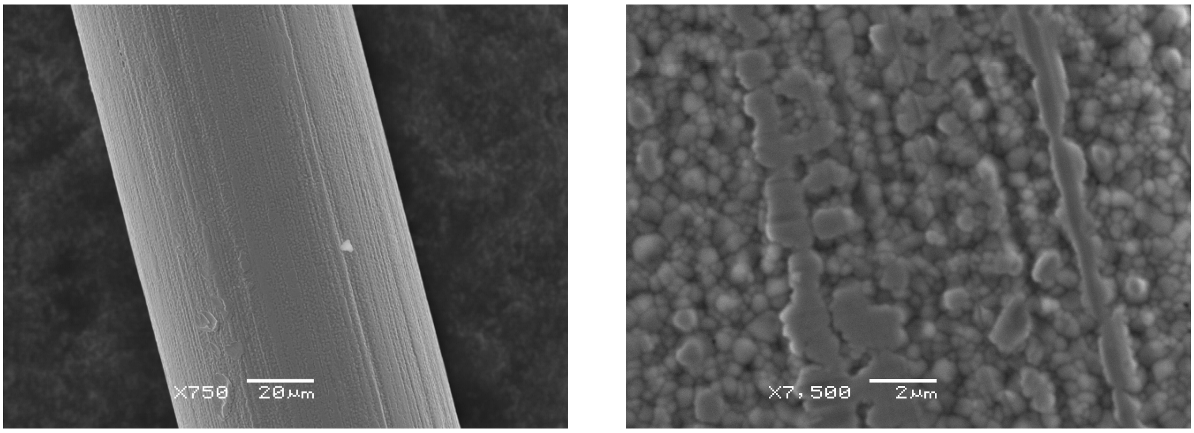

Figure 8.20 SEM images taken at point 6 of Cathode I (see Figure 8.17).

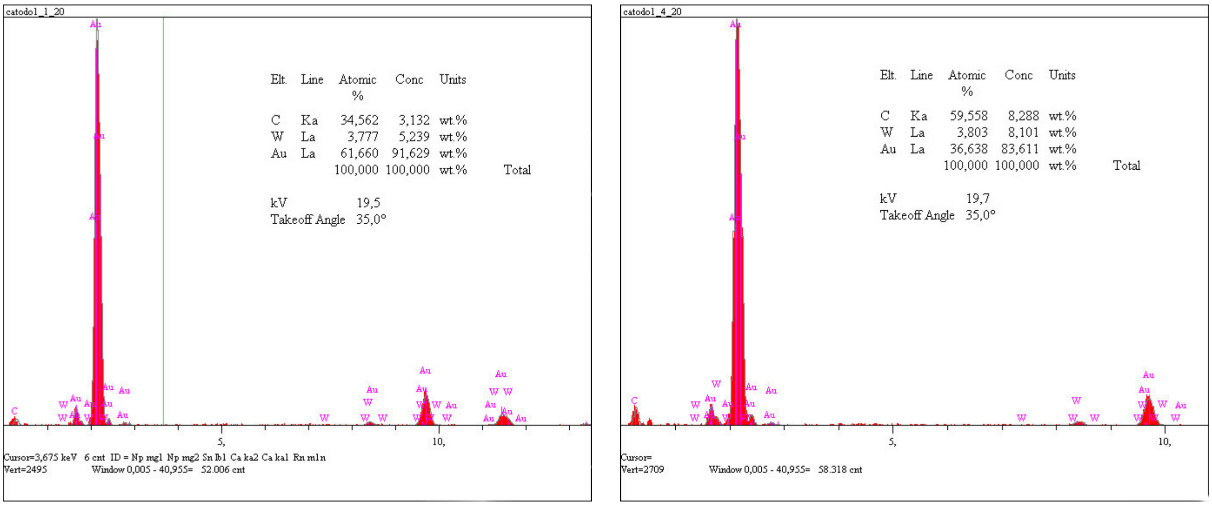

Elt.	Line	Atomic %	Conc	Units	
C	Ka	34,562	3,132	wt.%	
W	La	3,777	5,239	wt.%	
Au	La	61,660	91,629	wt.%	
		100,000	100,000	wt.%	Total

kV 19,5
Takeoff Angle 35,0°

Elt.	Line	Atomic %	Conc	Units	
C	Ka	59,558	8,288	wt.%	
W	La	3,803	8,101	wt.%	
Au	La	36,638	83,611	wt.%	
		100,000	100,000	wt.%	Total

kV 19,7
Takeoff Angle 35,0°

Figure 8.21 EDX analyses with 20 keV electrons at points 1 and 4 of Cathode I.

8.3.2 Cathode II

The analyzed areas of Cathode II are shown in Figure 8.22. Since the wire is placed straight on the carbon pads, distance measurements can be performed with sufficient accuracy.

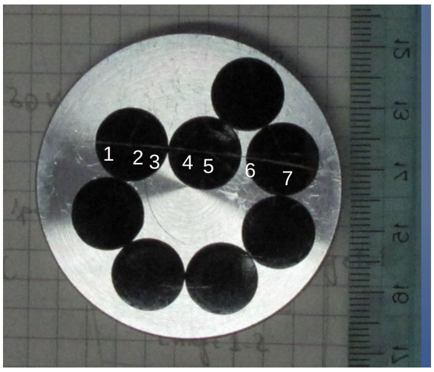

Figure 8.22 Cathode II sample: numbers represent the analyzed areas.

On Cathode II the surface appears clear too, as shown in Figure 8.23. A rough diameter measurement can be performed, giving a value of 79.6 µm.

For Cathode II, EDX analyses show the presence of carbon, nitrogen, oxygen and silicon, in addition to gold. Spectra were taken with a 5 keV electron beam, so electrons do not penetrate enough to excite tungsten. Actually this sets a lower limit on the gold-plating thickness of about 0.2 µm. X-ray spectra present more lines than those of Cathode I, and there are visible differences between the central part of the wire and the borders (about 2 cm from the centre).

The element composition of the wire at the seven points analyzed is reported in Figure 8.25. Among the impurities carbon is the most abundant and it is almost proportional to the oxygen

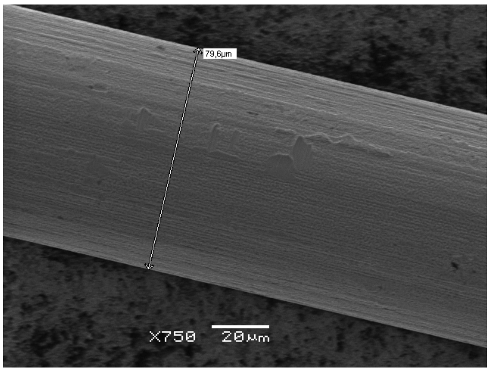

Figure 8.23 SEM image with estimate of Cathode II diameter at point 4.

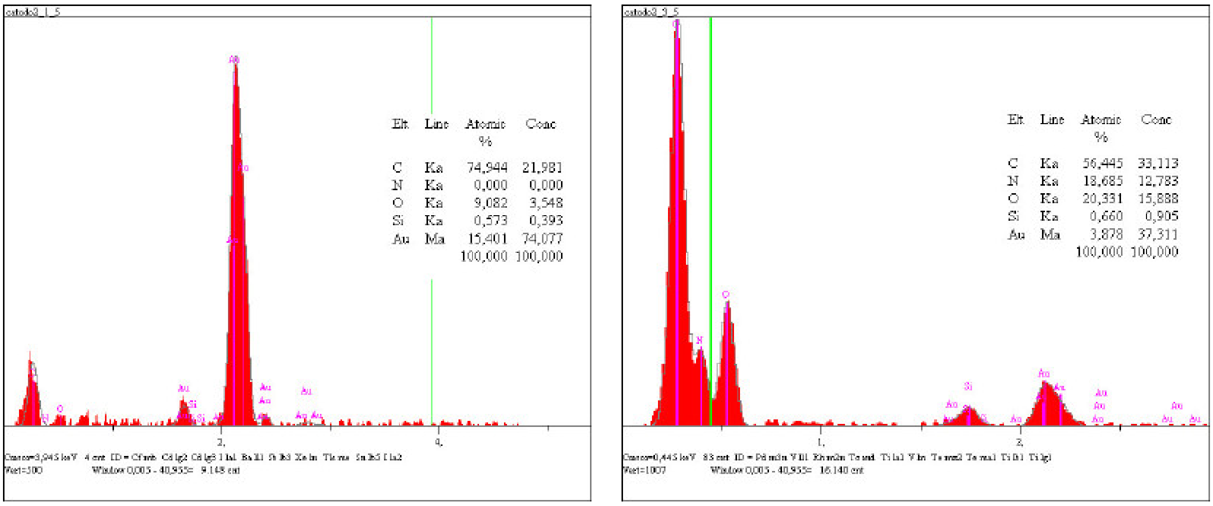

Elt	Line	Atomic %	Conc
C	Ka	74,944	21,981
N	Ka	0,000	0,000
O	Ka	9,082	3,548
Si	Ka	0,573	0,393
Au	Ma	15,401	74,077
		100,000	100,000

Elt	Line	Atomic %	Conc
C	Ka	56,445	33,113
N	Ka	18,685	12,783
O	Ka	20,331	15,888
Si	Ka	0,660	0,905
Au	Ma	3,878	37,311
		100,000	100,000

Figure 8.24 EDX analyses with 5 keV electrons at point 1 (left) and point 2 (right) of Cathode II.

concentration with a factor of about 2. This can be thought as the formation of carbon-oxygen polymer surface coating the wire. Silicon is present too, even if in minimal quantities ($\lesssim 3\%$). If oxygen and nitrogen may come from air residuals in the drift chamber or be the effect of the porosity of ealier deposits after the extraction of the prototype from the CF-100 cross, the only sources of silicon in the drift chamber are the two PCBs, which are made of glass fiber and epoxy compound.

8.3.3 Anode

The most interesting wire for microanalysis is clearly the anode wire. Because of the disposition of the wire on the carbon pads, it is not easy to quantify the distance between the analyzed points; anyway a rough estimate is given.

At about 4 cm from the centre the wire surfaces appear clear, as shown in Figure 8.26.

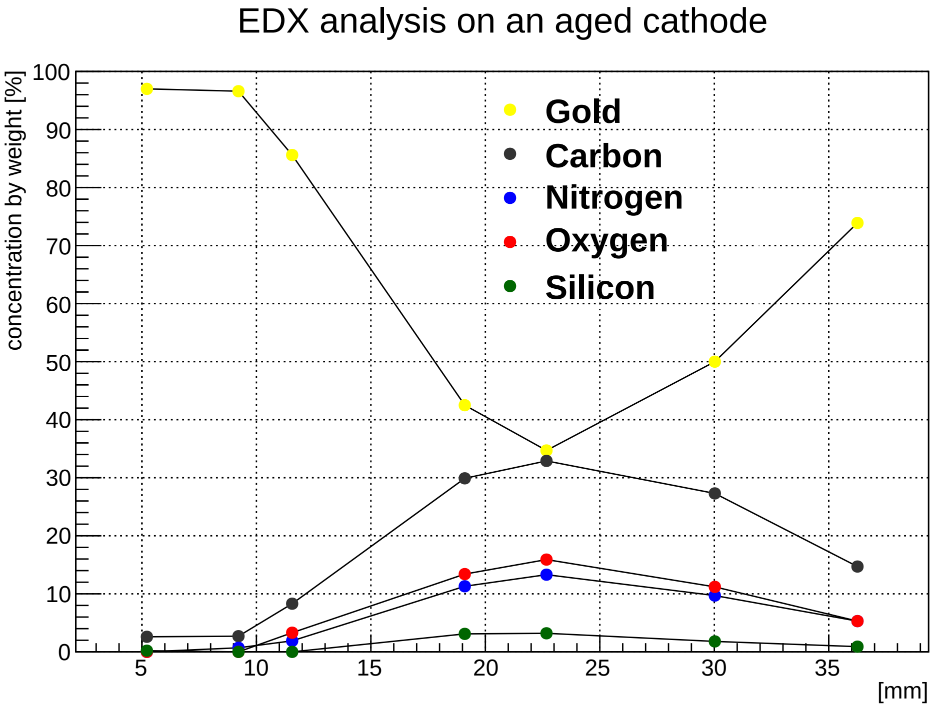

Figure 8.25 Concentrations of the detected elements as a function of the position on Cathode II. The origin of the abscissa is arbitrary.

However EDX analysis shows that there is a layer with a thickness of the order of about 1 μm ($E_e = 5$ keV) made of carbon, nitrogen and oxygen. A few percents of silicon are also detected.

At about 2 cm from the centre there is a clear presence of deposits (Figure 8.27). The layer thickness can be estimated to be of the order of 1 μm. EDX analyses were performed at several electron energies in order to have an idea of the depth of different elements. Figure 8.28 shows the spectra taken at 5 keV, 10 keV and 20 keV. Sulfur is found on the outer part of the coating, since it is visible at 5 keV but it is not at higher energies. Carbon and nitrogen are more abundant in the outer layer, while oxygen concentration decreases more slowly.

At about 1.5 cm from the centre the coating covers the anode wire almost uniformly (see Figure 8.29), with some ruptures which may be due to the handling of the wire or to the sudden loss of tension when the wire was cut during sample preparation. It is noteworthy that in the area without coating the wire appears definetely clear.

In the proximity of the centre, in an area extending for about 2 cm new kinds of deposits are visible, as in Figure 8.30: bubbles placed on the coating, with typical dimensions ranging from 1 to 10 μm, and whiskers emerging from isolated spots, which appear to be without uniform coating.

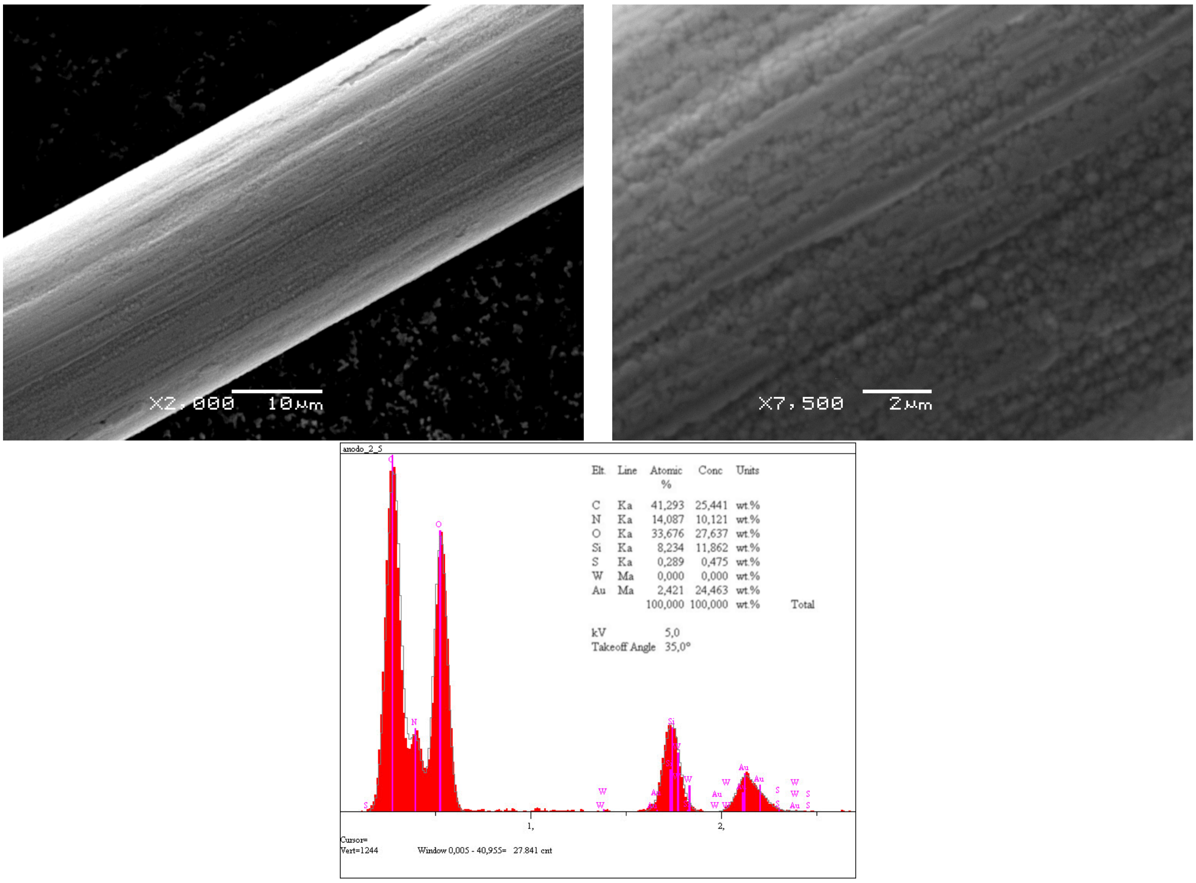

Elt.	Line	Atomic %	Conc	Units	
C	Ka	41,293	25,441	wt.%	
N	Ka	14,087	10,121	wt.%	
O	Ka	33,676	27,637	wt.%	
Si	Ka	8,234	11,862	wt.%	
S	Ka	0,289	0,475	wt.%	
W	Ma	0,000	0,000	wt.%	
Au	Ma	2,421	24,463	wt.%	
		100,000	100,000	wt.%	Total

kV 5,0
Takeoff Angle 35,0°

Cursor=
Vert=1244 Window 0,005 - 40,955= 27.841 cnt

Figure 8.26 SEM images and EDX spectrum at about 4 cm from of the anode centre.

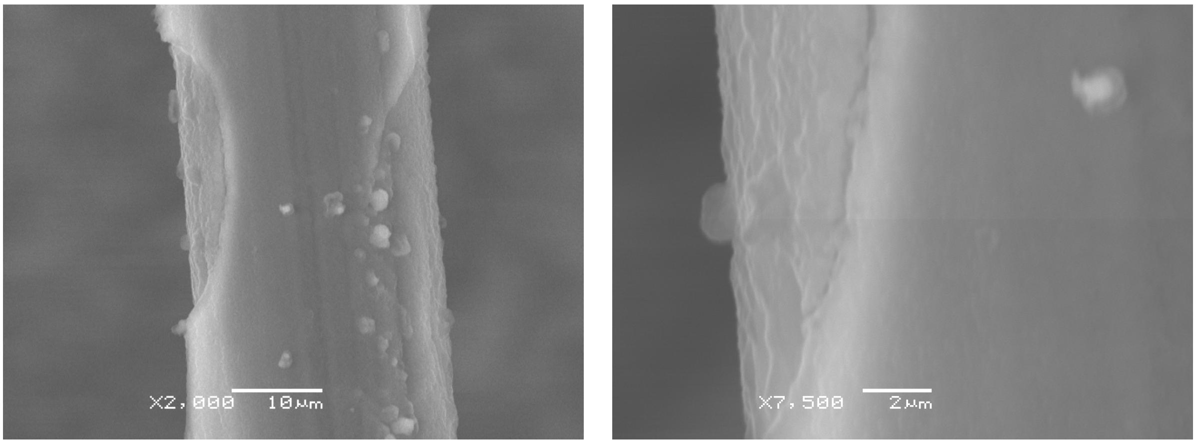

Figure 8.27 SEM images at about 2 cm from of the anode centre.

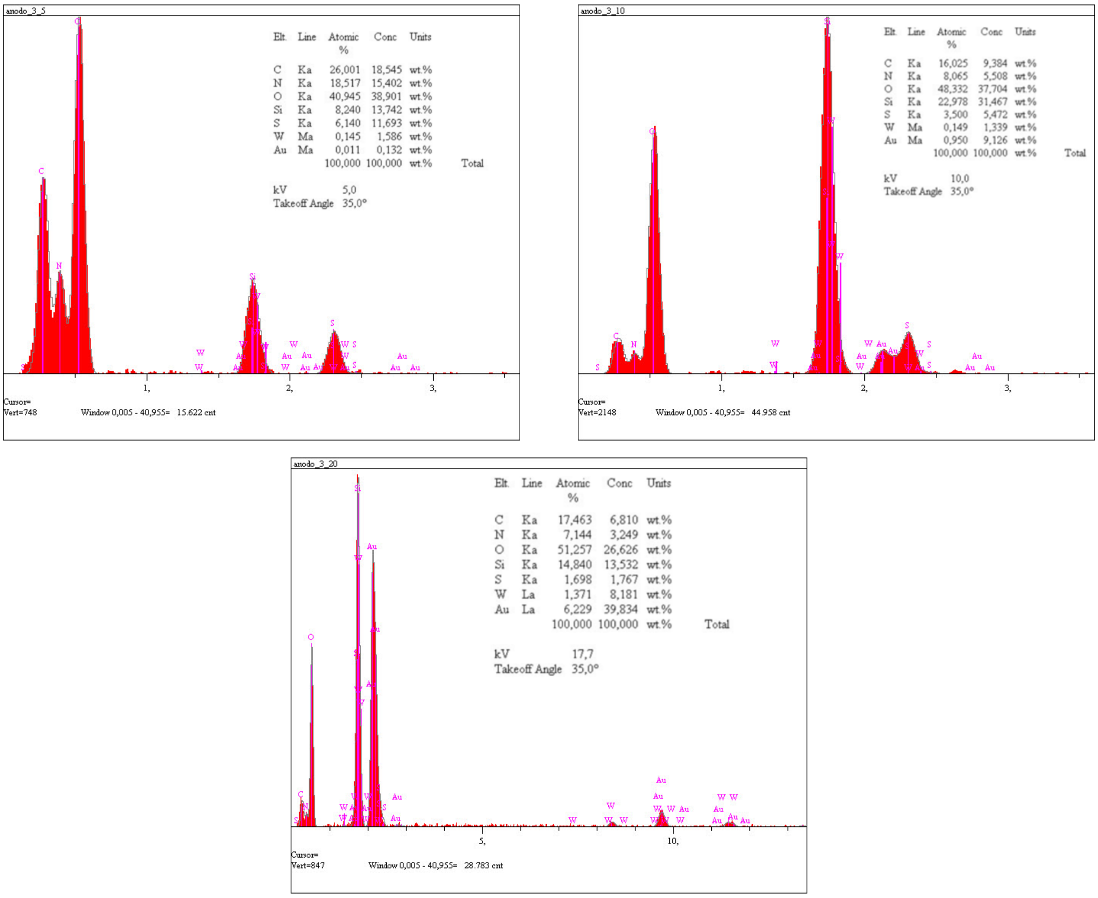

Elt.	Line	Atomic %	Conc	Units	
C	Ka	26,001	18,545	wt.%	
N	Ka	18,517	15,402	wt.%	
O	Ka	40,945	38,901	wt.%	
Si	Ka	8,240	13,742	wt.%	
S	Ka	6,140	11,693	wt.%	
W	Ma	0,145	1,586	wt.%	
Au	Ma	0,011	0,132	wt.%	
		100,000	100,000	wt.%	Total

kV 5,0
Takeoff Angle 35,0°

Elt.	Line	Atomic %	Conc	Units	
C	Ka	16,025	9,384	wt.%	
N	Ka	8,065	5,508	wt.%	
O	Ka	48,332	37,704	wt.%	
Si	Ka	22,978	31,467	wt.%	
S	Ka	3,500	5,472	wt.%	
W	Ma	0,149	1,339	wt.%	
Au	Ma	0,950	9,126	wt.%	
		100,000	100,000	wt.%	Total

kV 10,0
Takeoff Angle 35,0°

Elt.	Line	Atomic %	Conc	Units	
C	Ka	17,463	6,810	wt.%	
N	Ka	7,144	3,249	wt.%	
O	Ka	51,257	26,626	wt.%	
Si	Ka	14,840	13,532	wt.%	
S	Ka	1,698	1,767	wt.%	
W	La	1,371	8,181	wt.%	
Au	La	6,229	39,834	wt.%	
		100,000	100,000	wt.%	Total

kV 17,7
Takeoff Angle 35,0°

Figure 8.28 EDX spectra taken at different electron energies at about 2 cm from the anode centre.

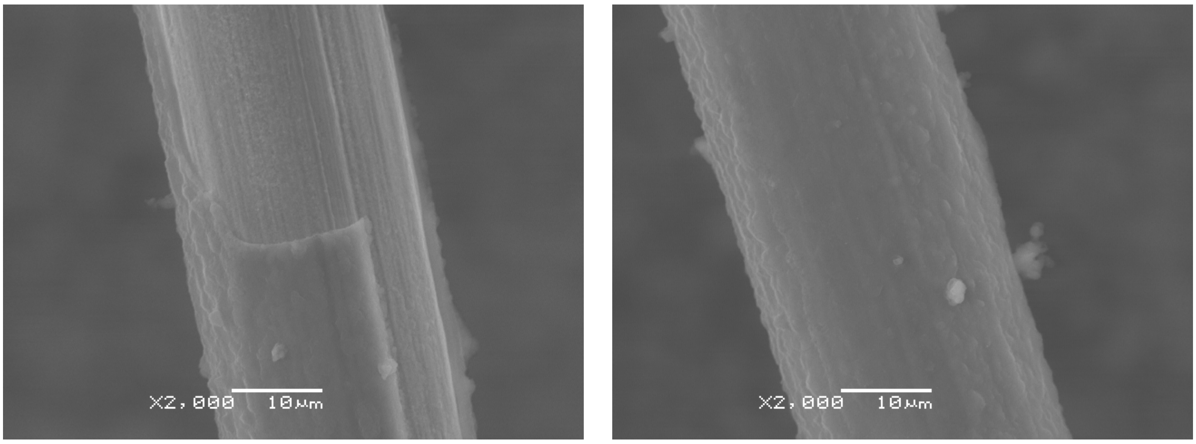

Figure 8.29 SEM images at about 1.5 cm from of the anode centre.

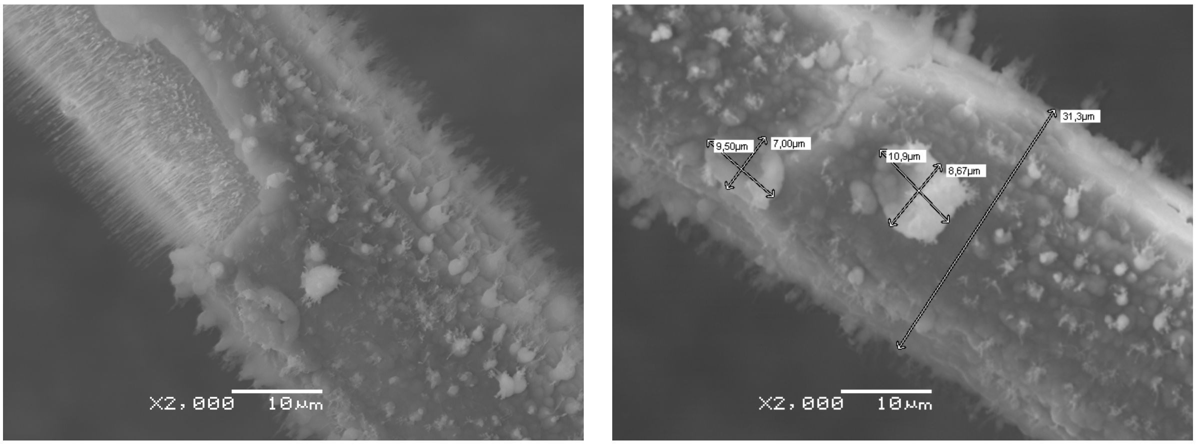

Figure 8.30 SEM images within 1 cm from the anode centre.

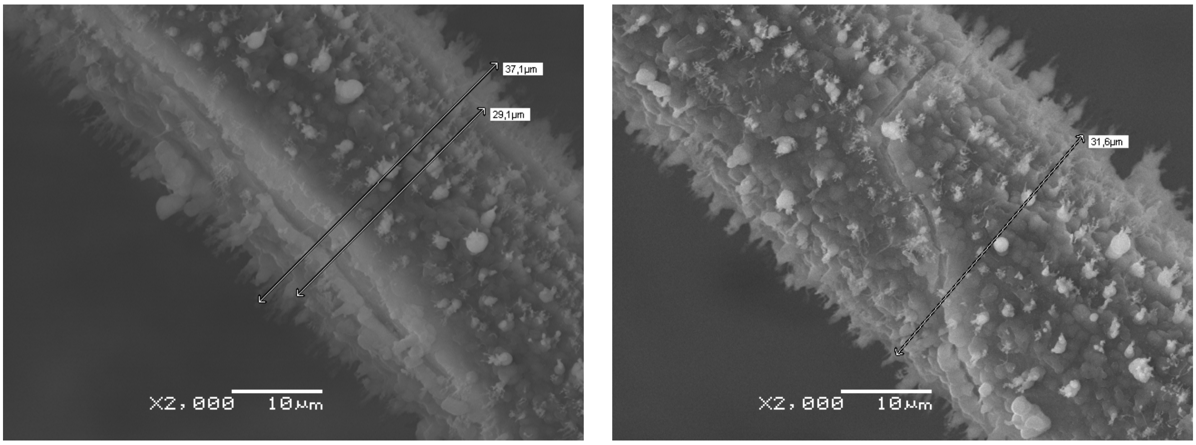

Figure 8.31 SEM images with estimates of the wire diameter within 1 cm from the anode centre.

Estimates of the overall diameter of the wire are provided in Figure 8.31: the diameter of the coating of the wire is about 29 µm, while the "peak to peak" diameter including the whiskers length reaches 37 µm (recall the wire diameter was 25 µm).

Punctual microanalysis was performed on such kinds of deposits. Whiskers, in Figure 8.32, extend for about 5 µm and the guess that they lie on the "naked" wire is confirmed from the presence of gold $\sim 10\%$ and the absence of nitrogen, assuming nitrogen as been absorbed by the coating. The silicon component can be interpreted as silicon and silicate polymers[1], or as a thin coating on the "naked" wire that in the other areas underlies the porous coating. Sulfur peak is also visible.

Figure 8.33 shows a particularly large bubble and its punctual microanalysis. The X-ray spectrum shows a decrease of the carbon concentration, corresponding to an increase in silicon

---

[1] Silicate components may also be prompted by the huge quantity of oxygen.

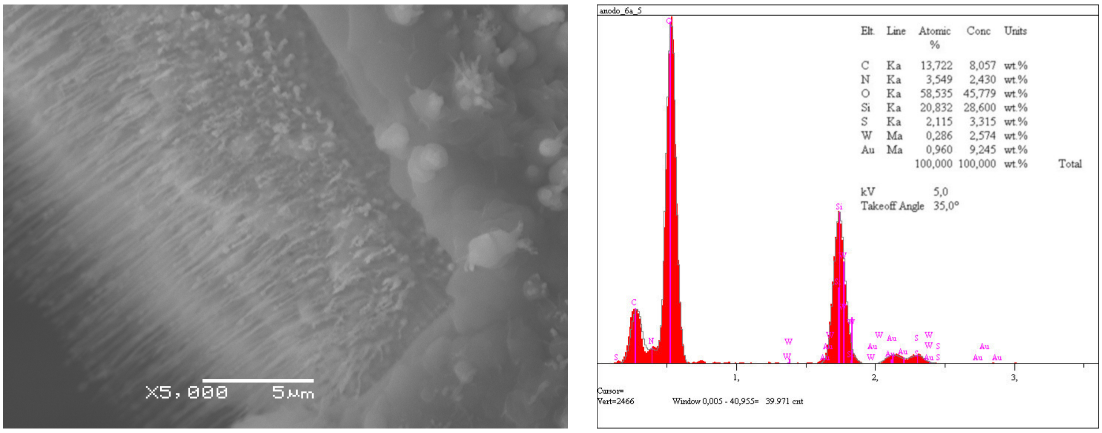

Elt.	Line	Atomic %	Conc	Units	
C	Ka	13,722	8,057	wt.%	
N	Ka	3,549	2,430	wt.%	
O	Ka	58,535	45,779	wt.%	
Si	Ka	20,832	28,600	wt.%	
S	Ka	2,115	3,315	wt.%	
W	Ma	0,286	2,574	wt.%	
Au	Ma	0,960	9,245	wt.%	
		100,000	100,000	wt.%	Total

kV 5,0
Takeoff Angle 35,0°

Figure 8.32 Whiskers on the anode wire and its relative EDX analysis.

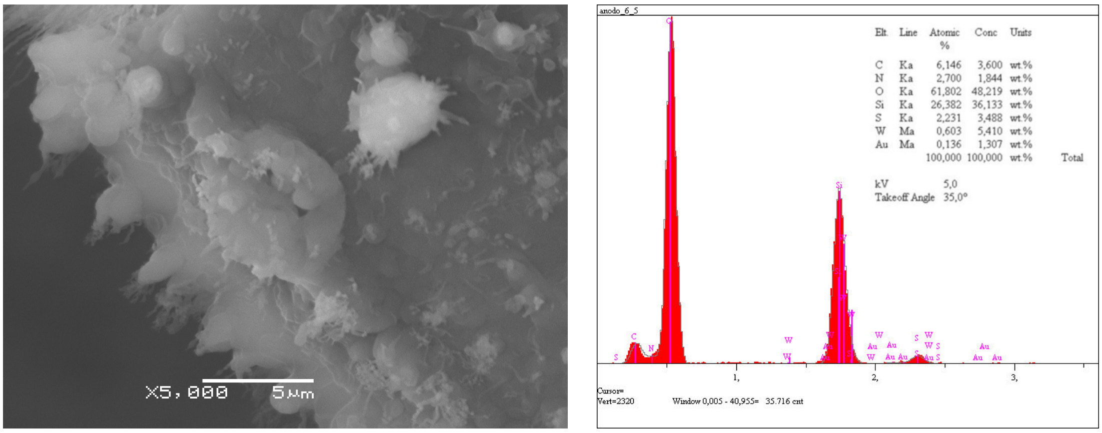

Elt.	Line	Atomic %	Conc	Units	
C	Ka	6,146	3,600	wt.%	
N	Ka	2,700	1,844	wt.%	
O	Ka	61,802	48,219	wt.%	
Si	Ka	26,382	36,133	wt.%	
S	Ka	2,231	3,488	wt.%	
W	Ma	0,603	5,410	wt.%	
Au	Ma	0,136	1,307	wt.%	
		100,000	100,000	wt.%	Total

kV 5,0
Takeoff Angle 35,0°

Figure 8.33 A bubble on the anode wire and its relative EDX analysis.

and oxygen concentrations.

In some rupture points the coating is lifted from the wire, as in Figure 8.34: this allows to determine a lower limit on the coating thickness of about 2 µm. Some ruptures extend for more than 100 µm: it is likely that they are due to mechanical stresses suffered after the chamber operation.

About 1 cm beyond the wire centre bubbles and whiskers gradually disappear, and at about 2 cm from the centre the coating is free from additional deposits. Going further the coating itself becomes thinner and thinner up to about 2.5 cm from the centre (see Figure 8.35). Here the wire appears clear of coatings, but EDX analysis shows almost no trace of gold and a large presence of oxygen and silicon, as in the case of cathodes.

In order to estimate the contaminations that are not ascribable to ageing, EDX analysis was performed on the wire section in the point at which the wire was cut (see Figure 8.36). The spectrum includes tungsten peaks with traces of gold and a carbon contamination of the order of

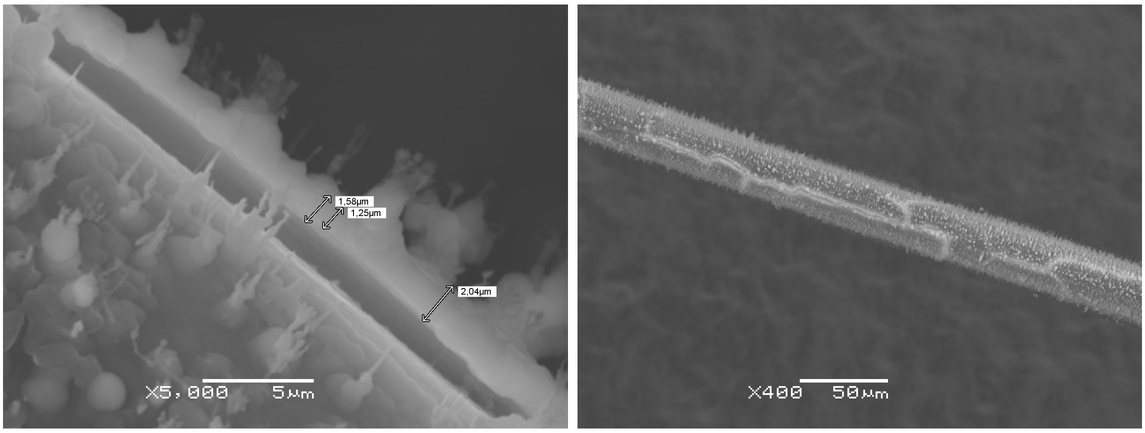

Figure 8.34 SEM images showing ruptures of the coating with estimates of the coating thickness.

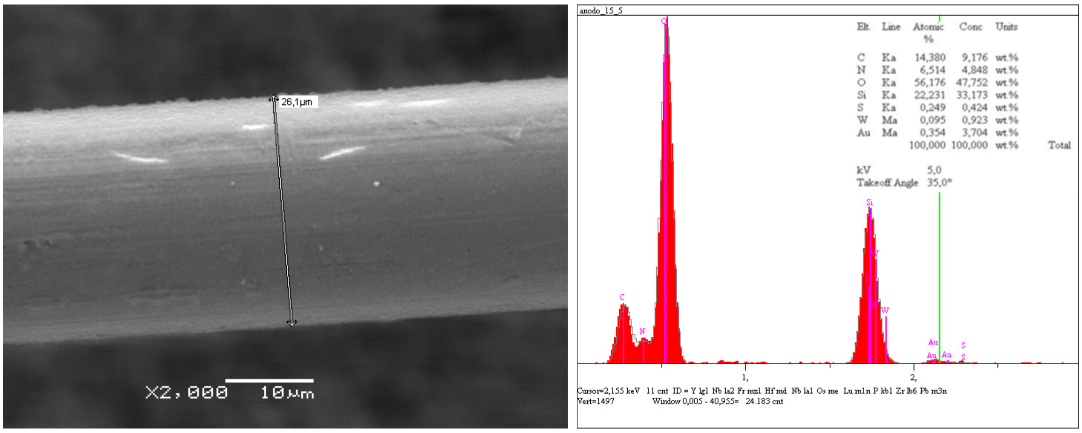

Elt.	Line	Atomic %	Conc	Units	
C	Ka	14,380	9,176	wt.%	
N	Ka	6,514	4,848	wt.%	
O	Ka	56,176	47,752	wt.%	
Si	Ka	22,231	33,173	wt.%	
S	Ka	0,249	0,424	wt.%	
W	Ma	0,095	0,923	wt.%	
Au	Ma	0,354	3,704	wt.%	
		100,000	100,000	wt.%	Total

kV 5,0
Takeoff Angle 35,0°

```
Cursor=2,155 keV   11 cnt  ID = Y lg1  Nb la2  Fr mz1  Hf md  Nb la1  Os me  Lu m1n  P kb1  Zr lb6  Pb m3n
Vert=1497              Window 0,005 - 40,955=   24.183 cnt
```

Figure 8.35 SEM image and EDX spectrum at about 2.5 cm from of the anode centre.

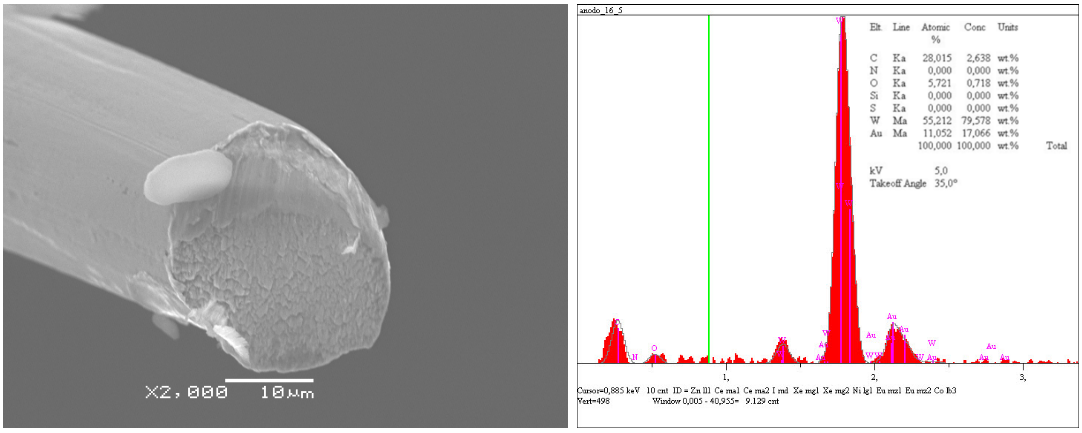

Elt.	Line	Atomic %	Conc	Units	
C	Ka	28,015	2,638	wt.%	
N	Ka	0,000	0,000	wt.%	
O	Ka	5,721	0,718	wt.%	
Si	Ka	0,000	0,000	wt.%	
S	Ka	0,000	0,000	wt.%	
W	Ma	55,212	79,578	wt.%	
Au	Ma	11,052	17,066	wt.%	
		100,000	100,000	wt.%	Total

kV 5,0
Takeoff Angle 35,0°

```
Cursor=0,885 keV   10 cnt  ID = Zn ll1  Ce ma1  Ce ma2  I md  Xe mg1  Xe mg2  Ni lg1  Eu mz1  Eu mz2  Co lb3
Vert=498               Window 0,005 - 40,955=   9.129 cnt
```

Figure 8.36 SEM image and EDX spectrum of a section of the aged anode wire.

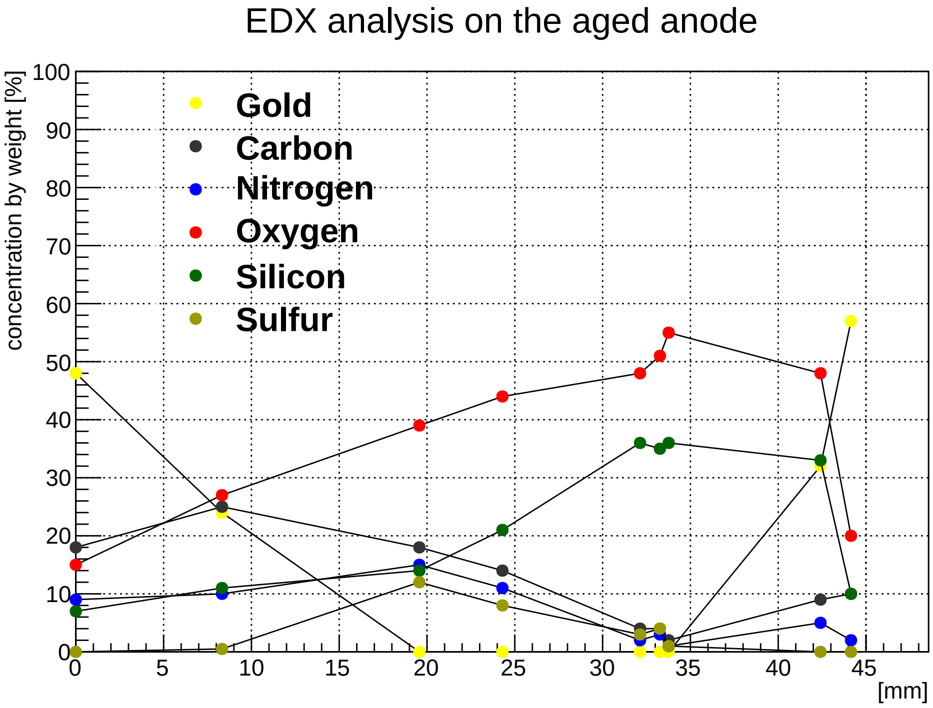

Figure 8.37 Concentrations of the detected elements as a function of the position on the anode wire. The origin of the abscissa is arbitrary.

the percent level. From the SEM image, the thickness of gold plating can be estimated to be about 1 µm.

In conclusion, SEM and EDX analyses confirm the presence of deposits. Figure 8.37 shows the indicative concentrations of the detected elements as a function of the position. The area where gold is shaded by other elements has an indicative length of about 3 cm. Silicon concentration seems to be positively correlated to th oxygen concentration. The length of the area where the coating is thicker is about 1.5 cm, compatible with the size of the portion of the wire that was irradiated during the ageing test. A slight left-right asymmetry may be present, but it cannot be traced back to the direction of the gas flow since such information was lost during sample preparation.

Summary

The ageing tests performed foresee moderate gain loss in the data acquisition period of the experiment. Figure 8.38 shows the percentage gain loss in one year of data taking in the various locations in the drift chamber. In the central region of the hottest wire the gain loss is about 16 %/year, while in most wires the gain loss is below 10%/year.

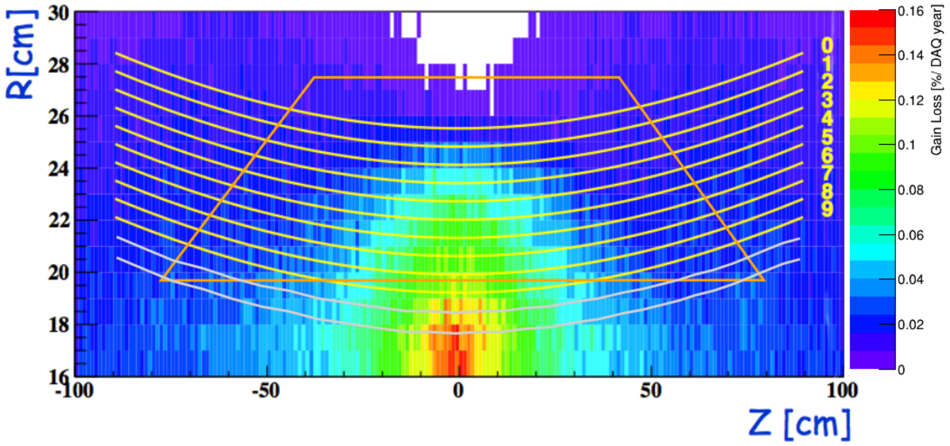

Figure 8.38 Percentage gain loss in the new drift chamber for MEG^{UP} .

As performed in the ageing test of Prototype I, the nominal gain can be restored by slightly incresing the high voltage of the chamber.

Conclusions and Outlook

Charged lepton flavour violating decays are prohibited in the framework of the Standard Model, but many of its extensions predict measurable values for such decays. Several experiments are running or being designed to measure (or to set a limit on) such processes. Among these, the MEG experiment has recently set a new upper limit of the $\mu \to e\gamma$ branching ratio. The process has a simple kinematics but very good resolutions are needed in order to discard the huge background. In order to improve its sensitivity, an upgrade of the experiment has been proposed; the new drift chamber will be a key detector in the upgrade, with performances and acceptance higher than that of the current experiment.

After reviewing basic concepts ofthe physics behind particle detection by means of a drift chamber, we showed the operation of a single-cell prototype as regards the measurement of its working point, response to radiation and gain. A more refined prototype was used to test all the chain involved in particle tracking with a drift chamber: a simple three-cell prototype was used to illustrate the basis of tracking in gaseous drift-chambers. Preliminary measurements of single-hit resolutions are very promising and show values of $\sigma \approx 100$ µm in a configuration very close to that expected for the MEG$^{\mathrm{UP}}$ experiment. Future campaigns of measurements with cosmic rays are envisaged, to confirm this value and to study its dependence on the various operating parameters. In what followed, we concentrated on the main focus of this thesis: drift chamber ageing.

We reviewed the causes of ageing and the parameters that can enhance or limit ageing effects. We also showed ageing tests procedures found in literature, highlighting their reliability and their limits. We contextualised in the MEG$^{\mathrm{UP}}$ the issues in realising ageing tests and set up the experimental apparatus needed for the tests. The geometrical and spectral characteristics of the irradiating sources were studied and their working points were determined.

Two ageing tests were performed and both of them foresee moderate gain loss in the data acquisition period of the experiment. In the central region of the hottest wire the gain loss is about 16 %/year, while in most wires the gain loss is below 10%/year. Microanalyses on aged wires showed the presence of silicones and carbon-rich deposits on wires.

The resolution and ageing measurements performed in this work of thesis contributed in proving the feasibility of the MEG$^{\mathrm{UP}}$ drift chamber, to have the proposal approved by the PSI scientific committee.

Ringraziamenti

Alla fine di questi anni di università sembra difficile riconoscere le persone che più o meno coscientemente meritano un "grazie", ma proviamoci...

Vorrei cominciare con le persone che mi hanno guidato, accompagnato e/o sostenuto nel periodo senza dubbio più intenso di questi ultimi anni: la tesi. Ringrazio l'intero gruppo MEG di Pisa per l'accoglienza e per quanto imparato alle riunioni. In particolare Alessandro Baldini, per avermi convinto che nel gruppo MEG avrei potuto fare il tipo di tesi che cercavo e Marco Grassi, per le chiacchierate sul nuovo tracciatore e per avermi insegnato che il modo migliore di pensare a come fare qualcosa, è cominciare a farla. Sentite grazie a Simeone per le ore passate in laboratorio, per avermi consacrato nell'albo dei "fisici pasticcioni" e per i ricchi e succulenti pasticciotti presi a Lecce. Ringrazio il prof. Grancagnolo e la dott.ssa D'Elia per la disponibilità nell'effettuare le analisi SEM e EDX a Lecce. Ringrazio infine il mio relatore Giovanni Signorelli, per la dedizione e l'entusiasmo spesi nel corso di quest'anno e specialmente negli ultimi mesi, per avermi dato fiducia nel lasciarmi gestire in modo indipendente alcune misure, tra cui il secondo test di *ageing*[1] e per avermi ripetuto più volte che il lavoro di gruppo necessita la vicinanza spaziotemporale tra le parti.

Ringrazio mio papà, mia sorella e tutta la mia famiglia per la fiducia e il supporto dimostrati in questi anni da studente “fuori sede”.

Diventa ora difficile ringraziare gli amici: non essendo possibile una separazione in categorie stagne seguirò la metodologia del regista Ferretti. Ringrazio coloro che mi sono stati vicino e che hanno condiviso con me questo periodo di tesi: Stefano ed Emanuele con cui ho trascorso giorni e notti in aula laureandi (anche se spesso qualche canzone...); Alberto, Stefania e Simone per la compagnia nelle cene in queste calde serate estive (in particolare a Stefania per non essersi lamentata, da brava vicina di scrivania); Tiziano e Davide per la compagnia e le risate dentro e fuori l'aulaureandi.

Arriviamo ora al ricco numero di amici che hanno allietato la mia vita pisana. *In primis* un grazie a Roberto per essere stato un coinquilino paziente per cinque lunghi anni di università nella *suîte* del PUSG e a Lev per l'insostituibile compagnia. Ringrazio Laura, Romualdo e Felice per le cene e le serate passate insieme. Adele, Anna, Niccolò, il Paglia e tutti gli amici con cui abbiamo condiviso gli alti e i bassi della vita universitaria. Un grazie ai Cisanello boys, Emilio,

---

[1] seppur con qualche biglietto minatorio.

Filippo, Giacomo e Stefano perché sono stati dei coinquilini eccezionali.

Ringrazio Federica, per tutti i bei momenti passati insieme, per esserci tirati su il morale a vicenda nei periodi più cupi della scrittura della tesi e perché anche per noi è finalmente giunto il momento di andare in vacanza.

Bibliography

[1] Seth H. Neddermeyer and Carl D. Anderson. Note on the nature of cosmic-ray particles. *Phys. Rev.*, 51:884–886, May 1937.

[2] E. P. Hincks and B. Pontecorvo. Search for gamma-radiation in the 2.2-microsecond meson decay process. *Phys. Rev.*, 73:257–258, Feb 1948.

[3] R. D. Sard and E. J. Althaus. A search for delayed photons from stopped sea level cosmic-ray mesons. *Phys. Rev.*, 74:1364–1371, Nov 1948.

[4] O. Piccioni. Search for photons from meson-capture. *Phys. Rev.*, 74:1754–1758, Dec 1948.

[5] C. L. Cowan, Jr., F. Reines, F. B. Harrison, H. W. Kruse, and A. D. McGuire. Detection of the Free Neutrino: A Confirmation. *Science*, 124:103–104, July 1956.

[6] G. Danby, J.M. Gaillard, Konstantin A. Goulianos, L.M. Lederman, Nari B. Mistry, et al. Observation of High-Energy Neutrino Reactions and the Existence of Two Kinds of Neutrinos. *Phys.Rev.Lett.*, 9:36–44, 1962.

[7] Michael E. Peskin and Daniel V. Schroeder. An Introduction to quantum field theory. *Levant Books*, 1995.

[8] I.J.R. Aitchison and A.J.G. Hey. Gauge theories in particle physics: A practical introduction. Vol. 1: From relativistic quantum mechanics to QED. *Taylor & Francis*, 2003.

[9] I.J.R. Aitchison and A.J.G. Hey. Gauge theories in particle physics: A practical introduction. Vol. 2: Non-Abelian gauge theories: QCD and the electroweak theory. *Taylor & Francis*, 2004.

[10] Riccardo Barbieri. Ten Lectures on the ElectroWeak Interactions. 2007, 0706.0684.

[11] V.N. Aseev, A.I. Belesev, A.I. Berlev, E.V. Geraskin, A.A. Golubev, et al. Measurement of the electron antineutrino mass in tritium beta decay in the Troitsk nu-mass experiment. *Phys.Atom.Nucl.*, 75:464–478, 2012.

[12] R.N. Mohapatra and P.B. Pal. Massive neutrinos in physics and astrophysics. Second edition. *World Sci.Lect.Notes Phys.*, 60:1–397, 1998.

[13] J. Beringer et al. Review of Particle Physics (RPP). *Phys.Rev.*, D86:010001, 2012.

[14] Samoil M. Bilenky, S.T. Petcov, and B. Pontecorvo. Lepton Mixing, $\mu \to e\gamma$ Decay and Neutrino Oscillations. *Phys.Lett.*, B67:309, 1977.

[15] D.N. Dinh, A. Ibarra, E. Molinaro, and S.T. Petcov. The μ-e Conversion in Nuclei, $\mu \to e\gamma$, $\mu \to eee$ Decays and TeV Scale See-Saw Scenarios of Neutrino Mass Generation. *JHEP*, 1208:125, 2012, 1205.4671.

[16] Mitsuru Kakizaki, Yoshiteru Ogura, and Fumitaka Shima. Lepton flavor violation in the triplet Higgs model. *Phys.Lett.*, B566:210–216, 2003, hep-ph/0304254.

[17] D.J.H. Chung, L.L. Everett, G.L. Kane, S.F. King, Joseph D. Lykken, et al. The Soft supersymmetry breaking Lagrangian: Theory and applications. *Phys.Rept.*, 407:1–203, 2005, hep-ph/0312378.

[18] Richard L. Arnowitt, Bhaskar Dutta, and B. Hu. Yukawa textures, neutrino masses and Horava-Witten M theory. *Nucl.Phys.*, B682:347–366, 2004, hep-th/0309033.

[19] Junji Hisano, Minoru Nagai, P. Paradisi, and Yasuhiro Shimizu. Waiting for $\mu \to e\gamma$ from the MEG experiment. *JHEP*, 0912:030, 2009, 0904.2080.

[20] S. Antusch, E. Arganda, M.J. Herrero, and A.M. Teixeira. Impact of theta(13) on lepton flavour violating processes within SUSY seesaw. *JHEP*, 0611:090, 2006, hep-ph/0607263.

[21] A. M. Baldini, F. Cei, C. Cerri, S. Dussoni, L. Galli, M. Grassi, D. Nicolò, F. Raffaelli, F. Sergiampietri, G. Signorelli, F. Tenchini, D. Bagliani, M. De Gerone, F. Gatti, E. Baracchini, Y. Fujii, T. Iwamoto, D. Kaneko, T. Mori, M. Nishimura, W. Ootani, R. Sawada, Y. Uchiyama, G. Boca, P. W. Cattaneo, A. de Bari, R. Nardò, M. Rossella, M. Cascella, F. Grancagnolo, A. L'Erario, A. Maffezzoli, A. Miccoli, G. Onorato, G. Palamà, M. Panareo, A. Pepino, S. Rella, G. F. Tassielli, G. Zavarise, G. Cavoto, A. Graziosi, G. Piredda, E. Ripiccini, C. Voena, D. N. Grigoriev, F. Ignatov, B. I. Khazin, A. Popov, Y. V. Yudin, T. Haruyama, S. Mihara, H. Nishiguchi, A. Yamamoto, M. Hildebrandt, P.-R. Kettle, A. Papa, F. Renga, S. Ritt, A. Stoykov, T. I. Kang, G. Lim, W. Molzon, Z. You, N. Khomutov, A. Korenchenko, N. Kravchuk, and N. Kuchinksy. MEG Upgrade Proposal. *ArXiv e-prints*, January 2013, 1301.7225.

[22] P. Depommier, J.P. Martin, J.M. Poutissou, R. Poutissou, D. Berghofer, et al. A New Limit on the $\mu \to e\gamma$ Decay. *Phys.Rev.Lett.*, 39:1113, 1977.

[23] A. van der Schaaf, R. Engfer, H.P. Povel, W. Dey, H.K. Walter, et al. A search for the decay $\mu \to e\gamma$. *Nucl.Phys.*, A340:249, 1980.

[24] W.W. Kinnison, H.L. Anderson, H.S. Matis, S.C. Wright, R.L. Carrington, et al. A search for the decay $\mu \to e\gamma$. *Phys.Rev.*, D25:2846, 1982.

[25] R.D. Bolton, M.D. Cooper, J.S. Frank, A.L. Hallin, P.A. Heusi, et al. Search for Rare Muon Decays with the Crystal Box Detector. *Phys.Rev.*, D38:2077, 1988.

[26] M.L. Brooks et al. New limit for the family number nonconserving decay $\mu \to e\gamma$. *Phys.Rev.Lett.*, 83:1521–1524, 1999, hep-ex/9905013.

[27] J. Adam, X. Bai, A. M. Baldini, E. Baracchini, C. Bemporad, G. Boca, P. W. Cattaneo, G. Cavoto, F. Cei, C. Cerri, A. de Bari, M. De Gerone, T. Doke, S. Dussoni, J. Egger, Y. Fujii, L. Galli, F. Gatti, B. Golden, M. Grassi, A. Graziosi, D. N. Grigoriev, T. Haruyama, M. Hildebrandt, Y. Hisamatsu, F. Ignatov, T. Iwamoto, D. Kaneko, P.-R. Kettle, B. I. Khazin, N. Khomotov, O. Kiselev, A. Korenchenko, N. Kravchuk, G. Lim, A. Maki, S. Mihara, W. Molzon, T. Mori, D. Mzavia, R. Nardò, H. Natori, D. Nicolò, H. Nishiguchi, Y. Nishimura, W. Ootani, M. Panareo, A. Papa, G. Piredda, A. Popov, F. Renga, E. Ripiccini, S. Ritt, M. Rossella, R. Sawada, F. Sergiampietri, G. Signorelli, S. Suzuki, F. Tenchini, C. Topchyan, Y. Uchiyama, C. Voena, F. Xiao, S. Yamada, A. Yamamoto, S. Yamashita, Z. You, Yu. V. Yudin, and D. Zanello. New constraint on the existence of the $\mu \to e\gamma$ decay. *Phys. Rev. Lett.*, 110:201801, May 2013.

[28] Yoshitaka Kuno and Yasuhiro Okada. Muon decay and physics beyond the standard model. *Rev.Mod.Phys.*, 73:151–202, 2001, hep-ph/9909265.

[29] J. Adam, X. Bai, A.M. Baldini, E. Baracchini, C. Bemporad, et al. The MEG detector for $\mu + \to e + \gamma$ decay search. *Eur.Phys.J.*, C73:2365, 2013, 1303.2348.

[30] F. Sauli. Principles of Operation of Multiwire Proportional and Drift Chambers. 1977.

[31] Walter Blum, Luigi Rolandi, and Werner Riegler. Particle detection with drift chambers. *Springer*, 2008.

[32] Claus Grupen and Boris Schwartz. Particle detectors. *Cambridge University Press*, 2008.

[33] B. Sadoulet. Fundamental Processes in Drift Chambers. *Phys.Scripta*, 23:434, 1981.

[34] Garfield++ – simulation of tracking detectors. http://garfieldpp.web.cern.ch/garfieldpp/.

[35] Gas Encyclopaedia. Air liquid. *Editor Elsevier*, 1976.

[36] J. F. Ziegler. SRIM-2003. *Nuclear Instruments and Methods in Physics Research B*, 219:1027–1036, June 2004.

[37] R.H. Pratt. Tutorial on fundamentals of radiation physics:: interactions of photons with matter. *Radiation Physics and Chemistry*, 70(4–5):595 – 603, 2004. <ce:title>Indo-US Workshop on Radiation Physics with Synchrotrons and Other New Sources</ce:title>.

[38] A. C. Thompson, editor. *X-ray Data Booklet.* Lawrence Berkeley National Laboratory, University of California, second edition, jan 2009.

[39] A. Andryakov et al. Results from the full-length prototype of the {KLOE} drift chamber. *Nuclear Instruments and Methods in Physics Research Section A: Accelerators, Spectrometers, Detectors and Associated Equipment*, 409(1–3):84 – 86, 1998.

[40] John A. Kadyk. Wire chamber aging. *Nucl.Instrum.Meth.*, A300:436–479, 1991.

[41] Aging workshop 2001. *Nuclear Instruments and Methods in Physics Research Section A: Accelerators, Spectrometers, Detectors and Associated Equipment*, 515(1–2), 2003.

[42] Lourdu M. Yeddanapalli. The decomposition of methane in glow discharge at liquid-air temperature. *The Journal of Chemical Physics*, 10(5):249–260, 1942.

[43] National Istitute of Standard and Technology. Isobutane. *http://webbook.nist.gov/cgi/cbook.cgi?ID=C75285*, July 2013.

[44] C. Niebuhr. Aging effects in gas detectors. *Nucl.Instrum.Meth.*, A566:118–122, 2006.

[45] T. Ferguson, G. Gavrilov, A. Korytov, A. Krivshich, Ekaterina Kuznetsova, et al. Aging studies of CMS muon chamber prototypes. *Nucl.Instrum.Meth.*, A488:240–257, 2002.

[46] V.E. Blinov. Procedure dependence of the ageing rate measurements. *Nuclear Instruments and Methods in Physics Research Section A: Accelerators, Spectrometers, Detectors and Associated Equipment*, 419(2–3):676 – 679, 1998.

[47] D. Allspach et al. Aging in the large CDF axial drift chamber. *IEEE Trans.Nucl.Sci.*, 52:2956–2962, 2005.

[48] H. A. Kramers. On the theory of x-ray absorption and of the continuous x-ray spectrum. *Philosophical Magazine Series 6*, 46(275):836–871, 1923, http://www.tandfonline.com/doi/pdf/10.1080/14786442308565244.

[49] R. Jenkins and J.L. de Vries. Practical x-ray spectrometry. *Springer-Verlag*, 1967.

[50] Olsen K. Dragoset R.A. Chang J. Kishore A.R. Kotochigova S.A. Chantler, C.T. and D.S. Zucker. X-Ray Form Factor, Attenuation and Scattering Tables (version 2.1). *National Institute of Standards and Technology, Gaithersburg, MD.*, [Online] Available: http://physics.nist.gov/ffast [Monday, 17-Jun-2013 10:06:04 EDT].